Intergranular Corrosion Propagation in Sensitized Al-Mg Alloys

A Dissertation

Presented to

the faculty of the School of Engineering and Applied Science

University of Virginia

in partial fulfillment

of the requirements for the degree

Doctor of Philosophy in Materials Science and Engineering

by

Mary Lyn C. Lim

May 2016

APPROVAL SHEET

The dissertation is submitted in partial fulfillment
of the requirements for the degree of
Doctor of Philosophy in Materials Science and Engineering

_____
Mary Lyn C. Lim
(Author)

The dissertation has been read and approved by the examining committee:

_____
Dr. Robert G. Kelly
(Dissertation Co-advisor)

_____
Dr. John R. Scully
(Dissertation Co-advisor)

_____
Dr. Richard P. Gangloff
(Committee Chairman)

_____
Dr. James T. Burns

_____
Dr. Patrick E. Hopkins

_____
Dr. N.J. Henry Holroyd

Accepted for the School of Engineering and Applied Science:

_____
Dr. Craig H. Benson
Dean, School of Engineering and Applied Science
May 2016

Abstract

Aluminum-magnesium alloys (AA5XXX) are currently used as a lightweight substitute for steel due to their low cost, high strength-to-weight ratio, good weldability, and excellent uniform corrosion resistance. These alloys are non-heat-treatable and derive their strength from the combination of work hardening through cold work and solid solution strengthening via addition of magnesium and manganese. During service, these alloys can become metallurgically sensitized and susceptible to intergranular corrosion (IGC) when an active β-phase (Al_3Mg_2) precipitates on grain boundaries. Intergranular corrosion can lead to mass loss through grain fall-out, and intergranular stress corrosion cracking (IGSCC) in the presence of stress.

Considerable propagation depth is required for transition from IGC to IGSCC or failure by IGC penetration. As such, the overall objective of this research to develop a quantitative understanding of IGC in sensitized AA5XXX from the threshold conditions for initiation, propagation mechanism, and kinetics standpoints. An electrochemical IGC characterization study of factors influencing IGC propagation depth in AA5083 in 0.6 M NaCl solution demonstrated that IGC propagation rate was governed by applied potential, degree of sensitization (DoS), exposure time, propagation orientation, sensitization temperature, and cold work temper. These results established that IGC propagation depth is linear with time; that the extent of IGC over the exposure of 100 h was linearly proportional to the applied potential, with the linear potential dependence increasing with DoS; and that there exists an IGC threshold potential below which only isolated pitting corrosion occurred. Electrochemical IGC characterization on specimens with various degrees of connectivity, coupled with computational resistor network analysis, proved that the linear dependencies on time, depth, and potential are due to a high degree of IGC fissure connectivity, an evolution of such connectivity over time, and its dependency on physical dimensions of test samples relative to grain size. Consequently, multiple interconnected fissure network led to a low resistance

ionic electrolyte path between the fissure tip and the external surface, given that the corrosion fissures are filled with an ionically conducting electrolyte. Long-term electrochemical testing demonstrated the extent of the linear IGC propagation kinetics, beyond which power law kinetics apply and IGC stifling occurred.

The explanation for an IGC threshold potential was elucidated via quantitative understanding of IGC propagation stabilization and repassivation phenomenon in terms of repassivation potential and the pit stability product linked to the need to maintain a depassivating fissure chemical environment. The absence of IGC propagation at or below the threshold potential was shown to be due to the repassivation of the fissure tip in the fissure chemistry. The more negative repassivation potential and higher pit stability product observed for the sensitized condition were attributed to the influence of β-phase dissolution, in terms of the chemical role of Mg^{2+}, on the fissure chemistry. The dissolution of β-phase generates a local surge of Mg^{2+}, acidifying the fissure tip environment via cation hydrolysis of Al^{3+} aided by $MgCl_2$, resulting in a more aggressive condition that allow further stable IGC propagation. Moreover, DoS further dictates the stability conditions for propagation in sensitized conditions by providing sufficient β-phase coverage on sensitized grain boundaries.

The output of the research summarized here is of both scientific and technological importance. The scientific interpretation of the IGC propagation kinetics with respect to the factors studied will provide insight for mechanistic understanding of IGC evolution and development that includes metallurgical, geometric, and electrochemical variables. This knowledge and understanding will aid in the development of new alloys and mitigation strategies, as well as optimization of structure design as well as development of predictive models that estimate and forecast the IGC damage progression in this class of alloy. Technological impacts included improved ability to anticipate and manage structural damage accumulation through control of electrochemical potential relative to threshold potentials in existing sensitized alloys in marine service.

To my parents, grandparents, and siblings

for the love, inspiration, and encouragement

To Dr. William van Ooij[†]

for introducing me to corrosion science and electrochemistry

Acknowledgements

I would like to express my sincerest gratitude to my co-advisors, Professors Robert G. Kelly and John R. Scully, for taking me under their wings. Unlike many of my peers, I was lucky enough to have two dedicated advisors, judicious mentors, and toughest critics to guide me through my graduate school journey. They gave me constant support and guidance in various aspects of my academic and research work. During the frustrating times, they stood by me with their unwavering encouragement and show of confidence. They provided me great learning avenues and taught me invaluable lessons to help me grow not only as a researcher but also as a person. This dissertation is in its current form because of their expert guidance, insightful inputs, and constructive criticisms.

A special thank you to each member of my committee, Profs. Richard P. Gangloff, James T. Burns, Patrick E. Hopkins, and Henry Holroyd for committing their time and effort, and for their thoughtful review and constructive comments. Their advice and guidance in this work is greatly appreciated.

I appreciate the help of all my colleagues at the Center for Electrochemical Science and Engineering (CESE) during the course of my dissertation. In particular, a very special thank you goes to those on the AA5XXX project, Wasiu Adedeji, Dr. Swati Jain, Dr. Lei Chen, Dr. Elissa Bumiller, Dr. Cortney B. Crane,

of Cincinnati. Without their guidance, I would certainly have traverse a very different academic path.

Finally, I am forever grateful to my family for the unconditional love, enduring support, and unwavering encouragement they provided throughout my graduate school journey. My parents and grandparents sacrificed everything and hurdled every obstacle with uncommon grace and courage to provide their children a better education. My siblings, through their diligence and patience, have set the bar high. They have been my role models and trailblazers, who inspire and prod me to dream big, to go outside of my comfort zone, and to be a better person. None of this could have been accomplished without my family.

Table of Contents

List of Tables

List of Figures

clean grain boundary if no β-phase decorate a grain boundary. For example, for a total of 80 grain boundaries, 42 grain boundaries have more than 70% of their lengths covered with β-phase, 22 have less than 70%, and the remaining 16 have no β-phase at all. This is equivalent to 52.5% of high β-phase coverage grain boundaries, 27.5% of low β-phase coverage grain boundaries, and 20% of clean grain boundaries. (b) Barker's etched revealing grain structure; (c) SEM LEI image of phosphoric acid etched revealing attacked sites on the ST surface.

AA5083 (2 mg/cm^2) are marked with dashed lines.[19] Also, the breakdown potential of β-phase (not included in the figure) is -0.96 V$_{SCE}$.[38]

points for 100 h exposure were taken from earlier measurements at various applied current densities (Chapter 3). As a comparison, the IGC spreading potential for sensitized AA5083 and the pitting potential for unsensitized AA5083 (2 mg/cm^2) are marked with dashed lines.[16] Also, the open circuit potential of β-phase (not included in the figure) is -1.162 V$_{SCE}$.[17]

List of Symbols

DoS	Degree of sensitization
β-phase	Al_3Mg_2
α-phase	Al-4Mg matrix phase
V_{SCE}	Potential measured vs SCE
α	Log-logistics distribution shape factor
δ	Log-logistics distribution scale factor
γ	Log-logistics distribution location factor
t_{exp}	Exposure time
β	T-test coefficient
i	Current density
i_{lim}	Limiting current density
i_{act}	Activation current density
i_{total}	Total current density
i_{pass}	Passive current density
r_{mean}	Mean-equivalent radius
T	Temperature
Q	Charge
EW	Equivalent weight
P	Density
A	area
R_{ohm}	Ohmic resistance
R_{sol}	Solution resistance
R_{pit}	Pit resistance
R_{eff}	Effective resistance
E_{rp}	Repassivation potential
θ_β	β-phase coverage
E_{pit}	Pitting potential
$E_{spreading}$	IGC spreading potential
E_{crit}	IGC threshold potential
pK_{xy}	Formation constant
Q_{xy}	Formation quotient
f_{act}	Fraction of active area
F	Faraday's constant
D	Diffusivity coefficient
t	time

1   Introduction

1.1   Background

The highly competitive field of commercial shipping and the expanding demands of the US Navy has resulted to the ever increasing demand for marine vessel efficiency. Rising fuel costs and the need to carry larger loads over greater distances are the main motivations for improving ship design and construction. This escalating requirement for speed, coverage, and fuel economy has emphasized the demand for lightweight structural materials that possess a challenging combination of material properties. Aluminum-magnesium alloys (Al-Mg or AA 5XXX series) are currently used as a lightweight substitute for steel due to their low cost, high strength-to-weight ratio, good weldability, and excellent uniform corrosion resistance.[1–3] However, alloys containing more than 3 wt% of Mg, when exposed to standard service temperatures for extended periods of time, can become sensitized and susceptible to localized corrosion; particularly intergranular corrosion (IGC).[2,4–8] Intergranular corrosion can lead to mass loss through grain fall-out, and transition to intergranular stress corrosion cracking (IGSCC), as well as corrosion fatigue in the presence of stress.[3,9–17]

1.1.1   Metallurgy, Microstructure, and Sensitization of Al-Mg Alloys

Al-Mg alloys are non-heat-treatable and derive their strength from a combination of solid solution strengthening via addition of magnesium and work hardening through cold working.[18–20] To further improve strength and prevent

grain growth upon recrystallization, small amounts of manganese, chromium, and titanium are added. Together with elemental impurities, these intentional additives create a range of different intermetallic or constituent particles distributed through the alloy microstructure. The most common intermetallic compounds are Al_6Mn, Al_6MnFe, Al-(Si, Mn, Fe, Cr), Mg_2Si, and Al_3Mg_2 phases.[18,20] Conventional Al-Mg alloys are used in annealed or strain hardened states, and various strain hardening tempers are shown in Table 1.1. The grain morphology and size in the final gauge plate, for a certain level of Mg, is controlled by both the level of cold work and the final annealing treatment. The orientation convention and microstructure of a strain hardened plate displayed in Figure 1.1 shows the presence of elongated grains, with constituent particles aligned in the rolling direction.

Table 1.1. Temper designations for strain-hardened alloys[21]

Temper	Description
O	Annealed, recrystallized. Temper with the lowest strength and greatest ductility.
H1	Strain hardened.
H2	Strain hardened and partially annealed.
H3	Strain hardened and stabilized.
H18	Strain hardened during fabrication. Temper with ultimate tensile strength (UTS) equivalent to about 75% cold reduction after full annealing.
H131	Strain hardened during fabrication. Temper with mean UTS equivalent to three-eighths of the UTS of a full-hard condition (H18).
H321	Strain hardened during fabrication. Amount of strain hardening controlled during hot and cold working.
H116	Special strain hardened. Corrosion resistant temper for aluminum magnesium alloys.
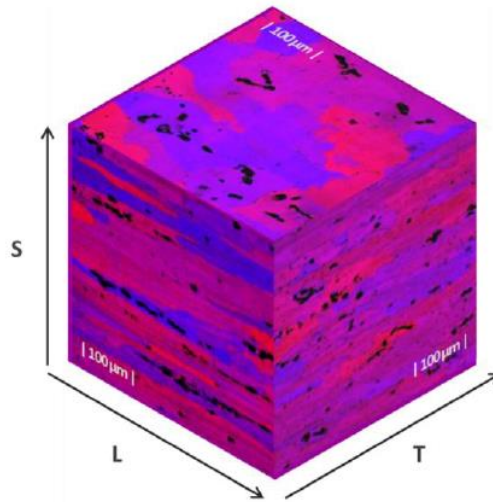
Figure 1.1. Microstructure of AA5083-H131 after electrolytic Barker's etching revealing elongated grains in the rolling direction (L) and thinnest through the thickness of the plate (S).

Table 1.2. Chemical composition (wt %) of select commercial AA 5XXX alloys[18,19]

Alloy	Mg	Si	Mn	Fe	Cr	Ti	Cu	Zn	Other
5005	0.5-1.1	0.30	0.20	0.70	0.10	-	0.20	0.25	0.15
5052	2.2-2.8	0.25	0.10	0.40	0.15-0.35	-	0.10	0.10	0.15
5083	4.0-4.9	0.40	0.4-1.0	0.40	0.05-0.25	0.15	0.10	0.25	0.15
5086	3.5-4.5	0.40	0.2-0.7	0.50	0.05-0.25	0.15	-	0.25	0.15
5154	3.1-3.9	0.25	0.10	0.40	0.15-0.35	0.20	0.10	0.20	0.15
5182	4.0-5.0	0.20	0.2-0.5	0.35	0.10	0.10	0.15	0.25	0.15
5456	4.0-4.5	0.40	0.4-0.7	0.50	0.05-0.25	0.15	0.10	0.25	0.15

Typical chemical compositions of commercial Al-Mg alloys are shown in

Error! Reference source not found.. Magnesium (Mg) concentrations up to 12

wt. % can be found in cast Al-Mg alloys, whereas commercial wrought alloys have

Mg concentrations ranging from 0.5 to 6 wt. %.[20,22]   Although Mg has a high

solid solubility in aluminum, 14.9 wt. % at 450°C, this high solubility reduces to approximately 1.7 wt. % at room temperature.[23]   This reduction in solubility results in these alloys having a supersaturated solid solution (SSSS) α matrix of aluminum and magnesium at room temperature, which is typically retained via a solutionizing heat treatment and subsequent quenching process. For the range of Mg content in commercial alloys, this is evident from the Al-Mg phase diagram in Figure 1.2, where a two-phase field of α + β is present at thermodynamic equilibrium. When Al-Mg alloys containing more than 3 wt. % Mg are exposed to temperatures as low as 50°C for long periods of time, the magnesium atoms diffuse from the SSSS α matrix to low energy sites like grain boundaries.[6,23,24] When the local Mg concentration is sufficiently high, the β-phase (Al_3Mg_2) will precipitate via heterogeneous nucleation and growth to reduce the high interfacial energies.[4,12,25,26]   The precipitation of β-phase is reported to occur in the following sequence:

SSSS α-Al matrix → GP Zones → β" → β' → β (Al_3Mg_2)
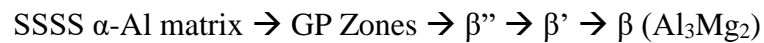
where GP zones are Guinier-Preston zones associated with Mg segregation, β" is an $L1_2$ phase, β' is a hexagonal phase, and finally the β is a complex face-centered cubic.[27] The temperature range over which Guinier-Preston Zones (GP zones) and β'' phases form is between 0 and 45°C (30 days), with their dissolution between 50° and 100°C. An increase in temperature from 100°C to 200°C marks the formation of the β' phase followed by the formation of the stable β-phase in the

4

range of 250-300°C.[27] The β-phase precipitates nucleate preferentially on grain boundaries, and at second-phase particles, then at dislocations, and finally throughout the bulk matrix.[28]
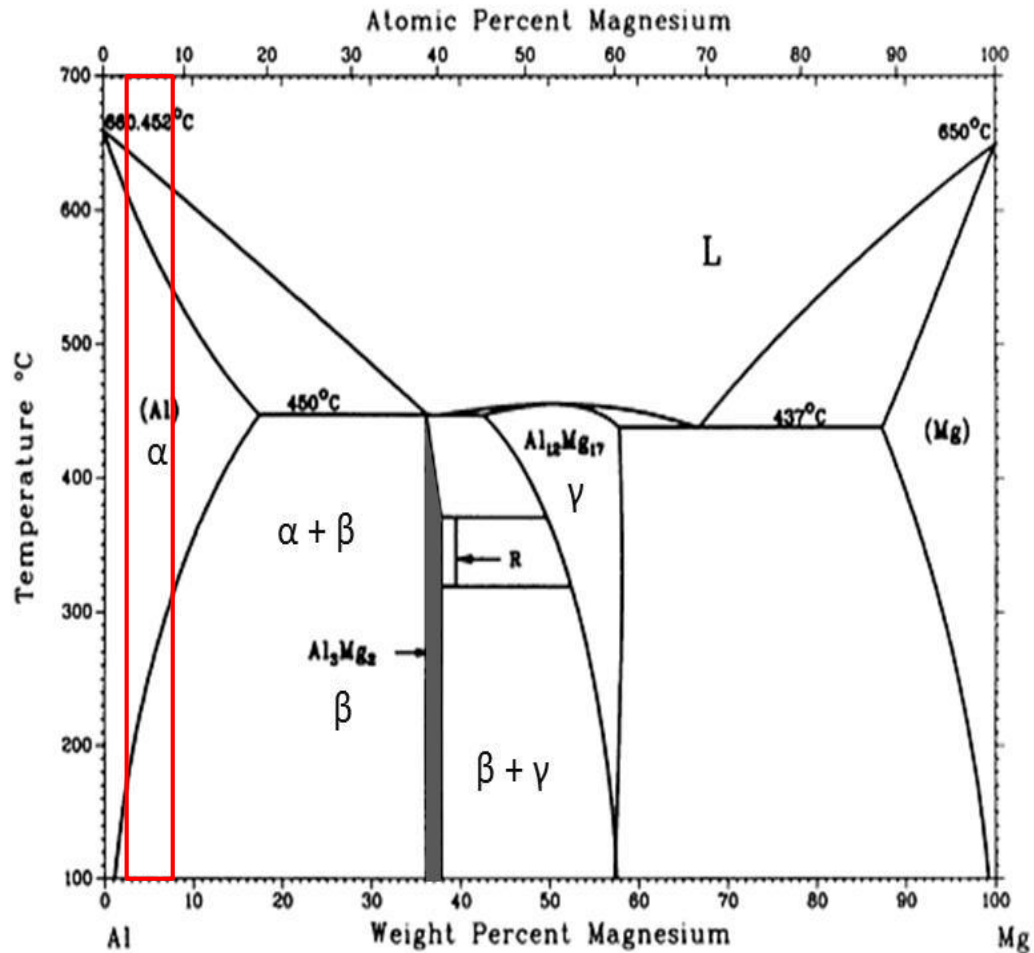
Figure 1.2. Al-Mg binary phase diagram with commercial alloy range highlighted (0.5 – 5 wt% Mg) and β-phase field shaded (~36 – 38 wt% Mg). Modified from [29]

The grain boundary precipitation of β-phase is dependent on alloy composition, temperature, exposure time, and grain boundary characteristics.[4,6,9,13,30–34] Davenport et al.[6] suggested that low angle grain boundaries ($\theta \leq 15^{\circ}$) do not facilitate β-phase precipitation based on the limited IGC occurrence observed, whereas Scotto D'Antuono et al.[31] reported that primary nucleation sites observed during in situ experiments are along low-angle grain boundaries. Nonetheless, both studies agreed that β-phase precipitate growth occurs along high-angle grain boundaries, with precipitate area increasing with misorientation angle. Besides grain boundary misorientation, grain boundary plane orientation was also reported to influence β-phase precipitation.[32] Precipitation occurs slowly at near-ambient temperatures, but proceeds quickly at elevated temperature (50-180°C).[6] Transmission electron microscopy (TEM) studies[4,13,25,26,30,35] on sensitized AA5083 revealed discrete β-phase precipitation along the grain boundaries and at the interface between manganese-rich intermetallics and the matrix after short exposure times (Figure 1.3a). After longer periods of exposure, the grain boundary β-phase precipitates coarsen, decorating the majority of the grain boundaries with longer precipitates (Figure 1.3b-d). The β-phase precipitates range from 50 nm to 190 nm in width and 100 nm to 1000 nm in length. These β-phase precipitates are anodic to the bulk matrix in near neutral salt solutions, which satisfy an electrochemical condition for an IGC path rendering the microstructure susceptible to IGC.[4,11,13,23,36,37]

Sensitization can occur either during alloy fabrication and processing or while in service, resulting in alloys that are susceptible to IGC.

To combat sensitization, many high-Mg content Al-Mg alloys are produced in stabilized tempers. Stabilization achieves a degree of IGC resistance by heat treatment at temperature just below the β-phase solvus temperature allowing much of the Mg to precipitate out of solid solution forming coarse β-phase intragranularly within the matrix, on sites away from grain boundaries.[38] This is believed to reduce the amount of Mg in solid solution, restricting the possibility of precipitation at the grain boundaries. The precise heat treatment temperature is dependent on the Mg content of the alloy. For an alloy with 4.4 wt. % Mg like AA5083, the stabilization temperature window is between 220°C and 240°C, whereas stabilization would occur between 260°C to 290°C for an alloy with 7 wt. % Mg.[38] Any temperatures below the lower bound of the stabilization temperature windows would result in grain boundary precipitation and sensitization. However, extended exposures at temperatures just below the temperature window is said to result in coarsening of the grain boundary β-phase and precipitation of intragranular β-phase, eventually providing stabilization.[38]
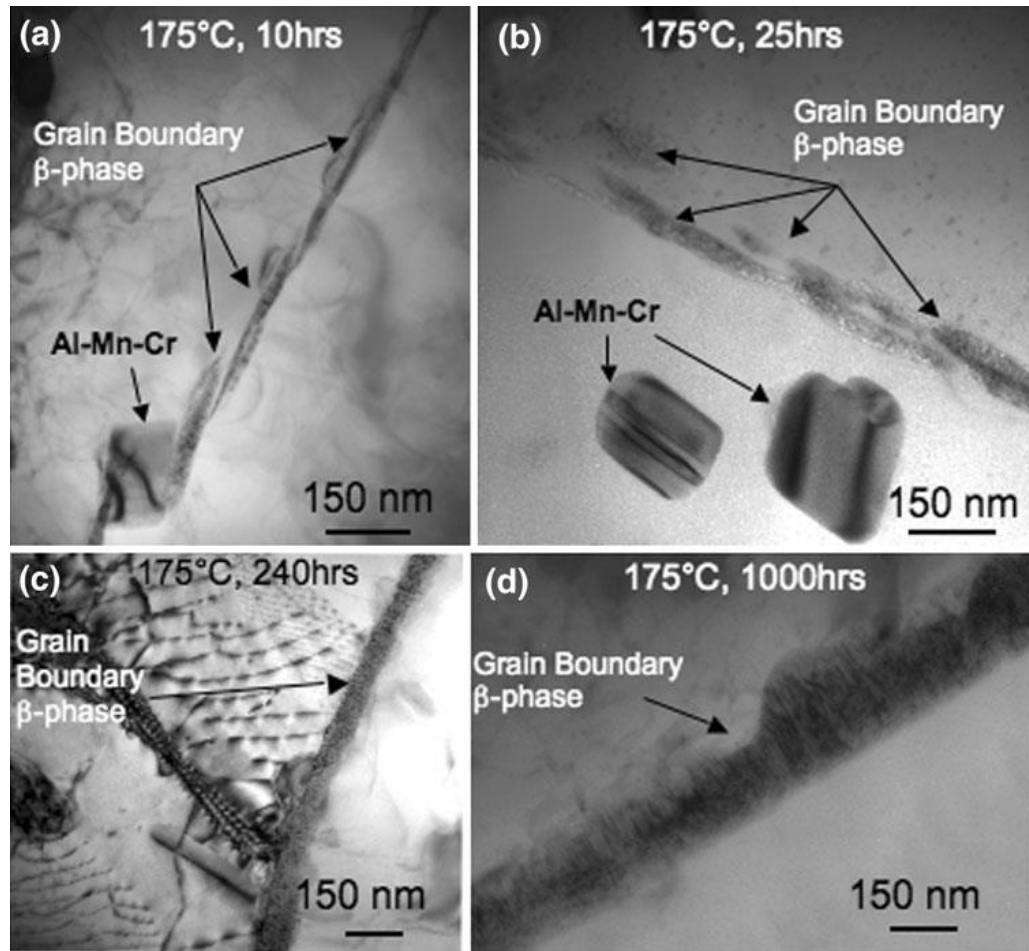
Figure 1.3. Bright-field TEM images showing the β-phase precipitation at the grain boundaries for AA5083-H131 sensitized for (a) 10 h, (b) 25 h, (c) 240 h, and (d) 100 h at 175°C.[26]

Nevertheless, the intragranular precipitation of β-phase ahead of grain boundary precipitation can only occur at iron constituent particles, manganese dispersoids, and dislocations, which promote heterogeneous precipitation. Unfortunately, there is no existing time-temperature transformation (TTT) diagram for β-phase precipitation. Metallurgical phenomena controlling precipitation processes suggest that, in general, for an alloy system with a matrix α-phase and a secondary precipitate β-phase, the lattice strain and the surface energy between the

8

heterogeneous site and the precipitated phase are lower than that between the homogeneous matrix of the parent phase and the precipitated phase.[39] As such, due to the large critical free energy of homogenous precipitation at temperatures below the β-phase solvus, the homogeneous precipitation rate is small. In addition to the smaller critical free energy of heterogeneous precipitation at such high temperatures, the diffusion of the solute is also faster, allowing heterogeneous precipitation to occur at a greater rate. Figure 1.4 illustrates the pertinent time and temperature aspects in relation to heterogeneous versus homogeneous precipitation. At temperatures above the β-phase solvus (T_e), any precipitates formed dissolve into solid solution and only the alloy matrix solid solution phase exists. Small undercooling below T_e for short exposure times promotes β-phase precipitation at the grain boundaries. With increasing exposure time, β-phase precipitation will also take place within the matrix. At lower cooling temperatures, β-phase precipitation occurs uniformly within the matrix.
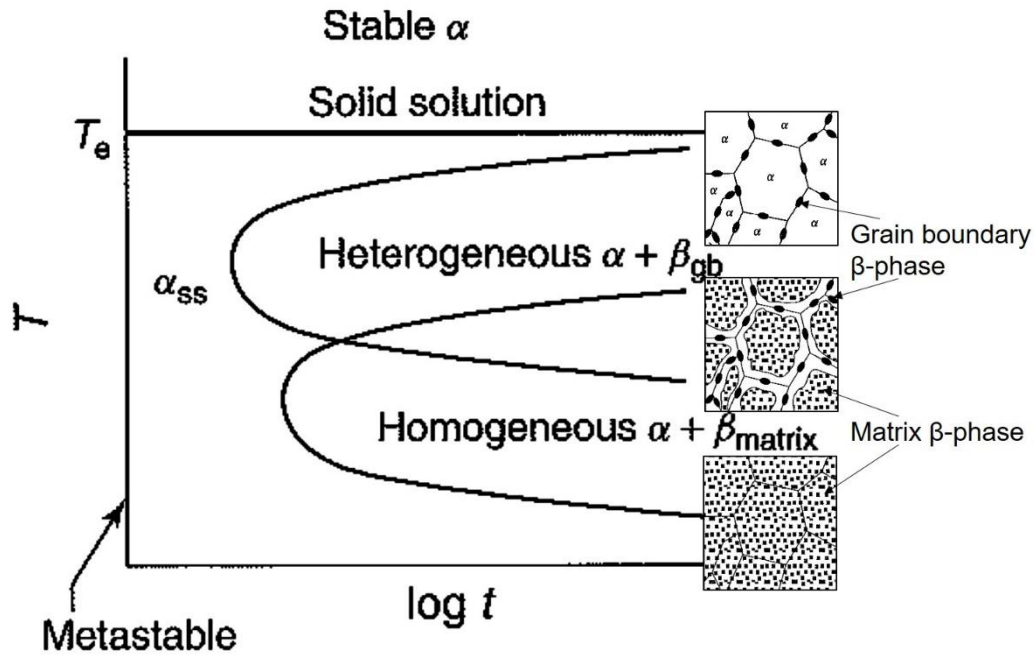
Figure 1.4. Time-temperature transformation (TTT) diagram for an alloy, with a matrix α-phase and a secondary precipitate β-phase, indicating regions of heterogeneous and homogeneous precipitation phenomena and associated microstructure.[39]

These stabilization procedures can be employed on either as-fabricated plates, as well as on plates that have been sensitized during service. According to a recent report,[38] stabilization has not been properly achieved due to inappropriate level of stabilization treatment during fabrication, which led to the numerous occurrence of associated IGC and IGSCC failures during service in the recent years.

1.1.2 Intergranular Corrosion Susceptibility in AA5XXX

Decades of corrosion studies on Al-Mg alloys have attributed IGC susceptibility as a consequence of sensitization.[2,4–7,23,36,40–42] The potential

difference between the β-phase and the α-matrix provides the driving force for the anodic dissolution of the β-phase precipitates along the grain boundaries, leading to IGC spreading to neighboring β-phase precipitates and grain boundaries.[41,41] The degree of sensitization (DoS), as dictated by β-phase precipitation, is dependent on several variables, including Mg content, sensitization time, sensitization temperature, plate thickness, and thermomechanical treatment (Figure 1.5).[2,7–9,25,26,34,43,44] The DoS or IGC susceptibility of Al-Mg alloys can be quantified based on the extent of mass loss from the nitric acid mass loss test (NAMLT) as guided by ASTM G-67. [45] The β-phase dissolves at a rate two orders of magnitude faster than the matrix in the G-67 environment.[45] As such, an increase in the amount and connectivity of grain boundary β-phase will cause grain fall-out, leading to higher mass loss per unit surface area, which is utilized to indicate extent of sensitization or DoS. The increase in DoS for AA5083-H131 given in Figure 1.5 indicates an increase in IGC susceptibility with sensitization temperature and residence time. ASTM G-67 defines traditional ranges of IGC susceptibility for Al-Mg alloys as resistant (DoS < 15 mg/cm^2), intermediate (15 mg/cm^2 < DoS < 25 mg/cm^2), and susceptible (DoS > 25 mg/cm^2).[45] The standard for material acceptance, ASTM B928, uses a 25 mg/cm^2 DoS as the threshold below which the material is said to be resistant to IGC.[46] The viability of DoS for predicting IGC susceptibility is in question due to recent studies, where materials of the same DoS resulted in different IGC morphology and IGC propagation rates after exposure to the same chloride environment.[47,48] It has

been generally thought that complete connectivity of β-phase precipitates along the

grain boundaries is necessary in order for a material to be susceptible to IGC.[49]

However, more recently, IGC has also been shown to occur in alloys even at

intermediate levels of mass loss with discrete non-continuous precipitate

pathways.[23,41,42]
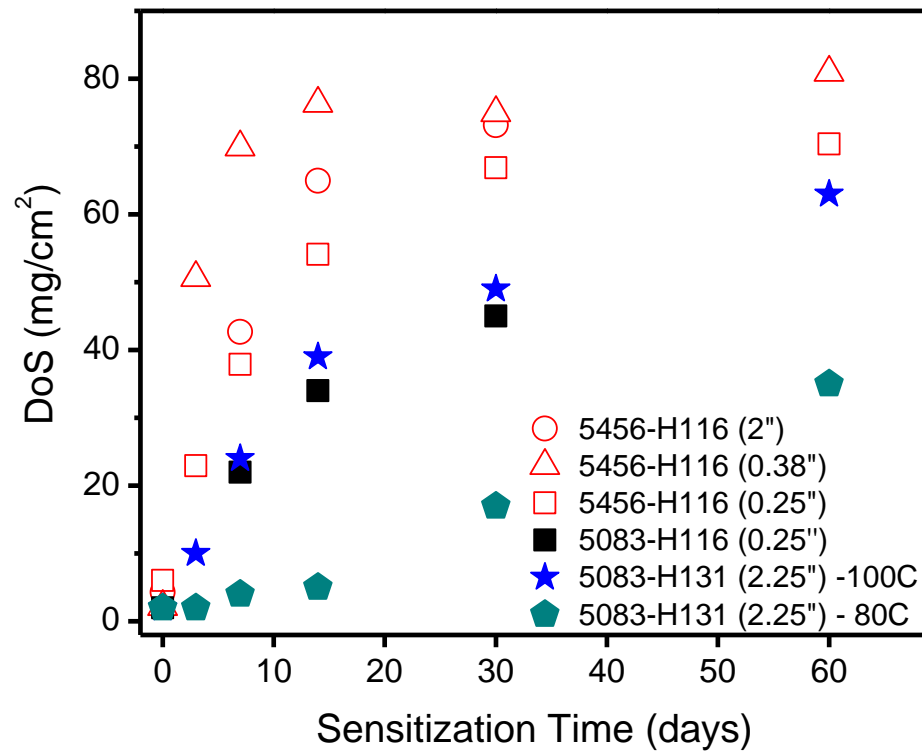
Figure 1.5. Influence of alloy Mg content, temper, plate gauge thickness, sensitization time, and sensitization temperature on degree of sensitization (DoS) of Al-Mg alloys after nitric acid mass loss test (NAMLT). Unless stated in the legend, sensitization temperature is 100°C.

Aside from the NAMLT, a phosphoric acid etch response test is widely

utilized as a qualitative assessment of IGC susceptibility for alloys of intermediate

DoS.[46,50] The test involves open circuit potential etching in either 40 vol. %

phosphoric acid (H_3PO_4) at $35^{\circ}C$ for 3 mins[46] or 10 vol. % H_3PO_4 at $55^{\circ}C$ for 30 to 90 s[50] to highlight the presence of β-phase at the grain boundaries. Susceptibility is assessed through metallographic examination of etched grain boundaries, which correlates to the location and extent of the β-phase precipitate connectivity. However, the observed etched lines or pits are much larger in size than the reported β-phase precipitate size range, causing ambiguous visualization of β-phase precipitates. This ambiguity led to the development of a new etchant, a 0.4 M ammonium persulfate solution ((NH_4)$_2S_2O_8$), which has shown to effectively reveal nearly all of the β-phase precipitate in a clear and consistent manner while preserving the integrity of the α matrix, as well as other phases present.[51] Efforts have been made to understand the selectivity of these etchants by evaluating the corrosion behavior of both bulk AA5083 and pure β-phase upon etchant exposure.[52] Additionally, non-destructive techniques for more accurate DoS probing,[53,54] as well as phenomenological models to predict β-phase precipitation and DoS,[25,43,55,56] are also developed to limit destructive empirical testing.

1.1.3 Stages of Intergranular Corrosion

It is assumed that like any other form of localized corrosion, intergranular corrosion along a grain boundary occurs through several stages: IGC initiation and spreading (dissolution at the alloy/bulk solution interface), IGC penetration, propagation and branching, IGC stifling, and IGC arrest.[23,57,58] The initiation

of IGC can occur at exposed metal surface sites where breakdown of the otherwise protective passive film or dissolution of the near surface deformed layer (NSDL) has occurred. The 1 μm NSDL can be removed via rapid cathodic dissolution or relatively slower passive dissolution.[59] The intermetallic compounds or constituent particles that contain relatively noble elements serve as primary cathodic sites.[60,61] The cathodic reaction generates hydroxide ions, which increases the local pH in the vicinity of the intermetallic particles, causing chemical breakdown of the oxide layer, thereby exposing the surrounding metal to anodic dissolution.[62,63] The anodic dissolution is in the form of matrix trenching and cavity formation or β-phase pitting surrounding the intermetallic particles.

The dissolution of the β-phase generates metal cations, which hydrolyze, causing local acidification and high chloride concentration within the pits. This change in chemistry generally decreases the breakdown potential further and increases the dissolution rate of β-phase, subsequently triggering corrosion of neighboring β-phase.[36] The chain of pits then progresses into a network of corroded grain boundaries or IGC spreading across the surfaces. The penetration and propagation of IGC from pits or surface IGC depends on the local electrolyte chemistry within, as well as the phase present in the local grain boundary area below, the surface corrosion sites or fissure tips. The rate at which IGC propagates may vary with penetration depth due to the potential distribution and the altered chemistry down the fissure resulting from the migration and diffusion of cations from the fissure tip, as well as the ingress of anions from the bulk electrolyte. In

14

the presence of a critical chemistry, an appropriate potential inside the fissure, or the combination of both, the steady state anodic dissolution drives stable IGC propagation. A reduction in the propagation rate or IGC stifling may occur if either the potential or the electrolyte chemistry at the fissure tip cannot maintain the fissure tip dissolution rate. At some propagation depth (time), the combination of the potential and the chemistry may not support fissure tip dissolution at all, leading to IGC arrest.

Figure 1.6 displays the 2D IGC spreading on the metal surface and the 3D penetration into the depth of the metal. The progress of IGC from one stage to another depends highly on the metallurgy and electrochemistry of the material as well as the chemistry of the environment it is exposed to. It is then essential at this point to look into these factors that affect IGC.
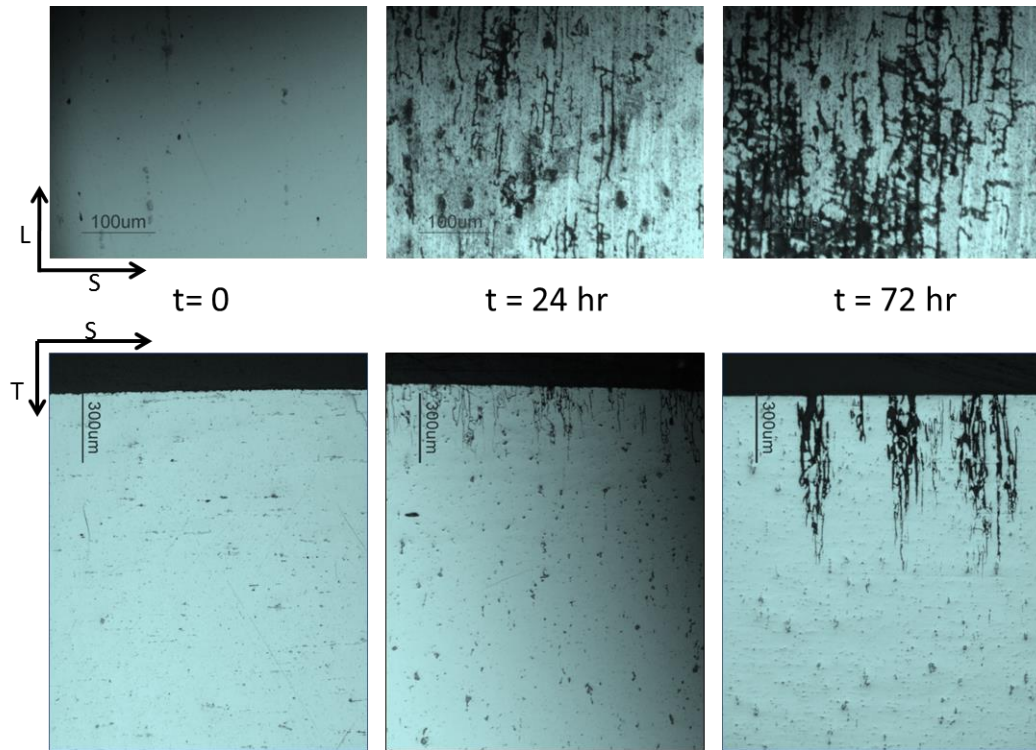
Figure 1.6. Surface IGC spreading on LS surface (top) and depth penetration in T direction (bottom) for an AA5083-H131-SHTQ with DoS of 49 mg/cm^2 exposed to 0.6 M NaCl solution, pH 8.3, and applied potential of -0.73 V$_{SCE}$.

1.1.4 Factors Affecting Intergranular Corrosion

There are numerous composition, processing, and environmental factors that influence IGC. These factors fuel the difference in the thermodynamic and kinetic properties, in terms of metallurgy, electrochemistry, and chemistry, between the matrix and the sensitized grain boundary. The following factors have been found to affect IGC in Al-Mg alloys:

Alloy metallurgy and microstructure: Several researchers have found that DoS is linked to the size of β-phase precipitates and the fraction of precipitates at the grain

16

boundaries, which depends upon sensitization temperature and time, magnesium content, and grain boundary characteristics.[4,6,8,12,30,64] Studies on β-phase morphology and distribution[6,36,50] showed that high DoS material can result in sufficient β-phase precipitation such that 50% of grain boundaries become almost completely covered with β-phase precipitates. In contrast, a low DoS will only have discrete β-phase precipitates on the grain boundaries, as well as some grain boundaries with very few β-phase precipitates.[6,36]
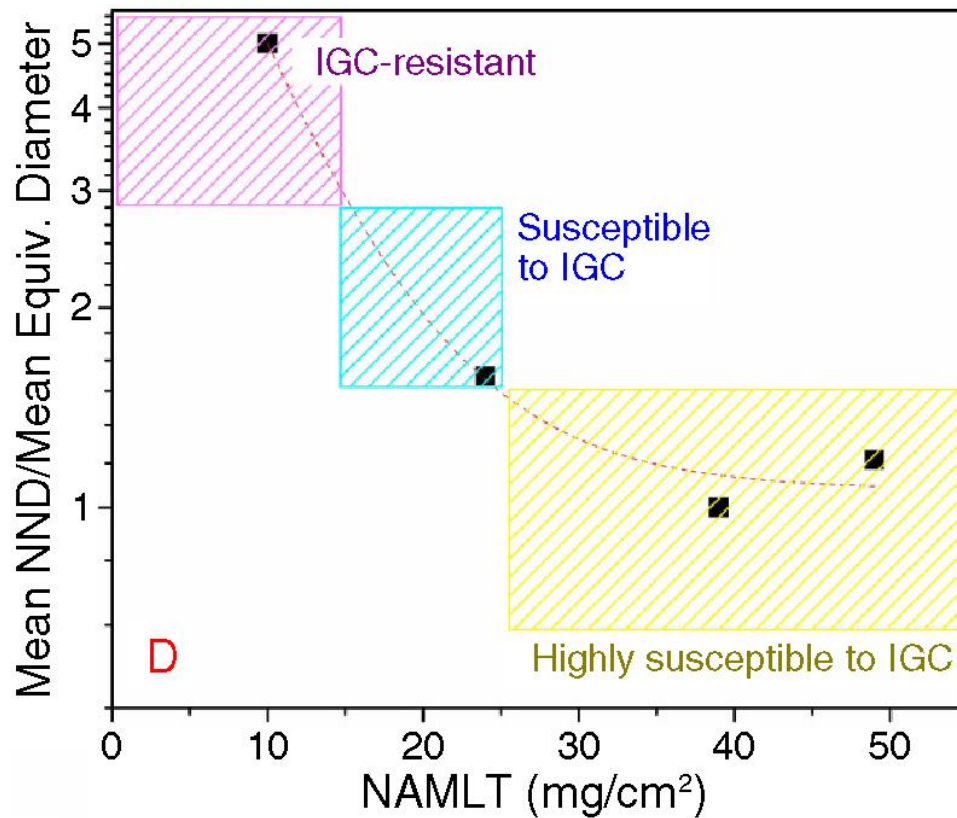
Figure 1.7. Average nearest neighbor distance (NND) divided by equivalent diameter or apparent β-phase continuity parameter vs DoS (NAMLT) as determined from the image analyses of HR-SEM of Ga-embrittled fracture surfaces.[64]

Recent investigation of Gallium-embrittled AA5083 intergranular fracture surfaces[64] suggests that continuous grain boundary β-phase does not exist even at high DoS, but the shape, number density, and equivalent diameter of the grain boundary β-phase change with DoS. The average nearest neighbor distance (NND) between grain boundary β-phase, when normalized by the average equivalent diameter ($\bar{d}$), yielded an apparent β-phase continuity parameter. The plot of this apparent continuity as a function of DoS in Figure 1.7 reveals that there exists a relationship between a microstructural parameter (NND/$\bar{d}$) and DoS that is independent of time and temperature. Birbilis, et al.[64] proposed using NND/$\bar{d}$ values to categorize the traditional ranges of IGC susceptibility: DoS is resistant or negligible, if NND/$\bar{d}$ > 3; DoS is intermediate if 3 > NND/$\bar{d}$ > 1.5; and DoS is extensive or highly susceptible, if NND/$\bar{d}$ > 1.5 It was further postulated that although β-phase precipitates were physically not connected when NND/$\bar{d}$ < 1.5, the apparent continuity is such that IGC occurs freely as in the IGC spreading observed in these materials.[36,64] As such, the amount and the proximity between the β-phase precipitates are important factors that control IGC susceptibility, and subsequently IGC spreading and IGC propagation. However, Bumiller specified that although the β-phase corrosion is vital, the dissolution of the α matrix is equally important as it controls the total IGC propagation rate along a single grain boundary, perhaps limited by the rate of dissolution of the α matrix grain boundary zone between the β-phase precipitates.[23] Moreover, the presence of cathodic constituent particles form microgalvanic couples with the matrix, triggering local

18

corrosion of β-phase precipitates proximate to the constituent particles, and later serving as initiation sites for IGC spreading.[65]

Additionally, because these alloys are strain hardened, it is expected that the grains are elongated in both the longitudinal (L) and long transverse (T) directions and are thinned in the short transverse (S) direction, forming a pancake-like microstructure (Figure 1.1). Such a directional microstructure has been found to be an important factor for IGC and exfoliation corrosion propagation in precipitation hardened and strain hardened Al alloys.[66–68] In AA5083, the spacing between β-phase precipitates was shown to decrease for the LS and ST surfaces, subsequently affecting IGC spreading,[41] and possibly IGC propagation into the depth.

Solution chemistry: The bulk chemical composition of the electrolytes is also a significant factor that determines whether or not IGC occurs. Aggressive chloride-free acidic test environments have been designed so that a metallurgical condition, like the one aforementioned, that leads to IGC susceptibility can be elucidated by direct evidence of grain boundary attack while avoiding localized pitting that could lead to excessive attack of the matrix in the accelerated test.[39] Test environments, which indicate IGC, promote differences in the electrochemical behavior of the matrix and the sensitized grain boundary. Almost 100% of the exposed β particles can be expected to be attacked in aggressive acids. In the case of Al-Mg alloys, solutions of HNO_3 (70 vol. %) and H_3PO_4 (10 vol. %) have been developed and

standardized as aggressive acidic test environments.[6,12,45]   The β-phase is robust, in that it is the most susceptible phase in many environments.

Aside from the standard test environments, most of the work on IGC of Al-Mg alloys has been conducted in near neutral, dilute sodium chloride solutions.[2,8,23,34,36,40,41,52,65,69,70]   This environment is of particular interest because it is often use to mimic the marine environment. Additionally, it has been well-documented that anions like chloride ions (Cl⁻) are known to ingress into and damage the oxide passive layer, and aid in the initiation of localized corrosion events.[71,72] It was also recognized that Cl⁻ ions hinder passive film reformation and play a role in the attack near constituent particles.[73] These effects are manifested in the decreasing breakdown potentials of both Al-Mg alloys and the β-phase as a function of increasing Cl⁻ ion concentration.[36] However, unlike in aggressive acids, the attack in neutral chloride solutions is a statistically distributed process such that not every β particle exposed to NaCl solution is attacked.[23,41]

Solution pH: Oxides and hydroxides of aluminum and magnesium form a passive layer over the metal surface protecting it from attack. These oxides, however, are only stable within certain pH ranges that differ from one another. As such, changes in pH could influence the corrosion activity, as is the case for AA7075, where anodic Mg_2Si and $MgZn_2$ particles at the grain boundaries caused IGC.[74] Aluminum oxide is stable only in slightly acidic to slightly basic conditions,

whereas magnesium hydroxide is stable only in alkaline pH.[75] The electrochemical behavior of the Mg-rich anodic particles is often determined by magnesium, making Mg_2Si stable at alkaline conditions. Thus, at strongly alkaline pH, corrosion involves more uniform matrix dissolution whereas at slightly acidic pH, corrosion is limited to grain boundary attack.[74] The dissolution kinetics in these pH ranges is also a significant factor. Recently, Lyndon et al.[70] looked into the electrochemical behavior of β-phase as a function of solution pH. In the acidic pH range, β-phase was highly active with anodic current densities of several hundreds of $\mu A/cm^2$ at the open circuit potential of AA5083. At the pH range between 4 and 8, β-phase anodic current densities were relatively low, approximately $100\ \mu A/cm^2$. In the alkaline condition (pH 10), the dissolution rates of this phase were significantly lower than those under lower acidic conditions. It can then be inferred that although β-phase takes the role of the anode and selectively dissolves within the pH range of 2 to 10, the dissolution kinetics, and thus IGC will still be a function of solution pH. In strongly alkaline environment, such as 0.01 M NaOH solution, uniform corrosion of AA5083 is observed instead of IGC.[76]

Applied potential: Applied potential influences localized corrosion morphology in a wide range of aluminum alloys.[77–82] The concept of a potential window for IGC is often utilized to define the zone of IGC in IGC-susceptible materials.[4,79,80,83,84] In general, the IGC zone is usually the potential range between the breakdown potentials of the more anodic intermetallic or Cu-depleted zone around an Al-Cu intermetallic and that of the matrix. In the case of Al-Cu-

Mg alloys, it was found that Cu-depleted zones were more important than the S-phase (Al_2CuMg).[84] In the case of AA5083, primarily the β-phase and any Mg segregation are the dominant aspects. It was observed that the sensitized alloy has a lower breakdown potential than the unsensitized alloy.[36] Moreover, the breakdown potential of a sensitized AA5083, when taken as the potential of abrupt increase in anodic current density, is not associated with discrete, isolated pitting of β-phase, which can be seen via metastable pit transient detection at lower potentials. Rather the breakdown potential is associated with the spreading of IGC on the surface.[36,85] In this regard, the lower potential is that for probable β-phase breakdown. The region between these two breakdown potentials forms the potential window for IGC spreading in AA5083. Obviously, breakdown potentials[1] are linked with large differences in anodic current density above and below the threshold. These potentials are often associated with stabilization.

The potential dependence was also observed for IGC propagation into the depth from the surface. Mizuno and Kelly[69] have reported that the maximum IGC damage depth in sensitized AA5083-H131 after 100 hours of galvanic coupling with 304 steel is linearly related to the galvanic coupling potential. This linear relationship was found for all DoS, with the dependence of rate on potential increasing with DoS. Furthermore, a threshold potential, the minimum potential at which IGC occurred, was observed. Moreover, IGC damage depths were also

---

[1] Critical breakdown potentials are associated with abrupt changes in current density.

observed to increase with steel to AA5083 area ratios due to the increase polarization brought on by galvanic coupling.[69] Recent speculations suggested that this threshold potential is related to the fissure environment.[23,40]

1.1.5 Fissure Environment

Several authors have shown that the chemical and electrochemical conditions within the fissure can be markedly different from the bulk environment.[10,86,87] The fissure environment plays a critical role in the IGC propagation process. The anodic dissolution at the pit or fissure tip introduces metal cations (Mg^{2+}, Al^{3+}), which cause acidification upon hydrolysis. Balance of the positive charge generated by anodic dissolution and hydrolysis is facilitated by the ingress of anions (Cl^-) from the bulk environment. Hence, the fissure environment may be composed of an aggressive, acidic, and concentrated solution. Although the restricted mass transport in these inherently tight fissures could help maintain the fissure chemistry, the heterogeneous metallurgical nature of the sensitized grain boundary would continuously produce a variation in the chemistry down the fissure. Additionally, the migration and diffusion of ions within an electrolyte of finite resistance results in potential drop, leading to local potentials that may differ significantly from the external value. Thus, chemical concentration, pH, and potential gradients likely exist within the fissure. At the fissure mouth, the chemistry must approach that of the bulk chemistry. The chemistry changes along

the depth of the fissure, reaching the more aggressive, concentrated acidic environment at the fissure tip.

These electrochemical and chemical changes in the fissure environment may alter the electrochemical behavior of the exposed material at the fissure tip during IGC propagation in several ways. Foremost, these changes may alter the anodic dissolution kinetics of the grain boundaries, which could evolve towards either more or less susceptible conditions. Secondly, it could increase or decrease the local cathodic reaction rates. Recently, Bumiller[23] examined the intergranular corrosion fissure growth in AA5083 through deconstruction of the heterogeneous grain boundary system into its primary phases. The corrosion of the matrix was considered along with the corrosion of the β-phase in electrolytes of varying compositions of aluminum chloride ($AlCl_3$) and magnesium chloride ($MgCl_2$). Her results suggest that IGC propagation can be sustained if the local solution chemistry is 80% to 100% saturated with Al-4 wt% Mg (the matrix solid solution composition) with the fissure tip potential between -0.850 and -0.830 V_{SCE}. Moreover, it was rationalized that there could be precipitates in the wake with subsequent potential drop and changes of the local chemistry for IGC propagation to proceed. As such, potential, local chemistry, and microstructure likely play a key role in defining limitations for IGC growth stability.

1.1.6 Electrochemical Framework for IGC in AA5XXX Alloys

Electrochemical frameworks are developed to (1) define a material's susceptibility to localized corrosion, and (2) explain metallurgical factors causal to localized corrosion. Generally, the difference between the breakdown potentials of the anodic grain boundary zones and the alloy matrix defines the IGC susceptibility of the alloys. [4,7,30,74,79,80,83,84,88–93] Literature holds an electrochemical framework for IGC spreading in AA5083, wherein the differences between the breakdown potentials of the β-phase and the bulk AA5083 alloys were utilized to establish a range of potential over which AA5083 is IGC susceptible in NaCl as a function of chloride ion concentration.[36] The breakdown potential of β-phase in 0.6 M NaCl solution is -0.959 V_{SCE}, around 200 mV lower than the open circuit potential of AA5083. [4,10,13,23,36,37] The relatively low breakdown potential of the β-phase with respect to the unsensitized AA5083 is preserved across a range of chloride concentration. The sensitized AA5083 has a lower breakdown potential compared to the unsensitized alloy, and has been reported to decrease with an increase in DoS and chloride concentration.[11,36,41] Conventionally, the breakdown potential is indicative of the pitting potential of discrete precipitates in IGC susceptible materials. In Al-Mg alloys in neutral chloride solutions, the breakdown potential of AA5083 may be associated instead with the spreading of IGC to nearby β-phase precipitates triggered by solution acidification and chloride ion concentration, instead of pit initiation and stabilization of individual β-phase precipitates.[36]
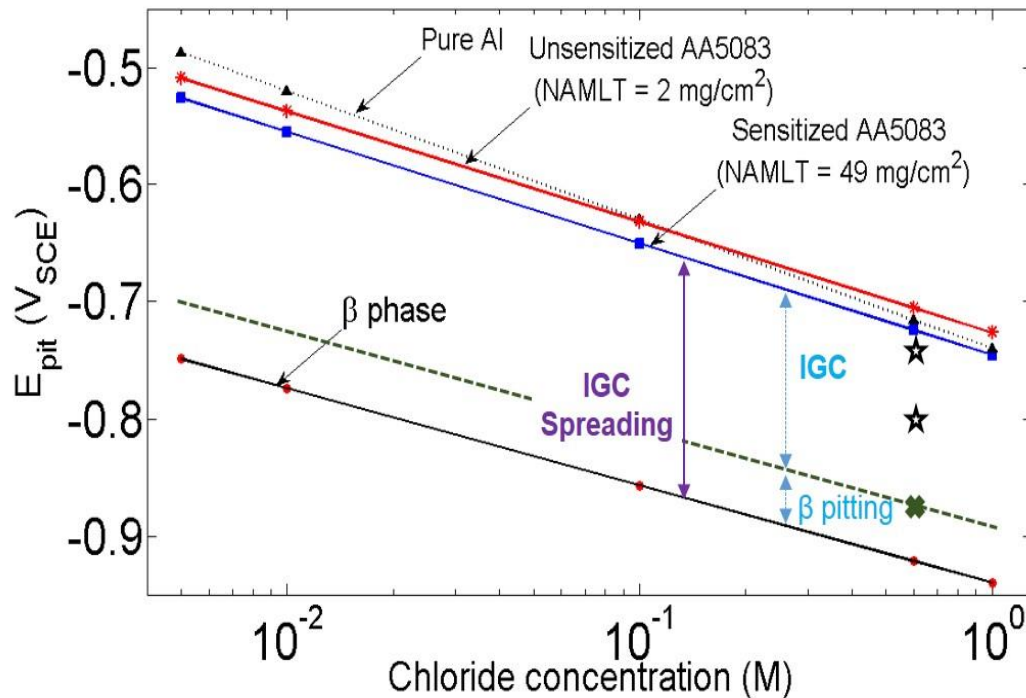
Figure 1.8. Pitting and spreading potential of AA5083-H131, high purity Al wire, and β-phase at pH 8.3 as a function of chloride concentration. The dashed line represents the IGC propagation threshold potential for sensitized AA5083. As a comparison, the open circuit potentials (☆) of unsensitized and sensitized AA5083 were included.[36,41,94]

A graphical representation of the electrochemical framework, shown in Figure 1.8, displays three potential zones corresponding to difference in susceptibility to corrosion of sensitized AA5083. The framework suggests that IGC spreading is expected at the range of potential between the breakdown potential of sensitized AA5083 or the spreading potential and the breakdown potential of the β-phase. Localized corrosion of the matrix is expected above this region, while no localized corrosion should occur below this region. The framework was substantiated via comparison of surface damage on sensitized AA5083-H131 with

DoS of 49 mg/cm^2 at three different potentials after 1 h in 0.6 M NaCl solution.[36] Only random pitting was exhibited at the lowest potential of -0.75 V$_{SCE}$. The surface showed limited corrosion spreading at a slightly higher potential of -0.74 V$_{SCE}$. A large area of IGC spreading occurred at the highest potential of -0.73 V$_{SCE}$, which is well above the breakdown potential of the β-phase and near the breakdown potential for the 49 mg/cm^2 in 0.6 M NaCl solution. The damage at this potential demonstrated localized corrosion that is characterized by spreading of corrosion to other adjacent corrosion sites on the surface, and not by the initial isolated pitting of grain boundaries or uniform matrix corrosion.

However, separate studies[59,73] on polished sensitized AA5083 in aerated 3.5 wt. % NaCl solution at open circuit potential for 24 h did not result in any surface IGC, even though these potentials were well above the breakdown potentials for bulk β-phase. Seong, et al.[59] suggested that the presence of a 1 μm NSDL as a result of specimen surface preparation blocked the exposure of β-phase precipitates to the environment. Removal of the NSDL via cathodic polarization or alkaline etching prior to exposures at -0.80 V$_{SCE}$ resulted in surface IGC of the sensitized AA5083, in agreement with the potential window suggested by the electrochemical framework.

It has to be noted that the above framework focuses on surface IGC spreading, IGC propagation into the depth after spreading may also have associated characteristic potentials. As was mentioned earlier, stable IGC propagation can

occur given the right combination of fissure chemistry and applied fissure tip potential. IGSCC work by Crane [95] on AA5083-H131 (DoS of 22 mg/cm^2) suggested potential windows, defined by breakdown potentials of bulk α and β phase, for fatigue crack tip corrosion growth kinetics. In order to produce significant IGC growth (~ 10 nm/s), the applied potential must be above –0.87 V$_{SCE}$, the breakdown potential of the matrix α-phase in the assumed near-saturated to saturated AlCl$_3$/MgCl$_2$ simulated crack tip solution. Above this potential, the dissolution of β-phase precipitate helps maintain the critical acidic chemistry necessary to sustain the matrix α-phase dissolution, whose breakdown potential drops from -0.79 V$_{SCE}$ in neutral 0.6 M NaCl solution, to -0.87 V$_{SCE}$ in the acidic fissure tip environment. Between -0.87 V$_{SCE}$ and -0.96 V$_{SCE}$, the breakdown potential of β-phase in neutral 0.6 M NaCl solution, the IGC growth rate decreases considerably to ~ 1 nm/s. Because β-phase is the only freely dissolving phase within this potential window, and the volume fraction of β-phase at the fissure tip of a DoS of 22 mg/cm^2 may not be sufficient to produce the critical fissure chemistry; the drop in IGC kinetics was proposed to be due to the limited source for acidic fissure tip chemistry. Below -0.96 V$_{SCE}$, only passive dissolution of both phases is possible, which hinders the development of the critical acidic chemistry, thereby eliminating IGC growth via anodic dissolution. However, with enough cathodic polarization, corrosion growth could occur via cathodic corrosion.

1.2   Key Unresolved Issues

The basic conceptual understanding of the IGC susceptibility of AA5XXX alloys as a consequence of sensitization during service is proven and accepted.[2,4–7,23,36,40–42]   However, there exists a need to fundamentally understand and explain how the various chemical, electrochemical, and metallurgical components of an Al-Mg IGC system quantitatively govern the nature and extent of IGC evolution. Particularly, it is essential to determine the controlling factors and their influence on the IGC propagation behavior and growth rates. This information will serve as the vital foundation to the understanding and development of a mechanism and criteria for stable IGC propagation in sensitized Al-Mg alloys without continuous grain boundary β-phase anodic path.

In terms of nitric acid mass loss value, there is a growing set of data on DoS as a function of sensitization conditions, alloy composition, plate thickness, and cold work temper.[2,8,34,47,48]   There is also some understanding of an electrochemical framework for IGC with efforts placed on developing more selective etchants as well as non-destructive tests for more accurate DoS probing.[51,52,54] Although HNO_3 promotes differences in the electrochemical behavior of the matrix and the susceptible β-phase precipitates, preservation of a potential window across many environments would help in many ways. A number of the etchants being tested involve other ionic species in either the acidic or

29

alkaline media, which provide information on the chemical and electrochemical reactivity of the sensitized material beyond a qualitative susceptibility approach.

Whereas ASTM DoS categorically defines the IGC susceptibility of a material, it is inadequate in that it fails to discriminate IGC susceptibility in environments more benign than nitric acid, specifically those with high mass loss values beyond 50 mg/cm^2. Additionally, there are other unresolved key factors that influence IGC evolution. Therefore, there is a need to identify and understand these additional important metallurgical, chemical, geometric, and electrochemical parameters that govern IGC in service-type environments. Some of these parameters, such as applied potential and exposure time, together with DoS, have been shown to strongly influence both IGC spreading and propagation with depth.[36,41] From a practical engineering perspective, considerable propagation is required for transition from IGC to IGSCC or failure by IGC penetration. This considerable propagation could be related to a critical electrochemistry geometry, a critical fracture geometry, or a combination of both. As such, the mere initiation and spreading of IGC would neither constitute transition nor failure. However, the only investigation of IGC penetration into AA5XXX was on galvanic coupling with stainless steel.[54] Furthermore, no relationship between IGC penetration depth, DoS, potential, and exposure time for various orientations of any AA5XXX alloy has been reported to date in any environment. A quantitative characterization of the IGC kinetics and the extent to which each factor affects IGC penetration remains a gap as well as an opportunity for study.

Propagation kinetics for pitting, crevice, and intergranular corrosion in other materials, such as titanium alloys and precipitation-hardened aluminum alloys, typically conform to a power law relationship between length or depth and time.[66,77,78,96,97] The power law behavior is justified by various controlling factors that influence corrosion stability. For pitting and crevice corrosion, the corrosion stability is defined by the steady state anodic dissolution in the presence of a critical chemistry, or an appropriate potential inside the corrosion cavity, or the combination of both.[98–104] A threshold potential exists in the form of pit or crevice repassivation potential, E_{rp}, below which these localized corrosion sites repassivate, and thereby terminates pit or crevice corrosion propagation.[105] Moreover, at potentials lower than E_{rp}, the current density at the corroding surface is too low to sustain the critical chemistry for localized corrosion growth.[99] Another threshold potential is the open circuit potential (OCP) at the pit base. At OCP, the critical chemistry, which is generally acidic, cannot be maintained as the cathodic reaction producing hydroxyl ions occurs at the same rate as the anodic dissolution reaction rate, thereby increasing the pH.

Another electrochemical threshold for localized corrosion stability, developed by Galvele,[98–100] is the pit stability product, $(i*x)_{crit}$, where i is the dissolution rate of the pit base, and x is the one-dimensional pit depth. The idea behind this criterion is based on the ability of the pit to maintain a critical chemistry at the pit base to stay active. If $(i*x) \geq (i*x)_{crit}$, the critical chemistry is sustained and pit can propagate stably. Otherwise, the critical chemistry is lost via diffusion,

the pit base repassivates in the more dilute chemical environment, stopping pit growth. An open question is whether these electrochemical thresholds apply to IGC in Al-Mg alloys.

To date, literature holds no record of any study conducted to address IGC growth stability and the existence of thresholds in the case of IGC of 5XXX alloys. Of particular interest is to understand if the threshold potential, like the pit stability product, is dependent on the fissure depth. Similarly, there has been very little work on the effect of grain boundary microstructure on IGC stabilization-propagation. In a simplified view, the Galvele model must be extended to heterogeneous grain boundaries of alternating α and β components or unsusceptible-susceptible zones. This aspect of the Galvele criterion has not been established.

Despite the lack of information on IGC stability, a link between IGC and other forms of localized corrosion, such as pitting and crevice corrosion, is expected because of the commonalities in required chemical conditions for active dissolution in the localized corrosion sites, and the need for separation of anode and cathode. The anodic and cathodic electrochemical reactions separate spatially during localized corrosion. As localized corrosion propagates, the local environment becomes depleted in cathodic reactant, which shifts most of the cathodic reaction to the boldly exposed surface where cathodic reactant is more abundant. The local environment, where the anodic reaction occurs, becomes enriched in metal cations and chloride ions, and develops internal acidities owing to cation hydrolysis. For

all three forms of localized corrosion, a special restrictive geometry limits interchange between the local and bulk environment. As such, the primary difference amongst these various types of localized corrosion lies in the corrosion morphology or geometry. Therefore, there exists an opportunity to utilize established pit stability theory to gain a fundamental understanding of IGC propagation stabilization as well as to define the critical electrochemical conditions leading to an IGC stability criterion as a function of DoS.

However, in the case of IGC, there are multiple paths of IGC perpendicular to the sample surface penetrating with connectivity between sites, which leads to an anode/cathode separation involving a complex resistive path. The question is how the resistive path between the external cathode and the propagating anode at the fissure tip evolves as IGC progresses. The connectivity between sites could influence the extent of ohmic potential drop within fissure depth, affecting the electrochemical behavior of the exposed material at the fissure tip. Additionally, for AA5XXX alloys in particular, the heterogeneous metallurgical nature of the sensitized grain boundary, composed of ligaments of α-phase and β-phase, would continuously vary the chemistry down the fissure as IGC propagation ensues. The change in chemistry is dependent on the dissolution rate of the component phases, which along with the influence of potential drop within the fissure depth will dictate the depassivation and dissolution rate of the fissure tip, and subsequently the IGC propagation behavior. With that said, both the connectivity and the grain boundary microstructure are integral to IGC propagation and must be considered in

understanding IGC propagation stabilization. If the research gap is realized, there could be a rational technical basis to consider the factors controlling critical potentials that will lead to IGC stifling and arrest in systems with multiple sites or continued linear growth overtime of these IGC networks. Additionally, this knowledge could be employed for practical mitigation strategies of IGC in AA5XXX alloy structures.

1.3   Problem Statement

Instances of sensitization during service and rapid cracking have occurred, bringing about an increasing body of research with regard to corrosion of AA5XXX over the past decade.[64,106] Because these damage phenomena are detrimental to the structural integrity of components, many of these studies have investigated IGSCC, concentrating on the intrinsic metallurgical factors which lead to IGSCC due to anodic dissolution-assisted stress corrosion, hydrogen embrittlement, or some combination of the two.[4,6,7,11,13,15,17,76,107,108] Although it is well accepted that IGSCC initiates at highly susceptible grain boundaries, there is little information regarding IGC rates or factors controlling those rates in AA5XXX. Limited studies on IGC have demonstrated that surface IGC evolution and growth is influenced by DoS, solution composition, applied potential, and applied current density. However, considerable depth propagation is required for transition from IGC to IGSCC or failure by IGC penetration. Thus, a fundamental understanding

of the detailed role and impact of the above factors, together with additional important parameters such as orientation of propagation, on stable IGC depth penetration and growth is necessary in an effort to establish a foundation for IGC and IGSCC life prediction models and mitigation strategies for AA5XXX marine structures.

1.4 Objective Statement

The main goal of this research is to establish a quantitative understanding of IGC in sensitized Al-Mg alloy 5083 from the propagation mechanism and kinetics standpoints. The project focus and objectives are as follows:

- Understand the precise mechanistic role and impact of select metallurgical, electrochemical, and chemical factors on the IGC susceptibility of sensitized AA5083 via characterization of IGC propagation kinetics and morphology acquired under electrochemical control in aqueous solutions that simulate the marine environment.

- Determine the nature, extent, and dependence of IGC propagation kinetics as a function of these selected variables. Particular focus is placed on correlating IGC propagation behavior with the description of DoS on the microstructural level in terms of β precipitate morphology and distribution on grain boundaries, as well as electrochemical dependence in the context of strong potential threshold and critical current density.

- Gain a fundamental understanding of what microstructural, chemical, and electrochemical factors control stable IGC propagation in sensitized Al-Mg alloy, taking into account the heterogeneous grain boundary metallurgy, the fissure chemistry, and the local electrochemistry.

1.5   Thesis Organization

Chapter 2 establishes a foundation for this work by presenting a combined experimental and modeling study of factors influencing IGC penetration depth into an Al-Mg alloy. The factors include DoS, applied potential, exposure time, orientation of propagation, and sensitization temperature. A scientific interpretation of IGC penetration and propagation mechanism was discussed based on the dependence of IGC rates on these select parameters, which led to evidence of an incubation time for IGC propagation, a linear IGC kinetics with time, as well as IGC propagation in the absence of a continuous anodic path. Moreover, the characterization of IGC damage distribution enables the development of validated phenomenological models that can estimate IGC damage progression as a function of the aforementioned variables.

Chapter 3 examines the critical role of applied potential via a series of galvanostatic tests to avoid influence of incubation time. A framework for IGC propagation establishing linear dependence of IGC damage depth with potential for a given time, and the existence of a threshold IGC propagation potential is

presented. This IGC propagation framework, together with polarization data of individual α and β phases in simulated fissure chemistry is utilized to predict the required grain boundary β-phase coverage for the sensitized conditions. Hypotheses behind the threshold potential and mechanism behind the linear dependence are discussed.

Chapter 4 seeks to understand the uncharacteristic linear dependence of IGC kinetics observed in Chapter 3. Computational resistor network analysis and laboratory experiments on specimens with difference geometries are presented to substantiate the hypothesis that a high degree of connectivity, evolution of such connectivity over time, and consequently, multiple paths to the external environment, explain this linear dependence. The extent of the linear propagation kinetics in the context of IGC stifling and arrest is also discussed.

Chapter 5 discusses the electrochemical and chemical parameters that control stable IGC propagation. The effects of alloying and sensitization on two stability criteria, repassivation potential and pit stability product, is discussed to explain the strong potential threshold observed in Chapter 3 and the proposed mechanism for stable IGC propagation.

Chapter 6 presents conclusions of this research project.

Chapter 7 presents a paper manuscript co-authored with researchers from Vextec detailing the three-dimensional IGC propagation modeling conducted

utilizing the results in Chapter 1. This paper manuscript was accepted for publication in Materials & Design.

1.6 References

[1] G.C. Blaze, Alcoa Green Letter: The 5000 Series Alloys Suitable for Welded Structural Applications, Aluminum Corporation of America, New Kensington, PA, 1972.

[2] I.N.A. Oguocha, O.J. Adigun, S. Yannacopoulos, Effect of sensitization heat treatment on properties of Al–Mg alloy AA5083-H116, J. Mater. Sci. 43 (2008) 4208–4214. doi:10.1007/s10853-008-2606-1.

[3] R.L. Holtz, P.S. Pao, R.A. Bayles, T.M. Longazel, R. Goswami, Corrosion-Fatigue Behavior of Aluminum Alloy 5083-H131 Sensitized at 448 K (175 °C), Metall. Mater. Trans. A. 43 (2011) 2839–2849. doi:10.1007/s11661-011-0866-x.

[4] J.L. Searles, P.I. Gouma, R.G. Buchheit, Stress corrosion cracking of sensitized AA5083 (Al-4.5Mg-1.0Mn), Metall. Mater. Trans. A. 32 (2001) 2859–2867. doi:10.1007/s11661-001-1036-3.

[5] J.L. Searles, P.I. Gouma, R.G. Buchheit, Stress Corrosion Cracking of Sensitized AA5083 (Al-4.5Mg-1.0Mn), Mater. Sci. Forum. 396 (2002) 1437–1442. doi:10.4028/www.scientific.net/MSF.396-402.1437.

[6] A.J. Davenport, Y. Yuan, R. Ambat, B.J. Connolly, M. Strangwood, A. Afseth, et al., Intergranular Corrosion and Stress Corrosion Cracking of Sensitised AA5182, Mater. Sci. Forum. 519-521 (2006) 641–646. doi:10.4028/www.scientific.net/MSF.519-521.641.

[7] D.R. Baer, C.F. Windisch, M.H. Engelhard, M.J. Danielson, R.H. Jones, J.S. Vetrano, Influence of Mg on the corrosion of Al, J. Vac. Sci. Technol. A. 18 (2000) 131–136. doi:10.1116/1.582129.

[8] R.K. Gupta, R. Zhang, C.H.J. Davies, N. Birbilis, Influence of Mg Content on the Sensitization and Corrosion of Al-xMg(-Mn) Alloys, Corrosion. 69 (2013) 1081–1087. doi:10.5006/0948.

[9]   G.M. Scamans, Low Temperature Sensitization of AA5XXX Alloys, Innoval, Oxon, UK, 2008.

[10]   G.M. Scamans, N.J.H. Holroyd, C.D.S. Tuck, The role of magnesium segregation in the intergranular stress corrosion cracking of aluminium alloys, Corros. Sci. 27 (1987) 329–347. doi:10.1016/0010-938X(87)90076-X.

[11]   R.H. Jones, D.R. Baer, M.J. Danielson, J.S. Vetrano, Role of Mg in the stress corrosion cracking of an Al-Mg alloy, Metall. Mater. Trans. A. 32 (2001) 1699–1711. doi:10.1007/s11661-001-0148-0.

[12]   J.S. Vetrano, R.E. Williford, S.M. Bruemmer, R.H. Jones, Influence of microstructure and thermal history on the corrosion susceptibility of AA 5083, in: Alum. Alloys, Orlando, FL, 1997.

[13]   R.H. Jones, J.S. Vetrano, C.F. Windisch, Stress Corrosion Cracking of Al-Mg and Mg-Al Alloys, Corrosion. 60 (2004) 1144–1154. doi:10.5006/1.3299228.

[14]   C.B. Crane, R.P. Gangloff, Stress Corrosion Cracking of Low Temperature Sensitized AA5083, in: Dep. Def. Corros. Conf., NACE, Palm Springs, CA, 2011.

[15]   C. Crane, R. Gangloff, Stress Corrosion Cracking of Al-Mg Alloy 5083 Sensitized at Low Temperature, Corrosion. (2015). doi:10.5006/1766.

[16]   R.L. Holtz, P.S. Pao, R.A. Bayles, T.M. Longazel, R. Goswami, Corrosion Fatigue of Al 5083-H131 Sensitized at 70, 100, and 175°C in relation to Microstructure and Degree of Sensitization, in: Dep. Def. Corros. Conf., NACE, Palm Springs, CA, 2011.

[17]   C.B. Crane, R.P. Gangloff, Dissolution and Hydrogen Diffusion Control of IGSCC in Sensitized Aluminum-Magnesium Alloys, in: Int. Hydrog. Conf. IHC 2012, ASME Press, 2014.

[18]   J.E. Hatch, Aluminum: Properties and Physical Metallurgy, American Society of Metals, Metals Park, OH, 1984.

[19]   J.R. Davis, Corrosion of Aluminum and Aluminum Alloys, American Society of Metals International, Materials Park, OH, 1999.

[20] M. Tiryakioglu, J.T. Staley, Physical Metallurgy and the Effect of Alloying Additions in Aluminum Alloys, in: G.E. Totten, D.S. Mackenzie (Eds.), Handb. Alum., Marcel Dekker, Inc., New York, NY, 2003.

[21] L. Katgerman, D. Eskin, Hardening, Annealing, and Aging, in: G.E. Totten, D.S. Mackenzie (Eds.), Handb. Alum., Marcel Dekker, Inc., New York, NY, 2003.

[22] L.F. Mondolfo, Aluminum Alloys: Structure and Properties, Butterworth, London, UK, 1976.

[23] E. Bumiller, Intergranular corrosion in AA5XXX aluminum alloys with discontinuous precipitation at the grain boundaries, PhD Dissertation, University of Virginia, 2011.

[24] E. Ghali, Aluminum and Aluminum Alloys, in: R.W. Revie (Ed.), Uhligs Corros. Handb., 2nd ed., New York, NY, 2000: p. 736.

[25] R. Goswami, G. Spanos, P.S. Pao, R.L. Holtz, Precipitation behavior of the ß phase in Al-5083, Mater. Sci. Eng. A. 527 (2010) 1089–1095. doi:10.1016/j.msea.2009.10.007.

[26] R. Goswami, G. Spanos, P.S. Pao, R.L. Holtz, Microstructural Evolution and Stress Corrosion Cracking Behavior of Al-5083, Metall. Mater. Trans. A. 42 (2010) 348–355. doi:10.1007/s11661-010-0262-y.

[27] M.J. Starink, A.-M. Zahra, β′ and β precipitation in an Al–Mg alloy studied by DSC and TEM, Acta Mater. 46 (1998) 3381–3397. doi:10.1016/S1359-6454(98)00053-6.

[28] J. Gunson, Effect of sensitisation on the corrosion fatigue properties of AA5456-H116, MS Thesis, University of Birmingham, 2011. http://etheses.bham.ac.uk/1767/ (accessed January 30, 2015).

[29] ASM Handbook, ASM International, 2002.

[30] L. Tan, T.R. Allen, Effect of thermomechanical treatment on the corrosion of AA5083, Corros. Sci. 52 (2010) 548–554. doi:10.1016/j.corsci.2009.10.013.

[31] D. Scotto D'Antuono, J. Gaies, W. Golumbfskie, M.L. Taheri, Grain boundary misorientation dependence of β phase precipitation in an Al–Mg alloy, Scr. Mater. 76 (2014) 81–84. doi:10.1016/j.scriptamat.2014.01.003.

[32]   Y. Zhao, M.N. Polyakov, M. Mecklenburg, M.E. Kassner, A.M. Hodge, The role of grain boundary plane orientation in the β phase precipitation of an Al–Mg alloy, Scr. Mater. 89 (2014) 49–52. doi:10.1016/j.scriptamat.2014.07.003.

[33]   L.I. Kaigorodova, The effect of grain-boundary structure formation on β-precipitation in aged Al-Mg alloys, Mater. Sci. Forum. 294-296 (1999) 477.

[34]   N. Birbilis, R. Zhang, S. Knight, R. Holtz, R. Goswami, C. Davies, A Survey of Sensitisation in 5xxx series Aluminium Alloys, Corrosion. (2015). doi:10.5006/1787.

[35]   Y. Zhu, D.A. Cullen, S. Kar, M.L. Free, L.F. Allard, Evaluation of Al_3Mg_2 Precipitates and Mn-Rich Phase in Aluminum-Magnesium Alloy Based on Scanning Transmission Electron Microscopy Imaging, Metall. Mater. Trans. A. 43 (2012) 4933–4939. doi:10.1007/s11661-012-1354-7.

[36]   S. Jain, M.L.C. Lim, J.L. Hudson, J.R. Scully, Spreading of intergranular corrosion on the surface of sensitized Al-4.4Mg alloys: A general finding, Corros. Sci. 59 (2012) 136–147. doi:10.1016/j.corsci.2012.02.018.

[37]   N. Birbilis, R.G. Buchheit, Electrochemical Characteristics of Intermetallic Phases in Aluminum Alloys - An Experimental Survey and Discussion, J. Electrochem. Soc. 152 (2005) B140–B151. doi:10.1149/1.1869984.

[38]   N.J. Holroyd, G. Scamans, Environmental Degradation of Marine Aluminum Alloys - Past, Present and Future, Corrosion. (2015). doi:10.5006/1927.

[39]   J.R. Scully, Intergranular Corrosion, in: M. Stratmann, G.S. Fankel (Eds.), Encycl. Electrochem., Wiley-VCH Verlag GmbH & Co. KGaA, Germany, 2003: p. 344.

[40]   E.M. Bumiller, R.G. Kelly, Intergranular corrosion in AA5XXX: a case for continuous attack with a discontinuous active path, in: Dep. Def. Corros. Conf., NACE, Palm Springs, CA, 2011.

[41]   S. Jain, Surface Spreading of Intergranular Corrosion on Stainless Steels and Al-Mg (AA5XXX) Alloys, PhD Dissertation, University of Virginia, 2011.

[42]   R.J. Winsley, Corrosion resistance of heat-treated and friction stir welded AA5083-H116, PhD Thesis, University of Birmingham, 2008.

[43]   R. Goswami, R.L. Holtz, Transmission Electron Microscopic Investigations of Grain Boundary Beta Phase Precipitation in Al 5083 Aged at 373 K (100 °C), Metall. Mater. Trans. A. 44 (2012) 1279–1289. doi:10.1007/s11661-012-1166-9.

[44]   R. Zhang, R.K. Gupta, C.H.J. Davis, A.M. Hodge, M. Tort, K. Xia, et al., The influence of grain size and grain orientation on sensitisation in AA5083, Corrosion. (2015). doi:10.5006/1703.

[45]   ASTM, ASTM: G67-04 Standard Test Method for Determining the Susceptibility to Intergranular Corrosion of 5XXX Series Aluminum Alloys by Mass Loss After Exposure to Nitric Acid (NAMLT Test), ASTM International, West Conshocken, PA, 2004.

[46]   ASTM, ASTM: B928 Standard Specification for High Magnesium Aluminum-Alloy Sheet and Plate for Marine Service and Similar Environments, ASTM International, West Conshocken, PA, 2004.

[47]   M.L.C. Lim, Unpublished Work, University of Virginia, 2016.

[48]   M.L.C. Lim, D.W. Ellis, S.C. Hahn, J.R. Scully, R.G. Kelly, Potential Dependence of Intergranular Corrosion Propagation in Sensitized Al-Mg Alloys, in: 228th Electrochem. Soc. Meet., Phoenix, AZ, 2015.

[49]   A.J. Field, C. Wong, Thermal stability of selected 5000 series Al alloys, in: TMS Annu. Meet., San Antonio, TX, 2006.

[50]   Y. Yuan, Localized corrosion and stress corrosion cracking of aluminum-magnesium alloys, PhD Dissertation, University of Birmingham, 2005.

[51]   Y.-K. Yang, T.R. Allen, Determination of the β Solvus Temperature of the Aluminum Alloy 5083, Metall. Mater. Trans. A. 44 (2013) 5226–5233. doi:10.1007/s11661-013-1837-1.

[52]   J. Buczynski, Electrochemical Analyses of Etchants Used to Detect Sensitization in Marine-Grade 5XXX Aluminum-Magnesium Alloys, MS Thesis, University of Virginia, 2012.

[53]   F. Li, D. Xiang, Y. Qin, R.B. Pond Jr., K. Slusarski, Measurements of degree of sensitization (DoS) in aluminum alloys using EMAT ultrasound, Ultrasonics. 51 (2011) 561–570. doi:10.1016/j.ultras.2010.12.009.

[54]   R. Dunn, R.G. Kelly, E.M. Bumiller, Development of a Degree of Sensitization (DoS) Probe for 5XXX Aluminum-Magnesium Alloys, in: ShipTech, Biloxi, MS, 2010.

[55]   M.A. Steiner, S.R. Agnew, Modeling sensitization of Al–Mg alloys via β-phase precipitation kinetics, Scr. Mater. (n.d.). doi:10.1016/j.scriptamat.2015.02.012.

[56]   M. Steiner, S. Agnew, Predictive Sensitization Modeling for AA5XXX Aluminum Alloys including Non-Isothermal Cases, Corrosion. (2015). doi:10.5006/1675.

[57]   J. Wloka, S. Virtanen, Detection of nanoscale η-MgZn2 phase dissolution from an Al-Zn-Mg-Cu alloy by electrochemical microtransients, Surf. Interface Anal. 40 (2008) 1219–1225. doi:10.1002/sia.2868.

[58]   H.H. Strehblow, P. Marcus, Mechanisms of Pitting Corrosion, in: Corros. Mech. Theory Pract., 2nd ed., Marcel Dekker, Inc., New York, NY, 2002.

[59]   J. Seong, F. Yang, F. Scheltens, G.S. Frankel, N. Sridhar, Influence of the Altered Surface Layer on the Corrosion of AA5083, J. Electrochem. Soc. 162 (2015) C209–C218. doi:10.1149/2.0321506jes.

[60]   J.R. Scully, D.E. Peebles, A.D. Romig, D.R. Frear, C.R. Hills, Metallurgical factors influencing the corrosion of aluminum, Al-Cu, and Al-Si alloy thin films in dilute hydrofluoric solution, Metall. Trans. A. 23 (1992) 2641–2655. doi:10.1007/BF02658068.

[61]   G.S. Chen, M. Gao, R.P. Wei, Microconstituent-Induced Pitting Corrosion in Aluminum Alloy 2024-T3, Corrosion. 52 (1996) 8–15. doi:10.5006/1.3292099.

[62]   V. Guillaumin, G. Mankowski, Localized corrosion of 2024 T351 aluminium alloy in chloride media, Corros. Sci. 41 (1998) 421–438. doi:10.1016/S0010-938X(98)00116-4.

[63]   J.O. Park, C.-H. Paik, R.C. Alkire, Scanning Microsensors for Measurement of Local pH Distributions at the Microscale, J. Electrochem. Soc. 143 (1996) L174–L176. doi:10.1149/1.1837020.

[64]   N. Birbilis, R. Zhang, M.L.C. Lim, R.K. Gupta, C.H.J. Davies, S.P. Lynch, et al., Quantification of Sensitization in AA5083-H131 via Imaging Ga-Embrittled Fracture Surfaces, Corrosion. 69 (2013) 396–402. doi:10.5006/0804.

[65] S. Jain, J.L. Hudson, J.R. Scully, Effects of constituent particles and sensitization on surface spreading of intergranular corrosion on a sensitized AA5083 alloy, Electrochimica Acta. 108 (2013) 253–264. doi:10.1016/j.electacta.2013.06.036.

[66] W. Zhang, G.S. Frankel, Anisotropy of Localized Corrosion in AA2024-T3, Electrochem. Solid-State Lett. 3 (2000) 268–270. doi:10.1149/1.1391121.

[67] M.J. Robinson, N.C. Jackson, The influence of grain structure and intergranular corrosion rate on exfoliation and stress corrosion cracking of high strength Al–Cu–Mg alloys, Corros. Sci. 41 (1999) 1013–1028. doi:10.1016/S0010-938X(98)00171-1.

[68] M.J. Robinson, N.C. Jackson, Exfoliation corrosion of high strength Al–Cu–Mg alloys: effect of grain structure, Br. Corros. J. 34 (1999) 45–49. doi:10.1179/bcj.1999.34.1.45.

[69] D. Mizuno, R.G. Kelly, Galvanically Induced Intergranular Corrosion of AA5083-H131 Under Atmospheric Exposure Conditions: Part 1—Experimental Characterization, Corrosion. 69 (2013) 580–592. doi:10.5006/0812.

[70] J.A. Lyndon, R.K. Gupta, M.A. Gibson, N. Birbilis, Electrochemical behaviour of the β-phase intermetallic (Mg_2Al_3) as a function of pH as relevant to corrosion of aluminium–magnesium alloys, Corros. Sci. 70 (2013) 290–293. doi:10.1016/j.corsci.2012.12.022.

[71] E. McCafferty, Sequence of steps in the pitting of aluminum by chloride ions, Corros. Sci. 45 (2003) 1421–1438. doi:10.1016/S0010-938X(02)00231-7.

[72] T.H. Nguyen, R.T. Foley, The Chemical Nature of Aluminum Corrosion III . The Dissolution Mechanism of Aluminum Oxide and Aluminum Powder in Various Electrolytes, J. Electrochem. Soc. 127 (1980) 2563–2566. doi:10.1149/1.2129520.

[73] A. Aballe, M. Bethencourt, F.J. Botana, M.J. Cano, M. Marcos, Localized alkaline corrosion of alloy AA5083 in neutral 3.5% NaCl solution, Corros. Sci. 43 (2001) 1657–1674. doi:10.1016/S0010-938X(00)00166-9.

[74] N. Birbilis, R.G. Buchheit, Investigation and Discussion of Characteristics for Intermetallic Phases Common to Aluminum Alloys as a Function of

Solution pH, J. Electrochem. Soc. 155 (2008) C117–C126. doi:10.1149/1.2829897.

[75]   M. Pourbaix, Atlas of Electrochemical Equilibria in Aqueous Solutions, NACE International, Houston, TX, 1974.

[76]   J.-H. Ai, M.L.C. Lim, J.R. Scully, Effective Hydrogen Diffusion in Aluminum Alloy 5083-H131 as a Function of Orientation and Degree of Sensitization, Corrosion. 69 (2013) 1225–1239. doi:10.5006/0987.

[77]   T.-S. Huang, G.S. Frankel, Kinetics of sharp intergranular corrosion fissures in AA7178, Corros. Sci. 49 (2007) 858–876. doi:10.1016/j.corsci.2006.04.015.

[78]   W. Zhang, G.S. Frankel, Localized Corrosion Growth Kinetics in AA2024 Alloys, J. Electrochem. Soc. 149 (2002) B510–B519. doi:10.1149/1.1513984.

[79]   S. Maitra, G.C. English, Mechanism of localized corrosion of 7075 alloy plate, Metall. Trans. A. 12 (1981) 535–541. doi:10.1007/BF02648553.

[80]   R.G. Buchheit, J.P. Moran, G.E. Stoner, Localized Corrosion Behavior of Alloy 2090—The Role of Microstructural Heterogeneity, Corrosion. 46 (1990) 610–617. doi:10.5006/1.3585156.

[81]   I.L. Muller, J.R. Galvele, Pitting potential of high purity binary aluminium alloys—I. Al☐Cu alloys. Pitting and intergranular corrosion, Corros. Sci. 17 (1977) 179–193. doi:10.1016/0010-938X(77)90044-0.

[82]   I.L. Muller, J.R. Galvele, Pitting potential of high purity binary aluminium alloys—II. AlMg and AlZn alloys, Corros. Sci. 17 (1977) 995–1007. doi:10.1016/S0010-938X(77)80014-0.

[83]   D.A. Little, B.J. Connolly, J.R. Scully, An electrochemical framework to explain the intergranular stress corrosion behavior in two Al–Cu–Mg–Ag alloys as a function of aging, Corros. Sci. 49 (2007) 347–372. doi:10.1016/j.corsci.2006.04.024.

[84]   K. Urushino, K. Sugimoto, Stress-corrosion cracking of aged Al☐Cu☐Mg alloys in NaCl solution, Corros. Sci. 19 (1979) 225–236. doi:10.1016/0010-938X(79)90008-8.

[85]   L. Guan, Y. Zhou, H.Q. Lin, B. Zhang, J.Q. Wang, E.-H. Han, et al., Detection and analysis of anodic current transients associated with

nanoscale β-phase precipitates on an Al–Mg microelectrode, Corros. Sci. 95 (2015) 6–10. doi:10.1016/j.corsci.2015.03.001.

[86]   A. Turnbull, The solution composition and electrode potential in pits, crevices and cracks, Corros. Sci. 23 (1983) 833–870. doi:10.1016/0010-938X(83)90014-8.

[87]   A. Turnbull, Modeling of the Chemistry and Electrochemistry in Cracks— A Review, Corrosion. 57 (2001) 175–189. doi:10.5006/1.3290342.

[88]   J.R. Galvele, S.M. de De Micheli, Mechanism of intergranular corrosion of Al-Cu alloys, Corros. Sci. 10 (1970) 795–807. doi:10.1016/S0010-938X(70)80003-8.

[89]   K. Sugimoto, K. Hoshino, M. Kageyama, S. Kageyama, Y. Sawada, Stress corrosion cracking of aged Al☐4%Cu alloy in NaCl solution, Corros. Sci. 15 (1975) 709–720. doi:10.1016/0010-938X(75)90035-9.

[90]   B.J. Connolly, J.R. Scully, Corrosion cracking susceptibility in Al-Li-Cu alloys 2090 and 2096 as a function of isothermal aging time, Scr. Mater. 42 (2000) 1039–1045.

[91]   C. Kumai, J. Kusinski, G. Thomas, T.M. Devine, Influence of Aging at 200 C on the Corrosion Resistance of Al-Li and Al-Li-Cu Alloys, Corrosion. 45 (1989) 294–302. doi:10.5006/1.3577857.

[92]   R.G. Buchheit, J.P. Moran, G.E. Stoner, Electrochemical Behavior of the T1 (Al2CuLi) Intermetallic Compound and Its Role in Localized Corrosion of Al-2% Li-3% Cu Alloys, Corrosion. 50 (1994) 120–130. doi:10.5006/1.3293500.

[93]   K.A. Yasakau, M.L. Zheludkevich, S.V. Lamaka, M.G.S. Ferreira, Role of intermetallic phases in localized corrosion of AA5083, Electrochimica Acta. 52 (2007) 7651–7659. doi:10.1016/j.electacta.2006.12.072.

[94]   M.L. Lim, S. Jain, R.G. Kelly, J.R. Scully, Intergranular Corrosion Penetration in AA5083 (UNS # A95083) as a Function of Electrochemical and Metallurgical Conditions, ECS Trans. 41 (2012) 177–191. doi:10.1149/1.3697588.

[95]   C.B. Crane, Validation of the Coupled Dissolution-Hydrogen Embrittlement Mechanism of IGSCC in Low Temperature Sensitized AA5083-H131, PhD Dissertation, University of Virginia, 2013.

[96]   T.-S. Huang, G.S. Frankel, Influence of grain structure on anisotropic localised corrosion kinetics of AA7xxx-T6 alloys, Corros. Eng. Sci. Technol. 41 (2006) 192–199. doi:10.1179/174327806X120739.

[97]   T.-S. Huang, G.S. Frankel, Effects of Temper and Potential on Localized Corrosion Kinetics of Aluminum Alloy 7075, Corrosion. 63 (2007) 731–743. doi:10.5006/1.3278422.

[98]   J. Galvele, Transport processes in passivity breakdown—II. Full hydrolysis of the metal ions, Corros. Sci. 21 (1981) 551–579. doi:10.1016/0010-938X(81)90009-3.

[99]   J.R. Galvele, Transport Processes and the Mechanism of Pitting of Metals, J. Electrochem. Soc. 123 (1976) 464–474. doi:10.1149/1.2132857.

[100]   S.M. Gravano, J.R. Galvele, Transport processes in passivity breakdown—III. Full hydrolysis plus ion migration plus buffers, Corros. Sci. 24 (1984) 517–534. doi:10.1016/0010-938X(84)90034-9.

[101]   N.J. Laycock, R.C. Newman, Localised dissolution kinetics, salt films and pitting potentials, Corros. Sci. 39 (1997) 1771–1790. doi:10.1016/S0010-938X(97)00049-8.

[102]   Y. Xu, M. Wang, H.W. Pickering, On Electric Field Induced Breakdown of Passive Films and the Mechanism of Pitting Corrosion, J. Electrochem. Soc. 140 (1993) 3448–3457. doi:10.1149/1.2221108.

[103]   H.W. Pickering, K. Cho, E. Nystrom, Microscopic and local probe method for studying crevice corrosion and its application to iron and stainless steel, Corros. Sci. 35 (1993) 775–783. doi:10.1016/0010-938X(93)90215-3.

[104]   H.W. Pickering, The role of electrode potential distribution in corrosion processes, Mater. Sci. Eng. A. 198 (1995) 213–223. doi:10.1016/0921-5093(95)80076-7.

[105]   G.S. Frankel, J.R. Scully, C.V. Jahnes, Repassivation of Pits in Aluminum Thin Films, J. Electrochem. Soc. 143 (1996) 1834–1840. doi:10.1149/1.1836912.

[106]   R. Schwarting, G. Ebel, T.J. Dorsch, Manufacturing techniques and process challenges with CG47 class ship aluminum superstructures modernization and repairs, in: Fleet Maint. Mod. Symp., San Diego, CA, 2011.

[107] J.R. Pickens, J.R. Gordon, J. a. S. Green, The effect of loading mode on the stress-corrosion cracking of aluminum alloy 5083, Metall. Trans. A. 14 (1983) 925–930. doi:10.1007/BF02644298.

[108] D. Tanguy, B. Bayle, R. Dif, T. Magnin, Hydrogen effects during IGSCC of pure Al–5Mg alloy in NaCl media, Corros. Sci. 44 (2002) 1163–1175. doi:10.1016/S0010-938X(01)00140-8.

2   Intergranular Corrosion Penetration in an Al-Mg Alloy as a Function of Electrochemical and Metallurgical Conditions

2.1   Abstract

An experimental and modeling study of factors influencing intergranular corrosion (IGC) penetration depth into an Al-Mg alloy, AA5083, is presented. Potentiostatic tests over a range of potentials in 0.6 M NaCl solution were conducted on LT, ST, and LS surfaces of sensitized AA5083. The IGC penetration rate was found to depend on applied potential, degree of sensitization (DoS), exposure time, and propagation direction relative to the rolling direction. Statistical IGC depth distributions were analyzed and served as inputs for a phenomenological model to estimate IGC damage progression for AA5083 during exposure to 0.6 M NaCl solution at pH 8.3. This model was validated by comparing the model predicted and experimental depths for the 100°C sensitization condition. Extension of this combined experimental and modeling approach to the 80°C sensitization demonstrated that sensitization temperature is another significant factor in IGC penetration depths.

2.2   Introduction

5XXX Al-Mg alloys (AA5XXX) are attractive for marine structures due to their low cost, high strength-to-weight ratio, weldability, and uniform corrosion resistance. These alloys derive their strength from work hardening through cold

49

work and solid solution strengthening by adding magnesium and manganese. Alloys containing above 3 wt% magnesium become susceptible to intergranular corrosion (IGC) when exposed to temperatures as low as 50°C over long periods of time.[1–5] IGC can lead to mass loss (through grain fall-out) and intergranular stress corrosion cracking (IGSCC) in the presence of stress.[6–10] These corrosion phenomena can progress undetected through the alloy and affect structural integrity. It is therefore critical to develop a model that can predict the extent and nature of the IGC propagation. Identifying and understanding the metallurgical, electrochemical, and chemical factors that govern IGC propagation is of a necessary first step towards the development of any predictive corrosion model.

Previous studies on IGC and SCC of AA5XXX alloys indicate these phenomena are a result of preferential precipitation of β-phase (Al$_3$Mg$_2$) at grain boundaries[1].[1–17] During exposure to elevated or even ambient temperature, magnesium diffuses to the grain boundaries forming the anodic β-phase via heterogeneous nucleation and growth, termed sensitization.[1–9,14,15,18–20] β-phase precipitation, which controls the degree of sensitization (DoS), occurs slowly at near-ambient temperatures, but quickly during short exposure periods at elevated temperatures (60-180°C).[7] Precipitation is also reported to be influenced by grain boundary characteristics such as misorientation and the boundary plane.[3,21–23] A high DoS can result in enough β-phase precipitation such that 50% of grain

---

[1] β-phase formation also occurs within the grains but that β-phase does not contribute to sensitization, and will hereafter not be discussed.

boundaries become almost continuously covered with β-phase precipitates.[3] In contrast, a low DoS will only have discrete β-phase precipitates on the grain boundaries, as well as some grain boundaries with very little β-phase precipitates.[3,24] Transmission electron microscopy (TEM) studies on AA5083 alloy showed that as the DoS increases, the β-phase precipitates coarsen and coalesce to form longer precipitates.[1,3,10,14,23,24] The size of the β-phase precipitates varies from 50 – 190 nm and 100 – 1000 nm in width and length, respectively.

Electrochemical frameworks have been developed to explain the role of potential and microstructure on IGC of aluminum alloys. In general, the difference between the breakdown potentials of the anodic grain boundary zones and the matrix defines the degree of IGC susceptibility of the alloys.[1,5,23,25–35] An alloy is considered susceptible if there is a large difference between the two potentials. In 0.6 M NaCl solution, the breakdown potential of β-phase was -1.162 V_{SCE}, which is 400 mV lower than the open circuit potential of either the sensitized or unsensitized AA5083.[1,8,10,36–38] The unsensitized AA5083 exhibited a high breakdown potential that decreased with chloride concentration. Moreover, the sensitized AA5083 had a breakdown potential lower than the unsensitized alloy, which decreased with both DoS and chloride concentration.[8,37] Recently, it was proposed that the critical breakdown potential is not associated with discrete, isolated pitting of β-phase precipitates, but rather with the spreading of IGC to adjacent β-phase precipitates across the surface.[37]. The spreading of IGC was

explained based on a cooperative interaction model, where the interactive effects of local acidification, spatial proximity of β-phase, chloride concentration, and applied potential were considered.[37] However, penetration of IGC into AA5083 as a function of DoS was not investigated. Furthermore, no relationship between IGC penetration depth, DoS, and exposure time for various orientations of any Al-Mg alloy has been reported to date.

In this work, the above electrochemical framework[37] was utilized to guide long-term IGC depth penetration studies under potentiostatic control on AA5083 (UNS A95083) in the zone of potentials where IGC is dominant. The effect of orientation, sensitization heat treatment, and DoS were variables. The data generated were utilized to develop a quantitative model that predicted the evolution and geometry of IGC penetration in AA5083 as a function of DoS, propagation direction, and time of exposure in a seawater environment. Validation of this model was conducted using experimental data from materials sensitized at 100°C. In addition, the combined experimental and modeling approach has been applied to the 80°C sensitization to assess the significance of sensitization temperature.

2.3   Objective

The primary objective of this chapter is to quantitatively characterize and understand the effects of select electrochemical and metallurgical factors on the IGC of sensitized AA5083 in aqueous solutions that simulate the marine environment. IGC depths will be measured as a function of DoS, applied potential,

orientation of propagation, and exposure time. To develop a scientific interpretation of IGC penetration and propagation mechanism, the dependence of IGC rates on these factors will be examined and IGC rates will be correlated with the description of DoS on the microstructural level in terms of β precipitate morphology and distribution on grain boundaries. Statistical IGC depth distribution will be analyzed and utilized to build phenomenological models that can estimate IGC damage progression as a function of the aforementioned variables. Phenomenological IGC models are vital to the development of component risk assessment analysis and life prediction models for AA5XXX.

2.4   Experimental Procedures

2.4.1   Material, Heat Treatment, and Degree of Sensitization

The AA5083 (UNS A95083) 2.25" plate materials used in this study were acquired in the H131 temper condition. In the H131 temper state, the AA5083 is strain hardened without supplementary thermal treatment to have a mean ultimate tensile strength (UTS) equivalent to three-eighths of the UTS of a full-hard condition (about 75% cold reduction after full annealing) for this alloy.[39] The nominal composition of AA5083 is given in Table 2.1. The orientation convention and the microstructure of the plate are given in Figure 2.1. The average grain sizes in the longitudinal (L), long transverse (T), and short transverse (S) directions are 80 μm, 60 μm, and 20 μm, respectively. The test specimens were cut from the center of the plate (S/2) into 5.1 cm x 2.5 cm x 0.6 cm (L x S x T) pieces, solution

heat treated at 275°C for 10 hours, and cold water quenched to room temperature (SHTQ). The specimens were solutionized to dissolve any existing β-phase precipitates from processing, and create a baseline unsensitized material. Subsequently, these materials were sensitized at 100°C or 80°C for various lengths of time. Duplicate specimens for each aging condition were prepared in accordance with ASTM G-67 for measurement of DoS via the nitric acid mass loss test (NAMLT).[40] The heat treatments and their respective DoS utilized in this study are summarized in Table 2.2.

Table 2.1. Nominal composition of AA5083 (UNS A95083)

Component	Al	Mg	Mn	Fe	Si	Cu	Cr	Zn	Ti	Others
Weight %	Bal	4.4	0.7	0.22	0.1	0.05	0.08	0.02	0.02	< 0.01
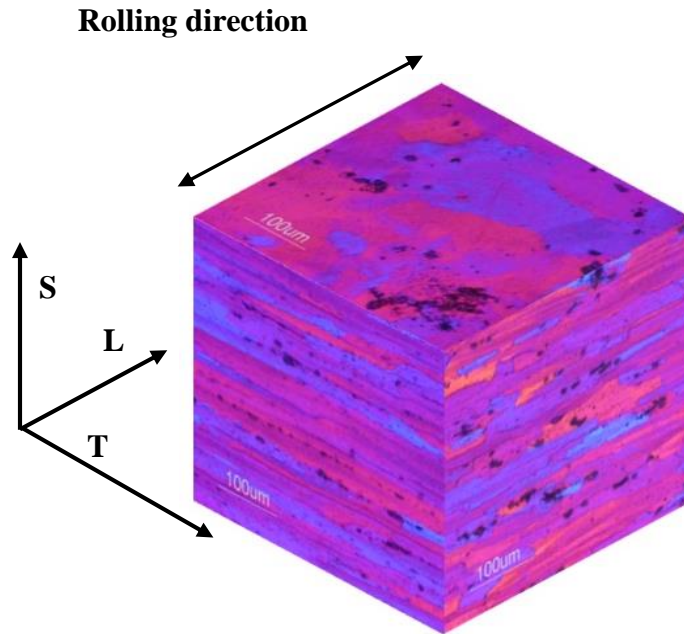
Figure 2.1. Optical micrographs of metallographic cross-section of AA 5083-H131 after electrolytic Barker's etching.

Table 2.2. Sensitization heat treatment conditions and DoS according to ASTM G-67 for AA5083-H131

Sensitization temperature (°C)	Sensitization time (days)	Degree of Sensitization (mg/cm²)
100	0 (SHTQ only)	2
	3	10
	7	24
	14	39
	30	49
80	40	22
	90	40
	180	48

2.4.2 Sample Preparation for Corrosion Testing and β-Phase Distribution

Samples mounted in Buehler EpoThin epoxy resin and allowed to cure at room temperature (~25°C) for 9 h. The mounted samples were alternatingly ground with SiC paper and rinsed with water down to 1200 grit. The samples were then polished with 1 μm diamond paste and finished with 0.06 μm colloidal silica. Samples were ultrasonically cleaned in ethanol to remove any silica debris and air dried prior to testing.

2.4.3 β-Phase Distribution

The β-phase morphology and distribution at different sensitization levels were estimated through image analyses of Barker's etching and phosphoric acid etching micrographs. Barker's etching revealed grain boundaries by growing oxide films on ST surfaces of samples immersed in 2.5 vol% HBF_4 solution at ambient temperature and polarized at 20 V for 40 to 80 s. The etched surfaces were viewed

with an optical microscope under polarized light. The light was cross-polarized at angles depending on the grain orientations, such that different grain orientations produced different colors. Micrographs of an area with about 80 grain boundaries, marked using diamond indentations, were taken at 500x magnification. Phosphoric acid etching was used to expose the location of β-phase precipitates on the grain boundaries. The Barker's-etched samples were lightly ground with SiC paper, and polished with 1 μm diamond paste and colloidal silica to remove the oxide film. The samples were then etched in 10 vol% H_3PO_4 solution for 30 s at 55ºC (3, 9). Micrographs of the marked areas were taken using the SEM in lower secondary electron imaging (LEI) mode.

2.4.4   Potentiostatic Testing

Potentiostatic holds were conducted on AA5083 in 0.6 M NaCl solution at a pH of 8.3 using a saturated calomel (SCE) reference electrode. The samples, with a surface area of 0.36 cm^2, were exposed to open circuit potential for 30 min and then held at -0.73 V_{SCE} for 24, 72, or 100 h, consistent with conditions where spreading was observed. [37] The tests were performed on ST, LT and LS surfaces. Images of cross-sectioned samples were taken with the optical microscope to determine IGC depth and distribution. The total cross-sectional area of 108 mm^2 was evaluated for each condition. The fissure count per area ranged from 6 to 110 fissures.

2.4.5   Validation Experiments

Potentiostatic holds utilizing a sensitization level of 29 mg/cm^2 (100°C for 10 days) validated the IGC propagation depth predicted from the IGC propagation model (L and T depths). Validations were conducted on ST and LS surfaces with 100 h of exposure time. Images of cross-sectioned samples were taken with the optical microscope to determine IGC depth and distribution for comparison to model predictions.

2.5   Results

2.5.1   β-phase Distribution

The optical micrograph shown in Figure 2.2b is a typical Barker's etch image revealing the grain boundary morphology. The grain structure is typical of rolled plate with long grains in the L direction and shorter grain diameters in the S and T directions. The SEM image (Figure 2.2c) shows phosphoric acid etching, where grain boundaries with β-phase precipitates were corroded. Note that the SEM images were taken at different magnifications, such that the resolutions of the images are different. For the high DoS condition (49 mg/cm^2), images have 43 nm per pixel resolution, while those of the low DoS condition (10 mg/cm^2) have 10 nm per pixel resolution. If isolated β-phase precipitates smaller than these detection limits were etched, corrosion would not have been detected.

Analysis of matching pairs of Barker's etch and phosphoric acid etched images provided the β-phase distribution morphology relative to the total length of

57

grain boundaries for each sensitized AA5083 condition. A trend of increasing β-phase precipitate coverage with DoS can be observed. The amount of clean grain boundaries or grain boundaries with no β-phase precipitate decrease monotonically with DoS. However, the percentage of grain boundaries that have low coverage plateaued at a DoS of 39 mg/cm^2. The β coverage was divided into two categories: high if 70% or more of the grain boundary length had β-phase precipitates, and low if less than 70% of a grain boundary length was covered with β-phase precipitates. 80% of the grain boundaries were etched for the most sensitized condition of 49 mg/cm^2. Amongst these, 52% of the grain boundaries have high β-phase coverage. In contrast, only 14% of the grain boundaries were etched in a sensitization condition of 10 mg/cm^2, none of which demonstrated a high β-phase coverage. This suggests that these discrete β-phase precipitates have grown, leading to structures that appear to be connected in the 2-dimensions. The unsensitized sample shows clean grain boundaries with no detected β-phase precipitates.[14,15]
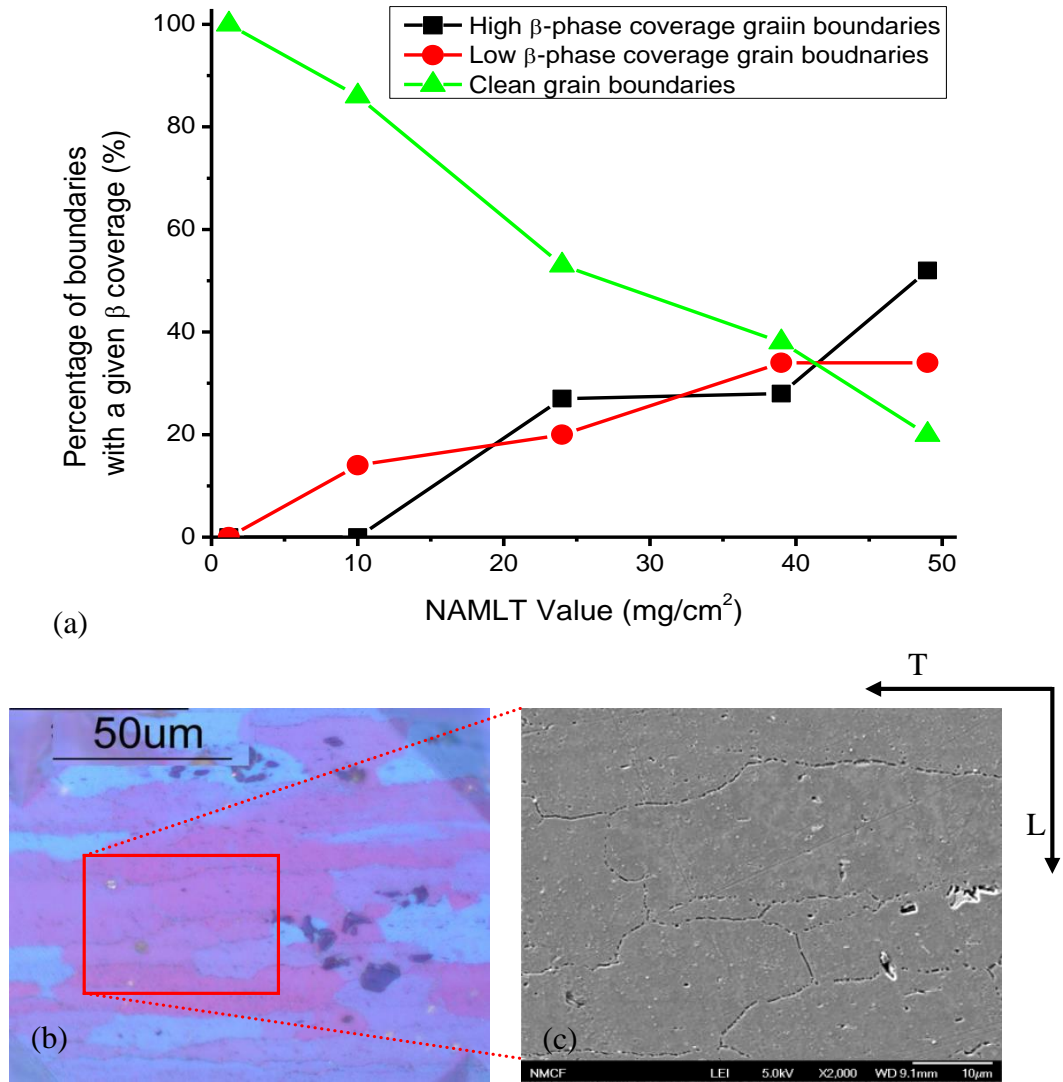
Figure 2.2. (a) Distribution of grain boundaries in AA5083-H131 as a function of β coverage and DoS (37). Grain boundaries are divided into three categories: high β-phase coverage grain boundary if 70% or more of a grain boundary length had β-phase; low β-phase coverage grain boundary if less than 70% of a grain boundary length was covered with β-phase; and clean grain boundary if no β-phase decorate a grain boundary. For example, for a total of 80 grain boundaries, 42 grain boundaries have more than 70% of their lengths covered with β-phase, 22 have less than 70%, and the remaining 16 have no β-phase at all. This is equivalent to 52.5% of high β-phase coverage grain boundaries, 27.5% of low β-phase coverage grain boundaries, and 20% of clean grain boundaries. (b) Barker's etched revealing grain structure; (c) SEM LEI image of phosphoric acid etched revealing attacked sites on the ST surface.

2.5.2 IGC Guided by the Electrochemical Framework

Traditionally, the breakdown potential is viewed as an indication of the pitting potential of discrete precipitates in IGC susceptible materials. However, the breakdown potential of AA5083 was not found to be associated with discrete pitting of β-phase precipitates but rather with the spreading of IGC to adjacent β-phase precipitates across the surface.[37] An electrochemical framework for IGC spreading in AA5083 was developed by comparing the mean critical breakdown potentials of β-phase, and unsensitized and sensitized alloys. The framework suggests that localized pitting of the β-phase is expected at potentials between the breakdown potentials of β-phase (-0.92 V_{SCE}) and the mean critical breakdown potential of the sensitized alloy. IGC spreading is expected at potentials between the critical breakdown potentials of the unsensitized and the sensitized conditions. In 0.6 M NaCl solution, AA5083 with a sensitization condition of 49 mg/cm^2 had a critical breakdown potential in the range of -0.74 to -0.71 V_{SCE}, and a mean value of -0.725 V_{SCE}.[37]

Based on the above information, it is clear that potentiostatic holds at -0.75 to -0.73 V_{SCE} in 0.6 M NaCl solution should produce IGC, including dissolution of β-phase precipitates and possibly spreading. Jain et al. [37] compared the surface damage for sensitized AA5083 with DoS of 49 mg/cm^2 exposed to 0.6 M NaCl solution at three different potentials for 1 hour. At the lowest potential, -0.75 V_{SCE}, only random pits were observed. At a slightly higher potential, -0.74 V_{SCE}, some corrosion was observed. At the highest potential, -0.73 V_{SCE}, a large area of IGC

spreading was observed. The potential of -0.73 V_{SCE} is the critical breakdown potential for IGC for the 49 mg/cm^2 condition in 0.6 M NaCl solution. This potential is well above the breakdown potential of the synthesized β-phase and at the critical breakdown potential for the DoS of 49 mg/cm^2 in 0.6 M NaCl solution.[1,37] Thus, it is evident that IGC spreading, and likely penetration, may be investigated across all DoS levels by conducting experiments at -0.73 V_{SCE}.

2.5.3 IGC Penetration

Effect of Time of Exposure: Unsensitized and sensitized AA5083 were exposed to 0.6 M NaCl solution at -0.73 V_{SCE} for three different exposure times (24, 72, 100 h). The images for the cross-sections of the 49 mg/cm^2 condition for a range of exposure times are shown in Figure 2.3. The horizontal dark regions associated with IGC grew from the left exposed surface towards the right in the L direction. After 24 hours, only a few narrow IGC fissures are evident. After 72 hours, the fissures have grown in depth and link more extensively along the S direction, forming a network. In some areas, this linking of IGC caused grain fall-out, leading to wider fissure mouths. As exposure time progresses, the IGC fissures widen making it easier to develop IGC networks and triggering more grain fall-out.

(a) 24 hours   (b) 72 hours   (c) 100 hours
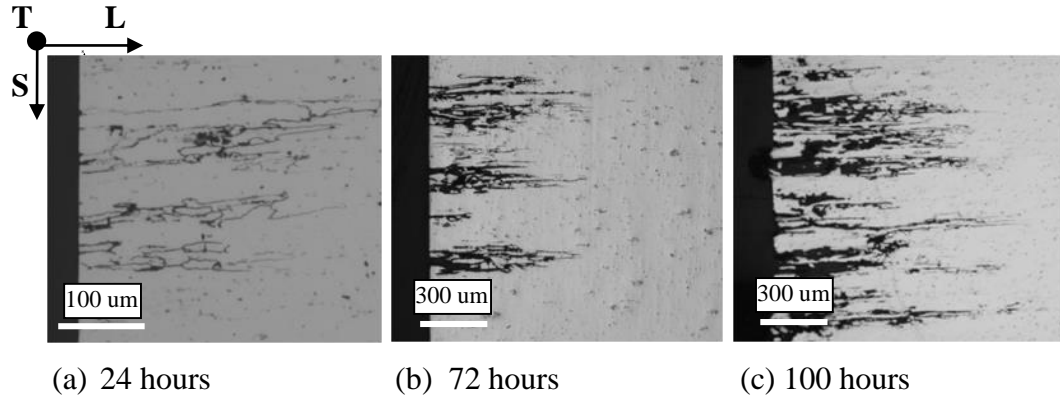
Figure 2.3. Time dependent damage depth of AA 5083-H131 in L direction from ST surface with DoS = 49 mg/cm^2 in 0.6 M NaCl solution, pH 8.3 at -0.73 V$_{SCE.}$ Damage initiated from the exposed left vertical surface. Note difference in magnifications.

Effect of Degree of Sensitization: Different sensitization levels were exposed to 0.6 M NaCl solution at -0.73 V$_{SCE}$. IGC propagation with focus on the penetration aspect in the T orientation for five DoS levels after 100 hours of exposure is shown in Figure 2.4. The unsensitized, 2 mg/cm^2, and the low sensitized conditions, 10 mg/cm^2, showed only a few isolated, short IGC fissures. For a total area of 108 mm^2, 20 IGC fissures with an average depth of 98 μm were observed in the 10 mg/cm^2 condition after 100 hours of exposure. These IGC fissures were usually observed to develop along bands of constituent particles, where β-phase precipitates may also be present [14, 23]. For the 24 mg/cm^2 condition, there were more IGC fissures, and some started to link together in the S directions. Apart from deeper fissures, more IGC networks were also observed for the 39 mg/cm^2 condition. The highly sensitized condition, 49 mg/cm^2, had numerous IGC

networks that propagate relatively fast to depths greater than 600 μm. Grain fall-out was also seen at the site of certain IGC networks.

(a) DoS = 2 mg/cm^2 (b) DoS = 10 mg/cm^2 (c) DoS = 24 mg/cm^2

(d) DoS = 39 mg/cm^2 (e) DoS = 49 mg/cm^2
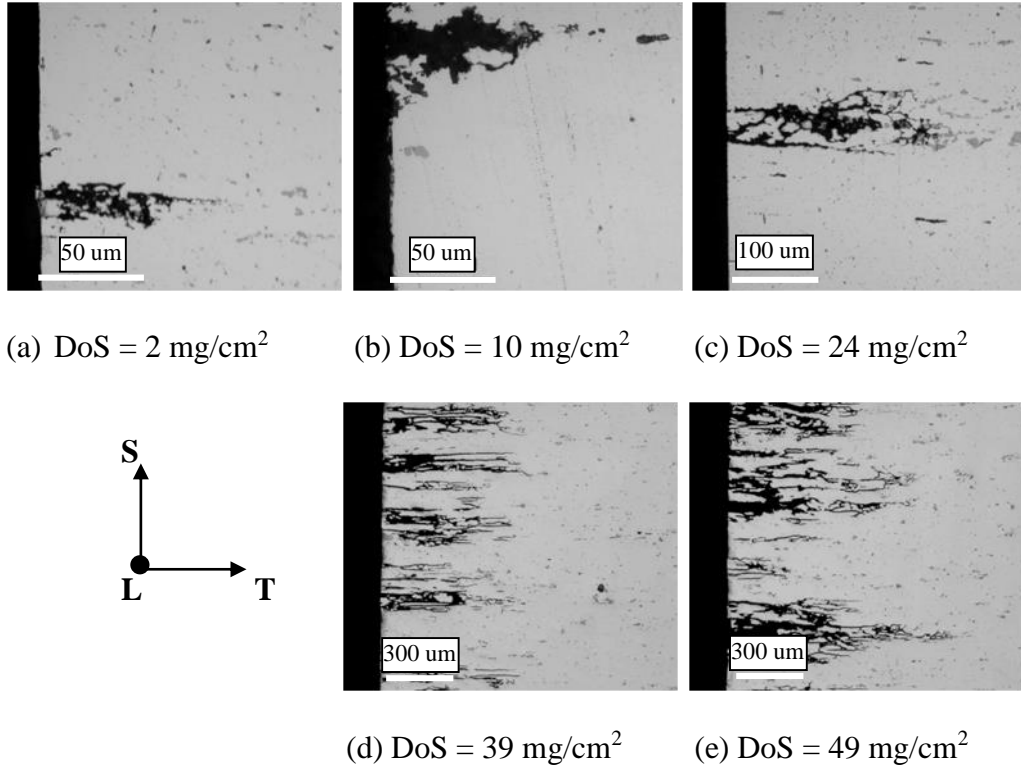
Figure 2.4. Optical micrographs showing damage depth in T direction from LS surface of sensitized AA5083-H131 exposed to 0.6 M NaCl solution, pH 8.3, for 100 hours at -0.73 V$_{SCE}$. Note the difference in magnifications.
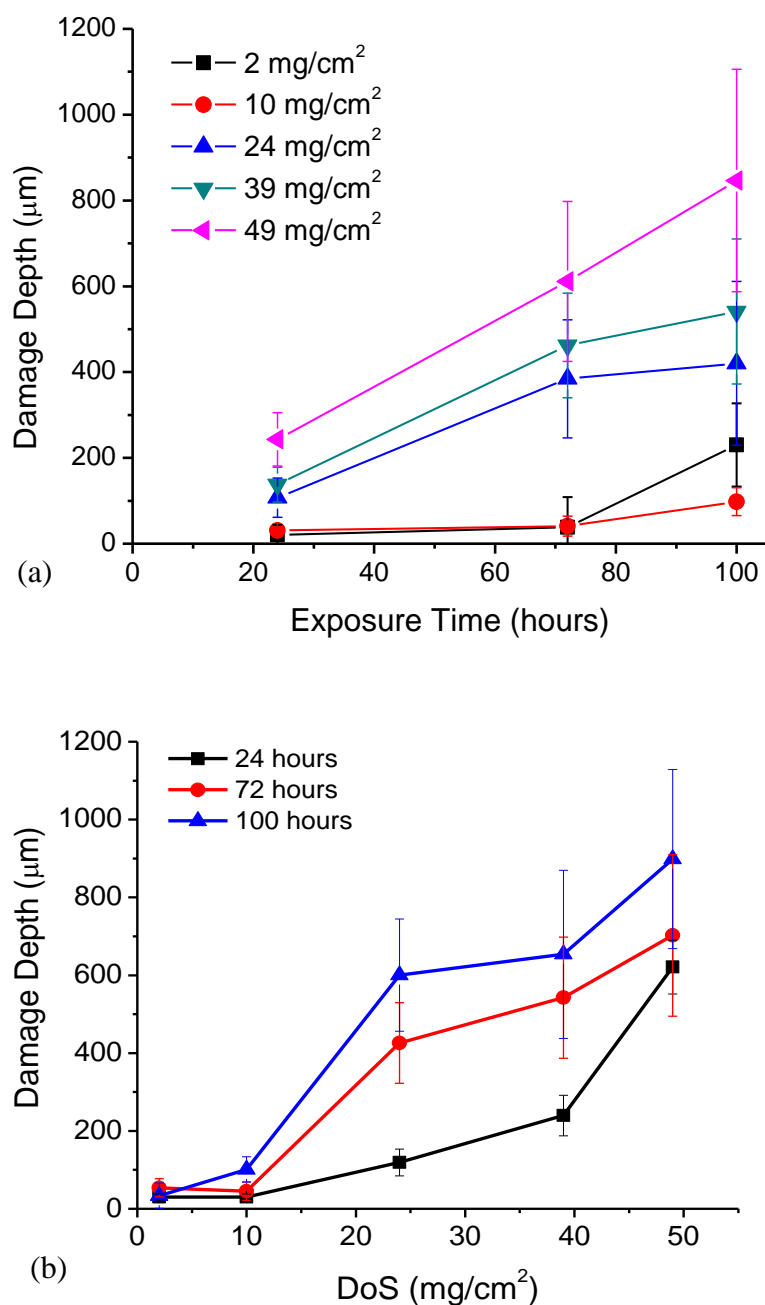
Figure 2.5. Mean damage depth from fissure measurements in T (a) and L (b) directions from LS and ST surfaces as a funtion of DoS and exposure time for AA5083-H131 in 0.6 M NaCl solution, pH 8.3 at -0.73 V$_{SCE}$. The number of fissures increases with both DoS and exposure time. Error bars represent 95% confidence interval.

The IGC fissure depths were quantified as a function of exposure time and DoS. The average damage depths in the T direction from the LS surface are displayed as a function of exposure time for the five DoS conditions in Figure 2.5a. The slopes of the lines noticeably increase with DoS, suggesting faster IGC penetration at higher DoS levels. For the 2 mg/cm^2 and 10 mg/cm^2 conditions, the lines are almost flat even at extended exposure times. The propagation rate in the T direction for the 10 mg/cm^2 condition was 0.24 nm/s assuming a linear propagation rate and immediate initiation upon exposure. This propagation rate is very slow compared to the rate of 1.27 nm/s for the 24 mg/cm^2 condition. This influence of DoS is also evident in Figure 2.5b, which displays average damage depth in the L direction from the ST surface versus DoS for the three exposure times. For all exposure times, there is a clear transition between DoS of 10 mg/cm^2 and 24 mg/cm^2, with a sharp increase in damage depth. This transition implies a shift from IGC resistance to susceptibility, which is in agreement with the guidance suggested in the ASTM G-67 Standard, stipulating that Al-Mg alloys with DoS of 15 mg/cm^2 and below are considered IGC resistant, whereas those of 25 mg/cm^2 or more are regarded to be IGC susceptible[2].[40]

Effect of Orientation: IGC propagation results in the L and S directions for the most sensitized condition, 49 mg/cm^2, over a range of exposure times are shown in

---

[2]The error bars on ASTM G-67 standard place 24 mg/cm^2 in the range where the transition from intermediate sensitized to IGC susceptible is observed.

Figures 2.3 and 2.6. Propagation in the S direction is shown to have started from the surface, then branched and propagated in a direction parallel to the surface along lengthy high-angle grain boundaries in the L direction. Grain fall-out was also more predominant for experiments with these orientations due to the shorter grain width in the S direction which allowed corrosion to penetrate to depths of multiple grain widths. On the other hand, propagation in T and L (Figures 2.3 and 2.4) directions is observed to originate from the exposed surface and progress in relatively straight paths, such that the IGC damage depths were greater for the same exposure time.

(a) 24 hours   (b) 72 hours   (c) 100 hours
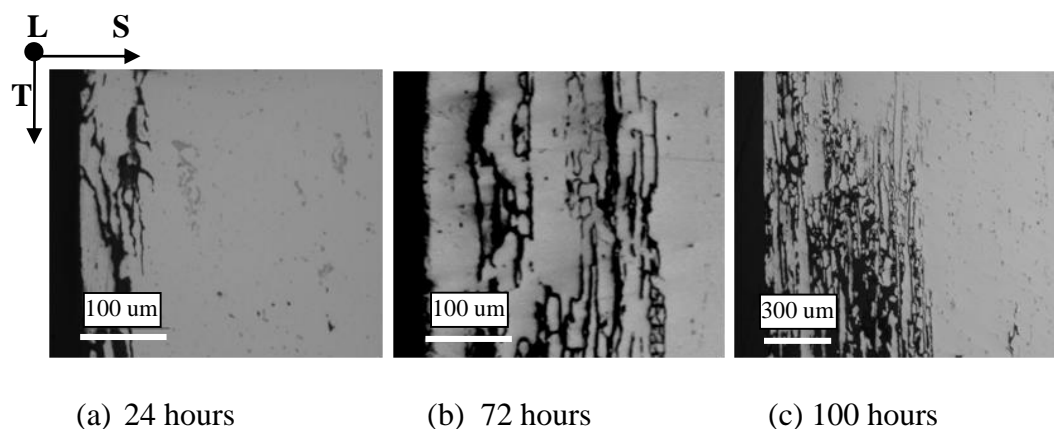
Figure 2.6. Time dependent damage depth of AA 5083-H131 in S direction from LT surface with DoS = 49 mg/cm^2 in 0.6 M NaCl solution, pH 8.3 at -0.73 $V_{SCE.}$ Damage initiated from the exposed left vertical surface. Note difference in magnifications.
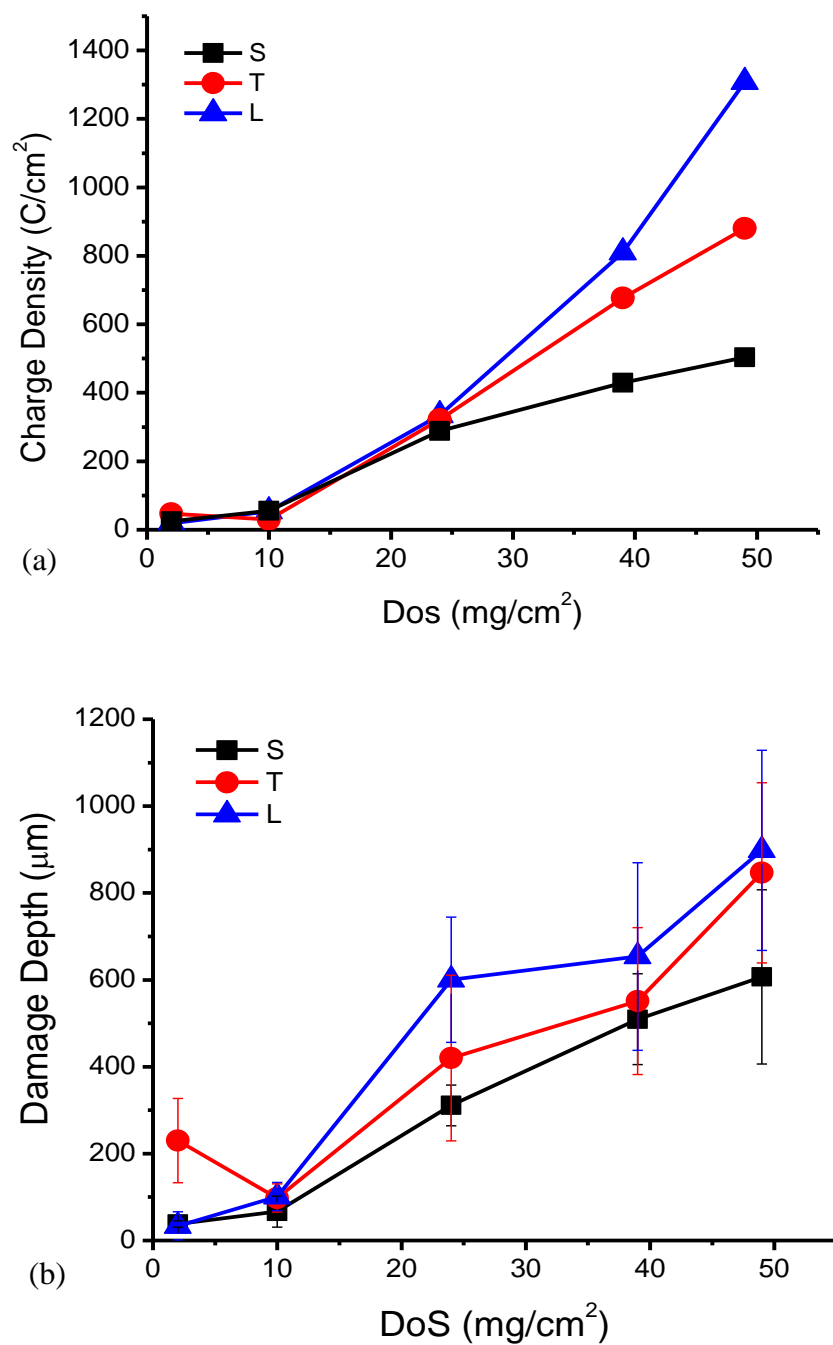
Figure 2.7. Anodic charge density (a) and damage depth (b) after 100 hours of exposure as a function of DoS and orientation of propagation for AA 5083-H131 in 0.6 M NaCl solution, pH 8.3 at -0.73 V_{SCE}. Error bars represent 95% confidence interval.

The experiments generated both electrochemical anodic charge and physical damage data. IGC propagation in AA5083-H131 exhibits a strong anisotropy (Figure 2.7). For DoS of 24 mg/cm^2 and above, the average damage depth is highest for the L propagation, followed by that in the T direction, while it is lowest in the S direction. For DoS of 49 mg/cm^2, the linear propagation rates in the L and T directions were ~2.64 nm/s and ~2.42 nm/s, respectively. In the S direction, the rate was ~1.54 nm/s (summarized in Table 2.3). The errors are based on linear fits to the damage depths versus time and indicate the mean and error bars representing 95% confidence interval. The charge densities also show orientation dependence, which is particularly pronounced for the higher DoS levels.

Table 2.3. Linear IGC propagation rates in three penetration directions for 100°C sensitization.

DoS (mg/cm^2)	L propagation (nm/s)	T propagation (nm/s)	S propagation (nm/s)
2	0.13 ± 0.09	0.46 ± 0.27	0.18 ± 0.02
10	0.25 ± 0.09	0.24 ± 0.09	0.15 ± 0.10
24	1.66 ± 0.40	1.27 ± 0.53	0.85 ± 0.13
39	1.96 ± 0.60	1.60 ± 0.47	1.22 ± 0.29
49	2.64 ± 0.80	2.42 ± 0.72	1.54 ± 0.44

2.5.4   Statistical Modeling

Damage Distribution: The IGC damage depths for each potentiostatic hold in 0.6 M NaCl solution, pH 8.3 at -0.73 V$_{SCE}$, were compiled and analyzed. The number of fissures varied with DoS and exposure time. From a total exposed or cross-sectional area of 108 mm^2, in the L direction of propagation, it ranged from 6 fissures for 2 mg/cm^2 after 24 hours to 110 fissures for 49 mg/cm^2 after 100 hours.

The total population of IGC depths from individual fissures was used to generate histograms. A probability density function (PDF) expressing probability versus damage depth was assembled for each unique combination of DoS, exposure time, and direction of propagation. A three-parameter log-logistics distribution function best fits these damage depth histograms as verified with a Kolmogorov-Smirnov test.[41] The histogram and the PDF of IGC damage depth in L direction for DoS of 39 mg/cm^2 after 100 hours of exposure is shown in Figure 2.8.

The three-parameter log-logistics cummulative distribution function (CDF) is described by the following equation:

$$F\left(x: \alpha, \delta, \gamma\right) = \left[1 + \left(\frac{\delta}{x-\gamma}\right)^{\alpha}\right]^{-1} \qquad \text{(Equation 1.1)}$$

where x is the damage depth in µm, α is the shape factor, δ is the scale factor and γ is the location factor.[42] The scale factor, δ, describes the width of the distribution. The location factor, γ, defines the damage depth at a probability of zero. The shape factor, α, is defined as the tilt of the curve with respect to the depth at a cumulative probability of 0.5. Each unique combination of DoS, exposure time, and direction of propagation has its own set of parameters.

The CDF of three sets of IGC damage depths at various DoS levels for the same time of exposure in the L direction is provided in Figure 2.9a. The CDF curves in the T direction for a single sensitization time (DoS) at three exposure times are shown in Figure 2.9b. The depth at a cumulative probability of 0.5 is a function of DoS and exposure time. In Figure 2.9b the increase in exposure time shifts the damage depth at zero probability to the right, setting the location factor, γ, to a

higher value. An increase of exposure time from 24 hours to 72 hours widens the distribution spread, increasing the scale factor, δ. Further increase in exposure time to 100 hours, however, narrows the distribution spread and decreases δ. Unlike the other two parameters, the effect of the shape factor, α, cannot be easily deciphered from the curves because secondary effects from the other two parameters also vary the tilt of the curves. Deconstructing the curves, however, showed that exposure time primarily influences the scale and location factors. It can be deduced that DoS also affects the scale and location factors, but to a lesser extent as compared to the influence of exposure time (Figure 2.9a).
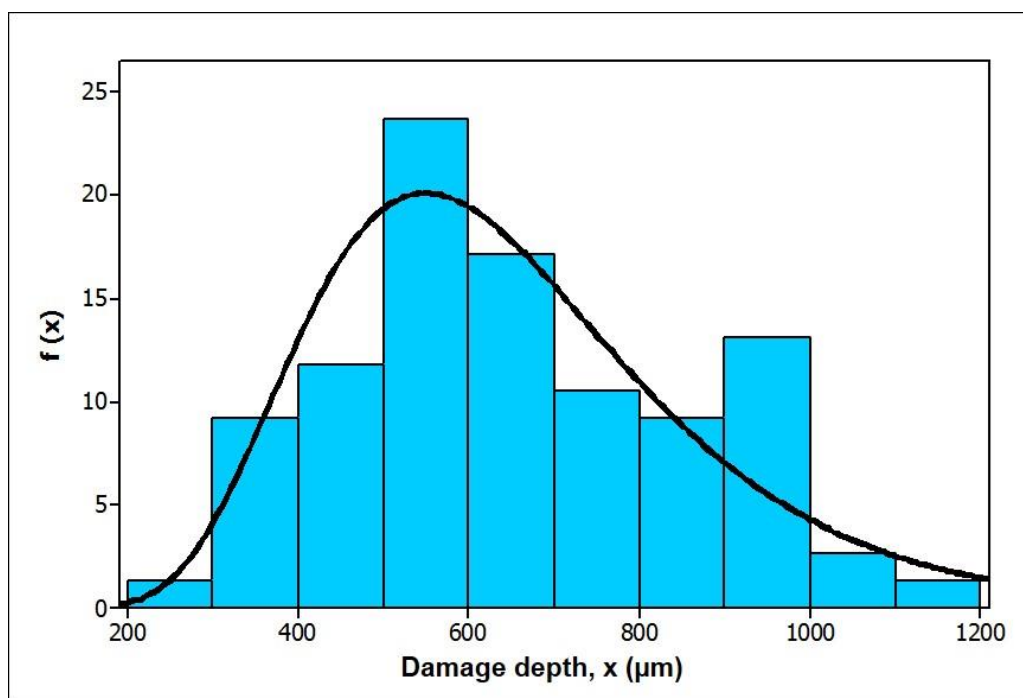
Figure 2.8. Histogram IGC damage depth in L of 39 mg/cm^2 after 100 h used to construct the probability density function (PDF) curve (solid line) with log-logistics parameters: shape (α) = 4.38, scale (δ) = 413.67, and location (γ) = 202.50.
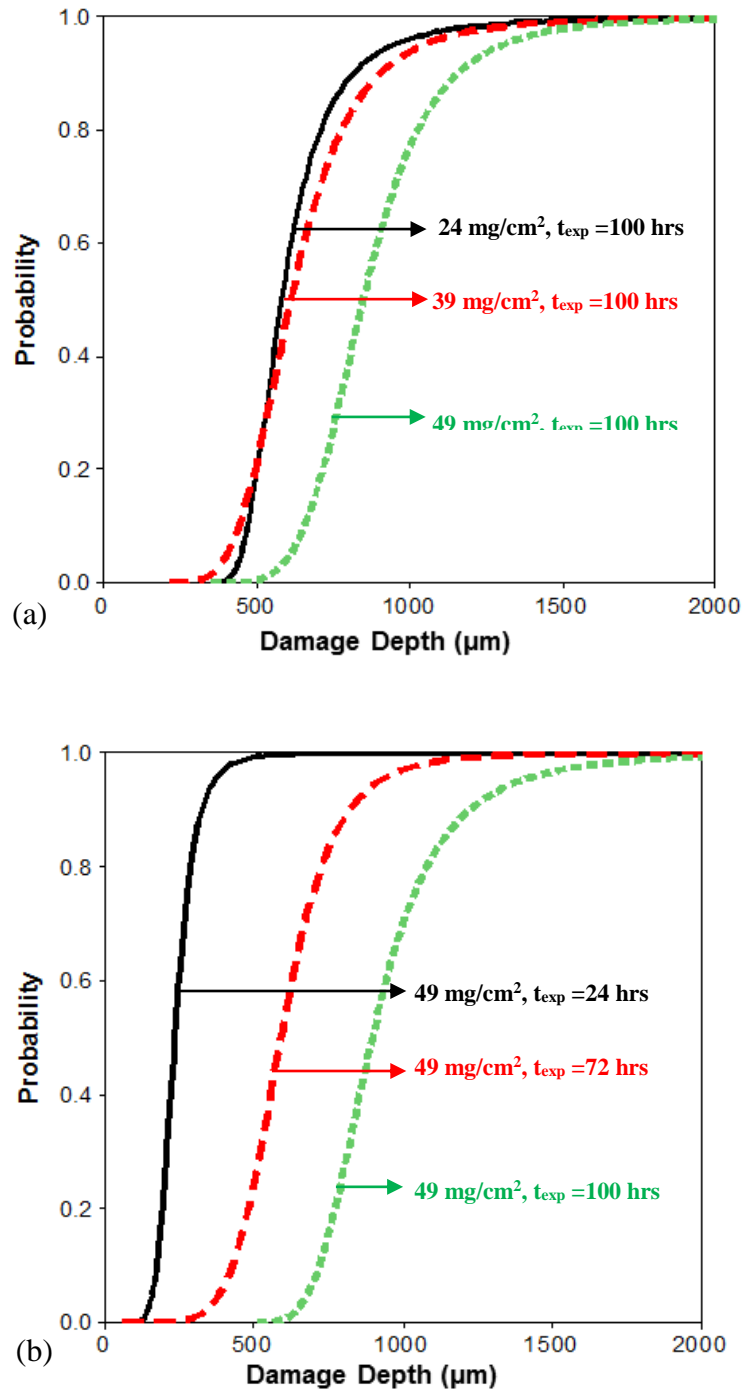
Figure 2.9. Cumulative density function (CDF) curves of IGC damage depth for L (a) and T (b) at a given DoS, direction of propagation, and exposure time, fitted with three parameter log-logistics distribution functions.

Phenomenological Model: The dependence of the mean damage depth on the experimental factors can be described by multi-linear regressions obtained from analysis of the probability density functions. These regressions describe empirical IGC penetration growth laws of sensitized AA5083 in a seawater environment, 0.6 M NaCl solution with a pH of 8.3 at -0.73 V$_{SCE,}$ in the three directions of propagation. The following expressions were obtained:

$$L_{depth} = (3.23 \pm 1.94)t_{exp} + (14.79 \pm 3.48)DoS - 239.69 \pm 165.16 \quad (1.2)$$

$$T_{depth} = (4.42 \pm 3.98)t_{exp} + (10.89 \pm 2.22)DoS - 271.04 \pm 188.45 \quad (1.3)$$

$$S_{depth} = (2.45 \pm 3.15)t_{exp} + (7.57 \pm 1.75)DoS - 156.50 \pm 149.05 \quad (1.4)$$

where depth is in µm, t$_{exp}$ is in hours, and DoS is in mg/cm^2. The uncertainties define the bounds for a 95% confidence level for each of the parameters. Note that in all three expressions the intercept terms are negative, which implies that there is an incubation time for IGC penetration. For a given exposure time and orientation of propagation, this incubation time decreases with DoS. These empirical equations are only applicable to IGC-susceptible sensitization levels of 24 mg/cm^2 and above.

The statistical significance of each of the terms in the equations can be assessed using p-values (see appendix for background on p-value). The p-values, together with the uncertainties at a 95% confidence level, for the coefficients of exposure time, DoS, and intercept in all three equations are tabulated in Table 2.4. In order for a term in Equations 2 to 4 to be statistically significant given a 95%

confidence, it should differ beyond 95% confidence and the p-value should be less than or equal to 0.05. All the p-values obtained are less than 0.05. The p-values for the DoS coefficient are also lower than those for the exposure time which implies that DoS has a larger influence than exposure time. In addition to this, the coefficients and uncertainties of DoS are lowest in the S direction, followed by that in the T direction, and highest in the L direction. This implies that the effect of DoS is largest in the L direction and least in the S direction. The uncertainties with respect to exposure time and intercept in the S, L and T directions are roughly the same, which indicates that the differences in their coefficients are not statistically significant.

Table 2.4. Statistical parameters of phenomenological models for 100°C sensitization

Factors	L_{depth}		T_{depth}		S_{depth}	
	P-value	Uncertainty at 95% confidence	P-value	Uncertainty at 95% confidence	P-value	Uncertainty at 95% confidence
t_{exp}	0.003	± 1.94	0.001	± 3.98	0.01	± 3.15
DoS	6×10^{-7}	± 3.48	7×10^{-5}	± 2.22	5×10^{-5}	± 1.75
Intercept	0.008	± 165.16	0.009	± 188.45	0.04	± 149.05

2.6 Discussion

2.6.1 Incubation Time and IGC Penetration

The phenomenological model established a trend of decreasing incubation time as a function of DoS. The incubation time is short at high DoS and is long at low DoS. Since the potentiostatic holds were conducted at -0.73 V_{SCE}, around 0.21 V above the breakdown potential of the β-phase,[1,8,10,36] then anodic dissolution

of β-phase precipitates most probably initiates pitting relatively quickly. Previous findings reveal that an incubation period is necessary for β-phase pitting to develop into IGC in sensitized AA5XXX exposed to chloride-containing solutions.[43,44] Yuan [43] showed that there is a much longer incubation period for IGC to develop in a low sensitized condition (20 mg/cm^2), whereas shorter times are required for highly sensitized conditions, such as 49 mg/cm^2. Based on the electrochemical framework presented by Jain et al.,[37] the pitting of β-phase causes local acidification and high chloride ion concentration within pits. This change in chemistry decreases the breakdown potential, subsequently triggering corrosion of neighboring β-phase precipitates. The chain of pits then progresses into a network of corroded grain boundaries. The probability of spreading is dependent on the proximity of two neighboring β-phase precipitates, which decreases with DoS. For a low DoS, the β-phase particles are not in close enough proximity to enable the progress the chain of pits, allowing random pitting events to dominate instead. In contrast, for a high DoS, the shorter distances between the β-phase particles allows for a coordinated attack of proximate β-phase precipitates to occur on the surface, providing networks of IGC sites that could penetrate into the depth. Thus, part of the incubation period could be attributed to delayed IGC initiation due to a spreading effect (or lack of spreading).

The incubation period could also be attributed to the time needed for a chemistry change in the pits or surface IGC. At the onset of penetration, it is possible that β-phase is not present in the local grain boundary area below a pit.

The surface of the pit site could expose the matrix, α-phase solid solution, whose open circuit potential (V_{OCP}) should be near that of the V_{OCP} of the AA5083-H131, which is a few millivolts below the applied potential (-0.73 V_{SCE}). In order for corrosion to proceed, it is necessary to achieve a critical chemistry, with sufficient amount of chloride ions to enable breakdown of the passive film. The migration of chloride ions towards the surface is a consequence of the local enhancement of the cation concentration and cation hydrolysis. At high DoS, β-phase pitting and IGC are more prevalent and occur at greater rates leading to shorter time and more easily attainable chemistry required to corrode through the matrix. Additionally, the distances between β-phase precipitates in high DoS are shorter, decreasing the probability of exposing only α-phase at pit sites relative to low DoS conditions.

More recently, Seong, et al.[45] suggested that the presence of a β-phase precipitate-free near surface deformed layer (NSDL), as a result of specimen surface preparation, blocked the exposure of β-phase precipitates to the environment. Turley and Samuels [46] found that plastically deformed surface layer forms via mechanical polishing on metals with face center cubic crystal structure. Liu, et al.[47] suggested that the development of this fine-grained NSDL is due to the significant surface shear stress on the near surface region during mechanical polishing. The presence of this NSDL has also be shown to occur on other aluminum alloy systems, AA3XXX, AA6XXX, and AA7XXX.[47–50] It has to be noted that the reported NSDL in AA5083 is only 1 µm thick and could be removed by passive dissolution in 80 h, given a current density of 10 µA/cm^2. At

a current density of 1 mA/cm^2, which was reached after 1000 s at -0.73 V$_{SCE}$, the dissolution of a 1µm NSDL would occur in 48 mins. However, IGC spreading was exhibited on surfaces of sensitized AA5083 after 30 mins at -0.73 V$_{SCE}$.[37] Moreover, given that electron backscattered diffraction (EBSD), which requires removal of plastic deformation due to mechanical polishing 100 nm below the sample surface, has been successfully performed on AA5083 specimens following the same routine metallographic procedure makes the presence of a NSDL as the explanation for the incubation time seems implausible.[51–53]

2.6.2 IGC Propagation

The present results show that the increase in IGC susceptibility expressed by depth is a strong function of DoS. This result can be linked to the β-phase distribution morphology on the grain boundaries. The unsensitized condition, 2 mg/cm^2, shows clean grain boundaries with no β-phase precipitates.[14,15] The lowest sensitized condition, 10 mg/cm^2, has 14% of low β-phase coverage grain boundaries, but no high β-phase coverage grain boundaries. For these two conditions, alloys exhibit low susceptibility to IGC (Figures 4, 5a and b). The large increase in IGC propagation depths as DoS increases from 10 to 24 mg/cm^2 can be correlated to the existence of a high percentage of high β-phase coverage grain boundaries as well as an increase in the percentage of the low β-phase coverage grain boundaries (Figure 2.2). Assuming that the high coverage produces a well-connected path, the percentage is above the 1-D percolation threshold of 23% active

boundaries,[54] but does not reach the 2-D percolation threshold of 65% active boundaries[55] at a DoS of 24 mg/cm^2 or greater as shown in Figure 2.10. This result implies that the increase in the amount of β-phase precipitates, as well as the closer proximity of these β-phase precipitates, aids the progression of IGC propagation. Damage depth versus the percentage of high β-phase coverage grain boundaries is shown in Figure 2.10. Although 24 mg/cm^2 and 39 mg/cm^2 DoS levels have very similar percentages of high β-phase coverage grain boundaries, their damage depths are distinctly different. One of the only differences between these two DoS levels is the percentage of low β-phase coverage grain boundaries (Figure 2.2). This suggests that the percent of low β-phase coverage grain boundaries is an important factor in IGC and that IGC can still propagate on the low β-phase coverage grain boundaries despite the absence of a connected anodic path consisting of closely spaced β-phase precipitates. It is speculated that the IGC propagation in such a discontinuous anodic path occurs due to the change in fissure environment caused by the dissolution of β-phase.[36,56] This issue is being investigated elsewhere.[36,56–58]
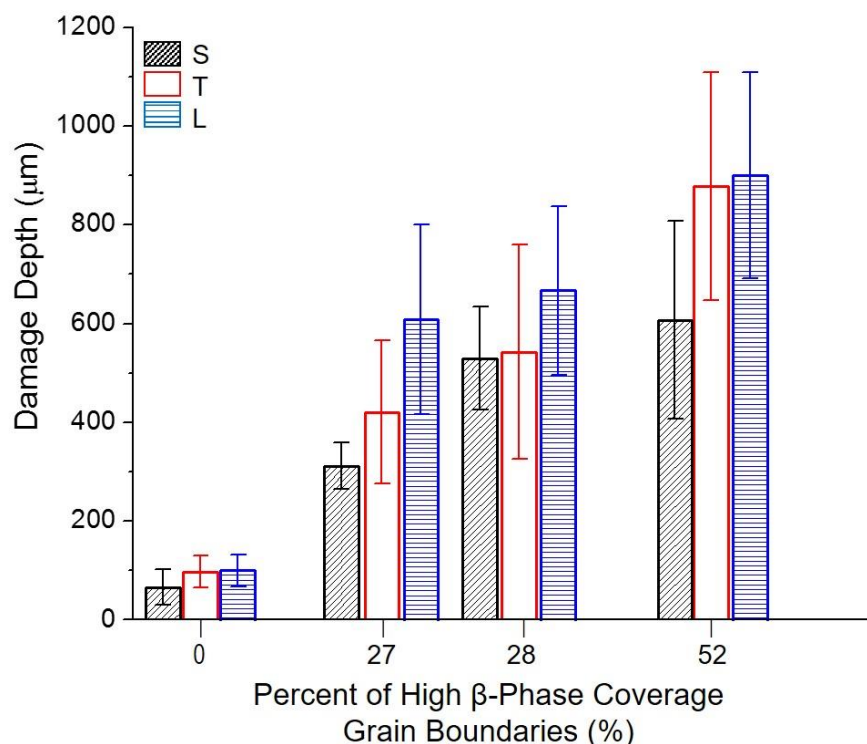
Figure 2.10. Damage depth of sensitized AA5083-H131 after 100 h in 0.6 M NaCl solution, pH 8.3 at -0.73 V_{SCE} as a function of β-phase distribution and orientation of propagation. Bar height corresponds to average damage depth, and error bars represent 95% confidence interval.

For all DoS levels (Figure 2.7b) and exposure times (Figures 3 and 6), the IGC propagation showed strong orientation dependence. This anisotropic propagation can be attributed to the microstructure anisotropy as shown in Figure 2.1. The combined effect of DoS and orientation was also evident. The damage depths show an almost linear relationship with respect to DoS in all three directions of propagation. The charge density had a roughly linear and possibly a power relationship with DoS. Although it is certain that the anodic charge density measured by a potentiostat does not account for the total anodic charge associated

78

with fissures due to local unaccounted for cathodic reactions, the trends suggest some relationship between anodic charge density and damage depth that tracks with DoS and orientation. This suggest that IGC fissure tips are anodically polarized and do not corrode at their local open circuit potential.

2.6.3 IGC Propagation without a Continuous Anodic Path

ASTM G-67 defines traditional ranges of IGC susceptibility for AA5XXX as resistant (DoS < 15 mg/cm^2), intermediate (15 mg/cm^2 < DoS < 25 mg/cm^2) and susceptible (DoS > 25 mg/cm^2).[40] The present work shows that IGC can occur and propagate even at the intermediate level of mass loss. Moreover, IGC can still propagate on the low β-phase coverage grain boundaries in the absence of a connected anodic path. This result contributes towards refuting the earlier thoughts that connectivity of β-phase precipitates along the grain boundaries in AA5XXX systems is necessary in order to be susceptible to IGC.[59]

One of the earlier hypotheses regarding the propagation of IGC in the case of a disconnected anodic path involves a change in alloy chemistry in the vicinity of the grain boundaries as postulated for Al-Cu alloys where the Cu-depleted regions are anodic to the Cu-rich regions leading to IGC.[25,27] In the precipitation-hardened Al-Mg-Zn alloys, the precipitation of the very anodic MgZn$_2$ (η) phase at the grain boundaries forms a precipitate-free region adjacent to the grain boundaries. Depending on the precipitation hardening temper, these regions can also give rise to electrochemical heterogeneity at the grain boundaries

allowing IGC to advance.[22,26,60–62]   However, this is not applicable to the AA5XXX system because the electrochemical potential difference between the Al-Mg matrix solid solution and the Mg-depleted zone, should it exist, is too small to induce significant galvanic interaction and selective dissolution.[1]   Moreover, Goswami conducted TEM studies on AA5083-H131 and has not found Mg depletion in the regions surrounding the grain boundaries for several aging temperatures.[24]

Davenport et al. speculated that for AA5XXX the IGC propagation in such a discontinuous anodic path occurs due to the local changes in electrolyte chemistry resulting from the dissolution of β-phase. The critical concentration of the Mg^{2+} ions in the solution at the dissolution front decreases the pH, leading to a solution aggressive enough to corrode the segment between the β-phase precipitates.[57] Recently, Bumiller demonstrated that for the IGC penetration rates reported in this study to occur, the fissure chemistry should be 80 to 100% saturated with Al-4wt%Mg (the α-phase solid solution composition).[36,56] If this is the only cause, then both the IGC fissure depth and width should grow at relatively similar rates. However, in this study the IGC fissure depth grows considerably faster than the IGC fissure width (Figure 2.3 and 4). One distinction could be the dissimilarity in the fissure chemistry at the mouth and at the tip. At the fissure mouth, the chemistry approached that of the bulk chemistry. The chemistry changes across the length of the fissure, reaching the suggested aggressive, nearly saturated environment at the fissure tip. Moreover, it was rationalized that there could be precipitates in the

wake with subsequent potential drop and changes of the local chemistry for IGC propagation to proceed.[56]

Another explanation could relate to hydrogen induced fracture of remaining ligaments between β-phase precipitates if there is sufficient residual stress.[58] The dissolution of even small amounts of β-phase can be a significant source of hydrogen production that may be transported and absorbed into the alloy,[5] while the stress can come from the build-up of corrosion product in the fissure tip.[63] Hydrogen permeation studies to determine diffusivities in AA5083 suggest that an interprecipitate β-phase spacing of 1 µm or less (10^{-4} cm) can be penetrated by hydrogen in 10 s.[64]

2.6.4   Phenomenological Model Validation

Phenomenological models for two directions, L and T, were validated by comparing model results to experimental findings using a sample with a sensitization level that was not included in establishment of the models. As shown in Figure 2.11, the predicted and experimental CDF curves compare well for both statistical models. Moreover, evaluating the measured mean damage depths of 541 µm in L and 383 µm in T against the predicted values of 512 µm and 363 µm yields an accuracy of 94%.
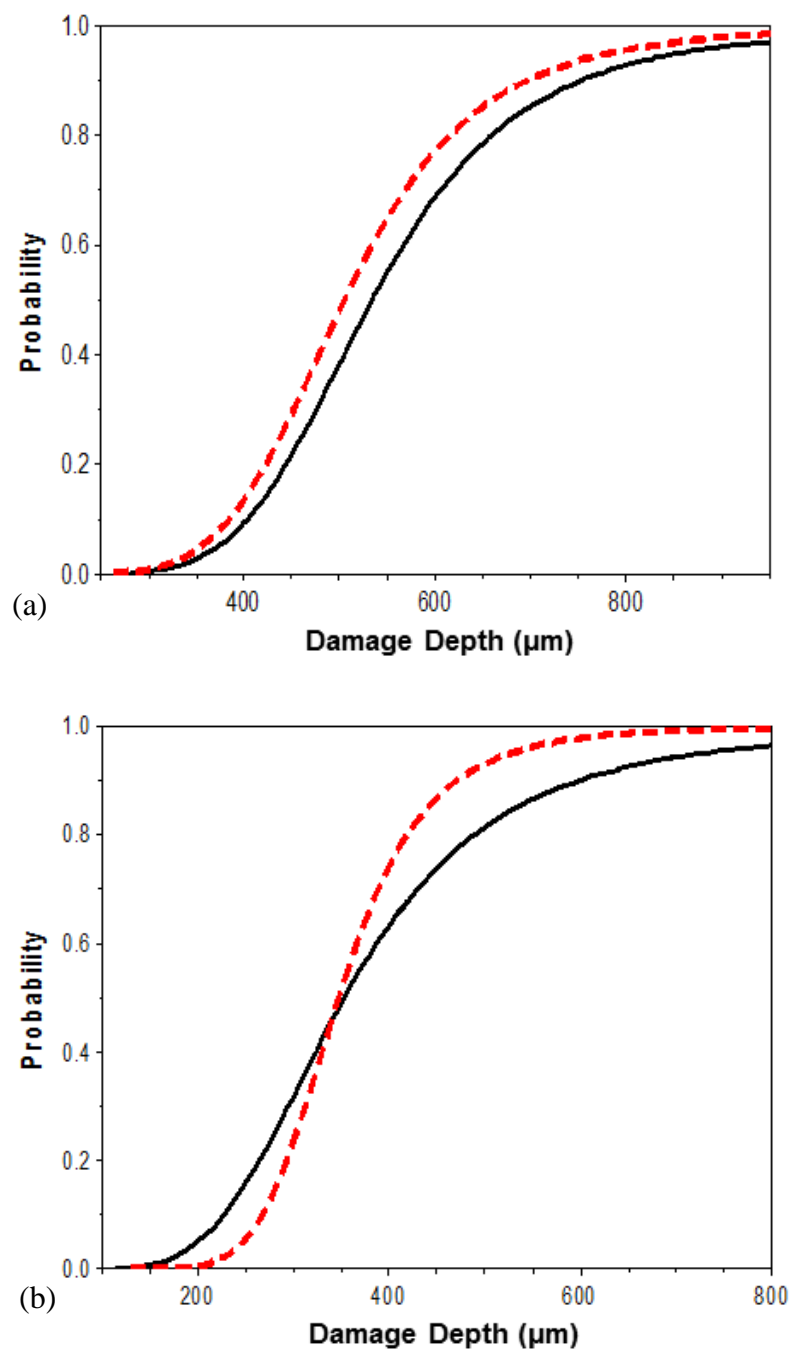
Figure 2.11. Experimental and predicted IGC damage depth CDF curves for L (a) and T (b) for of AA5083-H131, 29 mg/cm^2 after 100 hours in 0.6 M NaCl solution, pH 8.3, at -0.73 V$_{SCE}$.

2.6.5 Extension of Approach to 80°C Sensitization

The experimental approach described in the previous sections conducted on material sensitized at 100°C was extended to material sensitized at 80°C. The individual effects of DoS, exposure time, and orientation of propagation on IGC propagation in samples sensitized at 100°C were qualitatively the same for samples sensitized at 80°C. Despite these parallel qualitative trends, AA5083 of the same ASTM G-67 DoS value but different sensitization temperatures were observed to have very different IGC propagation rates. For 49 mg/cm², the linear IGC propagation rate in L for 80°C sensitization was 4.30 nm/s, which is faster by a factor of 1.63 with respect to the 100°C sensitization for the same DoS. For 24 mg/cm², the linear propagation rate in L for the 80°C sample was 0.67 nm/s, which is slower than the 1.66 nm/s of the 100°C sample. These results imply that DoS alone is not a sufficient indicator to completely characterize the sensitization characteristics of an alloy with respect to IGC propagation rates.

Because these experimental results show that sensitization temperature is an important factor, this implies that phenomenological models will then be specific to sensitization temperature. The following multi-linear regression expressions describing IGC propagation in the L and S directions were obtained for sensitization at 80°C, where IGC depth is in µm, t_{exp} is in hours, and DoS is in mg/cm².

$$L_{depth} = (5.16 \pm 6.51)t_{exp} + (18.25 \pm 11.52)\,DoS - 454.53 \pm 571.69 \quad (1.5)$$

$$S_{depth} = (2.05 \pm 5.17)t_{exp} + (5.49 \pm 3.66)\,DoS - 133.05 \pm 181.61 \quad (1.6)$$

These equations only apply to DoS of 24 mg/cm^2 and above. Again, an incubation time that decreases with DoS is suggested but the exact parameters differ.

Table 2.5. Statistical parameters of phenomenological models for 80°C sensitization

Factors	L$_{depth}$			S$_{depth}$		
	P-value	Uncertainty at 95% confidence	Uncertainty at 90% confidence	P-value	Uncertainty at 95% confidence	Uncertainty at 90% confidence
t$_{exp}$	0.10	± 6.51	± 5.28	0.05	± 2.07	± 1.68
DoS	0.006	± 11.52	± 9.35	0.008	± 3.66	± 2.96
Intercept	0.10	± 571.69	± 463.26	0.13	± 181.61	± 147.16

As in the case of 100°C sensitization, the p-values for 80°C sensitization in Table 2.5 are lower for the DoS coefficients than those for the exposure time, which suggest that influence of DoS on the propagation rate is greater than exposure time. Based on the criteria that p-values should be less than or equal to 0.05 to be meaningful, the only statistically significant term at a 95% confidence level in the L equation is DoS, while both exposure time and DoS terms are significant for the S equations. However, this does not signify that exposure time has no influence in the propagation in the L direction. It indicates that the population of data available, 12 data points, is not enough to determine the effect of exposure time on IGC propagation in the L direction. In addition, the p-value for exposure time in the L equation is 0.1, which indicates that this term is statistically significant at a 90% confidence level.

The different IGC propagation rates between the two sensitization temperatures could indicate the effect of temperature on the precipitation kinetics of β-phase. The effect of reduced isothermal sensitization times at 100°C compared

with 80°C (Table 2.2) implies faster growth with temperature. However, the IGC penetration rates for 80°C sensitization are not consistently lower than that for the 100°C sensitization for the same DoS. Therefore, evaluation and comparison of β-phase morphology and distribution between the two temperatures is a necessary step for future work.

2.7   Conclusions

1. IGC penetration rate in AA5083 in 0.6 M NaCl solution is governed by orientation of propagation, degree of sensitization, temperature of sensitization and exposure time.

   a. The morphology and distribution of β-phase precipitates was dictated by the sensitization conditions. IGC penetration rate increased sharply with sensitization for DoS above 24 mg/cm^2; however, IGC occurred for DoS between 2 and 24 mg/cm^2.

   b. IGC also propagated on grain boundaries without a continuous path.

   c. The IGC penetration rate showed strong anisotropy, with L direction penetration faster by a factor of 1.7 relative to the slowest (S) direction. The S direction exhibited more grain fall-out for the same amount of depth penetration than the L or T directions owing to small grain widths in this direction.

   d. Incubation time for IGC penetration is a function of DoS for conditions studied.

2. IGC damage distributions can serve as inputs for IGC models that predict IGC depth of penetration as a function of material conditions and time.

   a. IGC propagation depths can be well described by a three-parameter log-logistics distribution.

   b. The phenomenological model herein can determine IGC damage prognosis as influenced by DoS, time of exposure, and orientation of propagation in seawater environment (0.6 M NaCl solution, pH 8.3, V_{app} = -0.73 V_{SCE}).

3. Sensitization temperature significantly influences the IGC propagation rates even for material with the same ASTM G-67 DoS value.

2.8   References

[1]   J.L. Searles, P.I. Gouma, R.G. Buchheit, Stress corrosion cracking of sensitized AA5083 (Al-4.5Mg-1.0Mn), Metall. Mater. Trans. A. 32 (2001) 2859–2867. doi:10.1007/s11661-001-1036-3.

[2]   J.L. Searles, P.I. Gouma, R.G. Buchheit, Stress Corrosion Cracking of Sensitized AA5083 (Al-4.5Mg-1.0Mn), Mater. Sci. Forum. 396 (2002) 1437–1442. doi:10.4028/www.scientific.net/MSF.396-402.1437.

[3]   A.J. Davenport, Y. Yuan, R. Ambat, B.J. Connolly, M. Strangwood, A. Afseth, et al., Intergranular Corrosion and Stress Corrosion Cracking of Sensitised AA5182, Mater. Sci. Forum. 519-521 (2006) 641–646. doi:10.4028/www.scientific.net/MSF.519-521.641.

[4]   I.N.A. Oguocha, O.J. Adigun, S. Yannacopoulos, Effect of sensitization heat treatment on properties of Al–Mg alloy AA5083-H116, J. Mater. Sci. 43 (2008) 4208–4214. doi:10.1007/s10853-008-2606-1.

[5]   D.R. Baer, C.F. Windisch, M.H. Engelhard, M.J. Danielson, R.H. Jones, J.S. Vetrano, Influence of Mg on the corrosion of Al, J. Vac. Sci. Technol. A. 18 (2000) 131–136. doi:10.1116/1.582129.

[6]   G.M. Scamans, N.J.H. Holroyd, C.D.S. Tuck, The role of magnesium
        segregation in the intergranular stress corrosion cracking of aluminium
        alloys, Corros. Sci. 27 (1987) 329–347. doi:10.1016/0010-
        938X(87)90076-X.

[7]   G.M. Scamans, Low Temperature Sensitization of AA5XXX Alloys,
        Innoval, Oxon, UK, 2008.

[8]   R.H. Jones, D.R. Baer, M.J. Danielson, J.S. Vetrano, Role of Mg in the
        stress corrosion cracking of an Al-Mg alloy, Metall. Mater. Trans. A. 32
        (2001) 1699–1711. doi:10.1007/s11661-001-0148-0.

[9]   J.S. Vetrano, R.E. Williford, S.M. Bruemmer, R.H. Jones, Influence of
        microstructure and thermal history on the corrosion susceptibility of AA
        5083, in: Alum. Alloys, Orlando, FL, 1997.

[10]   R.H. Jones, J.S. Vetrano, C.F. Windisch, Stress Corrosion Cracking of Al-
        Mg and Mg-Al Alloys, Corrosion. 60 (2004) 1144–1154.
        doi:10.5006/1.3299228.

[11]   R.H. Jones, V.Y. Gertsman, J.S. Vetrano, C.F. Windisch Jr., Crack-
        particle interactions during intergranular stress corrosion of AA5083 as
        observed by cross-section transmission electron microscopy, Scr. Mater.
        50 (2004) 1355–1359. doi:10.1016/j.scriptamat.2004.01.038.

[12]   J.A.V.D. Hoeven, L. Zhuang, B. Schepers, P.D. Smet, J.P. Baekelandt, A
        New 5xxx Series Alloy Developed for Automotive Applications,
        Aluminum. 78 (2002) 750–754.

[13]   E.C.W. Perryman, S.E. Hadden, Stress-Corrosion Of Aluminium-7-
        Percent Magnesium Alloy, J Inst Mater. 77 (1950) 207.

[14]   R. Goswami, G. Spanos, P.S. Pao, R.L. Holtz, Precipitation behavior of
        the ß phase in Al-5083, Mater. Sci. Eng. A. 527 (2010) 1089–1095.
        doi:10.1016/j.msea.2009.10.007.

[15]   R. Goswami, G. Spanos, P.S. Pao, R.L. Holtz, Microstructural Evolution
        and Stress Corrosion Cracking Behavior of Al-5083, Metall. Mater. Trans.
        A. 42 (2010) 348–355. doi:10.1007/s11661-010-0262-y.

[16]   J.C. Chang, T.H. Chuang, Stress-corrosion cracking susceptibility of the
        superplastically formed 5083 aluminum alloy in 3.5 pct NaCl solution,
        Metall. Mater. Trans. A. 30 (1999) 3191–3199. doi:10.1007/s11661-999-
        0229-z.

[17]   E.H. Dix, W.A. Anderson, M.B. Shumaker, Influence of Service
         Temperature On the Resistance of Wrought Aluminum-Magnesium
         Alloys to Corrosion, Corrosion. 15 (1959) 19–26. doi:10.5006/0010-9312-
         15.2.19.

[18]   H. Yukawa, Y. Murata, M. Morinaga, Y. Takahashi, H. Yoshida,
         Heterogeneous distributions of Magnesium atoms near the precipitate in
         Al-Mg based alloys, Acta Metall. Mater. 43 (1995) 681–688.
         doi:10.1016/0956-7151(94)00266-K.

[19]   S. Nebti, D. Hamana, G. Cizeron, Calorimetric study of pre-precipitation
         and precipitation in Al-Mg alloy, Acta Metall. Mater. 43 (1995) 3583–
         3588. doi:10.1016/0956-7151(95)00023-O.

[20]   F.J. Esposto, C.-S. Zhang, P.R. Norton, R.S. Timsit, Segregation of Mg to
         the surface of an Al-Mg single crystal alloy and its influence on the initial
         oxidation at room temperature, Surf. Sci. 302 (1994) 109–120.
         doi:10.1016/0039-6028(94)91101-0.

[21]   L.I. Kaigorodova, The effect of grain-boundary structure formation on b-
         precipitation in aged Al-Mg alloys, Mater. Sci. Forum. 294-296 (1999)
         477.

[22]   P.N.T. Unwin, R.B. Nicholson, The nucleation and initial stages of growth
         of grain boundary precipitates in Al-Zn-Mg and Al-Mg alloys, Acta
         Metall. 17 (1969) 1379–1393. doi:10.1016/0001-6160(69)90155-2.

[23]   L. Tan, T.R. Allen, Effect of thermomechanical treatment on the corrosion
         of AA5083, Corros. Sci. 52 (2010) 548–554.
         doi:10.1016/j.corsci.2009.10.013.

[24]   R. Goswami, R.L. Holtz, Transmission Electron Microscopic
         Investigations of Grain Boundary Beta Phase Precipitation in Al 5083
         Aged at 373 K (100 °C), Metall. Mater. Trans. A. 44 (2012) 1279–1289.
         doi:10.1007/s11661-012-1166-9.

[25]   J.R. Galvele, S.M. de De Micheli, Mechanism of intergranular corrosion
         of Al-Cu alloys, Corros. Sci. 10 (1970) 795–807. doi:10.1016/S0010-
         938X(70)80003-8.

[26]   S. Maitra, G.C. English, Mechanism of localized corrosion of 7075 alloy
         plate, Metall. Trans. A. 12 (1981) 535–541. doi:10.1007/BF02648553.

[27]   K. Sugimoto, K. Hoshino, M. Kageyama, S. Kageyama, Y. Sawada, Stress corrosion cracking of aged Al□4%Cu alloy in NaCl solution, Corros. Sci. 15 (1975) 709–720. doi:10.1016/0010-938X(75)90035-9.

[28]   K. Urushino, K. Sugimoto, Stress-corrosion cracking of aged Al□Cu□Mg alloys in NaCl solution, Corros. Sci. 19 (1979) 225–236. doi:10.1016/0010-938X(79)90008-8.

[29]   D.A. Little, B.J. Connolly, J.R. Scully, An electrochemical framework to explain the intergranular stress corrosion behavior in two Al–Cu–Mg–Ag alloys as a function of aging, Corros. Sci. 49 (2007) 347–372. doi:10.1016/j.corsci.2006.04.024.

[30]   N. Birbilis, R.G. Buchheit, Investigation and Discussion of Characteristics for Intermetallic Phases Common to Aluminum Alloys as a Function of Solution pH, J. Electrochem. Soc. 155 (2008) C117–C126. doi:10.1149/1.2829897.

[31]   B.J. Connolly, J.R. Scully, Corrosion cracking susceptibility in Al-Li-Cu alloys 2090 and 2096 as a function of isothermal aging time, Scr. Mater. 42 (2000) 1039–1045.

[32]   C. Kumai, J. Kusinski, G. Thomas, T.M. Devine, Influence of Aging at 200 C on the Corrosion Resistance of Al-Li and Al-Li-Cu Alloys, Corrosion. 45 (1989) 294–302. doi:10.5006/1.3577857.

[33]   R.G. Buchheit, J.P. Moran, G.E. Stoner, Electrochemical Behavior of the T1 (Al2CuLi) Intermetallic Compound and Its Role in Localized Corrosion of Al-2% Li-3% Cu Alloys, Corrosion. 50 (1994) 120–130. doi:10.5006/1.3293500.

[34]   R.G. Buchheit, J.P. Moran, G.E. Stoner, Localized Corrosion Behavior of Alloy 2090—The Role of Microstructural Heterogeneity, Corrosion. 46 (1990) 610–617. doi:10.5006/1.3585156.

[35]   K.A. Yasakau, M.L. Zheludkevich, S.V. Lamaka, M.G.S. Ferreira, Role of intermetallic phases in localized corrosion of AA5083, Electrochimica Acta. 52 (2007) 7651–7659. doi:10.1016/j.electacta.2006.12.072.

[36]   E. Bumiller, Intergranular corrosion in AA5XXX aluminum alloys with discontinuous precipitation at the grain boundaries, PhD Dissertation, University of Virginia, 2011.

[37]   S. Jain, M.L.C. Lim, J.L. Hudson, J.R. Scully, Spreading of intergranular corrosion on the surface of sensitized Al-4.4Mg alloys: A general finding, Corros. Sci. 59 (2012) 136–147. doi:10.1016/j.corsci.2012.02.018.

[38]   N. Birbilis, R.G. Buchheit, Electrochemical Characteristics of Intermetallic Phases in Aluminum Alloys - An Experimental Survey and Discussion, J. Electrochem. Soc. 152 (2005) B140–B151. doi:10.1149/1.1869984.

[39]   R. Howard, N. Bogh, D.S. Mackenzie, Heat Treating Processes and Equipment, in: G.E. Totten, D.S. Mackenzie (Eds.), Handb. Alum., Marcel Dekker, Inc., New York, NY, 2003.

[40]   ASTM, ASTM: G67-04 Standard Test Method for Determining the Susceptibility to Intergranular Corrosion of 5XXX Series Aluminum Alloys by Mass Loss After Exposure to Nitric Acid (NAMLT Test), ASTM International, West Conshocken, PA, 2004.

[41]   A.J. Hayter, Probability and Statistics for Engineers and Scientists, 3rd ed., Thomson Brooks/Cole, Belmont, CA, 2007.

[42]   N.L. Johnson, S. Kotz, N. Balakrishnan, Continuous Univariate Distributions, 2nd ed., John Wiley & Sons, New York, NY, 1995.

[43]   Y. Yuan, Localized corrosion and stress corrosion cracking of aluminum-magnesium alloys, PhD Dissertation, University of Birmingham, 2005.

[44]   R.J. Winsley, Corrosion resistance of heat-treated and friction stir welded AA5083-H116, PhD Thesis, University of Birmingham, 2008.

[45]   J. Seong, F. Yang, F. Scheltens, G.S. Frankel, N. Sridhar, Influence of the Altered Surface Layer on the Corrosion of AA5083, J. Electrochem. Soc. 162 (2015) C209–C218. doi:10.1149/2.0321506jes.

[46]   D.M. Turley, L.E. Samuels, The nature of mechanically polished surfaces of copper, Metallography. 14 (1981) 275–294. doi:10.1016/0026-0800(81)90001-X.

[47]   Y. Liu, A. Laurino, T. Hashimoto, X. Zhou, P. Skeldon, G.E. Thompson, et al., Corrosion behaviour of mechanically polished AA7075-T6 aluminium alloy, Surf. Interface Anal. 42 (2010) 185–188. doi:10.1002/sia.3136.

[48]   Y. Liu, X. Zhou, G.E. Thompson, T. Hashimoto, G.M. Scamans, A. Afseth, Precipitation in an AA6111 aluminium alloy and cosmetic corrosion, Acta Mater. 55 (2007) 353–360. doi:10.1016/j.actamat.2006.08.025.

[49]   X. Zhou, G.E. Thompson, G.M. Scamans, The influence of surface treatment on filiform corrosion resistance of painted aluminium alloy sheet, Corros. Sci. 45 (2003) 1767–1777. doi:10.1016/S0010-938X(03)00003-9.

[50]   Z. Zhao, G.S. Frankel, Surface Layer Dissolution Kinetics of Aluminum Alloy 7075 in Various Tempers, Corrosion. 63 (2007) 613–624. doi:10.5006/1.3278411.

[51]   L. Chen, Image Fusion and An Outlier Detection Framework for Hierarchical Modeling with Application to Corrosion Prediction, PhD Dissertation, University of Virginia, 2012.

[52]   R. Zhang, R.K. Gupta, C.H.J. Davis, A.M. Hodge, M. Tort, K. Xia, et al., The influence of grain size and grain orientation on sensitisation in AA5083, Corrosion. (2015). doi:10.5006/1703.

[53]   Y. Zhu, Characterization of Beta Phase Growth and Experimental Validation of Long TErm Thermal Exposure Sensitization of AA5XXX Alloys, M.S. Thesis, University of Utah, 2013.

[54]   M.A. Gaudett, J.R. Scully, Applicability of bond percolation theory to intergranular stress-corrosion cracking of sensitized AlSl 304 stainless steel, Metall. Mater. Trans. A. 25 (1994) 775–787. doi:10.1007/BF02665454.

[55]   V.Y. Gertsman, M. Janecek, K. Tangri, Grain boundary ensembles in polycrystals, Acta Mater. 44 (1996) 2869–2882. doi:10.1016/1359-6454(95)00396-7.

[56]   E.M. Bumiller, R.G. Kelly, Intergranular corrosion in AA5XXX: a case for continuous attack with a discontinuous active path, in: Dep. Def. Corros. Conf., NACE, Palm Springs, CA, 2011.

[57]   A.J. Davenport, R.J. Winsley, G.M. Scamans, A. Afseth, J. Hunter, W. Tang, et al., Mg Effects in Corrosion of AA5083, (2010).

[58] C.B. Crane, R.P. Gangloff, Stress Corrosion Cracking of Low Temperature Sensitized AA5083, in: Dep. Def. Corros. Conf., NACE, Palm Springs, CA, 2011.

[59] A.J. Field, C. Wong, Thermal stability of selected 5000 series Al alloys, in: TMS Annu. Meet., San Antonio, TX, 2006.

[60] A.J. Cornish, M.K.B. Day, Precipitation in the Neighborhood of Grain Boundaries in an Aluminum-Zinc-Magnesium Alloy, J Inst Met. 97 (1969) 44–52.

[61] T. Asahi, F. Yabusaki, K. Osamura, Y. Murakami, Studies on microstructure and stress-corrosion cracking behaviour of Al-Zn-Mg alloys, in: Proc. 6th Int. Conf. Light Met., Aluminum-Verlag, Dusseldorf, Germany, 1975: pp. 64–67.

[62] T. Ramgopal, P.I. Gouma, G.S. Frankel, Role of Grain-Boundary Precipitates and Solute-Depleted Zone on the Intergranular Corrosion of Aluminum Alloy 7150, Corrosion. 58 (2002) 687–697. doi:10.5006/1.3287699.

[63] T.-S. Huang, G.S. Frankel, Kinetics of sharp intergranular corrosion fissures in AA7178, Corros. Sci. 49 (2007) 858–876. doi:10.1016/j.corsci.2006.04.015.

[64] J.H. Ai, M.L. Lim, J.R. Scully, Hydrogen Diffusion and Trapping in High Purity Al and Aluminum Alloy 5083-H131, Meet. Abstr. MA2012-02 (2012) 2170–2170.

[65] A.J. Hayter, Probability and Statistics for Engineers and Scientists, 3rd ed., Thomson Brooks/Cole, Belmont, CA, 2007.

2.9   Appendix

A p-value is a quantitative measure for reporting results of a hypothesis testing. It is the probability of the test statistic being at least as extreme as the one observed given that the null hypothesis is true. A small p-value is an indication that the null hypothesis is false, but a large p-value does not mean that the null

hypothesis is true. For the present case, the null hypothesis was that each of the individual terms in the equations is statistically unimportant to the dependent variable or damage depth. This condition will have a coefficient of zero. The test statistic used is a linear regression t-test[65] represented by the following equation:

$$t_{score} = \frac{\beta - \beta_0}{SE_\beta} \tag{1.7}$$

where, β is the coefficient, β_0 is zero (null hypothesis), SE_β is the standard error for the coefficient. The SE_β can be expressed as:

$$SE_\beta = \frac{\sqrt{\frac{1}{n-2}\sum_{i=1}^{n}(Y_i - \hat{Y}_i)^2}}{\sqrt{\sum_{i=1}^{n}(x_i - \bar{x})^2}} \tag{1.8}$$

where, n is the degrees of freedom (number of observations), Y_i is the mean damage depth, $\hat{Y}_i$ is the estimated mean damage depth, x is DoS or t_{exp}, and $\bar{x}$ is the mean of DoS or t_{exp}. The p-values for the obtained t-scores can be found using tables of values from Student's t-distributions.

3   The Critical Role of Potential on Intergranular Corrosion Propagation

      Kinetics in an Al-Mg Alloy

3.1   Abstract

The electrochemical kinetics of AA5083-H131 as influenced by the degree of sensitization (DoS) and applied potential were determined in the context of intergranular corrosion (IGC) propagation. Galvanostatic tests over a range of applied current densities in 0.6 M NaCl solution were conducted on ST surfaces of sensitized AA5083. More severe IGC was seen on AA5083-H131 with higher DoS, with damage depths of 3 mm or more after 100 h at an applied potential of 3 x 10^{-3} A/cm^2. The extent of IGC depth over the 100 h exposure was linearly proportional to the measured applied potential with the existence of a threshold below which no IGC was observed. This linear potential dependence increased with increasing DoS, resulting in a narrow threshold potential range of -0.85 to -0.8 V_{SCE} across the range of DoS levels studied. Quantitative predictions of fissure chemistry and grain boundary β-phase coverage were established using a total rate equation and dissolution kinetics of the individual α-matrix and β-precipitate phases in simulated fissure chemistry solutions. The true E-i behavior for IGC in sensitized AA5083-H131 yields a semi-logarithmic trend, typical of charge transfer control, and consistent with the pseudo-Tafel behavior of rate controlling α dissolution.

3.2   Introduction

Non-heat treatable Al-Mg alloys for marine applications exposed to aggressive marine environments require light weight, high strength-to-weight ratio, weldability, and excellent corrosion resistance.[1–3]   When the solid solution strengthening Mg content exceeds about 3 wt. %, the alloy can become sensitized and susceptible to intergranular corrosion (IGC) and intergranular stress corrosion cracking (IGSCC) upon prolonged thermal exposure.[4–8]   Sensitization occurs due to the preferential precipitation of the more anodic β-phase (Al_3Mg_2) along the grain boundaries, satisfying an electrochemical framework that establishes an IGC path. [4–8]

Efforts have been placed to prevent sensitization, where stabilized tempers achieved via heat treatment at temperatures just below the β-phase solvus temperature promote intragranular β-phase precipitation, restricting the possibility of precipitation along the grain boundaries.[9]   Thermomechanical treatment (TMT) and equal channel angular processing (ECAP) on AA5083 to alter grain boundary character distribution and grain refinement was shown to reduced sensitization.[10,11] A form of healing process attributed to the solutionizing effect of the friction stir processing (FSP) above 250°C has also shown to be a promising route.[12] Despite these promising routes, failures associated with IGC and IGSCC during service has yet to be understood in the context of degree of sensitization (DoS).

The degree of sensitization, which depends on magnesium content, sensitization time and temperature, and thermomechanical treatment, is linked to the distribution and morphology of β-phase.[2,7,8,11,13–17] Several parallel transmission electron microscopy (TEM) studies of AA5083 suggested that discrete β-phase precipitate form for all times up to 15 d at 70°C, 3 d at 100°C, and 10 h at 175°C. The β-phase coarsened and coalesced forming a connected ribbon morphology that did not fully cover the grain boundaries was observed after 15 to 125 d at 70°C, 3 to 42 d at 100°C, and 10 to 200 h at 175°C. While a continuous β-film formed on some grain boundaries for exposure times beyond 125 d at 70°C, 42 d at 100°C, and 200 h at 175°C. [3,8,18] Image analysis of scanning electron micrographs of etched grain boundaries established a quantitative distribution of β-phase coverage as a function of total length of grain boundaries for AA5083-H131 sensitized at 100°C.[19–21] These results demonstrate that the number of β-free grain boundaries decreases linearly with increasing DoS, whereas the number of high coverage (> 70% coverage per grain boundary) grain boundary and the number of low coverage (70% > coverage per grain boundary > 0%) grain boundary increase by about the same dependence on DoS for the range of 2 to 49 mg/cm^2.[19,20] More recent investigation of Ga-embrittled AA5083 intergranular fracture surfaces [22] suggests that continuous grain boundary β-phase morphology does not exist even at high DoS. However, the size of the β-phase increases with increasing sensitization time at 100°C, albeit a relatively constant β-phase spacing across the DoS levels.

Characterization of the size, morphology, and distribution of grain boundaries β-phase in Al-Mg alloys, as a function of DoS, indicates the connectivity or coverage of β-phase contributes to the continuity of IGC.[16,17,20] The spacing of β-phase is critical because the α-phase dissolution between β precipitates is rate controlling for IGC, and may compromise spreading and propagation stability. The size of β-phase is essential in providing a high Mg^{2+} concentration for additional acidity and for hydrolysis at the fissure tip, decreasing the breakdown potential of α phase, allowing depassivation of α and IGC propagation stability.

Applied potential has been found to influence localized corrosion morphology in a wide range of aluminum alloys.[23–28] The concept of a potential window for IGC is often utilized to define the zone of IGC in IGC-susceptible materials.[5,22,23,26,27] In general, the IGC zone is usually the potential range between the breakdown potentials of the more anodic intermetallic phase and that of the matrix phase. In the case of Al-Mg alloys, particularly AA5083, it was observed that the sensitized alloy has a lower breakdown potential then the unsensitized alloy.[19] Moreover, the breakdown potential of a sensitized AA5083, when taken as the potential of abrupt increase in anodic current density, is not associated with discrete, isolated pitting of β-phase, but rather with the spreading of IGC on the surface. The region between these two breakdown potentials was established as the potential window for IGC spreading in AA5083.

This potential dependence was also observed for IGC propagation into the depth from the surface. Mizuno and Kelly[29] have shown that the maximum IGC damage depth in sensitized AA5083 after 100 hours of galvanic coupling with 304 stainless steel is linearly related to the galvanic couple potential. The linear relationship was found for all DoS, with the dependence of rate on potential increasing with DoS. Furthermore, a threshold potential of -0.850 V_{SCE}, the minimum potential at which IGC occurred, was observed suggesting an IGC propagation zone within the IGC spreading zone. IGC modeling work by Bumiller[30] on AA5083 demonstrated that these IGC propagation kinetics is dependent on the fissure tip potential and the grain boundary β-phase coverage in a $AlCl_3/MgCl_2$ simulated fissure tip environment. Moreover, it was suggested that the observed threshold potential is associated with the breakdown potential of α in the saturated or near saturated Al-4Mg fissure tip solution.

IGSCC work by Crane [31] on AA5083-H131 (DoS of 22 mg/cm^2) suggested potential windows, defined by breakdown potentials of bulk α and β phase, for fatigue crack tip corrosion growth kinetics. In order to produce significant IGC growth (~ 10 nm/s), the applied potential must be above –0.87 V_{SCE}, the breakdown potential of the matrix α-phase in the assumed near saturated to saturated $AlCl_3/MgCl_2$ simulated crack tip solution. Above this potential, the dissolution of β-phase precipitate helps maintain the critical acidic chemistry necessary to sustain the matrix α-phase dissolution, which breakdown potential drops from -0.79 V_{SCE} in neutral 0.6 M NaCl solution, to -0.87 V_{SCE} in acidic fissure

tip environment. Between -0.87 V_{SCE} and -0.96 V_{SCE}, the breakdown potential of β-phase in neutral 0.6 M NaCl solution, the IGC growth rate decrease considerably to ~ 1 nm/s. Because β-phase is the only freely dissolving phase within this potential window, and the volume fraction of β-phase at the fissure tip of a DoS of 22 mg/cm^2 may not be sufficient to produce the critical fissure chemistry, the drop in IGC kinetics was proposed to be due to the limited source for acidic fissure tip chemistry. Below -0.96 V_{SCE}, only passive dissolution of both phases is possible, which hinders the development of the critical acidic chemistry, thereby eliminating IGC growth via anodic dissolution. However with enough cathodic polarization, corrosion growth could occur via cathodic corrosion.

Chapter 2 revealed that the IGC propagation kinetics are governed by orientation of propagation, DoS, and exposure time to chloride environment. However, these studies were limited to a single applied potential at the IGC spreading potential of -0.73 V_{SCE}. The influence of applied potential, specifically in the range between the IGC spreading potential and the β-phase breakdown potential needs to be investigated, in order to determine the appropriate potential window for IGC propagation, as well as the dependence of IGC propagation kinetics on potential with DoS in terms of grain boundary β-phase coverage.

3.3   Objective

The primary objective of this chapter is to quantitatively characterize and understand the critical effect of applied potential on IGC propagation kinetics of

sensitized AA5083 in aqueous solutions that simulate the marine environment. First, IGC depths will be measured as a function of DoS and applied potential to define dependence of propagation kinetics on potential, and identify electrochemical parameters critical to IGC such as threshold potential and threshold current density. The true potential-current density behavior of AA5083 will be obtained after current efficiency and Ohmic resistance corrections. The current efficiency will be measured via artificial pit experiments on as-received and sensitized AA5083 wires, while the Ohmic resistance will be measured via electrochemical impedance spectroscopy. The characteristic IGC propagation rates as a function of applied potential will be rationalized in terms of grain boundary β-phase coverage, focusing on the importance of fissure chemistry and its effects on both α-phase and β-phase dissolution properties.

3.4 Experimental Procedures

3.4.1 Materials, Tempers, Microstructure and Degree of Sensitization

3.4.1.1 Bulk Materials

The commercial AA5083 (UNS A95083) plates utilized in this work were provided by the Aluminum Company of America (Alcoa), in H131 temper and H116 temper with plate thickness of 2.25" (5.715 cm) and 2.5" (6.35 cm), respectively. In the H131 temper state, the AA5083 is strain hardened without supplementary thermal treatment to have a mean ultimate tensile strength (UTS) equivalent to three-eighths of the UTS of a full-hard condition (about 75% cold

reduction after full annealing) for this alloy.[32] On the other hand, in the H116 temper state, the AA5083 is only strain hardened (no supplementary thermal treatment) to have a mean UTS equivalent to one-eighths of the UTS of a full-hard condition.[32] Additionally, this temper designation achieved a degree of stabilization via a controlled cooling process of approximately 5° per minute, following casting onto a belt.[33]

In addition to utilizing both tempers in their as-received states, a separate set of samples from the as-received H131 plate was subjected to solution heat treatment at 275°C (compared to the equilibrium β-phase solvus of 290°C for 4.4 wt.% Mg) for 10 h and immediately followed by cold water quenching to room temperature. This solutionized set of samples will be referred hereafter as H131-SHT/Q temper.

Table 3.1. Nominal composition of AA5083 (UNS A95083)

Component	Al	Mg	Mn	Fe	Si	Cu	Cr	Zn	Ti	Others
Weight %	Bal	4.4	0.7	0.22	0.1	0.05	0.08	0.02	0.02	< 0.01
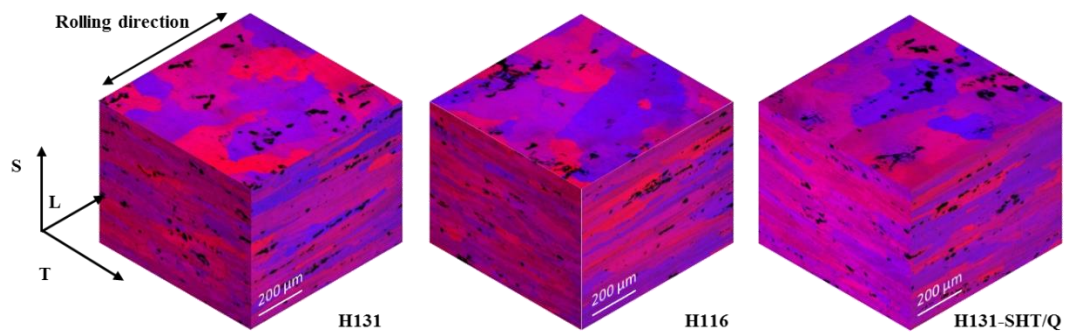
Figure 3.1 Microstructure of AA5083 after electrolytic etching Barker's etching revealing elongated grains in all three tempers: H131 (left), H116 (middle), and solutionized H131(right).

The nominal chemical composition of all AA5083 used in this study is presented in Table 3.1. The orientation convention and the microstructure of the three tempers showing anisotropic unrecrystallized grains after Barker's etching are given in Figure 3.1. The average grain widths at the relevant mid-thickness location in the longitudinal (L), long transverse (T), and short transverse (S) directions for all the three tempers are reported in Table 3.2.

Table 3.2. Average grain size at relevant mid-thickness in for AA5083 alloys

Temper	Longitudinal, L (μm)	Transverse, T (μm)	Short Transverse, S (μm)
H131*	80	60	20
H116	125	75	30
H131-SHT/Q*	80	60	20

*Barker's etching and grain size analysis performed by Wasiu Adedeji

Table 3.3. Sensitization heat treatment conditions and DoS according to ASTM G-67 for AA5083 alloys with different temper states

Sensitization time (days)	Degree of Sensitization (mg/cm^2)		
	AA5083-H131	AA5083-H116	AA5083-H131-SHT/Q
0	3	2	2
3	10	-	10
7	21	22	24
14	39	34	39
30	50	45	49

The specimens were cut from the center of the plate (S/2) into standard ASTM-G67[34] size of 5.1 cm x 2.5 cm x 0.6 cm (L x S x T) pieces, and were sensitized at 100°C for various lengths of time. Duplicate specimens for each aging condition were prepared in accordance with ASTM G-67 for measurement of DoS via the nitric acid mass loss test (NAMLT).[34] Measurements were conducted following specifications by sample immersion in 70% (v/v) HNO$_3$ for 24 h at 30°C.

The sensitization heat treatment conditions and their respective DoS utilized in this study are summarized in Table 3.3.

3.4.1.2 Wire Materials

Three wire materials were utilized in this study: AA5083-H131, magnesium, and aluminum. The AA5083-H131 wires with 112 µm diameter were prepared from the same bulk AA5083-H131 as described above through the Materials Preparation Center at Ames Laboratory, which is supported by the US DOE Basic Energy Sciences. The AA5083-H131 wire was utilized both in the as-received state as well as the sensitized state. Sensitization heat treatment was conducted at 100°C for 30 days, with a DoS of 50 mg/cm^2. Since the standard ASTM-G67 specimen size was designed based on rolled plate, the standard test is not applicable to wire specimen. Instead, the DoS values of the bulk AA5083-H131 subjected to the same sensitization heat treatment conditions were adapted for the wire specimens.

Table 3.4. Nominal composition of 99.99% Mg wire used in this study

Component	Mg	Al	Fe	Cu	Zn	Mn	Ni	Others
Weight %	Bal	0.02	0.008	0.003	0.03	0.005	0.01	< 0.01

The 127 µm diameter 99.99 % Mg wire from Sigma-Aldrich and the 50 µm diameter 99.99 % Al wire from California Fine Wires were used in artificial pit experiments. Table 3.4 and Table 3.5 show the nominal chemical composition of the Al and Mg wires, respectively.

Table 3.5. Nominal composition of 99.99% Al wire used in this study

Component	Al	Mg	Fe	Cu	Zn	Mn	Si	Others
Weight %	Bal	0.003	0.006	0.006	0.003	0.005	0.003	< 0.005

3.4.2 Sample Preparation for Electrochemical Testing

All bulk samples were cut from the center of the plate (S/2) into 6mm x 6mm x 6mm pieces. Samples were mounted in Buehler EpoThin epoxy resin and allowed to cure at room temperature ($\sim 25^{\circ}$C) for 9 h. The mounted samples were alternatingly ground with SiC paper and rinsed with water down to 1200 grit. The samples were then polished with 1 μm diamond paste and finished with 0.06 μm colloidal silica. Samples were ultrasonically cleaned in ethanol to remove any silica debris and air dried prior to testing.

3.4.3 Experimental Setup for Electrochemical Testing

A conventional three-electrode flat cell setup, composed of a working electrode, a reference electrode and a counter electrode, was utilized for electrochemical testing. In all cases, a saturated calomel electrode (SCE) equipped with a Luggin capillary was utilized as the reference electrode, and a platinum mesh as the counter electrode. This setup was connected to a potentiostat (PAR VersaStat, PAR 273, Gamry PCI4, or Gamry Femto-stat) with a computer interface software to control and measure potential and current during DC electrochemical experiments. A Gamry Reference 600 potentiostat was used for electrochemical impedance spectroscopy (EIS) measurements.

3.4.4 Characterization of Intergranular Corrosion Propagation Behavior

The intergranular corrosion behavior of various tempers across a range of DoS of bulk AA5083 were evaluated by conducting potentiostatic holds in quiescent 0.6 M NaCl solution at a pH of 8.3. The samples, with a surface area of 0.36 cm^2, were exposed to open circuit potential for 30 min and then held at -0.73 V$_{SCE}$ for 24, 72, or 100 h, consistent with conditions where spreading was observed.[19] The tests were performed on ST and the LT surfaces, allowing IGC to propagate in the L and S directions, respectively. Images of cross-sectioned samples were taken with the optical microscope to determine IGC damage depth and distribution. The total cross-sectional area of 108 mm^2 was evaluated for each condition.

Galvanostatic holds were also performed on bulk AA5083-H131 in quiescent 0.6 M NaCl solution at a pH of 8.3. The ST surface of the samples, with a surface area of 0.36 cm^2, were exposed to open circuit potential for 30 minutes and then at selected anodic current densities, ranging from 1.5 x 10^{-5} to 3 x 10^{-3} A/cm^2, for 100 h. Images of cross-sectioned samples were taken with the optical microscope to determine IGC damage depth and distribution. The total cross-sectional area of 72 mm^2 was evaluated for each condition.

3.4.5 Effect of Intergranular Corrosion Path Tortuosity on Depth Propagation in the S Direction

To describe the influence of the grain aspect ratios on the tortuous IGC path in the S direction, a grain structure model represented by pancake grains, based on AA5083-H131 grain morphology (Figure 3.2) was utilized. It was assumed that no grain fall out or exfoliation corrosion occurred, and that IGC penetrating in the S direction propagated in the perpendicular direction whenever it reached a triple point. The IGC path hit a triple point when it propagated a vertical length of a grain width in the S direction (20 µm) or horizontal length of half a grain width in the T direction (30 µm). Considering the above assumptions, the total IGC length is equivalent to the sum of the vertical and horizontal corroded grain boundary lengths in the S and the T directions, respectively. The vertical corroded grain boundary length is equivalent to S_{depth}, the measured IGC depth in the S direction. In order to calculate the horizontal corroded grain boundary length, the number of grain layers penetrated by S_{depth} has to be taken into account. The number of grain layers is simply the S_{depth} divided by 20 µm, the grain width in the S direction. As such, the total IGC length can be calculated using the following expression:

$$\text{Total } IGC \text{ } length = S_{depth} * \left(1 + \frac{30}{20}\right) \qquad \text{(Equation 3.1)}$$

where S_{depth} is the IGC damage depth in the S direction, and the multiplier, 30/20, accounts for the additional horizontal corrosion damage in the T direction.
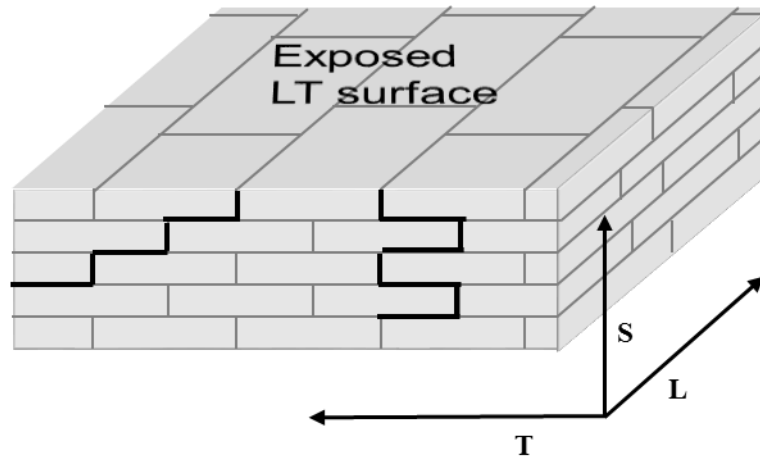
Figure 3.2. A grain structure model represented by pancake grains with AA5083-H131 grain morphology showing IGC tortuous IGC damage path in the S direction.

3.4.6 Characterization of Pit Growth Kinetics

One dimensional growth of the pit was examined by potentiostatic hold on flush mounted wires of as-received and sensitized AA5083, Mg, and Al in an artificial pit configuration using a flat cell setup. An artificial pit was initiated and grown by a potentiostatic hold in quiescent 0.6 M NaCl solution at pH of 8.3. The cross-sectional surface of the wires were exposed to open circuit potential for 30 minutes and then held at an anodic potential of 1 V_{SCE} for 1000 s. The pit grew uniformly along a direction perpendicular to the exposed surface. The measured current was integrated to determine the net charge, which was utilized to calculate the theoretical artificial pit depths via Faraday's law. The actual pit depth was determined independently via cross-sectioning and optical microscopy. The pit depths determined by the two techniques were compared to enable calculation of current efficiency factor and the local cathodic kinetics. Three separate

experiments were conducted for each material. The reported current efficiency factor is an average from the three tests.

Following the formation of artificial pits in as-received and sensitized AA5083-H131 wires, the polarization behavior was determined by a potentiodynamic downward scan at 50 mV/s from the pit initiation potential of 1 V_{SCE}. This fast scan allows for the preservation of the pit solution, where the diffusion length of the ionic species ($\sqrt{\pi D t}$) is smaller than the pit depth during the potentiodynamic downward scan. Given the diffusivity of Al^{3+} and the scan range of 1 V_{SCE} to -1.25 V_{SCE}, the diffusion length at the end of the scan (t = 45 s) is 160 µm. This is smaller than the artificial pit depths generated and examined in this study.

3.4.7 Solution Resistance Measurements

Electrochemical Impedance Spectroscopy (EIS) was conducted on bulk as-received AA5083-H131 electrodes in fresh quiescent 0.6 M NaCl solution at pH of 8.3, and in post-test 0.6 M NaCl solution. The post-test solution was previously used to conduct 100 h galvanostatic test on highly sensitized AA5083-H131 at 3 mA/cm^2. Polished bare electrodes were clamped to an electrochemical flat cell exposing a 1 cm^2 electrode surface area to the electrolyte. The EIS scans were conducted immediately after a 10 minute OCP. A typical EIS scan was acquired in sweep sine mode from 300 kHz to 0.1 Hz with 6 points per decade. The electrodes were scanned with an AC amplitude of 10 mV.

Cathodic potentiodyanamic scans were also conducted on polished bulk as-received AA5083-H131 in an electrochemical flat cell exposing a 1 cm^2 electrode surface area to quiescent 0.6 M NaCl solution at pH of 8.3. An OCP measurement for a duration of 10 minutes was conducted prior to the potentiodyanamic scan from 0.005 V above OCP and scanned down to -3 V$_{SCE}$ at a scan rate of 0.167 mV/s.

3.5   Results

3.5.1   Intergranular corrosion morphology and propagation kinetics under potentiostatic control as influenced by temper

The degree of sensitization (DoS) reveals that cold work temper does not influence sensitization when exposed to the same sensitization heat treatment conditions (Figure 3.3). The IGC propagation kinetics and morphology of these various cold work tempers of AA5083 (H131, H116, and H131-SHT/Q) with a DoS range of 22 to 50 mg/cm^2 exposed to 0.6 M NaCl solution at pH 8.3, were examined via potentiostatic holds at the IGC spreading potential of -0.73 V$_{SCE}$, for various periods of time. The potentiostatic tests generated both electrochemical anodic charge data shown in Figure 3.4, and physical damage depth data shown as distributions and IGC propagation rate in Figure 3.5 and Figure 3.6.
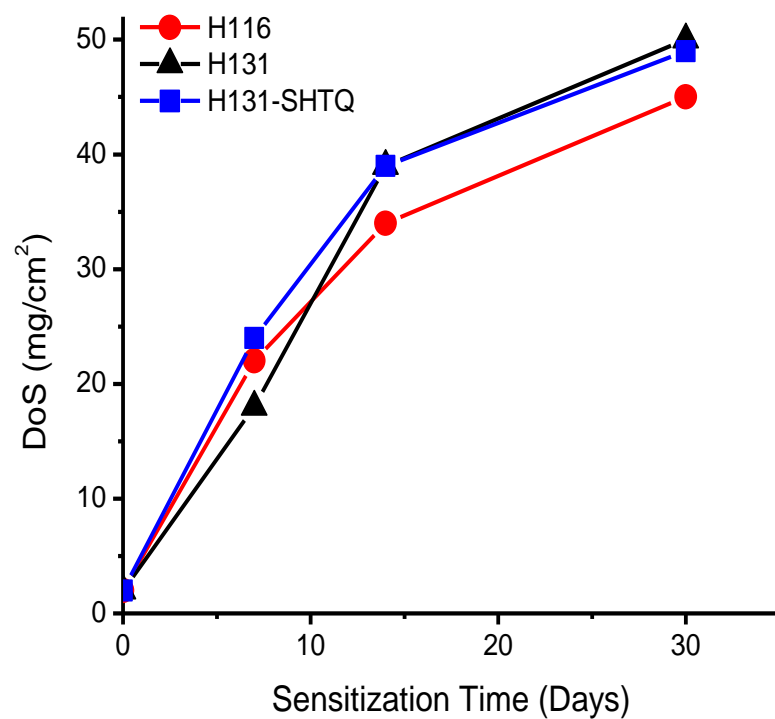
Figure 3.3. DoS of AA5083 alloys as a function of temper and sensitization conditions.
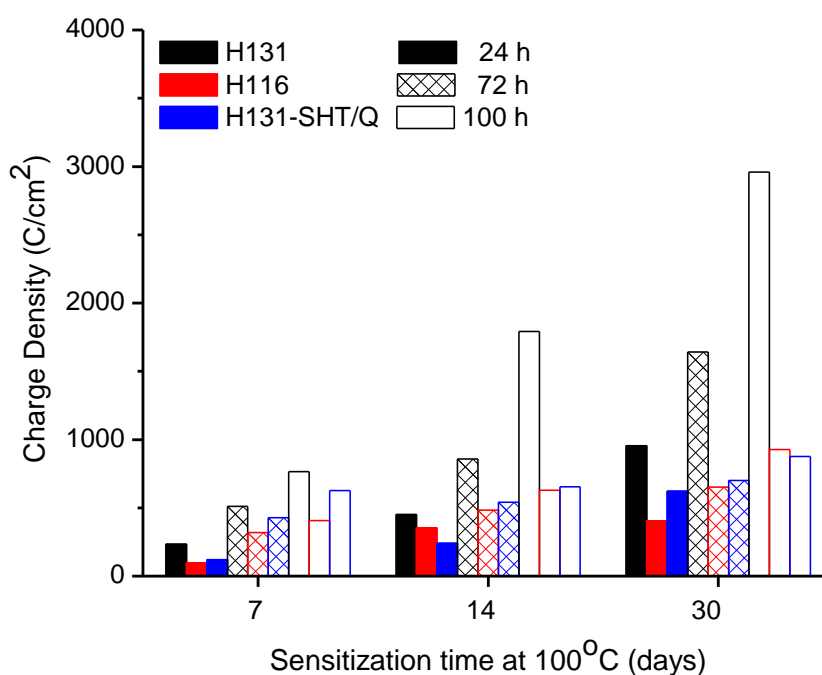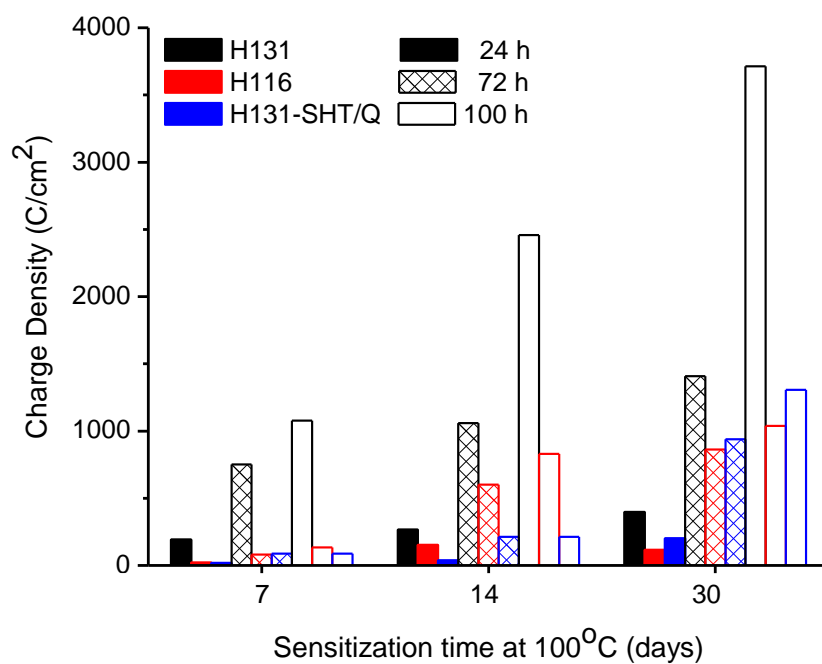
Figure 3.4 Anodic charge density as a function of sensitization time at 100°C, cold work temper, and exposure time for AA5083, with ST surface (top) and LT surface (bottom) exposed to 0.6 M NaCl solution, pH 8.3 at -0.73 V_{SCE}.
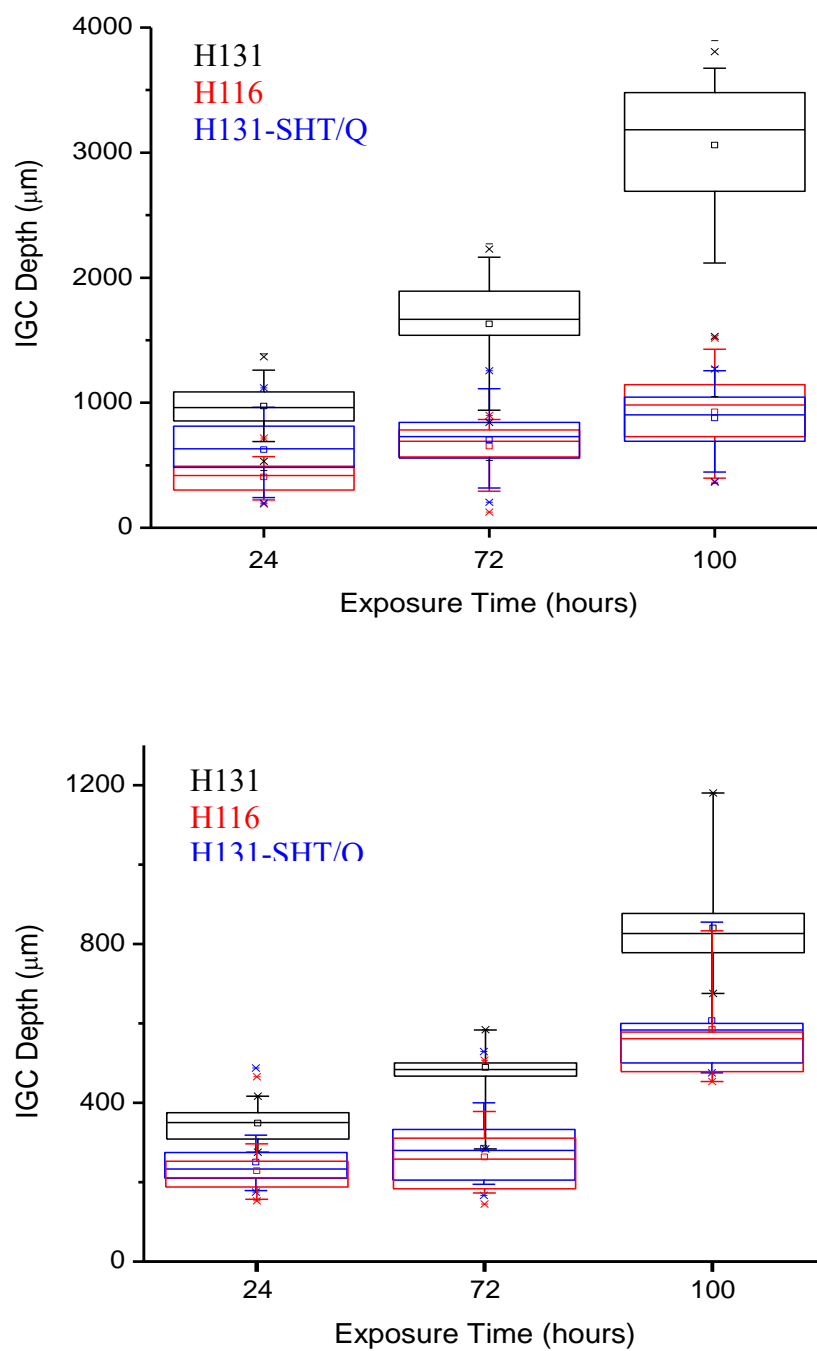
Figure 3.5. Damage depth distribution as a function of cold work temper, and exposure time for AA5083 sensitized at 100°C for 30 days, with ST surface, propagation in L (top) and LT surface, propagation in S (bottom) exposed to 0.6 M NaCl solution, pH 8.3 at -0.73 V_{SCE}.
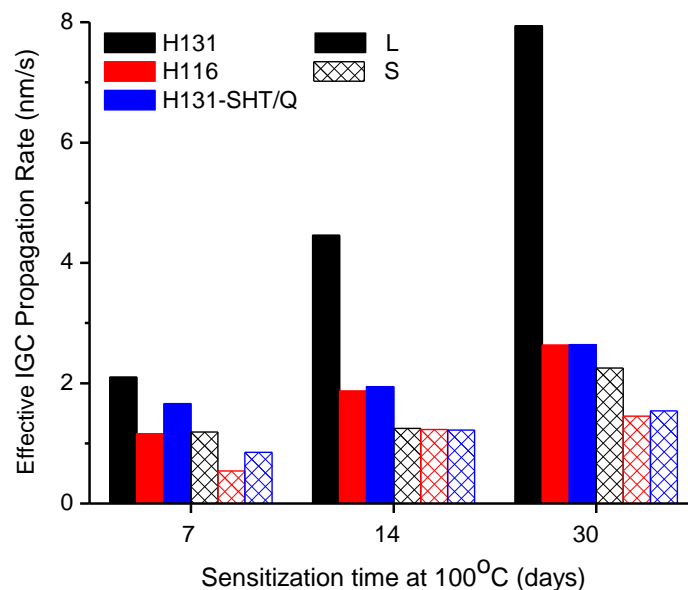
Figure 3.6. IGC propagation rate as a function of sensitization time at 100ºC, cold work temper, and orientation of propagation for AA5083 exposed to 0.6 M NaCl solution, pH 8.3 at -0.73 V_{SCE}.

Similar to the case of AA5083-H131-SHT/Q reported in Chapter 2, both the electrochemical anodic charge and the IGC damage depth data showed that the IGC propagation in sensitized AA5083-H131 and AA5083-H116 is also governed by DoS, exposure time, and orientation of propagation. The average and maximum IGC damage depth in both the L and the S directions increases with increasing DoS. The IGC damage depth increases with increasing exposure time to 0.6 M NaCl solution at -0.73 V_{SCE}. No signs of stifling were observed for any of the three DoS levels in all temper states, even after 100 h of exposures. Additionally, the IGC propagation in both tempers also exhibited strong anisotropy such that the propagation in the L direction was faster than that in the S direction, which can be

attributed to the tortuous path associated with microstructural anisotropy. Utilizing

Equation 3.1 to calculate the total IGC damage length in the S direction, considering

the effect of path tortuosity, shows that IGC damage length in S and L directions

(Figure 3.7) are similar. This is true for all tempers.
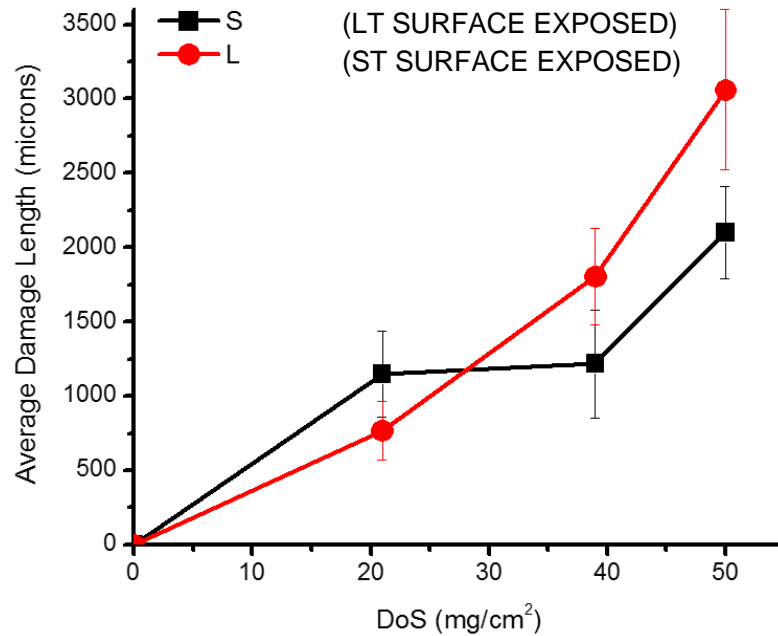
Figure 3.7. Average IGC damage length after 100 hours of exposure as a function of DoS and orientation of propagation for AA5083-H131 in 0.6M NaCl solution, pH 8.3 at -0.73V_{SCE}. Damage length in the S direction was calculated considering the effect of path tortuosity. Error bars represent one standard deviation.

Despite these similar trends in IGC propagation dependencies on the DoS,

exposure time, and orientation of propagation, the IGC fissure morphologies of

AA5083-H116, AA5083-H131, and AA5083-H131-SHT/Q materials of the same

sensitization after exposure to 0.6 M NaCl solution at pH 8, potentiostatically held

at -0.73 V_{SCE} for the length of time were morphologically very different. The IGC

fissures of H116 and H131-SHT/Q tempers are short, blunt, and wide, whereas those of H131 are long, sharp, and narrow for each DoS as shown in Figure 3.8. Additionally, a comparison of their IGC depth distributions after various periods of exposure times showed that H131 exhibited fastest IGC propagation kinetics than H116 and H131-SHT/Q for material of the same DoS. This suggests that DoS alone is not sufficient to define IGC susceptibility. Moreover, this implies that the differences in alloy processing impact precipitation behavior, such that the description of DoS on the microstructural level in terms of β-phase size, spacing, and grain boundary coverage is different across the tempers.
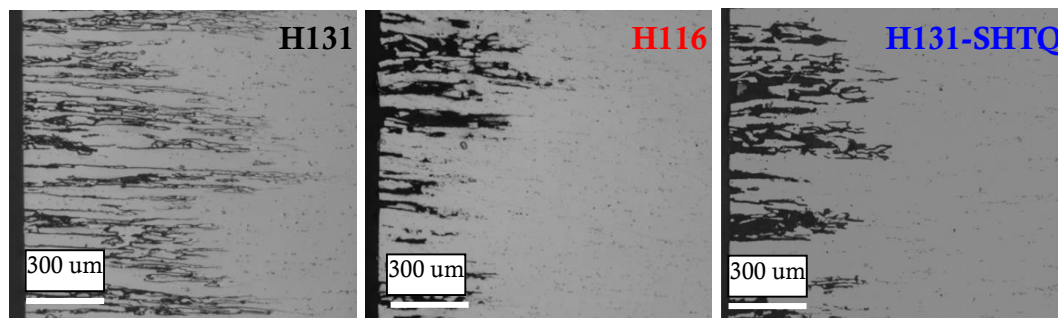
Figure 3.8. Cross section optical micrographs showing IGC depth penetration in the L direction after 72 hours of exposure to 0.6 M NaCl solution, pH 8.3, at -0.73 V_{SCE} for AA5083 alloys sensitized to 39 mg/cm^2 of varying temper.

Although the grain boundary β-phase microstructure dependence on DoS for AA5083 was broadly characterized, it was limited to only H131 and H131-SHT/Q tempers. However, given the similar fissure morphology and growth kinetics observed in the H131-SHT/Q and H116, the explanation for these two tempers should match up. No evidence of grain boundary β or free Mg segregation was shown for the as-received or the as-solutionized AA5083 prior to

sensitization.[7,8,17,35] For sensitization at 100ºC, SEM analysis of Ga-embrittled fracture surfaces shows β-phase as distributed spheres for each of the three DoS levels in both H131 and H131-SHT/Q temper states.[22,36] These image analyses also established that the mean equivalent radius of β-phase precipitates in H131 is a function of sensitization time and temperature described by the following expression:

$$r_{mean} = -0.73Te^{\frac{-t}{0.8T}} + 1.01T - 27.6 \qquad \text{(Equation 3.2)}$$

where r_{mean} is the mean-equivalent radius, t is sensitization time in hours (up to 80 days), and T is temperature in ºC (in the range of 70 to 200ºC).[36] Based on this equation, the β-phase size in H131 for 100ºC sensitization is constant at 74 nm for the three sensitization times (7, 14 and 30 days) in this study. For the H131-SHT/Q, the r_{mean} is 180, 185, and 330 nm for 7, 14, and 30 day sensitization, respectively.[22] The β-phase spacing in terms of nearest-neighbor (edge-to-edge) distance was observed to be fairly constant with sensitization time from 7 days (22 mg/cm^2) to 30 days (50 mg/cm^2) at 668 nm for H131, and 295 nm for H131-SHT/Q.[22,36] For all DoS levels, smaller β-phase precipitate size and longer edge-to-edge β-phase spacing was observed in the H131 temper relative to those in H131-SHT/Q. Based on this information, for a given grain boundary length with the same DoS, the H131 yields a lower β-phase grain boundary coverage and should have slower IGC kinetics, which contradicts experimental observations.

The IGC in H131-SHT/Q also produced more grain fall-out, as well as shorter and wider fissures. Based on this morphology, it can be argued that there was less ohmic drop in these fissures as opposed to the longer and tighter fissures in H131, and H131-SHT/Q should grow faster compared to H131. Both explanations point against trends for the experimental observations. In order to fully explain these differences, proprietary information from the supplier, as well as considerable TEM work, would be required, which is beyond the scope of the research.

These results were utilized instead to down-select the main alloy temper of focus for this IGC propagation research. From a practical point of view, the material with the fastest IGC propagation kinetics was considered the most critical as it can transition into IGSCC and consequently be the quickest to cause component failure. As such, AA5083-H131 was chosen for the remaining parts of this study.
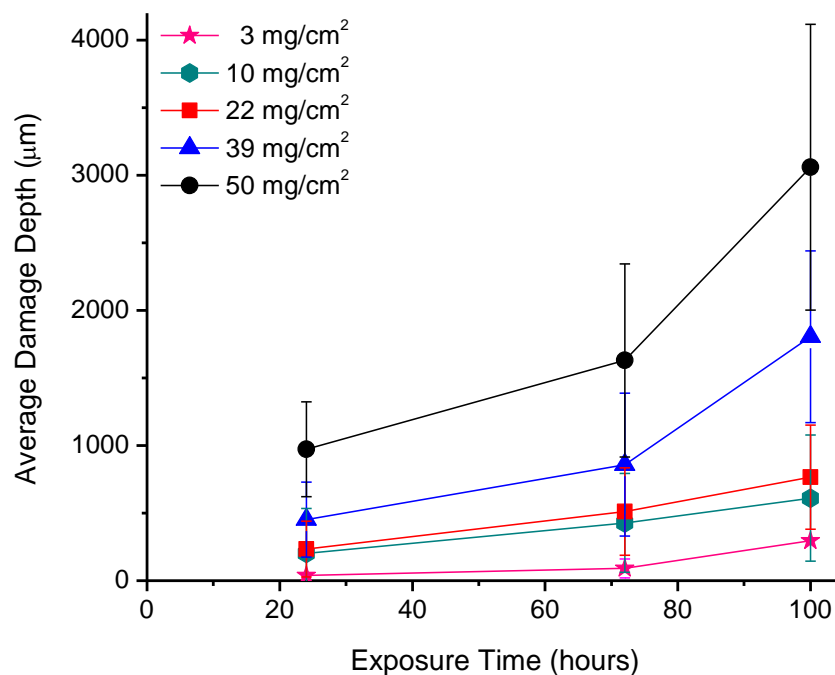
Figure 3.9. Average IGC damage depth from fissure measurements in L direction from ST surface as a funtion of DoS and exposure time for AA5083-H131 in 0.6M NaCl solution, pH 8.3 at -0.73 V_{SCE}. The number of fissures increases with both DoS and exposure time. Error bars represent 95% confidence interval.

The IGC damage depths in the L direction for all five DoS levels of AA5083-H131 under potentiostatic control at -0.73 V_{SCE} in 0.6 M NaCl solution are shown in Figure 3.9. Shallow IGC fissures were observed for the as-received DoS of 2 mg/cm^2 even at extended exposure times. However, the supposedly IGC-resistant DoS level of 10 mg/cm^2 has an average IGC damage depth of 203 µm after 24 h of exposure, and propagates to a depth of 611 µm after a total exposure time of 100 h. Assuming a linear propagation rate and immediate initiation upon exposure, the IGC propagation rate for the 10 mg/cm^2 was 1.47 nm/s. This rather

118

fast IGC growth rate was consistent with the observed fatigue crack tip IGC rate during constant low K hold period in 0.6 M NaCl solution at -0.8 V_{SCE} of 1.5 nm/s for this DoS level.[35]   This suggests that the presence of ribbon-like grain boundary β-phase (as seen using TEM) or the existence of low β-phase coverage grain boundaries (as observed from etching) triggers IGC propagation for this temper at this specific potential.[3,8,18–20,31]   The damage depth and IGC propagation rate increase slowly with DoS above 10 mg/cm^2, then increase substantially for DoS of 39 mg/cm^2 and above (Figure 3.6 and Figure 3.9).   A similar trend was observed for the DoS dependent fatigue crack tip IGC rates.[35] The shift is attributed to the increase in grain boundary β-phase connectivity, which is consistent with the increase in the percentage of the low β-phase coverage grain boundaries observed with etching.[20]

Because of the difference in the IGC propagation behavior between H131-SHT/Q and H131, a new set of IGC empirical growth laws for H131 as described by multi-linear regressions obtained from analysis of the probability density functions of experimental data. The IGC propagation rate of sensitized AA5083-H131 in 0.6 M NaCl solution with a pH of 8.3 at -0.73 V_{SCE} as a function of exposure time and DoS in the L and S directions can be described by the following expressions:

$$L_{depth} = (11.62 \pm 7.31)t_{exp} + (33.64 \pm 13.04)DoS - 789.52 \pm 619.17$$
(Equation 3.3)

$$S_{depth} = (4.16 \pm 1.70)t_{exp} + (7.25 \pm 3.03)DoS - 154.02 \pm 144.25$$
(Equation 3.4)

where depth is in µm, t_{exp} in hours, and DoS in mg/cm^2. The uncertainties define the bounds for a 95% confidence level for each of the parameters. The negative intercept at an exposure time of zero in these expressions demonstrated the existence of an incubation prior to IGC penetration in potentiostatic experiments, with a trend of decreasing incubation time with increasing DoS. This observation is in agreement with previous findings suggesting that incubation time is necessary for β-phase pitting to develop into IGC in sensitized Al-Mg alloys exposed to chloride environments.[33,37] The incubation time was hypothesized in Chapter 2 to be attributed to the delayed IGC depth penetration because of the time necessary to reach critical IGC spreading size or the time needed for a chemistry change in the pits or surface IGC or delay in penetration due to a β-phase precipitate-free near surface deformed layer.

In the context of IGC susceptibility, these results further question the viability of ASTM G-67 for predicting sensitization levels. Materials of the same DoS across different temper exhibited different levels of IGC susceptibility as manifested by the almost four-fold difference in IGC propagation rate (DoS 50 mg/cm^2). Additionally, a categorically IGC-resistant DoS of 10 mg/cm^2 (H131) was observed to have an IGC growth rate of 1.47 nm/s, which is almost as fast as that of DoS of 24 mg/cm^2 (H131-SHT/Q).

3.5.2 Critical Electrochemical Conditions for Intergranular Corrosion Propagation in AA5083-H131

In order to avoid incubation time, the influence of applied potential and applied current density on IGC damage propagation of AA5083-H131 in 0.6 M NaCl solution at pH of 8.3 was investigated via galvanostatic testing. The effect of applied current density and DoS on measured applied potential during galvanostatic test is shown in Figure 3.10 and Figure 3.11. Each of the galvanostatic curves started at a high potential, which lasted for up to several hours, followed by a rapid potential drop until a stable potential was reached. The initial high potentials, hereafter referred to as activation potentials, are reasonable for the given applied current density based on the polarization curves reported for AA5083-H131.[29] These transient activation potentials are more positive than the breakdown potential of β-phase (βE_{pit}), -0.96 V_{SCE}, and at times near, if not more positive than, the IGC spreading potential ($E_{spreading}$), -0.73 V_{SCE}, for AA5083.[19,38] As such, there is a sufficient chemical driving force to initiate localized corrosion on the surface, in the form of β-phase pitting and IGC spreading.
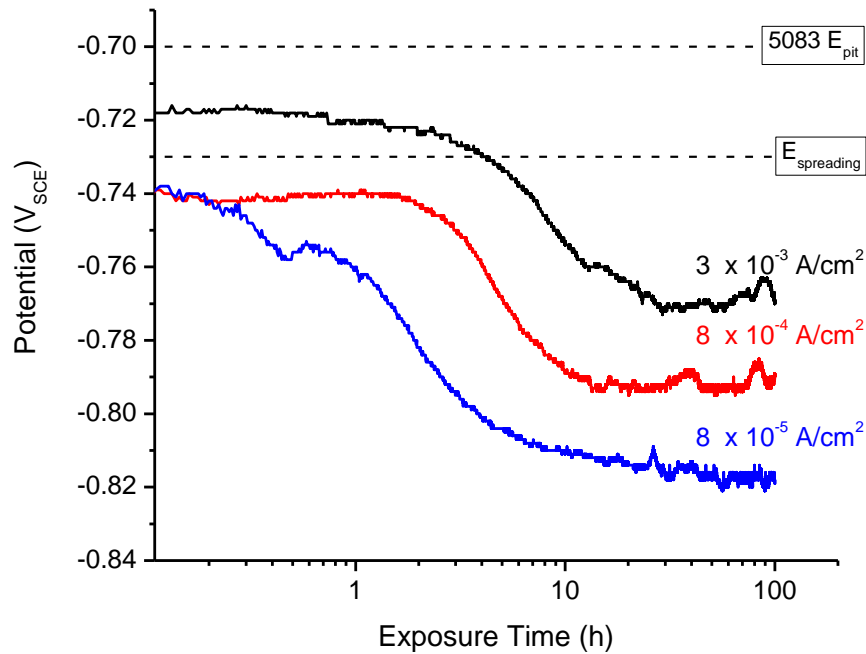
Figure 3.10. Potential as a function of exposure time for AA5083-H131 DoS of 39 mg/cm^2 at various applied current densities with ST surface exposed to 0.6 M NaCl solution at pH 8.3. As a comparison, the IGC spreading potential for sensitized AA5083 and the pitting potential for unsensitized AA5083 (2 mg/cm^2) are marked with dashed lines.[19] Also, the breakdown potential of β-phase (not included in the figure) is -0.96 V$_{SCE}$.[38]

For the same DoS (Figure 3.10), the activation potential decreases with decreasing applied current density, as would be expected from the relation between DoS and spreading potential. For the same applied current density (Figure 3.11), a trend of decreasing activation potential with increasing DoS was observed. This dependence is due to the higher grain boundary β coverage associated with the high DoS specimen [17,19,20] allowing pitting and IGC to occur without significant polarization. At a lower applied current density or a higher DoS, the drop in potential occurred earlier and reached a lower stable potential relative to those

measured at higher applied current densities. The drop in potential is speculated to be a response of the change in electrochemical behavior of AA5083 during corrosion. Mizuno and Kelly[29] reported that after a 100 h galvanic corrosion test, the OCP of AA5083 shifted to a much lower value and high anodic current densities were measured at potentials cathodic to the pristine AA5083. This shift is attributed to the local acidification and high chloride ion concentration that develops within pits, surface IGC and IGC fissures during corrosion, rendering lower breakdown potentials and higher anodic current densities.
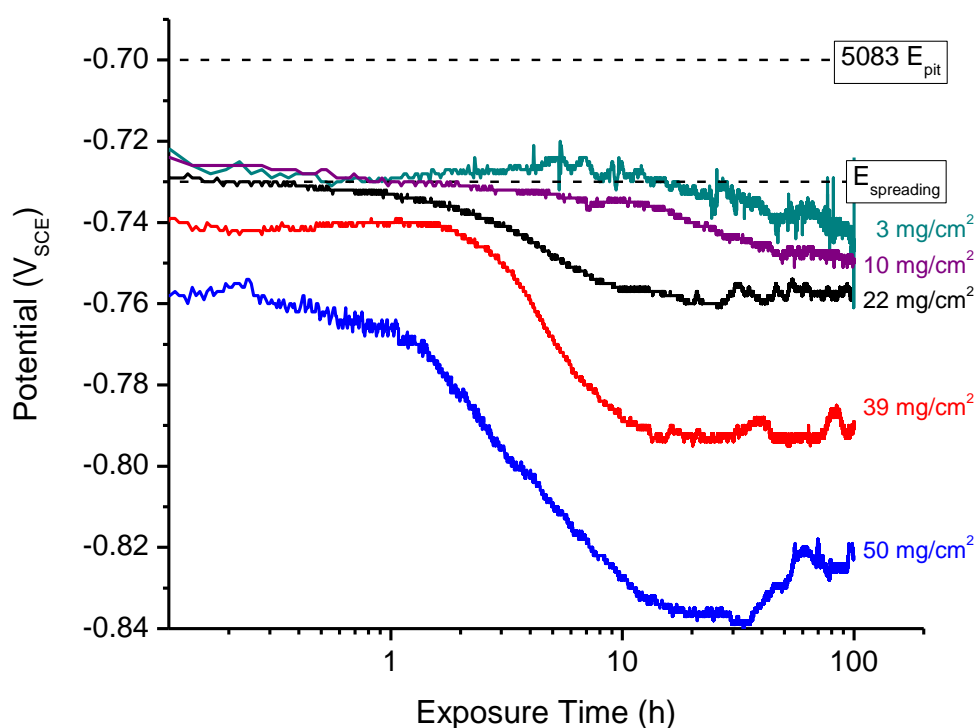
Figure 3.11. Potential as a function of exposure time for AA5083-H131 with varying sensitization levels held at an applied current density of 8 x 10^{-4} A/cm^2, with ST surface exposed to 0.6 M NaCl solution at pH 8.3. As a comparison, the IGC spreading potential for sensitized AA5083 and the pitting potential for unsensitized AA5083 (2 mg/cm^2) are marked with dashed lines.[19] Also, the breakdown potential of β-phase (not included in the figure) is -0.96 V$_{SCE}$.[38]
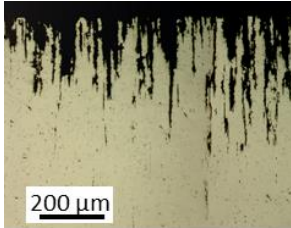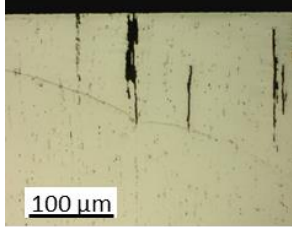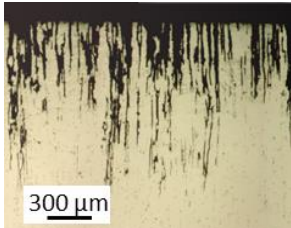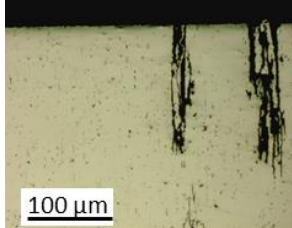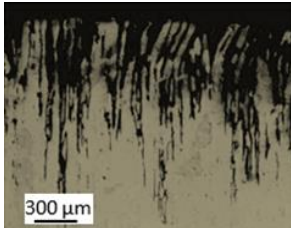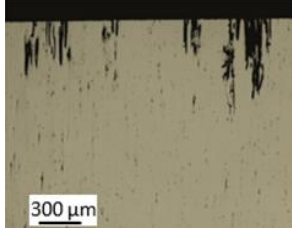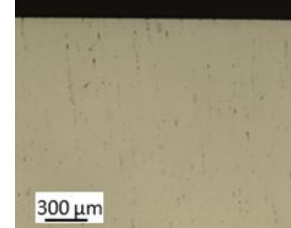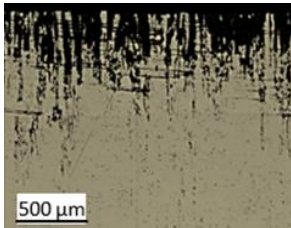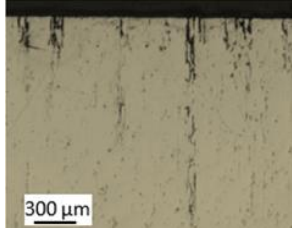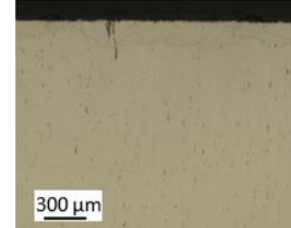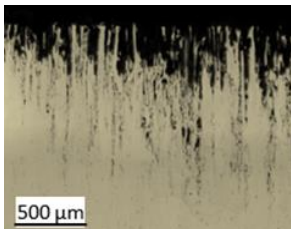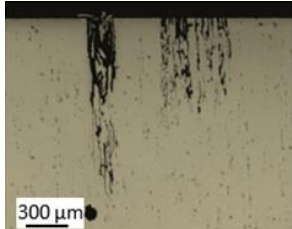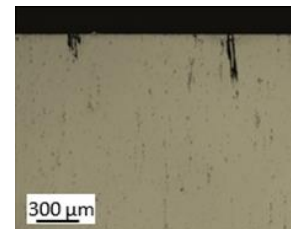
DoS	Applied Current Density (A/cm^2)		
(mg/cm^2)	3 x 10^{-3}	3 x 10^{-4}	3 x 10^{-5}
3			
10			
22			
39			
50			

Figure 3.12. Cross section optical micrographs showing IGC depth penetration in the L direction for various sensitized AA5083-H131 specimens that were galvanostatically held at three different applied current densities for 100 hours, with the ST surface exposed to 0.6 M NaCl solution at pH 8.3.
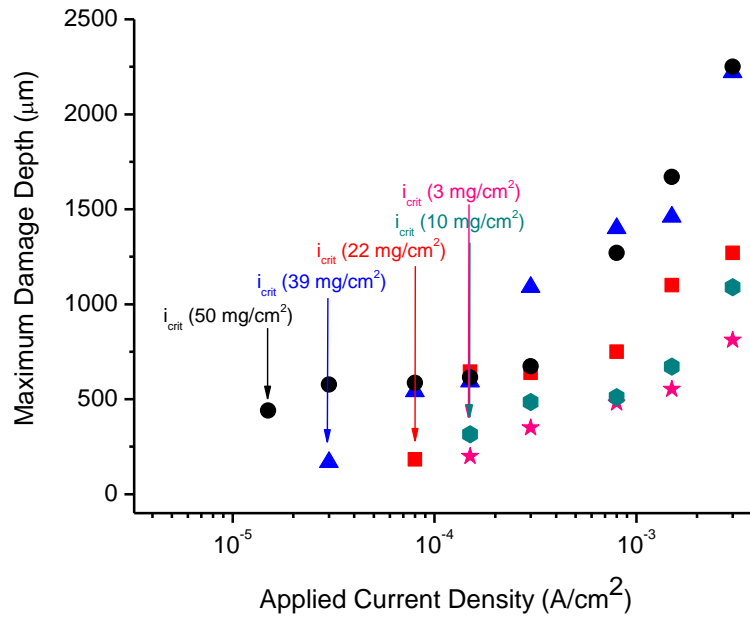
Figure 3.13. Maximum IGC depth in the L direction from fissure measurements as a function of applied current density for various sensitized AA5083-H131 galvanostatically held for 100 hours in 0.6 M NaCl solution at pH 8.3.

The cross section images showing IGC depth penetration in the L direction of specimens held galvanostatically are displayed in Figure 3.12. At the highest applied current density, almost all the grain boundaries intersecting the exposed surface suffered deep IGC. The extensive damage resulted in grain fall-out at the site of numerous IGC networks. This fall-out occurred even for the DoS levels below the ASTM G-67 susceptibility criterion of 25 mg/cm^2.[34] As the current density decreases, both the depth and the number IGC fissures decreases. At sufficiently low current densities, no IGC but only pitting was observed. The minimum current density at which IGC was observed, i_{crit}, decreases with increasing DoS as can be seen in the plots of maximum damage depths after 100 h versus applied current density in Figure 3.13. For all DoS levels, the maximum IGC damage depths decreased with decreasing applied current density.
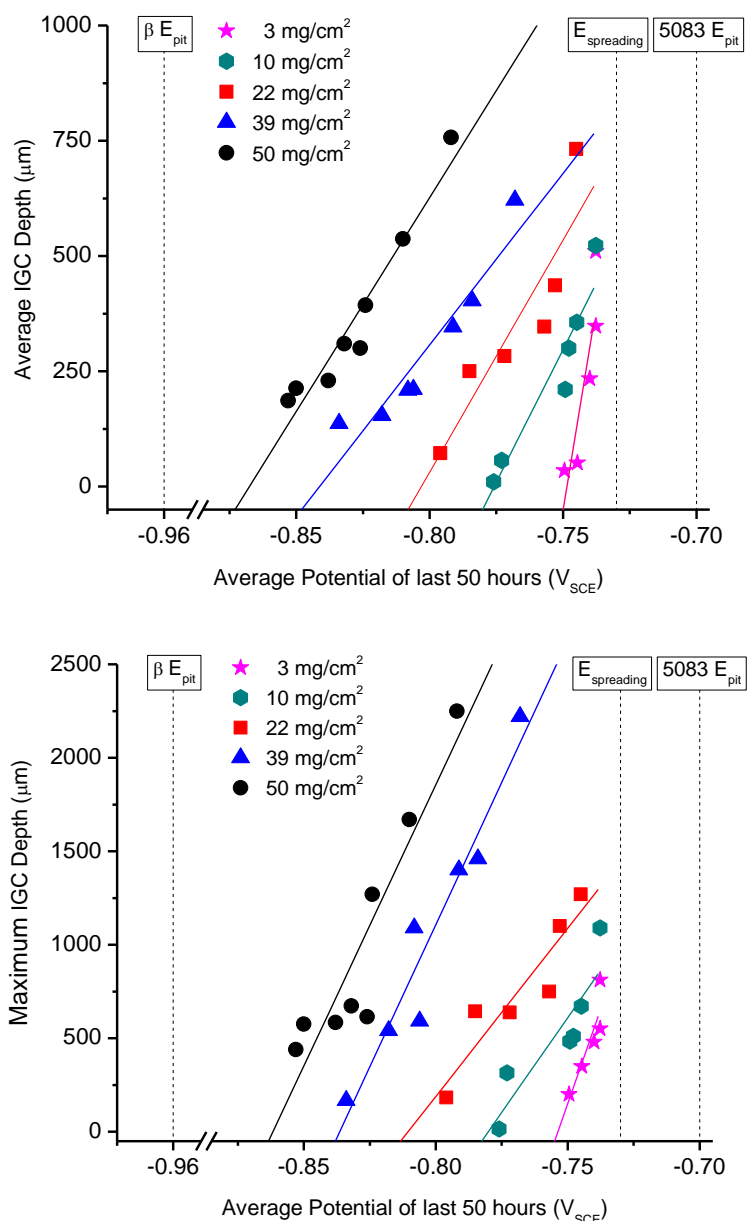
Figure 3.14. Average (top) and maximum (bottom) IGC depth in the L direction from fissure measurements as a function of average potential for various sensitized AA5083-H131 galvanostatically held for 100 hours in 0.6 M NaCl solution at pH 8.3. The average potentials are plotted together with error bars representing one standard deviation over the last 50 hours. As a comparison, the IGC spreading potential for sensitized AA5083 and the pitting potential for unsensitized AA5083 (2 mg/cm^2) are marked with dashed lines.[19] Also, the breakdown potential of β-phase (not included in the figure) is -0.96 V$_{SCE}$.[38]

Figure 3.14 shows the average and maximum IGC depth as a function of average potential and DoS. Only the potentials from the last 50 hours of galvanostatic hold were considered in the average. Both the average and the maximum damage depths after 100 h increased linearly with applied potential. The potential dependence of the IGC also increased with increasing DoS as can be seen based upon the differences in the slopes. In addition to that, an IGC threshold potential, E_{crit}, existed, below which no IGC was observed, in agreement with Mizuno.[29] The E_{crit} does decrease with increasing DoS, but only within a narrow range (-0.850 to -0.800 V_{SCE}). This threshold potential is more positive than the β-phase breakdown potential, but more negative than the IGC spreading potential for AA5083. Furthermore, plotting the average applied potentials against the logarithm of the applied current densities yields a semi-logarithmic or E-log i trend (Figure 3.15), suggesting a Tafel relationship where the E-i behavior for IGC over the range of potentials covered is primarily charge transfer-controlled.

The electrochemical framework for IGC spreading in AA5083[19] suggests that IGC is expected to occur at potentials between the IGC spreading potential, -0.73 V_{SCE}, and the β-phase breakdown potential, -0.96 V_{SCE}. However, comparing the measured E_{crit} values (Figure 3.14) indicates that those potential range is, in reality, divided into two different regions. The region between the $E_{spreading}$ and the E_{crit}, where IGC is expected to occur; and the region between E_{crit} and $βE_{pit}$, where only β-phase pitting can occur.
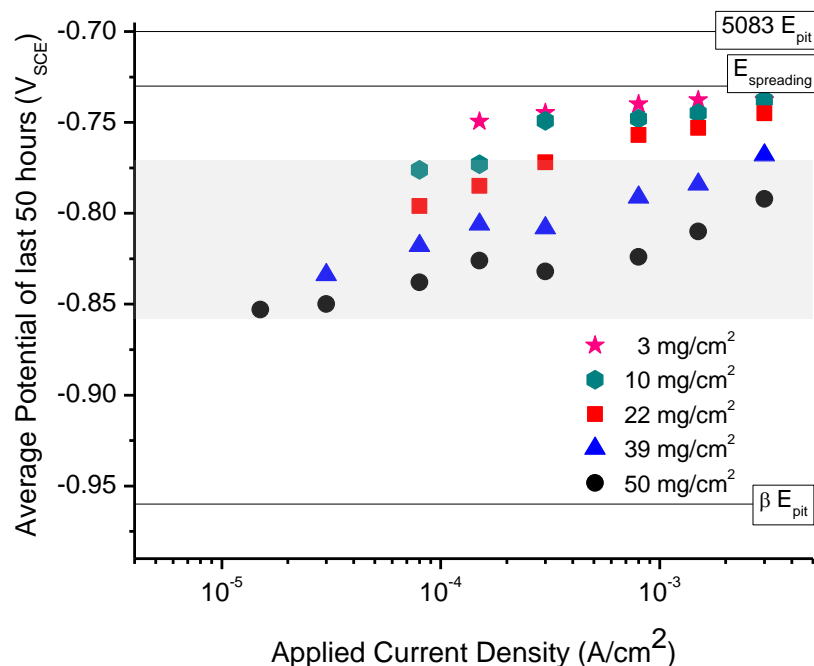
Figure 3.15. Average potential as a function of applied current density for various sensitized AA5083-H131 galvanostatically held for 100 hours in 0.6 M NaCl solution at pH 8.3. Only the last 50 hours, where the potential is stable, was considered in the average potential. The shaded region represents that range of E_{crit} for the range of DoS studied. As a comparison, the IGC spreading potential for sensitized AA5083 and the pitting potential for unsensitized AA5083 (2 mg/cm^2) are marked with dashed lines.[19] Also, the breakdown potential of β-phase (not included in the figure) is -0.96 V_{SCE}.[38]

3.5.3 Dissolution Kinetics and Ohmic Resistance in an Artificial Pit Growth

In order to measure the current efficiency factor, artificial pit experiments were conducted on as-received (3 mg/cm^2) and sensitized AA5083-H131 (50 mg/cm^2) wires under controlled corrosion at 1 V_{SCE} in 0.6 M NaCl solution at pH 8.3 to form recessed pits. For comparison purposes, the current efficiency factor of 99.99 % pure Al and 99.99 % pure Mg wires were also measured in this manner.

Representative current density as a function of time curves generated during the potentiostatic hold are shown in Figure 3.16. The current behavior of the metals are relatively similar to each other at 1 V_{SCE}. This could signify that the artificial growth kinetics on all metals were under full or partial mass transport control, where the rate of charge transfer dissolution was limited by ionic diffusion of the dissolving species towards the pit mouth. The large and repeated noise on the current data is most likely due to the repetitive formation and release of large H_2 bubbles within the artificial pit.
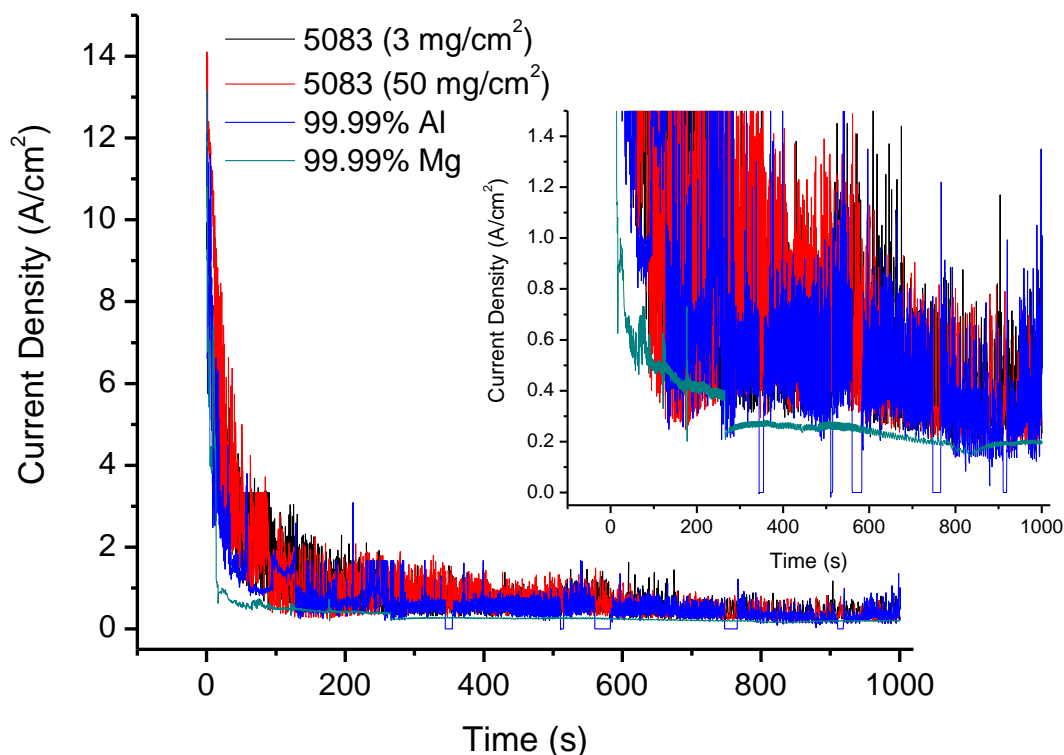
Figure 3.16. Measured anodic current density as a function of time during pit generation of as-received (3 mg/cm^2) and sensitized (50 mg/cm^2) AA5083-H131, 99.99% Al, 99.99% Mg exposed to 0.6 M NaCl solution, pH 8.3 at 1 $V_{SCE.}$ Limiting current densities in the range of 0.2 to 0.4 A/cm^2 were observed as shown in the inset image.

The current versus time data were integrated to give the total anodic charge associated with the artificial pit growth. These values were then used to calculate the theoretical damage depth using the Faraday's law (Equation 3.2).

$$\text{Theoretical Pit Depth (cm)} = \frac{Q\ (EW)}{FA\rho} \qquad \text{(Equation 3.5)}$$

Here Q is the total anodic charge (C), EW is the equivalent weight of the metal (g/eq), F is Faraday's constant (96, 485 C/eq), A is specimen surface area (cm^2), and ρ is the density of the metal (g/cm^3). The equivalent weight and density used for the metals are given in Table 3.6. The equivalent weight was calculated using the procedure described by Jones.[39]

Table 3.6. Equivalent weight, density, and estimated current efficiency factor after artificial pit experiment

Materials	Equivalent Weight (g/eq)	Density (g/cm³)	Current Efficiency Factor (%)
5083 (3 mg/cm²)	9.16	2.66	75
5083 (50 mg/cm²)	9.16	2.66	74
99.99% Al	8.99	2.70	86
99.99% Mg	8.10	1.70	64

Cross section micrographs of the artificial pit show that both alloys as well as the pure metals held at 1 V_{SCE} grew uniformly. The current efficiency factor of the as-received and sensitized AA5083, Al, and Mg wires calculated from the ratio of the measured actual pit depth to the estimated theoretical pit depth is 0.75, 0.74, 0.86, and 0.64, respectively. The calculated value for Al and Mg are within the

reported ranges of 0.75 to 0.90, and 0.50 to 0.65, respectively.[40–43] All of the estimated current efficiency factors are below 1, which implies that the measured anodic current is less than the actual current. Because the measured net current is the sum of the cathodic and anodic currents, this suggests that the rate of cathodic reaction, which is primarily the hydrogen evolution reaction, was least in pure Al, followed by the alloy, and greatest in Mg (which is known to corrode with copious hydrogen evolution).[44] Although lower current efficiencies were observed from the alloys, the little difference between the two alloys implies little to no effect of sensitization. This could very well be due to the sluggish cathodic kinetics of β-phase, (which readily dissolves at 1 V_{SCE}).[45]
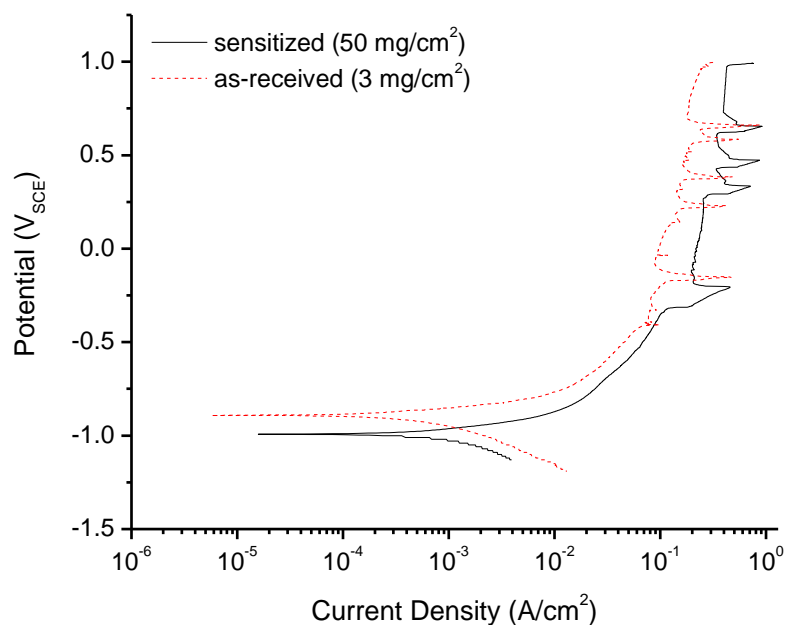
Figure 3.17. Polarization behavior (uncorrected) of artificial pits formed in as-received (3 mg/cm^2) and sensitized (50 mg/cm^2) AA5083-H131 alloys. The pits were generated by potentiostatic hold at 1 V_{SCE} for 1000 s in 0.6 M NaCl solution, pH 8.3. The polarization scans were obtained by an immediate potentiodynamic scan after pit generation at a scan rate of 50 mV/s.

131

The anodic dissolution kinetics of artificial pits in AA5083-H131 were determined by potentiodyanamic downward scans. The polarization curves of the as-received and sensitized AA5083-H131 shown in Figure 3.17 indicate a mass transfer regime with current spikes attributed to hydrogen bubbles. The polarization curves were further analyzed to determine the ohmic resistance, considering both the solution resistance within the pit and outside in the bulk. The activation charge density was extracted from the polarization curve, following the relationship between total current density (i_{tot}), charge transfer current density (i_{act}), and limiting current density (i_{lim}) as expressed by

$$\frac{1}{i_{tot}} = \frac{1}{i_{act}} + \frac{1}{i_{lim}}$$
(Equation 3.6)
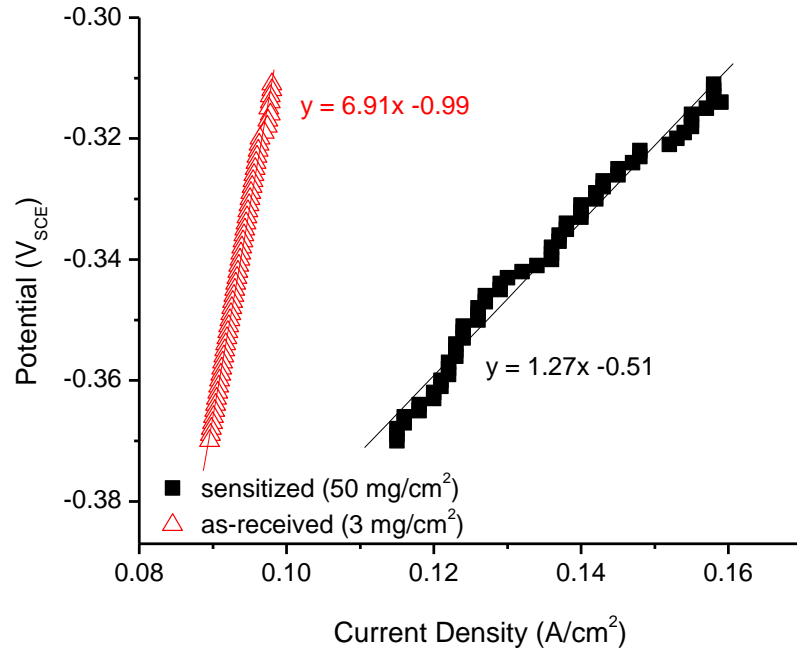
Figure 3.18. Limiting current density (i_{lim}) corrected E-i_{act} curves of artificial pit formed in as-received (3 mg/cm^2) and sensitized (50 mg/cm^2) AA5083-H131 at 1 V_{SCE} (Figure 3.17). The correction was performed assuming an i_{lim} of 0.3 A/cm^2 for both alloy.
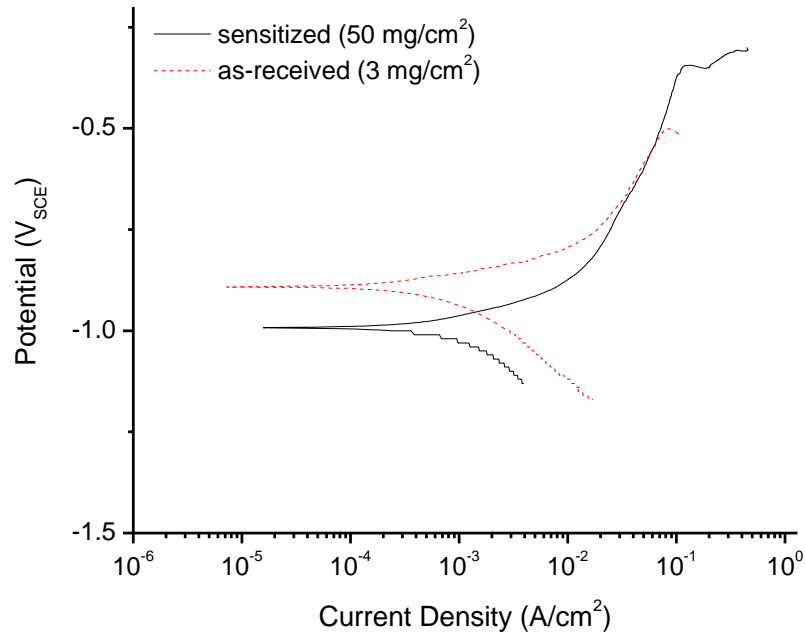
Figure 3.19. Limiting current density (i_{lim}) and ohmic potential drop (IR) corrected polarization curves of artificial pit formed as-received (3 mg/cm^2) and sensitized (50 mg/cm^2) AA5083-H131 at 1 V_{SCE} (Figure 3.17). IR correction was performed assuming resistance of 6.91 and 1.27 Ω-cm^2 for as-received and sensitized AA5083-H131, repectively.

An assumed limiting current density of 0.3 A/cm^2 was subtracted from the measured charge density. The ohmic resistance was determined from the slope of the high current density region of the corrected polarization curve plotted in linear scale shown in Figure 3.18. The ohmic resistance of artificial pits formed in the as-received and sensitized AA5083 alloys were determined to be 6.91 and 1.27 Ω-cm^2 or 70,139 and 12,891 Ω for a pit radius of 56 µm, respectively. These values were utilized to calculate the potential drop, and to obtain the iR-corrected polarization curves in Figure 3.19. The highlighted region shows that the sensitized condition is more active relative to the as-received AA5083 in this potential range of interest, -0.85 to -0.73 V_{SCE}.

The ohmic resistance is the sum of the resistance between the reference electrode and the pit mouth (R_{sol}), and the solution resistance within the pit (R_{pit}). Both terms can be estimated from the geometry and intrinsic conductivity of the electrolyte, as described by the following equation:

$$R_{ohm} = R_{sol} + R_{pit} = \frac{\pi r}{4\sigma_{bulk}} + \frac{d_{pit}}{\sigma_{pit}}$$ (Equation 3.7)

where r is the radius of the wire electrode in cm, σ_{bulk} is the conductivity of the bulk electrolyte in S/cm, d_{pit} is the pit depth in cm, and σ_{pit} is the conductivity of the pit chemistry in S/cm.[46] The conductivity of the bulk solution is 7.49×10^{-3} S/cm for 0.6 M NaCl. Given that the radius of the wire electrode is 56 µm, the bulk solution resistance is 0.587 Ω-cm^2. The pit chemistry conductivity was assumed to be 6.9×10^{-2} S/cm, the average of the measured conductivities for an 80% and a 100 % saturated Al-4wt% Mg chloride solution, which is the predicted IGC fissure chemistry in AA5083.[30] The solution resistance within a pit depth of 470 µm is 0.681 Ω-cm^2. Based on this calculation, the total solution resistance or ohmic resistance is 1.268 Ω-cm^2 or 12,870 Ω for a pit radius of 56 µm, which is comparable to the estimated value of 12,891 Ω for the sensitized AA5083. Because the generated pit depths for both alloys are equal, the only difference is the solution resistance within the pit brought on by dissimilarity in the pit chemistries. However, the pit chemistry within the as-received AA5083 can only be based on Al-4wt% Mg composition. Therefore, it is safe to assume a conductivity of 4.5×10^{-2} S/cm for 100% saturation within the pit. For a pit depth of 470 µm, the solution resistance is 0.534 Ω-cm^2 or 5419 Ω. The difference is small, as compared to the

308 Ω estimated for the sensitized AA5083, and cannot account for the large ohmic resistance (70,139 Ω) for the as-received AA5083. This considerable resistance is most likely due to hydrogen bubbles or gelatinous corrosion product acting as huge resistors during the polarization scan.

3.5.4 Solution Resistance of Bulk Electrolyte

For ohmic potential drop correction of the E-i behavior during IGC of planar electrodes, the solution resistances of fresh and post-galvanostatic test 0.6 M NaCl solution were determined for via high frequency electrochemical impedance spectroscopy, as well as cathodic polarization scans, on as-received bulk AA5083-H131. The post-test solution utilized was a 0.6 M NaCl electrolyte from 100 h of galvanostatic test at 3 mA/cm^2 on a sensitized AA5083-H131 (DoS 50 mg/cm^2). The impedance spectra displayed as a Bode magnitude plot on Figure 3.20 show nominally the same solution resistance of 14.03 and 15.96 Ω-cm^2 at 100 kHz for the fresh and post-test solutions, respectively. This similarity in solution resistance implies that the diffusion of the dissolved cations into the bulk solution, formation of corrosion products, and ingress of the anions into the fissure tips across the 100 h of exposure time have minimal change on the bulk solution resistance. This is supported by the impedance spectra displayed as Bode magnitude plot in Figure 3.21 showing that there is little to no change in the solution resistance of the electrolyte after every 24 h galvanostatic hold at 1.5 mA/cm^2 of an AA5083-H131 DoS 22 mg/cm^2 specimen. Similar trend was also observed for observation taken using a highly sensitized specimen of 50 mg/cm^2. Figure 3.22 displays the almost

constant solution resistance of the electrolyte as a function of maximum IGC damage depth generated after different exposure times at 1.5 mA/cm^2, suggesting that the ohmic resistance is constant with increasing damage depth.
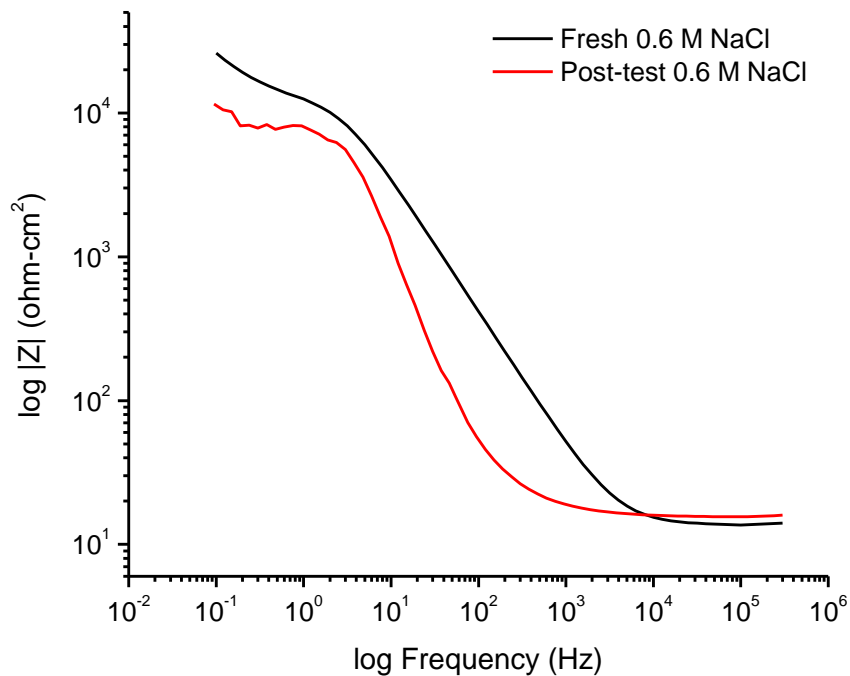
Figure 3.20. Electrochemical impedance Bode magnitude and phase plots of as-received AA5083-H131 exposed to fresh and post galvanostatic test (100 h) 0.6 M NaCl solution. Solution resistance is taken as the plateau at the high frequency range.
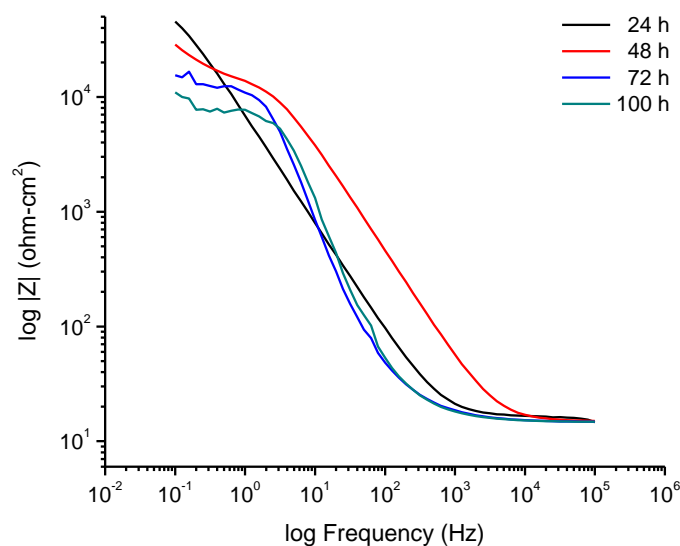
Figure 3.21. Electrochemical impedance Bode magnitude and phase plots of AA5083-H131 sensitized to 22 mg/cm^2 taken after every 24 h interval of galvanostatic hold at 1.5 mA/cm^2 in 0.6 M NaCl solution, pH 8.3. Solution resistance is taken as the plateau at the high frequency range.
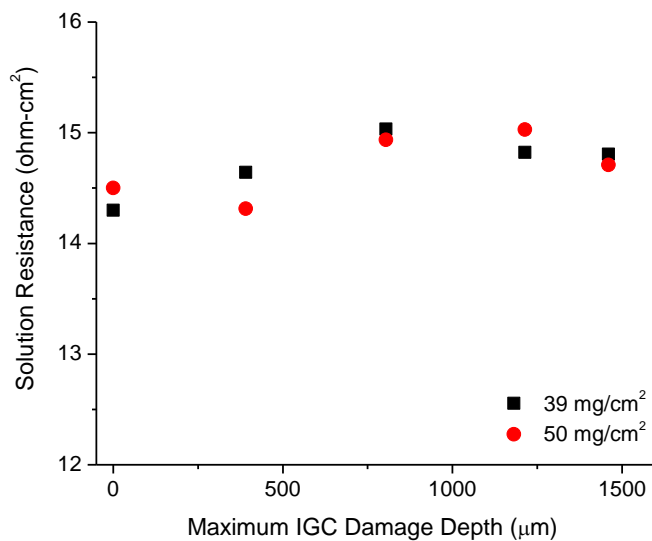
Figure 3.22. Solution resistance of electrolyte from high frequency EIS measurements (Figure 3.21) as a function of damage depth and sensitization for AA5083-H131. IGC damage depth corresponds to damage after 24 h, 48 h, 72 h, and 100 h of galvanostatic hold at 1.5 mA/cm^2 in 0.6 M NaCl solution, pH 8.3.

137
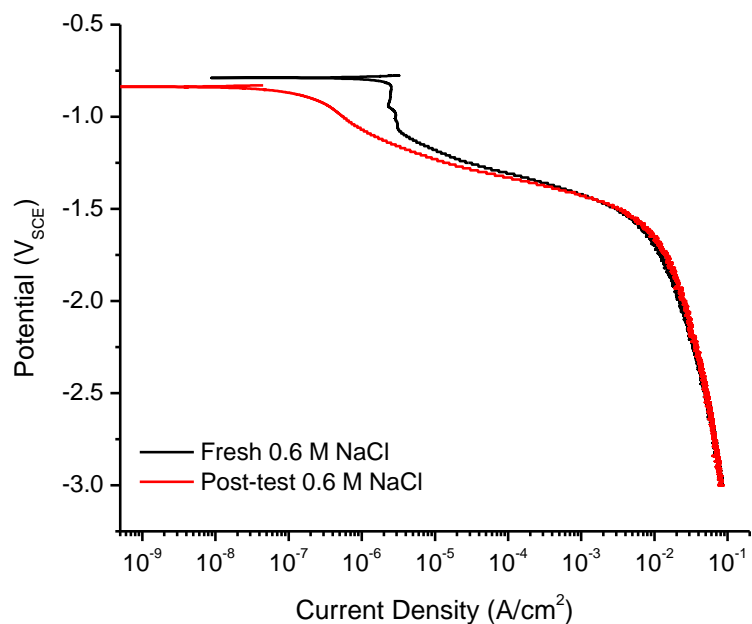
Figure 3.23. Cathodic polarization scans of as-received AA5083-H131 exposed to fresh and post galvanostatic test (100 h) 0.6 M NaCl solution. Potentiodynamic scans down to -3 V_{SCE} were conducted to obtain the ohmic control regime.
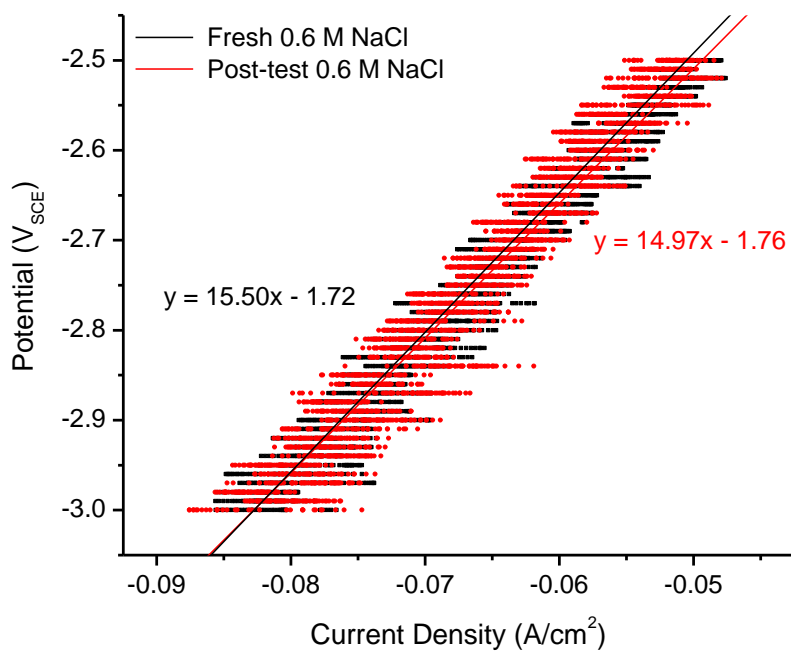
Figure 3.24. Linear plot of ohmic controlled regime from the cathodic polarization scans (Figure 3.23) of as-received AA5083-H131 exposed to fresh and post galvanostatic test (100 h) 0.6 M NaCl solution. Potentiodynamic scans down to -3 V_{SCE} were conducted to obtain ohmic control regime.

138

As a secondary check, the data from the ohmic regime of the cathodic polarization scans in Figure 3.23 were replotted in linear scale (Figure 3.24). Linear fitting of the data yield a solution resistance of 14.97 Ω-cm^2 for the fresh solution and 15.50 Ω-cm^2 for the post-test electrolyte, which is a good match with the EIS results.

3.6   Discussion

3.6.1   Constant and Accelerating Intergranular Corrosion Propagation Kinetics

In general, the IGC propagation kinetics observed for Al-Mg alloys across the range of DoS levels studied and amongst the three tempers is either constant or accelerating with time. This behavior is uncharacteristic of localized corrosion propagation kinetics, which usually follows a power law of the form $d = Kt^n$, where d is depth t is time, $0 < n < 1$, and K is a constant.[23,24,47–51] When $n < 1$, the reaction becomes slower with time, while $n > 1$ the reaction speeds up with respect to time. In theory, the ohmic potential drop associated with current flowing through the fissure solution of finite resistance decreases the potential at the fissure tip as the IGC propagates, which reduces dissolution rate and causes IGC stifling. However, the constant propagation rate with time suggests that the potential drop down the fissures is insignificant and does not vary with depth. It has to be noted that the IGC spreading on the surface allows for depth penetration to occur on multiple nearly parallel sites, subsequently causing simultaneous IGC propagation of multiple IGC fissures, and formation of IGC networks. The limited to no change

in solution resistance with increasing IGC damage depth (Figure 3.22) suggests that the multiple, interconnected IGC fissures provide a low resistance path between a given fissure tip and the external surface at any depth, resulting in minimal ohmic potential drop and constant IGC propagation rate with time (depth). This will be discussed in further detail in Chapter 4.

The case of accelerating IGC propagation kinetics with time (Figure 3.9) could be due to a combination of the minimal ohmic potential drop brought on by fissure interconnectedness and the development of a more aggressive fissure tip chemistry. The dissolution of β-phase precipitates generates metal cations, Al^{3+} and Mg^{2+} at the pit bottom or fissure tip. Hydrolysis of these cations produces local acidification and high chloride concentration within the fissure, decreasing the breakdown potential and increases the dissolution rate of β-phase, as well as triggering depassivation and dissolution of α-phase solid solution matrix. Assuming ohmic potential drop is negligible and constant with depth, the dissolution rate of both phases along the grain boundaries or the IGC propagation rate will only depend on fissure tip chemistry. At shorter times, the damage depths are shorter allowing cation to diffuse out of the fissure tip and stifling acidity. At longer times, the longer diffusive path as dictated by the damage depth aids in maintenance of the acidic chemistry, increasing dissolution rate and thereby accelerating IGC propagation kinetics.

These accelerating IGC propagation kinetics were only observed in alloys with DoS of 39 mg/cm^2 and above indicating the significance of grain boundary β-

phase distribution on the fissure tip chemistry development and the ensuing dissolution kinetics of the component phases thereafter. The amount and spacing of β-phase is important in terms of cation concentration, hydrolysis, and acidification. Although β-phase is the culprit for IGC, it was demonstrated that the α-phase dissolution is the rate controlling step in IGC propagation.[30] Stoichiometric dissolution of α-phase and β-phase would yield a 2 M Al^{3+} solution with Mg^{2+} concentrations of 0.09 M and 1.3 M respectively.[30] Measurements of solution pH for 2 M $AlCl_3$ in Figure 3.25 showed that addition of more than 0.1 M $MgCl_2$ caused a severe drop in pH. This suggests that β-phase dissolution triggers a local burst of acidification, which helps sustain the fissure tip pH and promotes α-phase dissolution. If the grain boundary β-phase coverage yet to dissolve on a propagating IGC fissure is high enough to yield and maintain fissure tip cation concentration and acidity in the face of the outward diffusion of the aggressive environment, then IGC propagation may progress at an accelerated rate. However maximum dissolution rate will be achieved at saturated cation concentration, such that IGC propagation rate no longer accelerates.
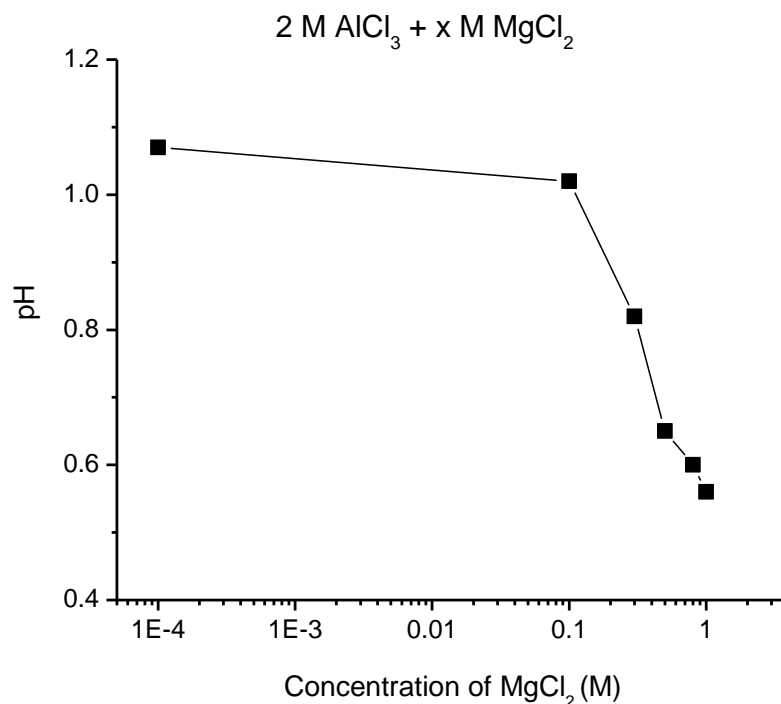
Figure 3.25. pH measurements for 2M AlCl₃ solutions with varying amounts of MgCl₂.

3.6.2   Intergranular Corrosion Growth Kinetics in Aluminum Alloys

Intergranular corrosion is a common phenomenon in several precipitation-hardened aluminum alloy systems. In Al-Cu-Mg (AA2XXX) systems, aging leads to precipitation of Cu-rich phases, which is cathodic to the Cu-depleted regions along the grain boundaries leading to IGC.[52–55] The IGC characteristics of Al-Zn-Mg-Cu (7XXX) systems, with the η-phase (Mg_2Zn) precipitation along the grain boundaries, are parallel to that of 5XXX.[25] In this case, the η-phase is more susceptible to corrosion than the Al-rich solid solution matrix. The η-phase composition and reactivity would be best considered for comparison with Al-Mg

of different sensitizations. As such, AA7XXX alloys with and without copper, or cases of aging differences on copper-bearing alloys are of particular interest. IGC growth rates in the form of power law were reported for both alloy systems.[24,49] Quantitative comparisons between these reported growth rates and the current results for Al-Mg are complicated by differences in critical variables including Cl$^-$ concentration, applied potential, quiescent vs. aerated environment, and exposure time as limited by foil penetration technique. Nevertheless, the comparisons of these growth rates will aid in further understanding of the qualitative role of the anodic phase on IGC propagation.

Intergranular corrosion damage for AA7075 (1.7 wt. % Cu) in different tempers, various orientation, at potentials above the breakdown potential, in aerated 1 M NaCl solution were measured using foil penetration technique.[49] Penetration times for specimens with various thickness were determined and inverted to get the damage depths of the fastest growing site as a function of time. Three temper conditions were considered: W (solutionized and water-quenched or underaged), T6 (peak aged), and T7 (overaged). Across the various tempers, at an applied potential of -0.725 V_{SCE}, growth rate is fastest in the L direction and slowest in the S direction, analogous with the current observations for Al-Mg, which is typical of rolled plates. Damage along the L direction showed that the W temper exhibited more uniform attack with matrix grain dissolution, whereas the T6 and T7 tempers had more localized corrosion morphology due to either the formation of the η-phase or the presence of Zn-depleted zones surrounding the grain boundaries.

Comparison of the growth rates show that the penetration is faster in the T6 temper as compared to the T7 temper, which is consistent with reports that the overaged condition is more resistant to corrosion than the peak aged condition.[20,46] This penetration rate difference can be attributed to the grain boundary distribution of the η-phase between the two tempers. Although this information was not reported for AA7075, a separate study by the same authors on AA7178 (1.95 wt. % Cu) revealed that the T6 temper have a high density of fine particles of η or η'-phase along the grain boundary, whereas T7 have widely spaced large η or η' phase particles.[23]

While the above observations on Al-Zn-Mg-Cu are analogous to the influence of grain boundary β-phase size and spacing on the IGC propagation rates in Al-Mg alloys, a direct quantitative comparison is limited due to the differences in grain boundary anodic phase morphology and distribution along the grain boundary, and the difference in dissolution reactivity due to electrochemical and chemical parameters. Characterization of grain boundary β-phase distribution suggested that as the sensitization time and temperature increases, the size of β-phase increases while the spacing between β-phase particles decreases.[3,17,20,22] This is not the case for AA7178, where both the size and the spacing of η-phase increase with aging temperature. However, the fact remains that the distribution, morphology, and size of the grain boundary anodic phase directly impacts the electrochemical IGC path, thereby influencing the overall IGC penetration kinetics in both alloy systems.

3.6.3 Electrochemical Kinetic Limitation of Anodic Dissolution in Sensitized AA5083

The linear relationship between the maximum IGC damage depth after 100 h of galvanostatic test and the applied potential suggest that IGC propagation is ohmically controlled (Figure 3.14). However, a Tafel relationship between the applied potential and the applied current densities suggests that the E-i behavior over the range of potentials covered are primarily charge transfer controlled (Figure 3.15). A current efficiency of 75% was measured for AA5083-H131, suggesting that the actual current for dissolution is greater than the apparent current measured (applied) and has to be corrected. Likewise, the apparent applied potential can be higher than the true interfacial potential due to ohmic resistance effects.

As discussed earlier, the total ohmic drop is the sum of the potential drop between the reference electrode and the electrode surface due to bulk solution resistance and the fissure ohmic drop. However, the linear IGC rate (over 100 h) dependence on potential suggested a fixed ohmic resistance between the reference electrode and the fissure tip, which does not change with time or depth. The constancy of rate with time implies that the potential drop down the fissures is negligible and relatively constant with depth. This lack of an increasing ohmic drop effect on rate is due to the presence of multiple, interconnected IGC fissures might lead to a low resistance path between any given fissure tip and the external electrode surface at any depth (Figure 3.22). Evaluation of the effective fissure tip resistance via computational analysis of resistor networks (Chapter 4) suggested for a 900 µm

fissure that was part of an interconnected IGC network in the form of an inverted Christmas tree would be < 3% of that of a single fissure of the same depth, resulting to ohmic drops of 3 mV or less.
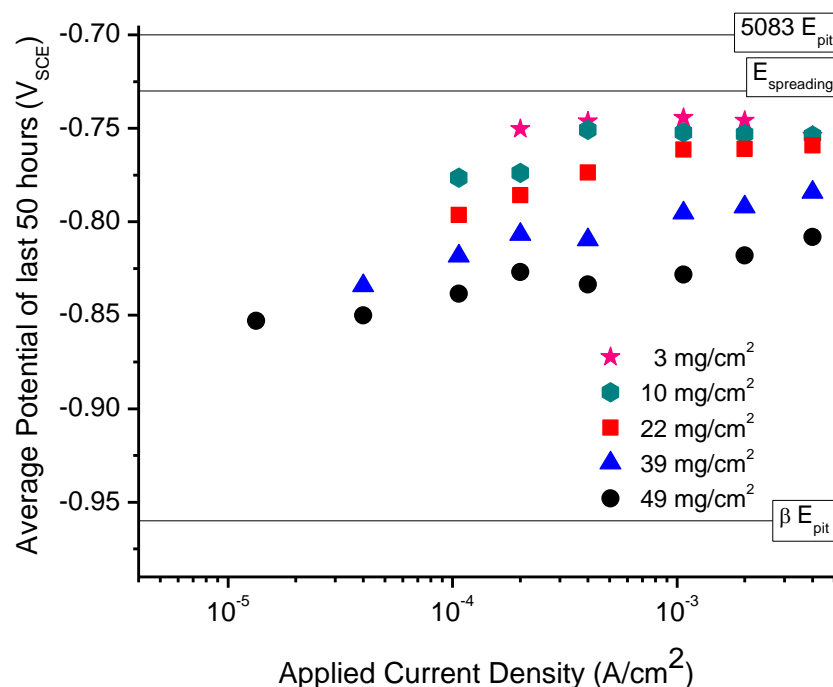
Figure 3.26. Ohmic potential drop (IR) and current efficiency corrected E-i curves for AA5083-H131 of various sensitization in 0.6 M NaCl solution, pH 8.3. IR correction was performed assuming a solution resistance of 15 Ω-cm^2.

Based on these observations, only the resistance between the reference electrode and the electrode surface was taken into consideration for true applied potential calculation. A 75% current efficiency factor for AA5083 and a 15 Ω-cm^2 resistance for 0.6 M NaCl solution were used to correct for the true E-i plot displayed in Figure 3.26. With the exception of the two highly sensitized conditions, the potentials were overcorrected at high current densities. While a lower resistance of 4 Ω-cm^2 (Figure 3.27) appears appropriate for the 10 mg/cm^2

condition, it undercorrected the higher sensitization levels. The reason behind the overcorrected potentials for the as-received condition is unclear, especially because the 15 Ω-cm^2 resistance was measured with an as-received AA5083-H131 electrode. In both cases, however, it is clear that the E-i curves follow a Tafel behavior, which implies that the electrochemical limitation of the anodic dissolution is a charge transfer process. This is assuming that the number of fissures is fixed or new new fissure is generated within the last 50 hours, such that the anode area does not increase with time. The limitations on the ability to accurately measure shallow IGC fissure (< 50 µm) leads to the observation of linear kinetics, with respect to potential, as the range of potentials of interest is narrow and the low rate tail, for which the nonlinearity is most obvious, is inaccessible.
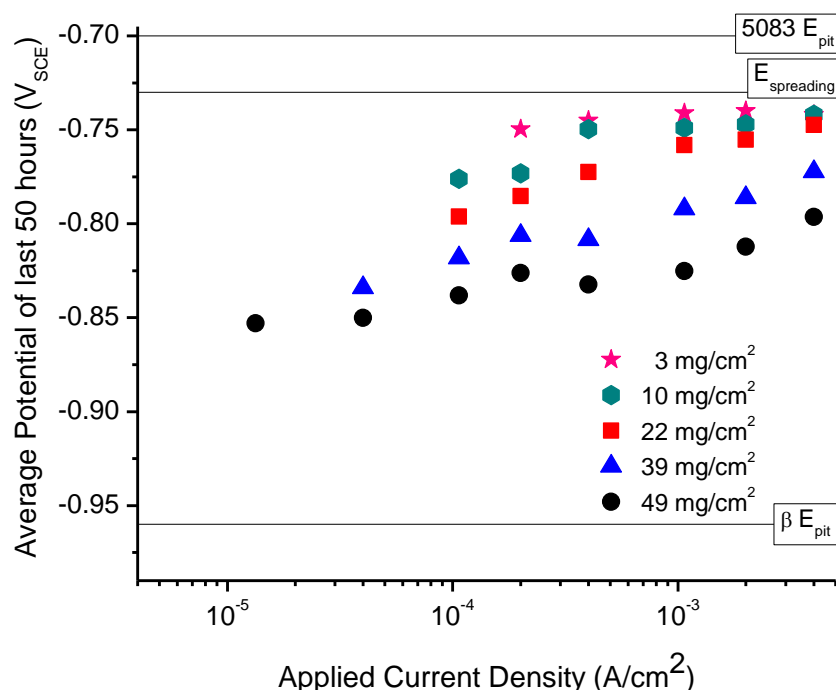
Figure 3.27. Ohmic potential drop (IR) and current efficiency corrected E-i curves for AA5083-H131 of various sensitization in 0.6 M NaCl solution, pH 8.3. IR correction was performed assuming a solution resistance of 4 Ω-cm^2.

3.6.4 Potential-Dependent Local Dissolution Behavior of Al-Mg Alloys as a Function of β-phase Coverage

Bumiller[30] modeled IGC penetration rates for AA5083 in bulk 0.6 M NaCl solution as a function of potential and grain boundary β-phase coverage as defined by DoS. The IGC penetration rate along β-phase decorated grain boundary was defined as a total rate equation of the dissolution of the α-matrix phase and the β-phase in series. The dissolution rates was based on the current densities obtained from anodic potentiodynamic scans of composite matrix α-phase and β-phases in quiescent simulated IGC fissure chemistries. Although the occluded chemistry in Al-Mg IGC fissures has not been directly measured, the fissure chemistry was considered to be bounded by the saturated solutions resulting from stoichiometric dissolution of each phase. For α-phase, the saturated solution composition was determined experimentally to be 3.11 M Al^{3+}, 0.14 M Mg^{2+}, 9.6 M Cl^- and will be referred to hereafter as the saturated Al-4Mg solution. For the β-phase, the saturated solution was 2.04 M Al^{3+}, 1.3 M Mg^{2+}, 8.8 M Cl^- and will be referred to hereafter as the saturated Al_3Mg_2 solution. The IR-corrected anodic polarization curves of α and β phases in an array of diluted saturated solutions of Al-4Mg and Al_3Mg_2 are shown in Figure 3.28 and Figure 3.29, respectively.
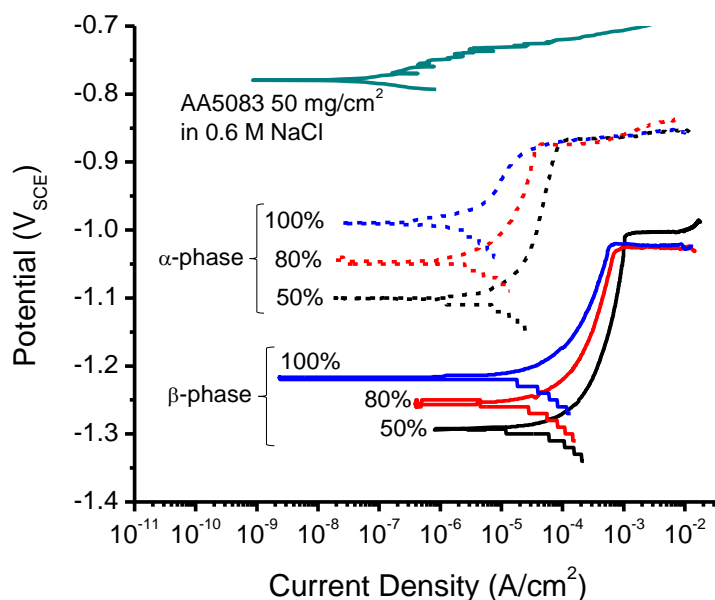
Figure 3.28. Anodic polarization curves of α (dashed lines) and β (solid lines) phases in Al-4Mg solutions with different saturation levels.[30] The range of potentials anodic to α and β phases in saturated solutions are cathodic to AA5083-H131 in 0.6 M NaCl solution as shown by the anodic polarization curve of a sensitized AA5083-H131 with DoS of 50 mg/cm^2 in 0.6 M NaCl solution.
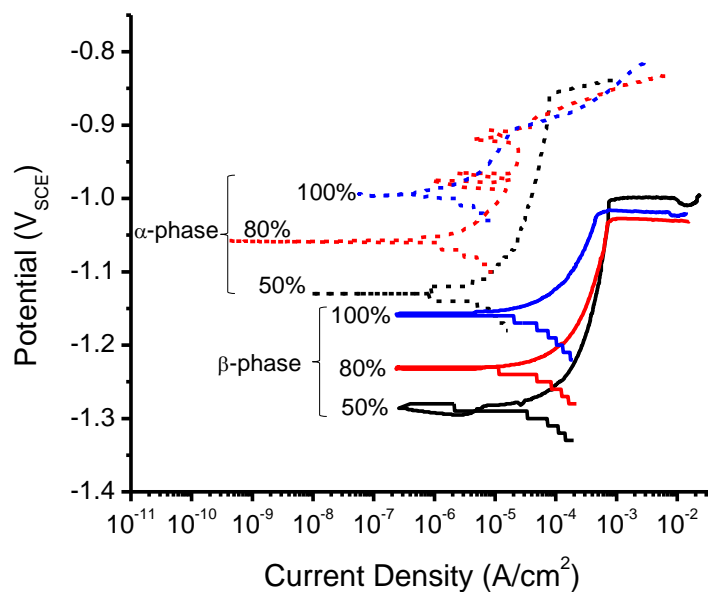
Figure 3.29. Anodic polarization curves of α (dashed lines) and β (solid lines) phases in Al$_3$Mg$_2$ solutions with different saturation levels.[30]

As mentioned earlier, the coverage of the β-phase on grain boundaries for AA5083-H131 has been broadly characterized.[7,8,17–20,22] However, by virtue of the characterization methods, coverage measurements are difficult to do with statistical confidence. The β-phase coverages (as a function of DoS) obtained pertain to averages over the limited number of fields of view of a given cross section with 2-dimensional lineal view of grain boundaries. Another aspect that is important is the connectivity and/or distribution of sufficiently sensitized grain boundaries, which is challenging to measure in 3-dimensions. Given that an IGC system is comprised of potential, fissure chemistry, IGC propagation growth rate, and β-phase coverage, knowledge of the first three components based on experimental data can be utilized to assess apparent β-phase coverage (θ_β) for the different DoS via comparison with predictions from the total rate equation for various θ_β values in the array of saturated chemistries.

In order to consider the high aspect ratios of length to width for IGC fissures, the propagation rate along the grain boundary must be in the order of 6 to 30 times the rate of dissolution of the fissure walls. Post-test, cross-sectional image analysis revealed that the IGC flank dissolution rate or fissure widening rate in AA5083 was between 0.1 and 0.6 nm/s, and an average rate of 0.47 nm/s, at -0.73 V_{SCE}. Considering the ohmic drop due to a bulk solution resistance of 15 Ω-cm^2, the average rate of 0.47 nm/s occurs at -0.784 V_{SCE}. As such, the measured dissolution rate of the α-phase at -0.784 V_{SCE} was divided by a factor to arrive at 0.47 nm/s. This factor was also utilized to correct the dissolution rates and to

generate the Tafel fit of the α-phase curves. The potential drop down the fissures was ignored, consistent with the observed constant IGC rate with fissure depth and constant effective resistance calculated from resistor network analysis. Additionally, it was assumed that the β-phase corroded under diffusion control at potentials above -0.9 V_{SCE}, using a critical pit stability product, i*x, of 0.07 A/cm (Chapter 5). Considering these assumptions, the IGC propagation rate as a function of β-phase coverage and potential was predicted using the total rate equation and dissolution rates of the individual phases in the array of Al_3Mg_2 and Al-4Mg solutions.

Figure 3.30 to Figure 3.33 show the predicted IGC propagation rates as a function of potential and θ_β in 100% and 80% saturated Al_3Mg_2 and Al-4Mg solutions. The predicted IGC propagation rates are consistent with the observations of the existence a critical potential below which no IGC occurs, the linear dependence of IGC rate with potential, and the high aspect ratios of IGC fissures. The high fissure aspect ratio is attributed to the large difference between the dissolution rates of α and β in the fissure chemistry. The dissolution of grain boundary β-phase occurs at high rate, extending the fissure length. While the dissolution of α-phase is much slower, leading to gradual corrosion of fissure flank and widening of fissures. The additional Mg^{2+} from β-phase dissolution increases the fissure chemistry aggressiveness, but only transiently as it would be overwhelmed by the larger area of α-phase.
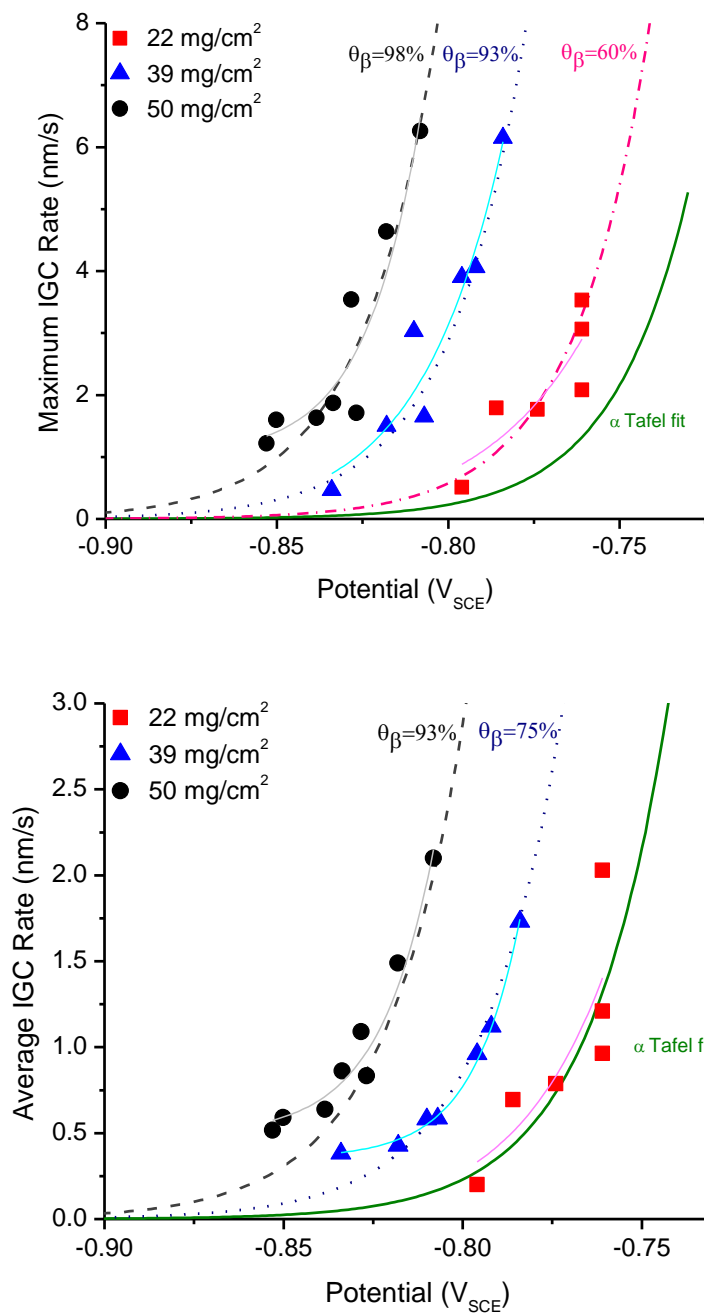
Figure 3.30. Maximum and average IGC propagation rates as a function of β-phase coverage and applied potential calculated using dissolution rate equation and the corresponding current density data from the α and β polarization curves in saturated Al-4Mg solution. The experimental IGC propagation rate data from galvanostatic testing and corresponding IR-corrected fissure tip potentials are plotted as symbols. Exponential fit of the experimental data are also presented in solid curves.
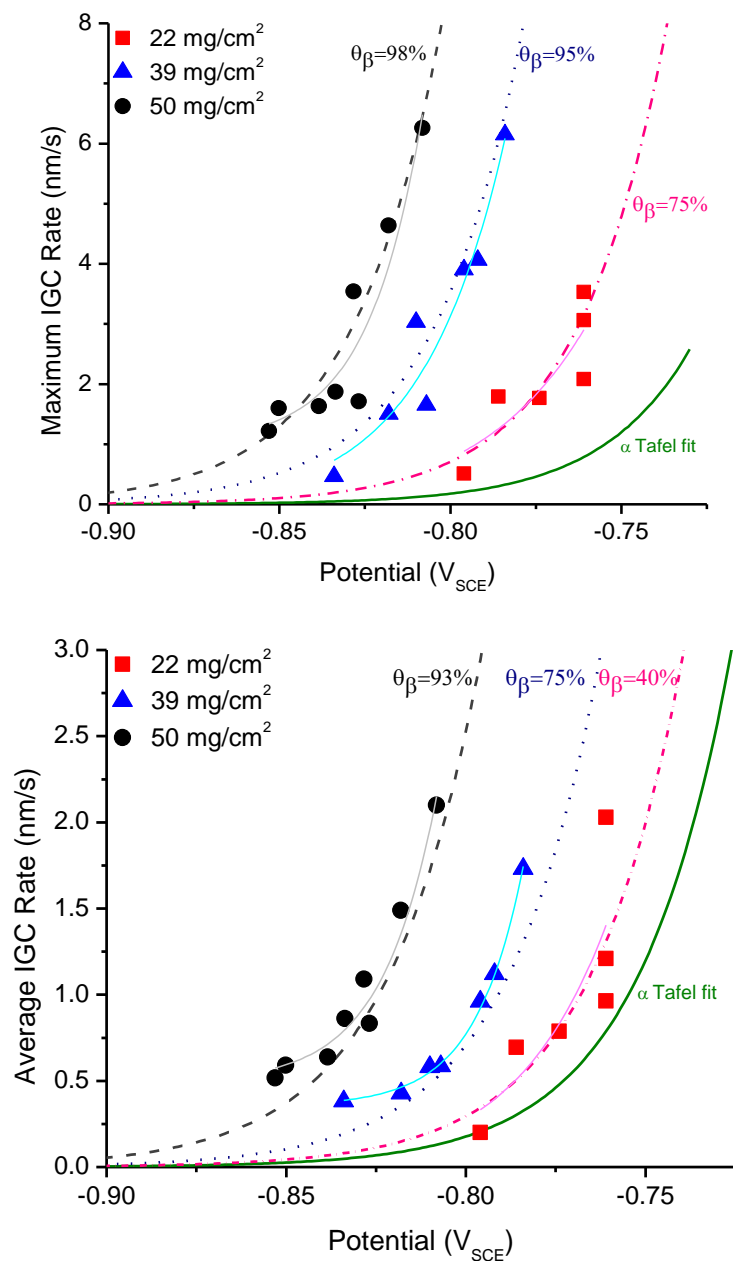
Figure 3.31. Maximum and average IGC propagation rates as a function of β-phase coverage and applied potential calculated using dissolution rate equation and the corresponding current density data from the α and β polarization curves in saturated Al_3Mg_2 solution. The experimental IGC propagation rate data from galvanostatic testing and corresponding IR-corrected fissure tip potentials are plotted as symbols. Exponential fit of the experimental data are also presented in solid curves.
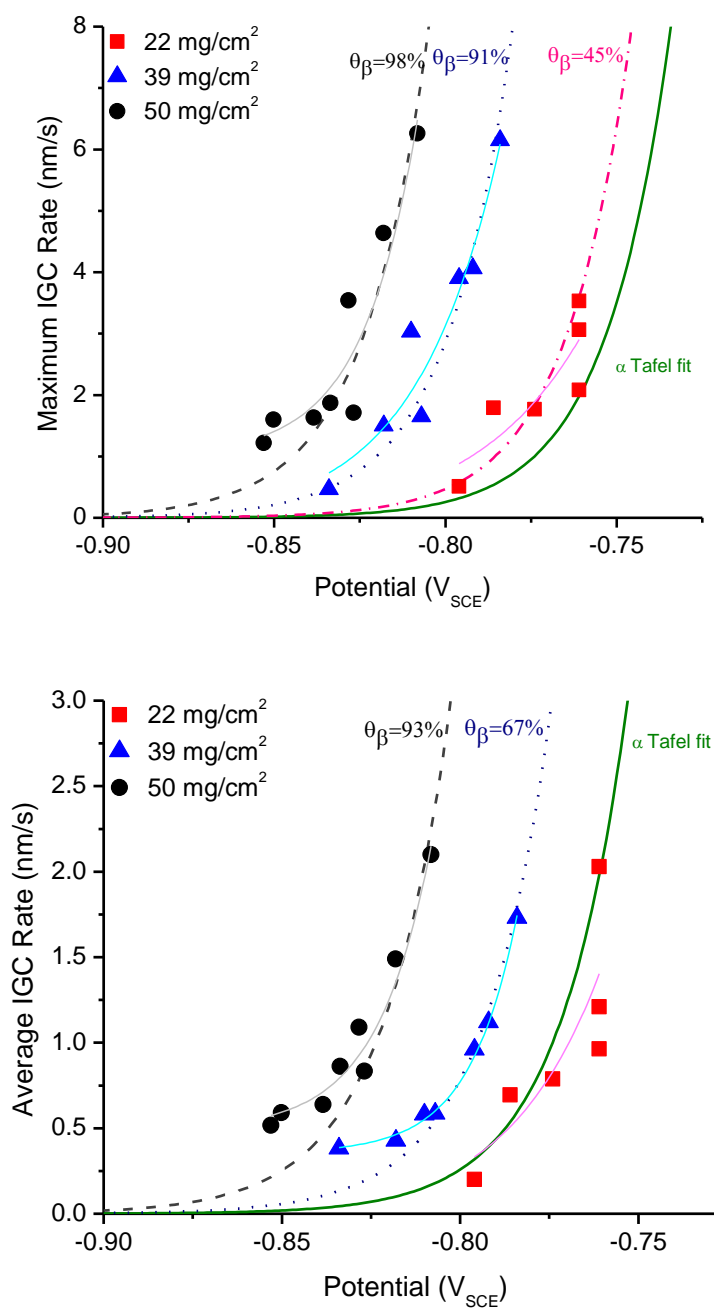
Figure 3.32. Maximum and average IGC propagation rates as a function of β-phase coverage and applied potential calculated using dissolution rate equation and the corresponding current density data from the α and β polarization curves in 80% saturated Al-4Mg solution. The experimental IGC propagation rate data from galvanostatic testing and corresponding IR-corrected fissure tip potentials are plotted as symbols. Exponential fit of the experimental data are also presented in solid curves.
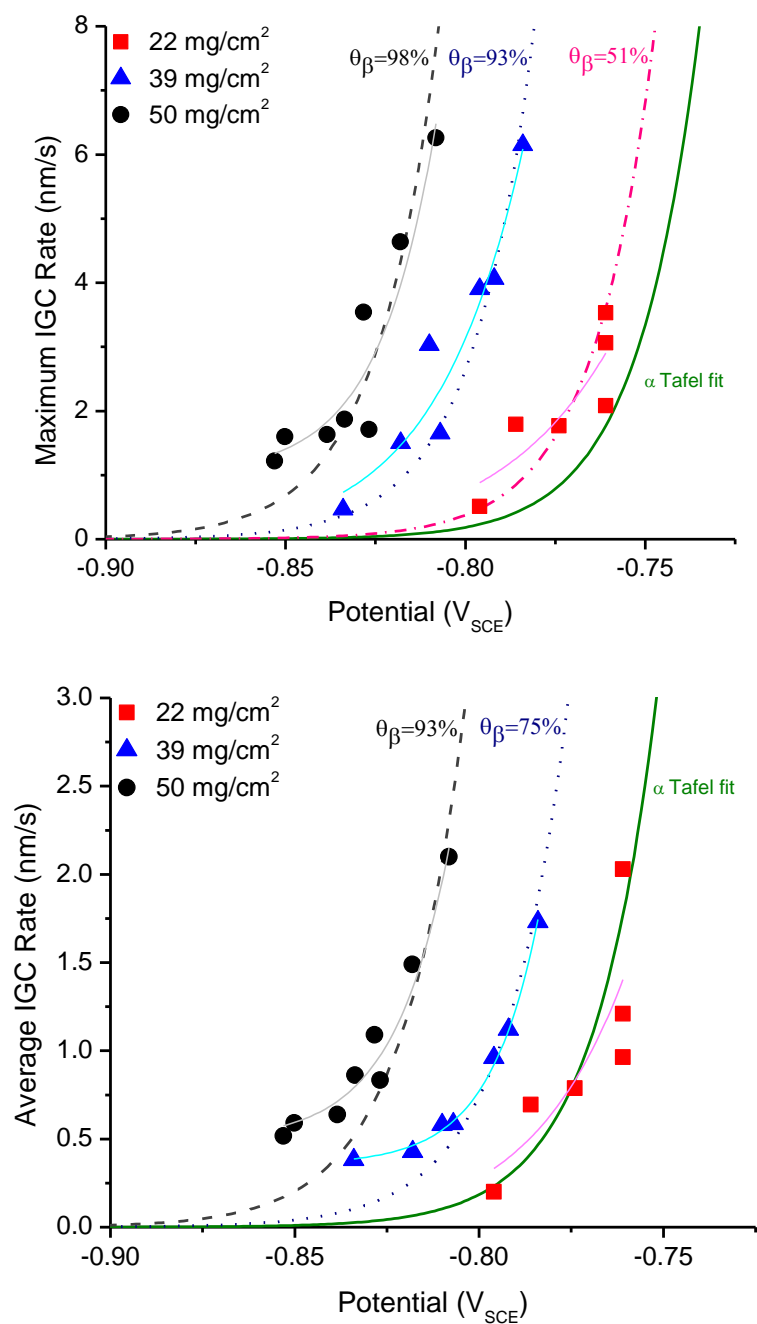
Figure 3.33. Maximum and average IGC propagation rates as a function of β-phase coverage and applied potential calculated using dissolution rate equation and the corresponding current density data from the α and β polarization curves in 80% saturated Al₃Mg₂ solution. The experimental IGC propagation rate data from galvanostatic testing and corresponding IR-corrected fissure tip potentials are plotted as symbols. Exponential fit of the experimental data are also presented in solid curves.

The fits of the rate equation to the measured maximum IGC rates and corresponding IR-corrected fissure tip potentials from the IGC susceptible materials (Figure 3.30 to Figure 3.33) demonstrate that the fissure chemistry can be composed of any of the four solutions, with small change in θ_β across the fissure chemistry for the high DoS material and still fit experimental trends. However, fitting the rate equation to the measured average IGC rates shows that the matrix dissolution alone was nearly as high as the DoS 22 rates in 80% saturated electrolytes and the saturated Al-4Mg (Figure 3.32). Thus, the assumption of a saturated or nearly saturated solution of Al-4Mg in majority of the fissures with a saturated solution Al_3Mg_2 at the fissure tip is the best fit for the three DoS that undergo IGC for both the average and maximum rates observed.

In the saturated Al_3Mg_2 environment, a set of connected grain boundaries with an average θ_β of 75% is required to rationalize the maximum rates observed for the DoS of 22 mg/cm^2, a θ_β of 95% for the DoS of 39 mg/cm^2, and a θ_β of 98% for the DoS of 50 mg/cm^2. These high values demonstrate the importance of the connectedness of susceptible grain boundaries that establish the most favorable single path. For the average rates, the DoS of 22 mg/cm^2 corresponds to a θ_β of 40%, the DoS of 39 mg/cm^2 corresponds to a θ_β of 70%, the DoS of 50 mg/cm^2 corresponds to a θ_β of 93%. Although in these cases, the connectivity of susceptible boundaries is less important than the maximum rate case, but is still significant. This is also consistent with observations that full coverage of β-phase precipitates is not a necessary condition for IGC in this alloy. Moreover, these predicted

effective β-phase coverage are reasonable as compared to the actual percentage of 27% and 52% of high β-phase coverage grain boundaries with physical coverage greater than 70% in AA5083 sensitized to 24 mg/cm^2 and 50 mg/cm^2, respectively.

3.6.5 Probable Basis for Threshold Potential

The existence of an IGC threshold potential was previously observed in galvanic corrosion of sensitized AA5083 coupled with steel,[29] as well as in IGSCC of AA5083.[31] It is evident that neither the IGC spreading potential nor the β-phase breakdown potential is the basis for this IGC threshold potential, as presented in Figure 3.14 and Figure 3.15. The observed E$_{crit}$ is believed to be due to the substantial decrease in α-phase dissolution with decreasing potential and to a lesser extent solution composition especially below -0.8 V$_{SCE}$ as defined by the pseudo-Tafel behavior. Bumiller[30] and Crane[31] recently proposed that this threshold potential is related to the breakdown potential of α phase in the fissure solution, 80 to 100 % saturated with Al-4wt% Mg (the α-phase solid solution composition), below which the α-phase is passive. At lower potentials, the system will not be able to maintain the acidity required to keep the fissure chemistry acidic, leading to an increase in pH and repassivation of the fissure.

Interestingly enough, the breakdown potential of α-phase in the fissure solution, -0.875 V$_{SCE}$, is near the range of IGC threshold potentials of -0.850 to -0.800 V$_{SCE}$.[30] Knowing that the grain boundaries are not fully covered with β to

form a continuous network, it would seem inevitable that during IGC penetration the exposed phase at the fissure tip or pit surface is the matrix α and not the β phase. For IGC propagation to continue, it is necessary that the applied potential be above the critical potential for α to enable breakdown of the passive film and dissolution of the α-phase. However, this can only be true if the local fissure chemistry is within the saturation levels stated in an Mg^{2+} enriched solution facilitated by an "effective" β-phase coverage above.

Because the grain boundaries is composed of ligaments of α-phase and β-phase, there is a continuous changing chemistry along the fissures as the IGC progresses. Galvele[56–58] postulated that pit stability requires a critical chemistry to develop at the pit surface, as characterized by the pit stability product, $i*x$, where i is the dissolution current density at the pit bottom, and x is the pit depth, which characterizes the diffusion length. When local pit stability product is below a critical value, the pit will cease to grow due to either the current being insufficient to maintain dissolution, or the diffusion distance being too short to sustain a critical pit chemistry. The IGC threshold could then be related to the potential at which the critical chemistry in the fissure cannot be sustained for a given β-phase coverage, especially since critical current densities were also observed (Figure 3.13). The true nature of the threshold potential, along with electrochemical criteria for stable IGC propagation is evaluation and discussed in detail in Chapter 5.

158

3.7   Conclusions

1. The partial IGC study involving the effect of cold work temper on sensitization
   revealed that:

   a. DoS does not vary significantly with tempers when exposed to the same
      sensitization heat treatment conditions.

   b. The IGC fissure morphologies of H116 and H131-SHT/Q tempers are short
      and wide, whereas those of H131 are long, sharp, and narrow.

   c. For the same DoS, the depth distribution after various periods of exposure
      times to 0.6 M NaCl solution at -0.73 V_{SCE} showed that H131 exhibited
      fastest IGC propagation kinetics, while H116 and H131-SHT/Q exhibited
      nominally the same kinetics.

2. The IGC propagation depth in AA5083-H131 exposed to 0.6 M NaCl solution
   depends linearly on potential. This potential dependence of IGC propagation
   increases with increasing DoS.

3. The true E-i behavior during IGC follows Tafel behavior and illuminates the
   constant IGC propagation rates with time (and depth).

4. A threshold potential (-0.85 to -0.8 V_{SCE}) exists where no IGC, but only pitting,
   was observed. This threshold potential was found to be more positive than the
   β breakdown potential, but more negative than the IGC spreading potential.

5. A saturated or nearly saturated solution of Al-4Mg in the majority of the fissure
   with a saturated solution of Al_3Mg_2 at the fissure tip provides the best fits for
   the IGC propagation rates of the sensitized AA5083-H131

6. Analysis using the total rate equation suggested effective grain boundary β-phase coverage and connectivity to justify the characteristic IGC propagation rates observed. The effective β-phase coverage explains the additional Mg^{2+} concentration required to maintain stable IGC propagation following Galvele's critical pit stability product. The predicted θ_β illustrated the significance of the connectedness of susceptible grain boundaries for a favorable IGC path.

3.8   References

[1]   G.C. Blaze, Alcoa Green Letter: The 5000 Series Alloys Suitable for Welded Structural Applications, Aluminum Corporation of America, New Kensington, PA, 1972.

[2]   I.N.A. Oguocha, O.J. Adigun, S. Yannacopoulos, Effect of sensitization heat treatment on properties of Al–Mg alloy AA5083-H116, J. Mater. Sci. 43 (2008) 4208–4214. doi:10.1007/s10853-008-2606-1.

[3]   R.L. Holtz, P.S. Pao, R.A. Bayles, T.M. Longazel, R. Goswami, Corrosion-Fatigue Behavior of Aluminum Alloy 5083-H131 Sensitized at 448 K (175 °C), Metall. Mater. Trans. A. 43 (2011) 2839–2849. doi:10.1007/s11661-011-0866-x.

[4]   A.J. Davenport, Y. Yuan, R. Ambat, B.J. Connolly, M. Strangwood, A. Afseth, et al., Intergranular Corrosion and Stress Corrosion Cracking of Sensitised AA5182, Mater. Sci. Forum. 519-521 (2006) 641–646. doi:10.4028/www.scientific.net/MSF.519-521.641.

[5]   J.L. Searles, P.I. Gouma, R.G. Buchheit, Stress corrosion cracking of sensitized AA5083 (Al-4.5Mg-1.0Mn), Metall. Mater. Trans. A. 32 (2001) 2859–2867. doi:10.1007/s11661-001-1036-3.

[6]   J.S. Vetrano, R.E. Williford, S.M. Bruemmer, R.H. Jones, Influence of microstructure and thermal history on the corrosion susceptibility of AA 5083, in: Alum. Alloys, Orlando, FL, 1997.

[7]   R. Goswami, G. Spanos, P.S. Pao, R.L. Holtz, Precipitation behavior of the ß phase in Al-5083, Mater. Sci. Eng. A. 527 (2010) 1089–1095. doi:10.1016/j.msea.2009.10.007.

[8]   R. Goswami, G. Spanos, P.S. Pao, R.L. Holtz, Microstructural Evolution and Stress Corrosion Cracking Behavior of Al-5083, Metall. Mater. Trans. A. 42 (2010) 348–355. doi:10.1007/s11661-010-0262-y.

[9]   H. Holroyd, G. Scamans, Environmental Degradation of Marine Aluminum Alloys - Past, Present and Future, Corrosion. (2015). doi:10.5006/1927.

[10]   L. Tan, T.R. Allen, Effect of thermomechanical treatment on the corrosion of AA5083, Corros. Sci. 52 (2010) 548–554. doi:10.1016/j.corsci.2009.10.013.

[11]   N. Birbilis, The influence of grain size and grain orientation on sensitisation in AA5083, Corrosion. (2015). doi:10.5006/1703.

[12]   A. P. Reynolds, J. Chrisfield, Use of Friction Stir Processing to Eliminate Sensitization in an Al-Mg Alloy, Corrosion. 68 (2012) 913–921. doi:10.5006/0632.

[13]   D.R. Baer, C.F. Windisch, M.H. Engelhard, M.J. Danielson, R.H. Jones, J.S. Vetrano, Influence of Mg on the corrosion of Al, J. Vac. Sci. Technol. A. 18 (2000) 131–136. doi:10.1116/1.582129.

[14]   R. K. Gupta, R. Zhang, C. H. J. Davies, N. Birbilis, Influence of Mg Content on the Sensitization and Corrosion of Al-xMg(-Mn) Alloys, Corrosion. 69 (2013) 1081–1087. doi:10.5006/0948.

[15]   G.M. Scamans, Low Temperature Sensitization of AA5XXX Alloys, Innoval, Oxon, UK, 2008.

[16]   N. Birbilis, R. Zhang, S. Knight, R. Holtz, R. Goswami, C. Davies, A Survey of Sensitisation in 5xxx series Aluminium Alloys, Corrosion. (2015). doi:10.5006/1787.

[17]   R. Goswami, R.L. Holtz, Transmission Electron Microscopic Investigations of Grain Boundary Beta Phase Precipitation in Al 5083 Aged at 373 K (100 °C), Metall. Mater. Trans. A. 44 (2012) 1279–1289. doi:10.1007/s11661-012-1166-9.

[18]   R.L. Holtz, P.S. Pao, R.A. Bayles, T.M. Longazel, R. Goswami, Corrosion
         Fatigue of Al 5083-H131 Sensitized at 70, 100, and 175°C relation to
         Microstructure and Degree of Sensitization, in: Dep. Def. Corros. Conf.,
         NACE, Palm Springs, CA, 2011.

[19]   S. Jain, M.L.C. Lim, J.L. Hudson, J.R. Scully, Spreading of intergranular
         corrosion on the surface of sensitized Al-4.4Mg alloys: A general finding,
         Corros. Sci. 59 (2012) 136–147. doi:10.1016/j.corsci.2012.02.018.

[20]   M.L.C. Lim, J.R. Scully, R.G. Kelly, Intergranular Corrosion Penetration
         in an Al-Mg Alloy as a Function of Electrochemical and Metallurgical
         Conditions, Corrosion. 69 (2013) 35–47. doi:10.5006/0722.

[21]   Y.-K. Yang, T. Allen, Direct visualization of β phase causing intergranular
         forms of corrosion in Al–Mg alloys, Mater. Charact. 80 (2013) 76–85.
         doi:10.1016/j.matchar.2013.03.014.

[22]   N. Birbilis, R. Zhang, M.L.C. Lim, R.K. Gupta, C.H.J. Davies, S.P.
         Lynch, et al., Quantification of Sensitization in AA5083-H131 via
         Imaging Ga-Embrittled Fracture Surfaces, Corrosion. 69 (2013) 396–402.
         doi:10.5006/0804.

[23]   T.-S. Huang, G.S. Frankel, Kinetics of sharp intergranular corrosion
         fissures in AA7178, Corros. Sci. 49 (2007) 858–876.
         doi:10.1016/j.corsci.2006.04.015.

[24]   W. Zhang, G.S. Frankel, Localized Corrosion Growth Kinetics in AA2024
         Alloys, J. Electrochem. Soc. 149 (2002) B510–B519.
         doi:10.1149/1.1513984.

[25]   S. Maitra, G.C. English, Mechanism of localized corrosion of 7075 alloy
         plate, Metall. Trans. A. 12 (1981) 535–541. doi:10.1007/BF02648553.

[26]   R.G. Buchheit, J.P. Moran, G.E. Stoner, Localized Corrosion Behavior of
         Alloy 2090—The Role of Microstructural Heterogeneity, Corrosion. 46
         (1990) 610–617. doi:10.5006/1.3585156.

[27]   I.L. Muller, J.R. Galvele, Pitting potential of high purity binary aluminium
         alloys—II. AlMg and AlZn alloys, Corros. Sci. 17 (1977) 995–1007.
         doi:10.1016/S0010-938X(77)80014-0.

[28]   I.L. Muller, J.R. Galvele, Pitting potential of high purity binary aluminium
         alloys—I. Al□Cu alloys. Pitting and intergranular corrosion, Corros. Sci.
         17 (1977) 179–193. doi:10.1016/0010-938X(77)90044-0.

[29]   D. Mizuno, R.G. Kelly, Galvanically Induced Intergranular Corrosion of
         AA5083-H131 Under Atmospheric Exposure Conditions: Part 1—
         Experimental Characterization, Corrosion. 69 (2013) 580–592.
         doi:10.5006/0812.

[30]   E. Bumiller, Intergranular corrosion in AA5XXX aluminum alloys with
         discontinuous precipitation at the grain boundaries, PhD Dissertation,
         University of Virginia, 2011.

[31]   C.B. Crane, Validation of the Coupled Dissolution-Hydrogen
         Embrittlement Mechanism of IGSCC in Low Temperature Sensitized
         AA5083-H131, PhD Dissertation, University of Virginia, 2013.

[32]   R. Howard, N. Bogh, D.S. Mackenzie, Heat Treating Processes and
         Equipment, in: G.E. Totten, D.S. Mackenzie (Eds.), Handb. Alum., Marcel
         Dekker, Inc., New York, NY, 2003.

[33]   R.J. Winsley, Corrosion resistance of heat-treated and friction stir welded
         AA5083-H116, MS Thesis, University of Birmingham, 2008.

[34]   ASTM, ASTM: G67-04 Standard Test Method for Determining the
         Susceptibility to Intergranular Corroaion of 5XXX Series Aluminum
         Alloys by Mass Loss After Exposure to Nitric Acid (NAMLT Test),
         ASTM International, West Conshocken, PA, 2004.

[35]   C. Crane, R. Gangloff, Stress Corrosion Cracking of Al-Mg Alloy 5083
         Sensitized at Low Temperature, Corrosion. (2015). doi:10.5006/1766.

[36]   N. Birbilis, C.H.J. Davies, S.P. Knight, H. Shi, Unpublished work, (2014).

[37]   Y. Yuan, Localized corrosion and stress corrosion cracking of aluminum-
         magnesium alloys, PhD Dissertation, University of Birmingham, 2005.

[38]   N. Birbilis, R.G. Buchheit, Electrochemical Characteristics of
         Intermetallic Phases in Aluminum Alloys - An Experimental Survey and
         Discussion, J. Electrochem. Soc. 152 (2005) B140–B151.
         doi:10.1149/1.1869984.

[39]   D.A. Jones, Principles and prevention of corrosion, CERN Doc. Serv.
         (1992). http://cds.cern.ch/record/245067 (accessed November 15, 2015).

[40]   R.C. Alkire, K.P. Wong, The corrosion of single pits on stainless steel in
         acidic chloride solution, Corros. Sci. 28 (1988) 411–421.
         doi:10.1016/0010-938X(88)90060-1.

[41]   D.W. Buzza, R.C. Alkire, Growth of Corrosion Pits on Pure Aluminum in 1M NaCl, J. Electrochem. Soc. 142 (1995) 1104–1111. doi:10.1149/1.2044137.

[42]   A.M. Lucente, J.R. Scully, Localized Corrosion of Al-Based Amorphous-Nanocrystalline Alloys with Solute-Lean Nanocrystals: Pit Stabilization, J. Electrochem. Soc. 155 (2008) C234–C243. doi:10.1149/1.2868764.

[43]   J.E. Sweitzer, J.R. Scully, R.A. Bley, J.W.P. Hsu, Nanocrystalline Al87Ni8.7 Y 4.3 and Al90Fe5Gd5 Alloys that Retain the Localized Corrosion Resistance of the Amorphous State, Electrochem. Solid-State Lett. 2 (1999) 267–270. doi:10.1149/1.1390807.

[44]   G.S. Frankel, A. Samaniego, N. Birbilis, Evolution of hydrogen at dissolving magnesium surfaces, Corros. Sci. 70 (2013) 104–111. doi:10.1016/j.corsci.2013.01.017.

[45]   J.A. Lyndon, R.K. Gupta, M.A. Gibson, N. Birbilis, Electrochemical behaviour of the β-phase intermetallic (Mg2Al3) as a function of pH as relevant to corrosion of aluminium–magnesium alloys, Corros. Sci. 70 (2013) 290–293. doi:10.1016/j.corsci.2012.12.022.

[46]   H.J. Pearson, G.T. Burstein, R.C. Newman, Resistance to Flow of Current to Scratched Electrodes, J. Electrochem. Soc. 128 (1981) 2297–2303. doi:10.1149/1.2127238.

[47]   W. Zhang, G.S. Frankel, Anisotropy of Localized Corrosion in AA2024-T3, Electrochem. Solid-State Lett. 3 (2000) 268–270. doi:10.1149/1.1391121.

[48]   T.-S. Huang, G.S. Frankel, Influence of grain structure on anisotropic localised corrosion kinetics of AA7xxx-T6 alloys, Corros. Eng. Sci. Technol. 41 (2006) 192–199. doi:10.1179/174327806X120739.

[49]   T.-S. Huang, G.S. Frankel, Effects of Temper and Potential on Localized Corrosion Kinetics of Aluminum Alloy 7075, Corrosion. 63 (2007) 731–743. doi:10.5006/1.3278422.

[50]   S. Zhao, D.A. Wolfe, T.-S. Huang, G.S. Frankel, Generalized model for IGC growth in aluminum alloys, J. Stat. Plan. Inference. 137 (2007) 2405–2412. doi:10.1016/j.jspi.2006.09.021.

[51]   X. He, J.J. Noël, D.W. Shoesmith, Crevice corrosion damage function for grade-2 titanium of iron content 0.078 wt% at 95 °C, Corros. Sci. 47 (2005) 1177–1195. doi:10.1016/j.corsci.2004.06.022.

[52]   K. Sugimoto, K. Hoshino, M. Kageyama, S. Kageyama, Y. Sawada, Stress corrosion cracking of aged Al☐4%Cu alloy in NaCl solution, Corros. Sci. 15 (1975) 709–720. doi:10.1016/0010-938X(75)90035-9.

[53]   K. Urushino, K. Sugimoto, Stress-corrosion cracking of aged Al☐Cu☐Mg alloys in NaCl solution, Corros. Sci. 19 (1979) 225–236. doi:10.1016/0010-938X(79)90008-8.

[54]   J.R. Galvele, S.M. de De Micheli, Mechanism of intergranular corrosion of Al-Cu alloys, Corros. Sci. 10 (1970) 795–807. doi:10.1016/S0010-938X(70)80003-8.

[55]   D.A. Little, B.J. Connolly, J.R. Scully, An electrochemical framework to explain the intergranular stress corrosion behavior in two Al–Cu–Mg–Ag alloys as a function of aging, Corros. Sci. 49 (2007) 347–372. doi:10.1016/j.corsci.2006.04.024.

[56]   J.R. Galvele, Transport Processes and the Mechanism of Pitting of Metals, J. Electrochem. Soc. 123 (1976) 464–474. doi:10.1149/1.2132857.

[57]   J. Galvele, Transport processes in passivity breakdown—II. Full hydrolysis of the metal ions, Corros. Sci. 21 (1981) 551–579. doi:10.1016/0010-938X(81)90009-3.

[58]   S.M. Gravano, J.R. Galvele, Transport processes in passivity breakdown—III. Full hydrolysis plus ion migration plus buffers, Corros. Sci. 24 (1984) 517–534. doi:10.1016/0010-938X(84)90034-9.

4 Understanding the Linear Intergranular Corrosion Propagation Kinetics with respect to Potential and Exposure Time

4.1 Abstract

The testable hypothesis for the linear intergranular corrosion (IGC) propagation kinetics with potential and depth in sensitized Al-Mg alloys in simulated marine environment was substantiated by electrochemical experiments and validated by computational resistor network analysis. The lack of a strong ohmic potential drop effect on the IGC kinetics was traced or linked to the multiple, interconnected fissures, which lead to a low resistance path between any given fissure tip and external surface at any depth. Electrochemical tests in 0.6 M NaCl solution were conducted on AA5083-H131 sensitized to 39 mg/cm^2 with three different geometries, which enabled variation in the degree of connectivity from one-dimensional to three-dimensional. The most severe and fastest IGC propagation rates were seen in the specimens with the three-dimensional degree of connectivity, where spreading on both lateral directions as well as propagation into the depth occurred while held at an applied potential of -0.73 V$_{SCE}$. The linear propagation kinetics were observed up to 192 h of exposure, and transitioned to power law kinetics at longer exposure times. The transition occurred at 100 h for specimens with two-dimensional degree of connectivity, whereas specimens with one-dimensional connectivity only exhibited power law kinetics, implying

resistance increase with penetration. Only power law kinetics was observed at an applied potential of -0.8 V_{SCE} for all the degrees of connectivity. The relationship between the IGC rates and potential for the three-dimensional degree of connectivity showed a single strong linear trend up to an exposure time of 192 h. For the one-dimensional and two-dimensional degree of connectivity, at exposure time of 100 h and longer, linear dependence of IGC rate on potential was also observed, with the dependence decreasing to a lesser extent with increasing exposure time due to increased ohmic resistance. The quantitative relationship of damage depth with time established via power law fitting suggested that the power law exponent n was primarily influenced by applied potential, with secondary effects from degree of connectivity.

4.2   Introduction

Localized corrosion propagation kinetics, typically conform to a power law relationship between damage length or depth and exposure time, $d = Kt^n$, where d is depth, t is time, $0 < n < 1$, and K is a constant.[1–9] When $n < 1$, the reaction becomes slower with time, while $n > 1$ the reaction speeds up with respect to time. In theory, the ohmic potential drop associated with current flowing through the fissure solution of finite resistance decreases the potential at the localized corrosion site as the corrosion propagates, which reduces dissolution rate and causes stifling. However, this behavior is not observed in the intergranular corrosion (IGC) propagation kinetics of non-heat-treatable Al-Mg alloys.[10–12]

167
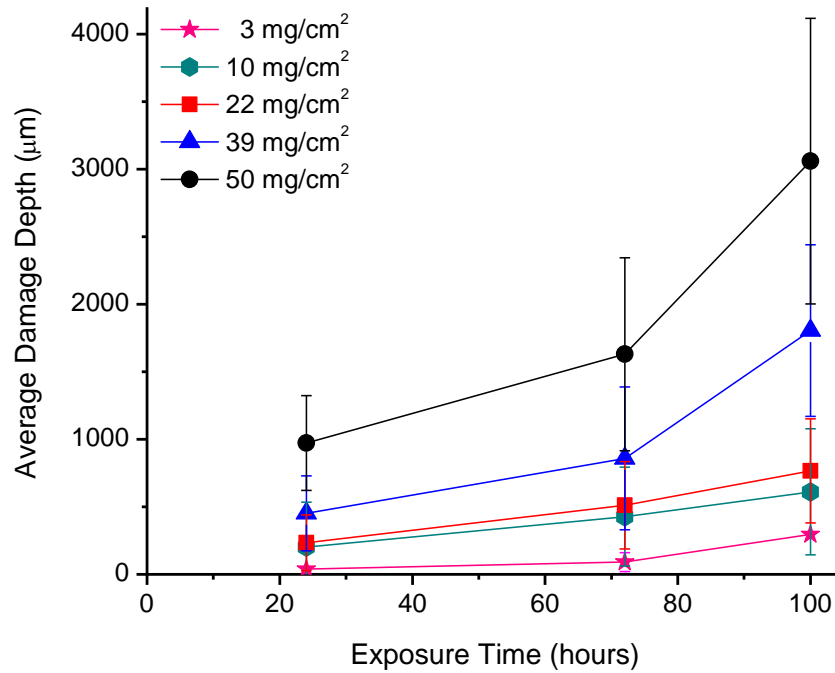
Figure 4.1. Average IGC damage depth in L direction as a funtion of DoS and exposure time for AA5083-H131 in 0.6 M NaCl solution, pH 8.3 at -0.73 V_{SCE}. Error bars represent 95% confidence interval.

Chapter 2 and Chapter 3 show that the intergranular corrosion (IGC) propagation kinetics observed for AA5083 across a range of degrees of sensitization (DoS) and amongst the three cold work tempers is either constant or accelerating with time (Figure 4.1). Stifling was not exhibited even after 100 h of exposure in IGC damage depth in the longitudinal (rolling) direction up to 3.6 mm in an AA5083-H131sensitized to DoS of 50 mg/cm^2. Moreover, Chapter 3 also indicates a strong linear relationship between both IGC propagation rate of AA5083-H131 and the applied potential (Figure 4.2). This linear potential dependence was also observed for maximum IGC damage depth in sensitized AA5083-H131 after 100 hours of galvanic coupling with 4340 steel.[10] This

linear dependence on potential implies a fixed ohmic resistance between the reference electrode and the fissure tip, which does not change with time. The constancy of propagation rate with time suggests that the potential drop down the fissures is negligible and relatively constant with depth. The most likely reason for such a lack of an increasing ohmic drop effect on rate is the presence of multiple, interconnected fissures leading to a low resistance path between any given fissure tip and external surface at any depth.
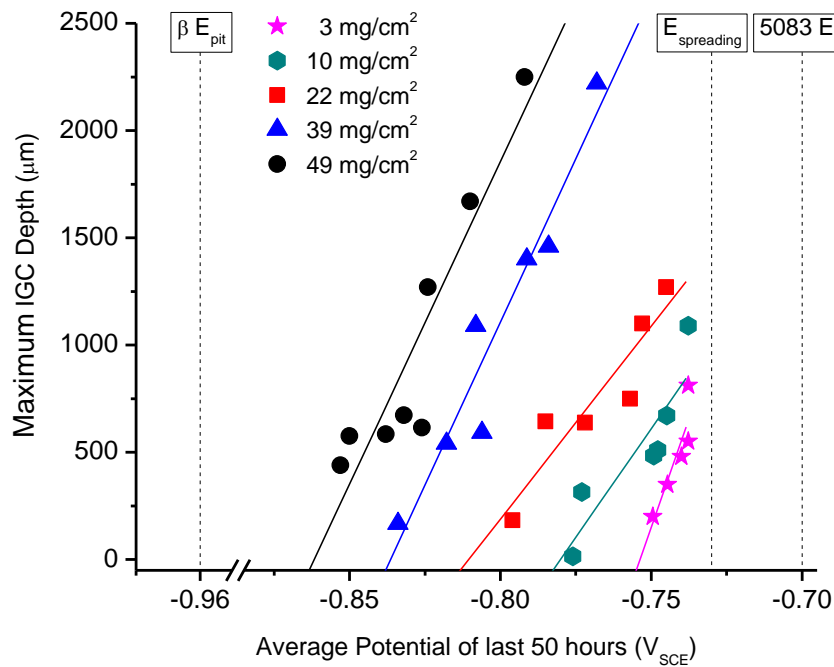
Figure 4.2. Maximum IGC depth in the L direction from fissure measurements as a function of average potential for various sensitized AA5083-H131 galvanostatically held for 100 h in 0.6 M NaCl solution at pH 8.3. The average potentials were taken from the last 50 hours. As a comparison, the IGC spreading potential for sensitized AA5083 and the pitting potential for unsensitized AA5083 (2 mg/cm^2) are marked with dashed lines.[10] Also, the open circuit potential of β-phase (not included in the figure) is -1.162 V_{SCE}.[17]

The intergranular corrosion spreading on the surface allows for depth penetration to occur on multiple parallel sites, subsequently causing simultaneous

propagation of multiple IGC fissures. These individual fissures can branch out directions perpendicular to penetration, eventually forming IGC networks. The extent of IGC network can be described in terms of the degree of connectivity. This degree of connectivity influences the extent of ohmic potential drop within the fissure depth, thereby affecting the dissolution kinetics at the fissure and thus IGC propagation kinetics. A hypothetical schematic of this notion, with each grain boundary segment acting as a resistor, for three different degrees of connectivity is presented in Figure 4.3. In a 1-dimensional degree of connectivity (Figure 17a), the grain boundary segments are connected in series, such that the effective resistance, R_{eff}, at the bottom of the fissure is equivalent to the sum of the individual resistances. For the cases of a 2-dimensional and a 3-dimensional degree of connectivity (Figure 4.3b and Figure 4.3c), IGC spreading along perpendicular grain paths enabled formation of an IGC network such that the grain boundary segments make up resistor networks involving connections both in series and in parallel. It is a known fact that resistors connected in parallel will always yield a lower effective resistance than resistors connected in series. As such, given the same depths or number of grain boundary layers in the penetration direction, but different degrees of connectivity, $R_{eff,1} > R_{eff,2} > R_{eff,3}$, where 1, 2 , and 3 refers to degree of connectivity. As the depth increases, $R_{eff,1}$ is expected to increase causing potential drop with depth. Due to spreading effects, $R_{eff,2}$ will increase but only to a certain extent, whereas the increase in $R_{eff,3}$ will be relatively small because the increase in resistance with depth is offset by the well-connected path. These effects

170

would enable linear ohmically controlled propagation rates. This testable hypothesis will be explored in this chapter by studying IGC at the same DoS with 1D, 2D, and 3D specimens enabling 1D, 2D, and 3D IGC paths.
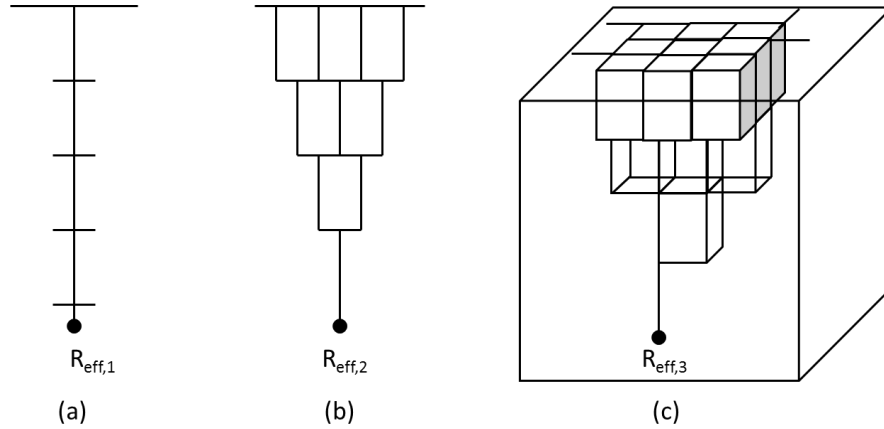
Figure 4.3. Hypothetical schematic of IGC network with different degrees of connectivity. (a) 1-dimensional, no surface IGC spreading results in a single fissure penetration; (b) 2-dimensional, limited surface and subsurface spreading results in penetration of multiple IGC fissures and formation of 2D IGC network; (3) 3-dimensional, surface and subsurface IGC spreading is not restricted and results in 3D IGC network.

4.3   Objective

The primary objective of this chapter is to understand the origins of the linear dependence of IGC propagation kinetics with potential for a given time (depth) of AA5083-H131 exposed to 0.6 M NaCl solution. First, the hypothesis regarding the effect of degree of connectivity on IGC is substantiated via intergranular corrosion propagation experiments and characterization on specimens with different geometries to elucidate the mechanism behind the linear kinetics. Second, the extent of the linear kinetics is investigated thorough long-term

electrochemical tests to probe the rate limitation of IGC propagation, and occurrence of IGC stifling, and to establish IGC propagation growth laws.

4.4   Experimental Procedures

4.4.1   Materials, Degree of Sensitization, and Specimen Geometry

The commercial AA5083 (UNS A95083) plates utilized in this work were provided by the Aluminum Company of America (Alcoa), in H131 temper with plate thickness of 2.25" (5.715 cm). In the H131 temper state, the AA5083 is strain hardened without supplementary thermal treatment to have a mean ultimate tensile strength (UTS) equivalent to three-eighths of the UTS of a full-hard condition (about 75% cold reduction after full annealing) for this alloy.[13] The nominal chemical composition of all AA5083 used in this study is presented in Table 4.1. The orientation convention and the microstructure of the three tempers showing anisotropic grains after Barker's etching are given in Figure 4.4. The average grain widths at the relevant mid-thickness location in the longitudinal (L), long transverse (T), and short transverse (S) directions is 80 µm, 60 µm, and 20 µm, respectively.

The specimens were cut from the center of the plate (S/2) into standard ASTM-G67[14] size of 5.1 cm x 2.5 cm x 0.6 cm (L x S x T) pieces, and were sensitized at 100°C for 14 days. Duplicate specimen was prepared in accordance with ASTM G-67 for measurement of DoS via the nitric acid mass loss test (NAMLT).[14] After immersing the specimens in 70% (v/v) HNO_3 for 24 h at 30°C, an average DoS of 39 mg/cm^2 was measured for this sensitization condition.

Table 4.1. Nominal composition of AA5083 (UNS A95083)

Component	Al	Mg	Mn	Fe	Si	Cu	Cr	Zn	Ti	Others
Weight %	Balance	4.4	0.7	0.22	0.1	0.05	0.08	0.02	0.02	< 0.01

Sensitized specimens with different geometries were cut from the center of the plate (S/2) into 6 mm x 6 mm x 6 mm 3D pieces, and 0.1 mm x 1 mm x 6 mm 2D thin foil pieces, in the T, S, and L directions, respectively. A third geometry in the form of a 112 µm diameter wire was prepared from the same AA5083-H131 plate through the Materials Preparation Center at Ames Laboratory, which is supported by the US DOE Basic Energy Sciences. The microstructure of the wire after Barker's etching of the wire surface and cross-section along the drawing direction is shown in Figure 4.5 The AA5083-H131 wire was also sensitized at 100°C for 14 days, adapting a DoS value of 39 mg/cm^2 from that of the bulk AA5083-H131 subjected to the same sensitization heat treatment condition.

The specimen geometries (cube, foil, and wire) considered had varying degrees of network connectivity. The limited number of grains on the wire surface (Figure 4.5) hindered lateral IGC spreading making the wire a case of 1-dimensional (1D) degree of connectivity in the penetration direction. In addition to penetration, the lateral IGC spreading limited in one direction created a 2-dimensional (2D) degree of connectivity for the thin foil. A case of 3-dimensional (3D) degree of connectivity existed in the cube where lateral IGC spreading occurred in both directions orthogonal to the penetration direction.
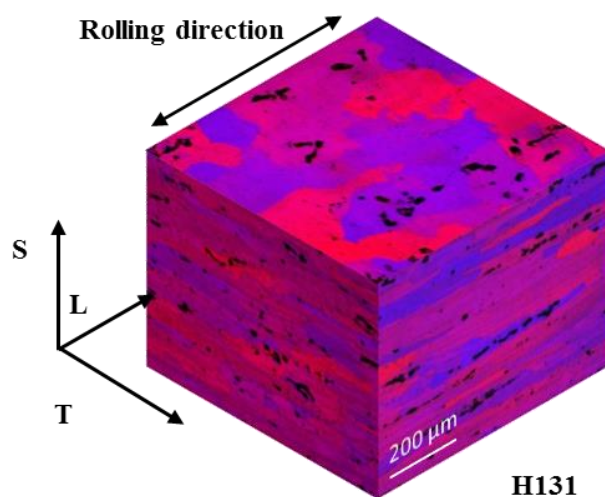
Figure 4.4. Microstructure of AA5083-H131 after electrolytic etching Barker's etching revealing elongated unrecrystallized grains.
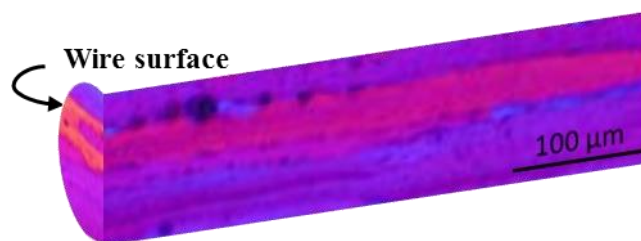
Figure 4.5. Microstructure of AA5083 wire after electrolytic etching Barker's etching revealing multiple elongated unrecrystallized across the wire diameter. The wire surface area of 9.852×10^{-5} cm^2 contains about 6 to 8 grains.

4.4.2   Sample Preparation for Electrochemical Testing

All samples were mounted in Buehler EpoThin epoxy resin with the exposed surface perpendicular to the longitudinal or drawing direction, and allowed to cure at room temperature (~25°C) for 9 h.   The mounted samples were alternatingly ground with SiC paper and rinsed with water down to 1200 grit. The samples were then polished with 1 μm diamond paste and finished with 0.06 μm

colloidal silica. Samples were ultrasonically cleaned in ethanol to remove any silica debris and air dried prior to testing.

4.4.3   Experimental Setup for Electrochemical Testing

A three-electrode cell setup, composed of a working electrode, a reference electrode and a counter electrode, was utilized for electrochemical testing. In all cases, a platinum mesh was utilized as the counter electrode. For the setup involving 3D planar and thin foil working electrodes, a saturated calomel electrode (SCE) equipped with a Luggin capillary was used as the reference electrode in a conventional flat cell setup. Whereas a vertical cell setup limiting possibility of trapped gas bubbles, and allowing a SCE reference electrode to be situated close enough to the working electrodes, was used for the wire specimens. This setup was connected to a potentiostat (PAR VersaStat, PAR 273, Gamry PCI4, or Biologic VMP 3) with an interface software to control and measure potential and current during DC electrochemical experiments. For experiments involving wire specimens, Gamry Femto-stat, Gamry Reference 600, and Biologic SP-200, which are capable of low current measurements, were utilized.

4.4.4   Characterization of Intergranular Corrosion Propagation Behavior

The intergranular corrosion behavior of sensitized AA5083-H131 was evaluated by conducting potentiostatic and galvanostatic holds in quiescent 0.6 M

NaCl solution at a pH of 8.3. The samples of different geometries were exposed to open circuit potential for 30 min and then either potentiostatically or galvanostatically held for various lengths of time. Three applied potentials (-0.73, -0.75, and -0.8 V_{SCE}), three applied current densities (1.5×10^{-3}, 8×10^{-4}, and 8×10^{-5} A/cm^2), and 6 exposure times (short-term 24, 72, and 100 h; and long-term 8, 20, and 40 days) were considered. The tests were performed on ST surfaces, allowing IGC to propagate in the L or drawing direction. Images of cross-sectioned samples were taken with the optical microscope to determine the maximum IGC damage depth.

4.4.5 X-ray Computed Tomography

Select post-electrochemical test AA5083-H131 specimens were characterized via X-ray tomographic analysis. The surface of the epoxy encapsulated specimen was sealed off with a layer of fast-setting adhesive, and the perimeter of the epoxy resin was reduced by grinding. This procedure was performed in order to improve the signal to noise ratio, by reducing the absorption contribution from the resin relative to the AA5083-H131 specimen. The specimens were characterized using a chromatic beam at 80 kV and 8 Watts. A 2x objective lens with an approximately 4 mm field of view was used for all assessments. The data were binned (2 x2) during acquisition, and a total number of 2000 projections was recorded over an 182° rotation. Exposure times of 30 seconds per projection

176

were chosen. A filtered back projection algorithm was used for 3D volume reconstruction, with the data corrected for center-shift and beam hardening.

Visualization, segmentation, and analysis of the data was carried out using Avizo Fire. The 3D rendered volume was resliced perpendicular to the longitudinal or depth propagation direction at a 5 µm interval in a stack of images. Image analysis was conducted on each slice to determine the percentage of area corroded as a function of depth. The maximum IGC was characterized as the deepest depth (or slice) at which corrosion was detected.

4.5   Results

4.5.1   Effect of Degree of Connectivity of Multiple Intergranular Paths on Damage Depth as Elucidated by Specimen Geometry

The influence of degree of connectivity on IGC propagation kinetics of a sensitized AA5083-H131 with a DoS of 39 mg/cm^2 was examined via potentiostatic holds for various periods of time on specimens with varying geometries. The typical current density behavior of the three geometries during a short-term (24 h to 100 h) potentiostatic hold at -0.73 V_{SCE} in 0.6 M NaCl solution at pH 8.3 is shown in Figure 4.6. The current density behavior of the 1D wire specimen is characteristic of a microelectrode response with three stages: the initial current density rise as pits form and stabilize, the active dissolution at high current density (and decay), and the steady-state dissolution at low current density. The current density behavior of the 2D foil specimen only exhibited the first two stages,

177

while the 3D planar surface specimen had an incubation period to reach the steady state current density. The maximum IGC damage depths were characterized via cross-section image analysis as well as via x-ray computed tomography (XCT).
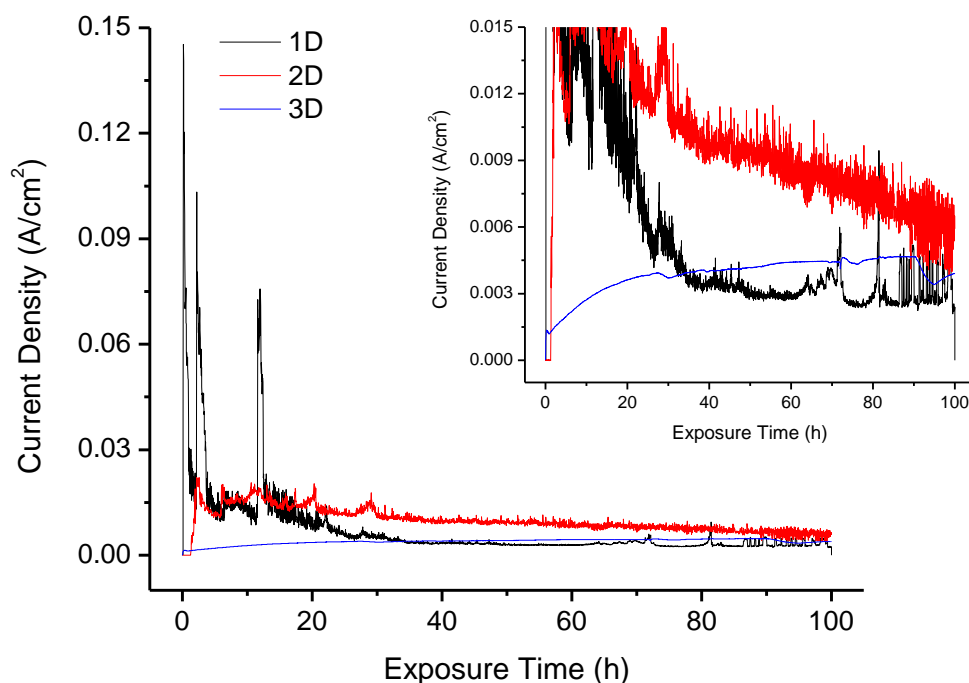
Figure 4.6. Measured anodic current density as a function of exposure time and specimen geometry (degree of connectivity) of AA5083-H131 sensitized to 39 mg/cm^2 at an applied potential of -0.73 V$_{SCE}$ in 0.6 M NaCl solution, pH 8.3. Anodic current densities in the range of 0.003 to 0.006 A/cm^2 were observed as shown in the inset image. The respective specimen surface areas were utlized to normalized the current. The surface areas for the 1D wire, 2D foil, and 3D planar specimen are 9.852 x 10^{-5} cm^2, 1 x 10^{-3} cm^2, and 0.36 cm^2, respectively.
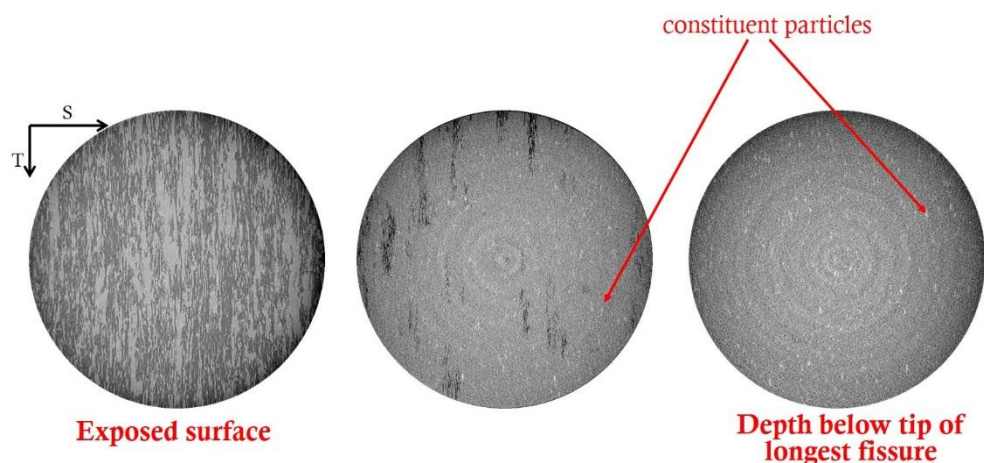
Figure 4.7. Examples of 2D reconstructed tomographic ST surface slices showing (a) exposed, (b) at depth less than maximum fissure, and (c) at depth below maximum fissure of AA5083-H131 sensitized to 39 mg/cm^2 (3D planar surface) and exposed to 0.6 M NaCl solution, pH 8.3 at -0.73 V$_{SCE}$ for 72 h. The dark regions are corroded areas, showing IGC as the mode of attack; whereas the white specs are constituent particles inherent to the alloy.
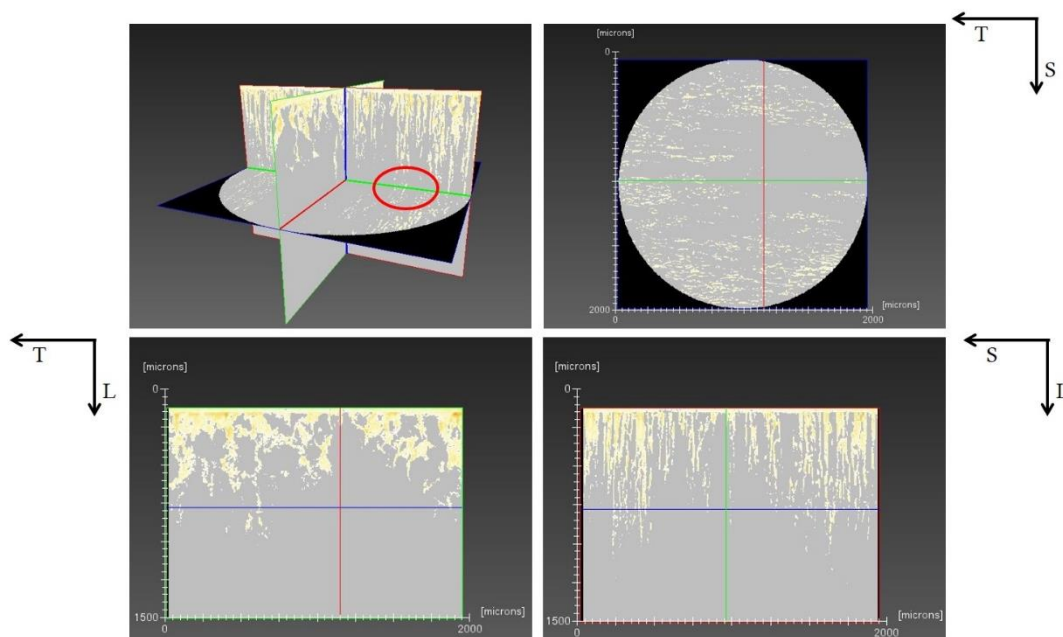
Figure 4.8. Examples of 2D orthogonal views of IGC damage in AA5083-H131 sensitized to 39 mg/cm^2 (3D planar surface) and exposed to 0.6 M NaCl solution, pH 8.3 at -0.73 V$_{SCE}$ for 72 h from three different directions on three different surfaces. The gray regions are not corroded, whereas the yellow regions are the corroded areas, which conforms to the microstructure anisotropy of grains.

179

Figure 4.7 exhibits examples of 2D reconstructed tomographic slices for a 72 h potentiostatic hold at -0.73 V_{SCE} of a 3D planar surface specimen. Figure 4.7a shows a slice of the exposed surface, where the dark regions are the corroded areas, evident that the mode of attack is IGC. Figure 4.7b shows a slice of the ST surface several hundreds of micrometers below the exposed surface, while the Figure 4.7c is from a depth below the tip of the longest fissure observed in this specimen. In addition to detecting IGC, other interior features such as constituent particles that are inherent to the alloy are also revealed through the XCT. The IGC damage from the three different directions on the three different surfaces are displayed in Figure 4.8. The yellow regions are the corroded areas whereas the gray regions are not corroded. These damage morphologies captured by the XCT are truly IGC as the fissures follow the microstructure anisotropy, where grain widths are shorter in the S directions relative to the L and T directions, as evident in the ST and SL damage surfaces. The 2D rendered orthogonal slices shows minimal grain fall-out after 72 h of exposure as evident by the straight edges of the 2D slices. This is however not the case for the 2D foil (Figure 4.9), which showed a tremendous amount of grain fall-out and crevice corrosion on the specimen perimeter. The increased amount of grain fall-out is expected given that the average grain width in the T direction is 60 µm and the foil thickness is only 100 µm in this direction. Although anodic dissolution of both the limited grain boundaries as well as the α-matrix was observed in the 1D wire (Figure 4.9), the corrosion is not uniform through the depth.

180

This case of surface roughening is commonly observed in aluminum microelectrodes, especially on wires with diameters greater than 25 µm.[15]

Planar surface (3D)   **thin foil (2D)**   **wire (1D)**
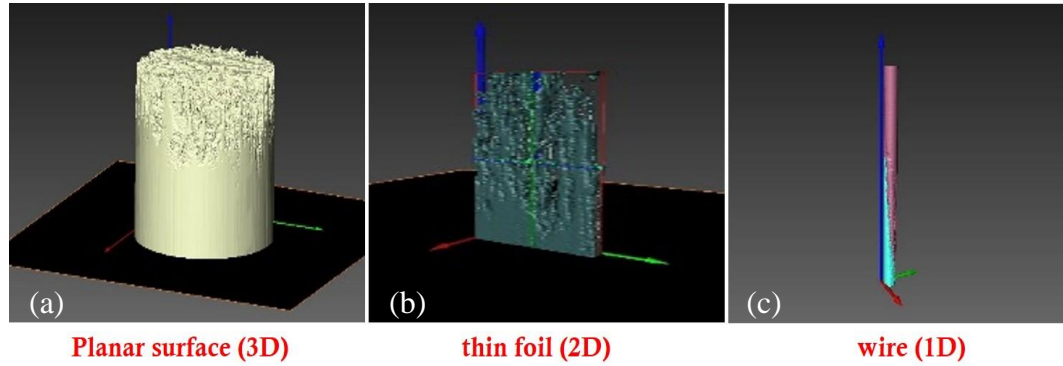
Figure 4.9. 3D reconstructed tomographic volumes of AA5083-H131 sensitized to 39 mg/cm^2 and exposed to 0.6 M NaCl solution, pH 8.3 at -0.73 V$_{SCE}$. (a) 3D planar surface exposed for 100 h, (b) 2D thin foil exposed for 24 h, and (c) 1D wire exposed for 24 h. Note the difference in magnification of the tomographic volumes.
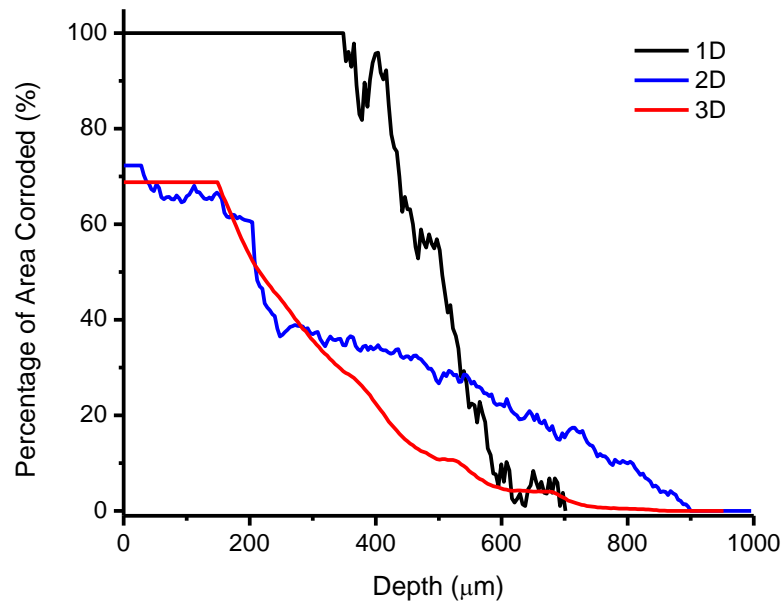
Figure 4.10. Percentage of area corroded (ST surface) after 100 h of exposure as a function of specimen depth (L direction) and degree of connectivity for AA5083-H131 sensitized to 39 mg/cm^2 and exposed to 0.6M NaCl solution, pH 8.3 at -0.73V$_{SCE}$.

181

To characterize IGC depth, the percentage of area corroded for each 2D reconstructed tomographic slice across the depth was analyzed. The percentage of area corroded as a function of depth for the three geometries in Figure 4.10 shows that only the 1D wire exhibited 100% area corroded, which occurred down to a depth of 348.5 µm. The maximum percentage of area corroded for the 2D foil and the 3D planar surface is 72 and 69, respectively. Although these numbers may appear to be nominally the same, it has to be recognized that the surface areas of these two specimens were very different. The 2D foil had a surface area of 1×10^5 µm^2, containing approximately 83 grains, whereas the 3D planar surface was 9×10^6 µm^2 with 7500 grains. Given the minimal grain fall-out observed on the 3D planar surface, it can then be inferred that IGC spreading was prevalent on the surface. Additionally, this implies that the decrease in percentage of area corroded with depth for the 2D foil can be attributed primarily to the reduced grain-fall out with IGC propagation. In contrast, for the case of the 3D planar surface, this decrease meant reduction in IGC spreading with depth.
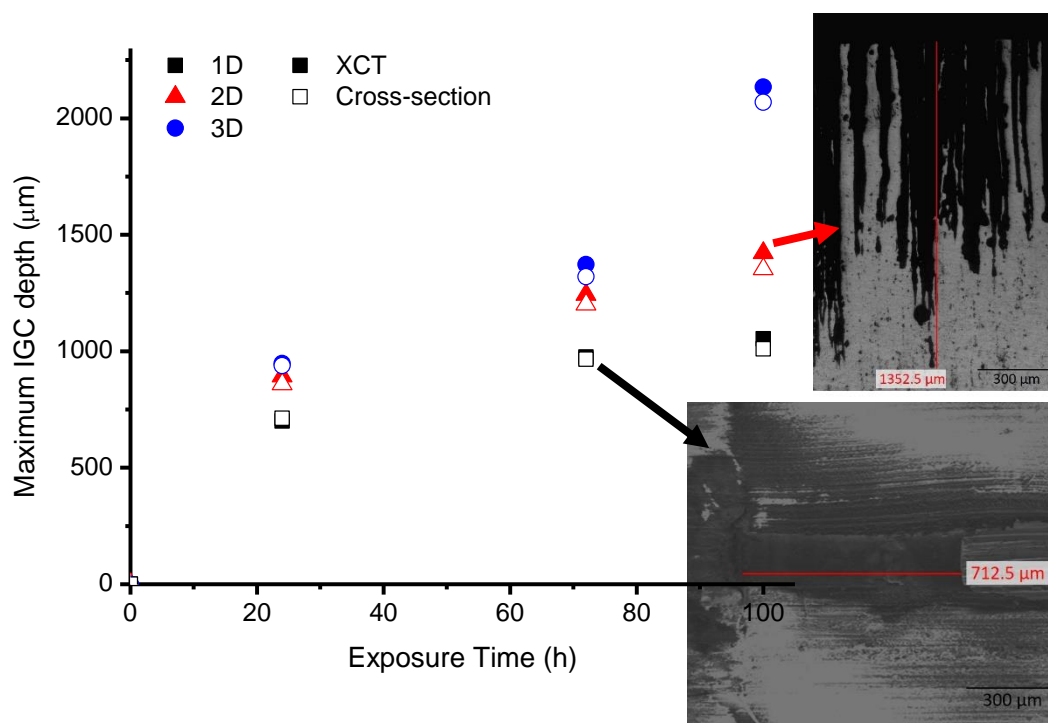
Figure 4.11. Maximum IGC depth (L direction) as a function of exposure time and degree of connectivity for AA5083-H131 sensitized to 39 mg/cm^2 and exposed to 0.6 M NaCl solution, pH 8.3, at -0.73 V$_{SCE}$. Damage depths were taken from corroded area analysis of 2D tomographic slices and cross-section optical micrograph image analysis. Cross section optical micrographs showing IGC depth penetration in the L direction in thin foil (top) and wire (bottom).

The maximum IGC depth is taken as the depth at which zero percent corrosion or no corrosion was observed. This depth is determined to be 972.5 µm, 1243.4 µm, and 1372.8 µm for the 1D wire, 2D foil, and 3D planar surface specimens, respectively.   These maximum IGC depths are in agreement with measurements determined from cross-section image analysis as shown in Figure 4.11. This implies that the maximum damage depths obtained through cross-section is a reliable representation of the real maximum IGC depth.   For all exposure times, a trend of increasing maximum damage depth with the

183

dimensionality of the specimen geometry was observed. It is also evident that while propagation progresses linearly with time in the 3D planar surface specimen, IGC propagation stifling was observed in the 2D foil and 1D wire specimens. This behavior suggests that the degree of connectivity of the IGC path as established by the different sample geometries influences the IGC damage progression. IGC stifling is related to the ohmic potential drop associated with current flowing through the fissure solution of finite resistance decreasing the potential at the fissure tip as the IGC propagates. It is then hypothesized that the degree of connectivity governs the effective resistance at the fissure tip, subsequently influencing the extent of ohmic potential drop within the fissure depth. The drop in potential at the fissure tip affects the dissolution kinetics at the fissure, thereby influencing IGC propagation kinetics. The effect on the dissolution kinetics is also manifested in the current density behavior during potentiostatic hold (Figure 4.6), wherein the current densities decreased with exposure time for the 1D wire and 2D foil, while the steady-state current density was maintained for the 3D planar surface throughout the 100 h exposure.
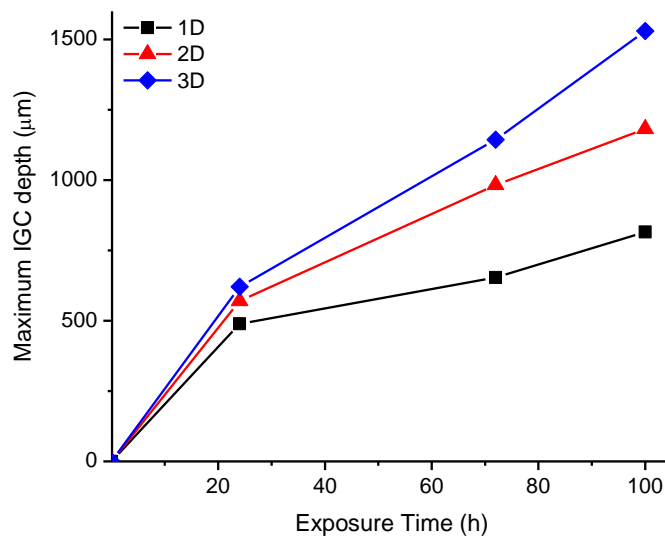
Figure 4.12. Maximum IGC damage depth from fissure measurements in L direction propagating from ST surface as a funtion of degree of connectivity and exposure time for AA5083-H131 sensitized to 39 mg/cm^2 in 0.6 M NaCl solution, pH 8.3 at -0.75 V$_{SCE}$.

To establish if this behavior holds true at applied potentials lower than the spreading potential of -0.73 V$_{SCE}$, potentiostatic holds at -0.75 V$_{SCE}$ and -0.80 V$_{SCE}$ were conducted. The IGC damage depth in AA5083-H131 sensitized to 39 mg/cm^2 and exposed in 0.6 M NaCl solution with pH 8.3 held at -0.75 V$_{SCE}$ as a function of exposure time and specimen geometry is shown in Figure 4.12. As expected, the measured damage depths after exposures at -0.75 V$_{SCE}$ were lower than those held at -0.73 V$_{SCE}$ (Figure 4.12). The 3D planar surface demonstrated linear kinetics, while IGC stifling was apparent in the other two geometries. It is important to note that although -0.75 V$_{SCE}$ is lower than the spreading potential, given enough time IGC spreading and propagation does occur at this potential. Similar trend of increasing damage depth with exposure time for all three

185

geometries were observed, with the propagation in the 1D wire slowest, followed by that in the 2D foil, and fastest in the 3D planar surface.
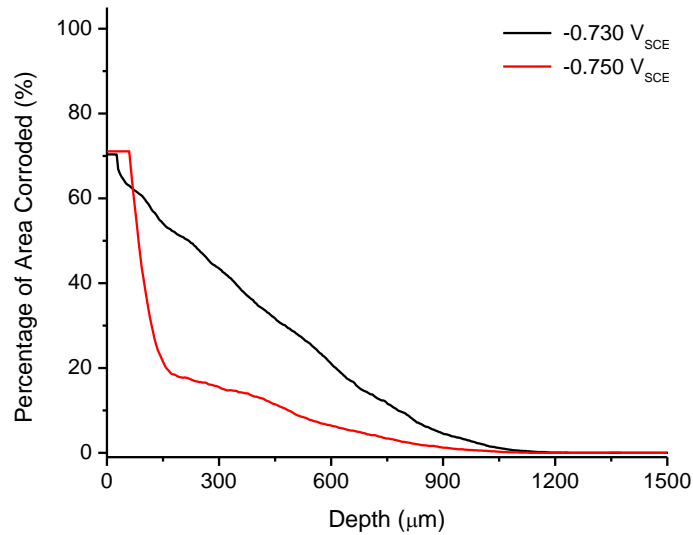
Figure 4.13. Percentage of area corroded (ST surface) after 100 h of exposure as a function of specimen depth (L direction) and applied potential for 3D planar surface specimens of AA5083-H131 sensitized to 39 mg/cm^2 and exposed to 0.6 M NaCl solution, pH 8.3.

Figure 4.13 to Figure 4.15 shows a comparison of the percentage of area corroded after 100 h as a function of depth between -0.73 V_{SCE} and -0.75 V_{SCE} for the three geometries. For the 3D planar surface, the percentage of area corroded at -0.75 V_{SCE} decreased at a sharper slope with depth. This implies that a lower applied potential resulted in shallower damage depths and fewer fissures. For the 2D foil, the two curves are relatively the same, deviating only at depths beyond 650 μm depth. This suggests that a lower applied potential still rendered the limited IGC spreading on the surface, but caused shallower damage depths. Aside from a

186

decreased in damage depth in the wire, surface roughening was exhibited at a lower depth of 199 µm at -0.75 V_{SCE} as compared to at 417 µm for -0.73 V_{SCE}.
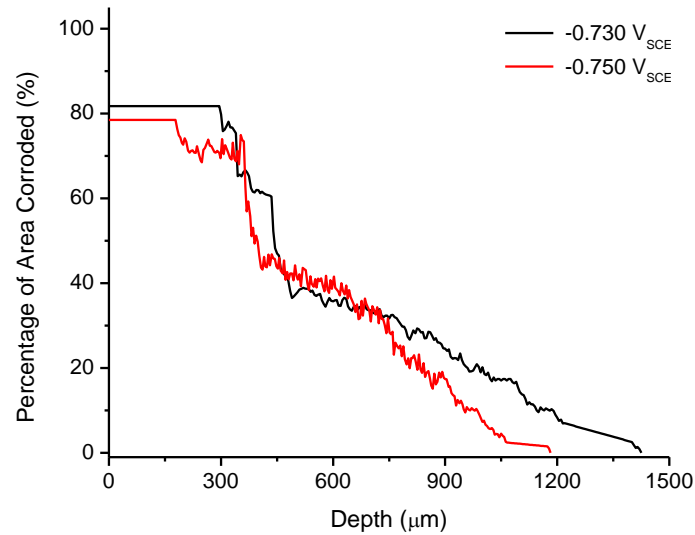
Figure 4.14. Percentage of area corroded (ST surface) after 100 h of exposure as a function of specimen depth (L direction) and applied potential for 2D foil specimens of AA5083-H131 sensitized to 39 mg/cm^2 and exposed to 0.6 M NaCl solution, pH 8.3.

As for the potentiostatic holds at -0.8 V_{SCE}, the current densities started out cathodic, eventually switching to anodic current densities in the order of 10^{-4} A/cm^2. As a result, only the 100 h exposure exhibited corrosion damage. The measured maximum damage depths in the 1D wire, the 2D foil, and the 3D planar surface are 66 µm, 36 µm, and 69 µm, respectively. These damage depths will be revisited in a later section together with results from long-term potentiostatic holds to determine possibility of power law IGC propagation kinetics.
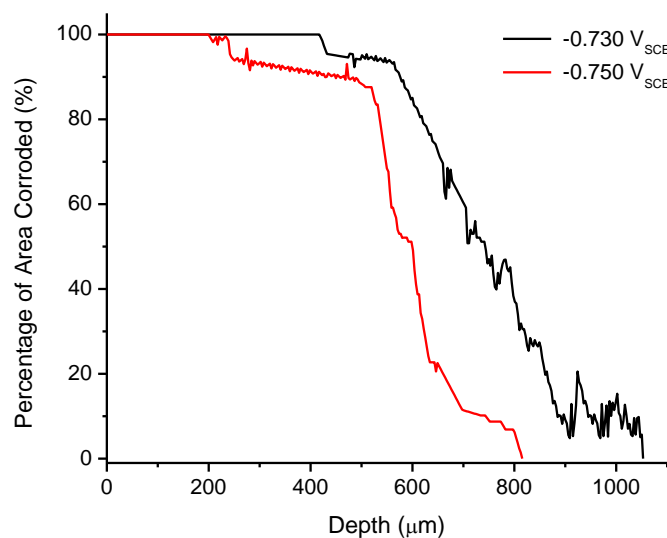
Figure 4.15. Percentage of area corroded (ST surface) after 100 h of exposure as a function of specimen depth (L direction) and applied potential for 1D wire specimens of AA5083-H131 sensitized to 39 mg/cm^2 and exposed to 0.6 M NaCl solution, pH 8.3.

4.5.2 Critical Electrochemical Conditions for Intergranular Corrosion Propagation by Geometry

In order to determine the effect of geometry on the critical current density and the threshold potential, varying geometries of AA5083-H131 DoS 39 mg/cm^2 were exposed to 0.6 M NaCl solution at pH of 8.3 under galvanostatic hold at various applied current densities and exposure times. The effect of geometry on measured applied potential during galvanostatic hold is shown in Figure 4.16. Each of the galvanostatic curves started at a high potential followed by a rapid decrease in potential until a stable potential was reached. The initial high potentials, hereafter referred to as activation potentials, are reasonable for the given applied

current density based on the polarization curves reported for AA5083-H131.[10] These transient activation potentials are more positive than the breakdown potential of β-phase (βE_{pit}), -0.96 V_{SCE}, and at times near, if not more positive than, the IGC spreading potential ($E_{spreading}$), -0.73 V_{SCE}, for AA5083.[16,17] As such, for all three geometries, there is a sufficient chemical driving force to initiate localized corrosion on the surface, in the form of β-phase pitting and IGC spreading. The drop in potential is suggested to be an effect of the change in electrochemical response as a result of the local acidification and high chloride ion concentration that develops within the pits and fissures during corrosion.
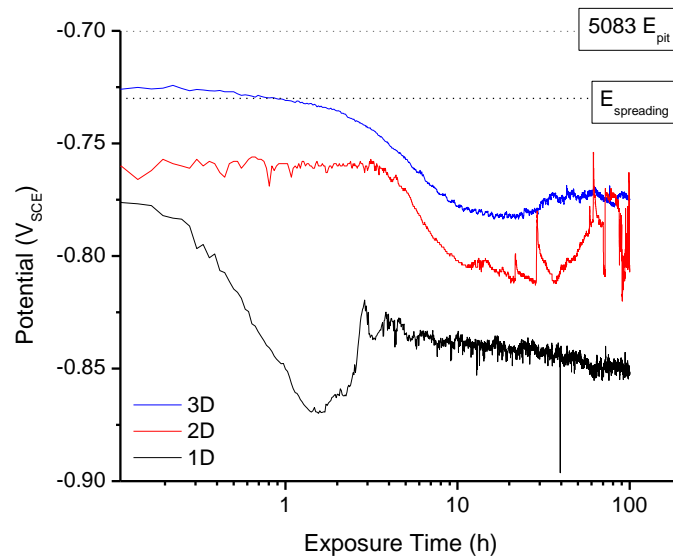
Figure 4.16. Potential as a function of exposure time and degree of connectivity for AA5083-H131 sensitized to 39 mg/cm^2 held at an applied current density of 1.5 x 10^{-3} A/cm^2, with ST surface exposed to 0.6 M NaCl solution at pH 8.3. As a comparison, the IGC spreading potential for sensitized AA5083 and the pitting potential for unsensitized AA5083 (2 mg/cm^2) are marked with dashed lines.[16] Also, the open circuit potential of β-phase (not included in the figure) is -1.162 V_{SCE}.[17]
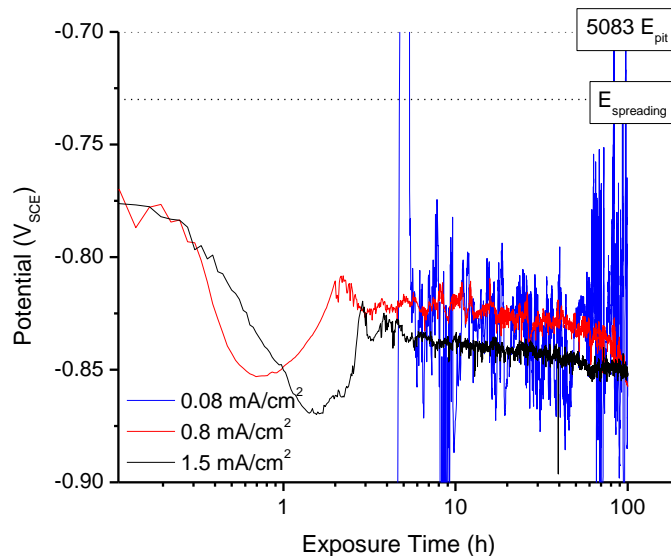
Figure 4.17. Potential as a function of exposure time for 1D wire specimens of AA5083-H131 sensitized to 39 mg/cm^2 and held at various applied current densities in 0.6 M NaCl solution at pH 8.3. As a comparison, the IGC spreading potential for sensitized AA5083 and the pitting potential for unsensitized AA5083 (2 mg/cm^2) are marked with dashed lines.[16] Also, the open circuit potential of β-phase (not included in the figure) is -1.162 V$_{SCE}$.[17]

For the same applied current density, the activation potential decreases with decreasing degree of connectivity, such that it is highest for the 3D planar surface (-0.726 V$_{SCE}$), followed by that for the 2D foil (-0.767 V$_{SCE}$), and lowest for the 1D wire (-0.776 V$_{SCE}$). Because the activation is associated with the β-phase pitting and IGC spreading on the surface, this decrease can be attributed to the limited β-phase sites and the restricted degree of connectivity for additional pitting and spreading events to occur in the case of the 1D wire and 2D foil. Moreover, the range of open circuit potential (OCP) measured for the 1D wire is -1.29 to -0.94 V$_{SCE}$, which is significantly lower as compared to the range for the 3D planar

surface of -0.84 to -0.75 V_{SCE}. This difference is due to the presence of cathodic constituent particles, which increases the OCP of the 3D planar surface.

Additionally, the decrease in potential occurred earlier for the 1D wire, followed by a sharp rise, and settled at a stable potential, which is relatively more negative than those measured for the 2D wire and 3D planar surface. The small surface area of the 1D wire limited the extent of anodic activation and surface corrosion, such that surface recession or penetration occurred immediately at the beginning of the tests. While penetration may have also commenced on some of the IGC sites for the other two geometries, the activation potential was still necessary to trigger and drive the simultaneous IGC spreading on the surface at this early stage. The decrease in potential for the 1D wire is then related to the transient change in chemistry at the pit bottom, rendering lower breakdown potentials and higher anodic current densities. However, the pit depth at 1 h is expected to be shallow, such that the developing chemistry is hardly sustained owing to the outward diffusion along a short diffusive path. The sharp rise in potential immediately after the decrease is driven by the need to maintain this developing pit chemistry. This saddle shape behavior of drop and rise in potential was observed for all instances of 1D wire galvanostatic holds at current densities above 0.8 mA/cm^2 (Figure 4.17). The applied current density of 0.08 mA/cm^2 is near passive current density, and could be switching between active passive behavior causing the fluctuating potential response.
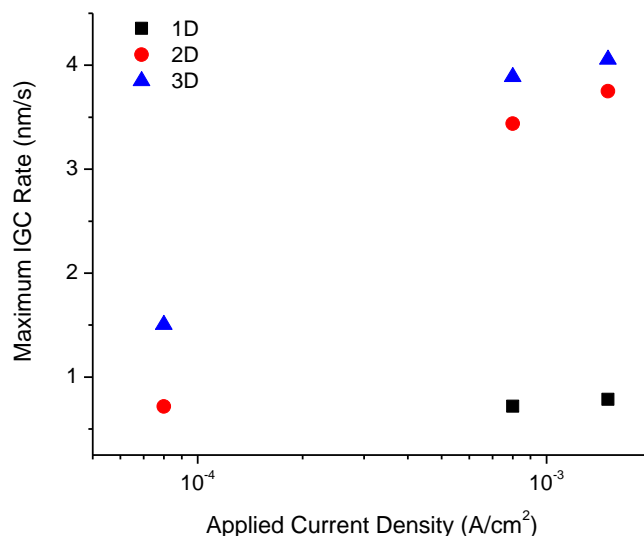
Figure 4.18. Maximum IGC propagation rate in the L as a function of applied current density and degree of connectivity for AA5083-H131 sensitized to 39 mg/cm^2 exposed to 0.6 M NaCl solution, pH 8.3, after 100 h.

The measured stable potential also decreases with decreasing degree of connectivity for a given current density (Figure 4.16). This difference is attributed to the active and passive area partitioning with IGC penetration. Although the 1D wire exhibited surface roughening, total surface recession relative to the epoxy mount was observed, suggesting that the passive area is small. Both the 2D foil and the 3D planar surface exhibited grain fall out, albeit only a small fraction for the latter. Mainly passive dissolution occurred at these intact grains on the surface, as well as on the generated fissure walls. Hence, the true active area was lower than the original surface area accounted for, such that the apparent applied current density was in reality higher than intended. Relative to the 2D foil, the higher number of fissures in the 3D planar surface results in larger deviation from the true

active area, subsequently yielding a higher apparent applied current density and increasing the stable potential response. As such, at the same applied current density, the observed IGC propagation rate in the 3D planar surface were faster than the 2D foil, while the 1D wire exhibited the lowest propagation rates (Figure 4.18). In light of this and the aforementioned difference in OCP with respect to the geometries, the damage depth and potential response amongst the three geometries were analyzed independently.
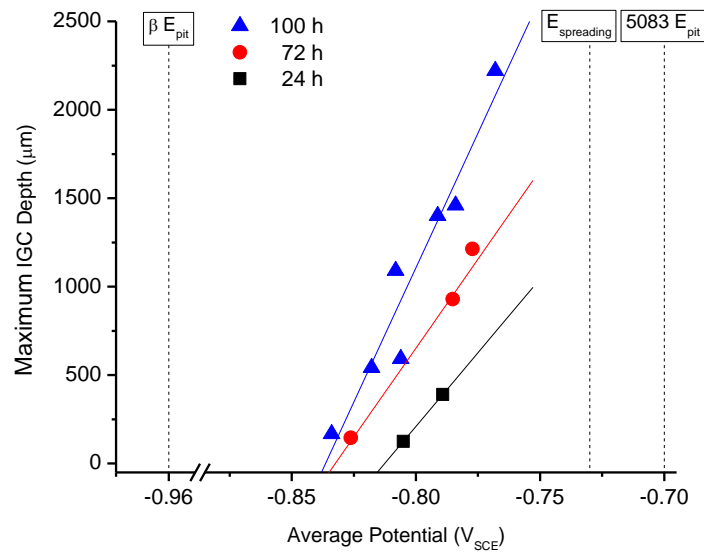
Figure 4.19. Maximum IGC depth in the L direction from fissure measurements as a function of average potential and exposure time for 3D planar surface specimens of AA5083-H131 sensitized to 39 mg/cm^2 and galvanostatically held in 0.6 M NaCl solution at pH 8.3. Only the measured potentials from the latter half the galvanostatic tests were included in the average. Additional data points for 100 h exposure were taken from earlier measurements at various applied current densities (Chapter 3). As a comparison, the IGC spreading potential for sensitized AA5083 and the pitting potential for unsensitized AA5083 (2 mg/cm^2) are marked with dashed lines.[16] Also, the open circuit potential of β-phase (not included in the figure) is -1.162 V$_{SCE}$.[17]

Figure 4.20. Maximum IGC rate in the L direction from fissure measurements as a function of average potential and exposure time for 3D planar surface specimens of AA5083-H131 sensitized to 39 mg/cm^2 and galvanostatically held in 0.6 M NaCl solution at pH 8.3. Only the measured potentials from the latter half the galvanostatic tests were included in the average. Additional data points for 100 h exposure were taken from earlier measurements at various applied current densities (Chapter 3). As a comparison, the IGC spreading potential for sensitized AA5083 and the pitting potential for unsensitized AA5083 (2 mg/cm^2) are marked with dashed lines.[16] Also, the open circuit potential of β-phase (not included in the figure) is -1.162 V_{SCE}.[17]

Figure 4.19 shows the maximum IGC depth as a function of average potential and exposure times for the 3D planar surface. Only the potentials from the latter half of the galvanostatic hold period were considered in the average. The IGC damage depths increased linearly with increasing applied potentials. Based on the difference in slopes, the potential dependence of the IGC depths also increased with increasing exposure time. As such, the measured IGC threshold potential, E_{crit}, below which no IGC damage was observed, increases from -0.834 VS_{CE} for 100 h exposure to -0.804 V_{SCE} for 24 h exposure. However, plotting the same data

194

in terms of IGC rate as a function of potential (Figure 4.20) shows that these three

sets of data collapsed to fit a single linear IGC rate trend line. This constancy of

rate with exposure time implies that the potential drop down the IGC fissures is

relatively constant with depth, supporting earlier hypothesis on the effect of degree

of connectivity on ohmic potential drop.

Figure 4.21. Maximum IGC depth in the L direction from fissure measurements as a function of average potential and exposure time for 2D foil specimens of AA5083-H131 sensitized to 39 mg/cm^2 and galvanostatically held in 0.6 M NaCl solution at pH 8.3. Only the measured potentials from the latter half the galvanostatic tests were included in the average. As a comparison, the IGC spreading potential for sensitized AA5083 and the pitting potential for unsensitized AA5083 (2 mg/cm^2) are marked with dashed lines.[16] Also, the open circuit potential of β-phase (not included in the figure) is -1.162 V_{SCE}.[17]

The maximum IGC depth as a function of average potential and exposure

time for the 2D wire is displayed in Figure 4.21. The measured E_{crit} for IGC

propagation is -0.89 V_{SCE}, which is substantially more negative than that for 3D

planar surface (-0.83 V_{SCE}). These three sets of data were replotted as maximum

IGC rate as a function of average potential in Figure 4.22. Fitting of the data

demonstrates that maximum IGC growth is exponential with potential, specifically

at 24 h and 72 h exposures, but could be linear with potential at 100 h.

Figure 4.22. Maximum IGC propagation rate in the L direction from fissure measurements as a function of average potential and exposure time for 2D foil specimens of AA5083-H131 sensitized to 39 mg/cm^2 and galvanostatically held in 0.6 M NaCl solution at pH 8.3. Only the measured potentials from the latter half the galvanostatic tests were included in the average. As a comparison, the IGC spreading potential for sensitized AA5083 and the pitting potential for unsensitized AA5083 (2 mg/cm^2) are marked with dashed lines.[16] Also, the open circuit potential of β-phase (not included in the figure) is -1.162 V_{SCE}.[17]

Figure 4.23. Maximum IGC depth in the L direction from fissure measurements as a function of average potential and exposure time for 1D wire specimens of AA5083-H131 sensitized to 39 mg/cm^2 and galvanostatically held in 0.6 M NaCl solution at pH 8.3. Only the measured potentials from the latter half the galvanostatic tests were included in the average. As a comparison, the IGC spreading potential for sensitized AA5083 and the pitting potential for unsensitized AA5083 (2 mg/cm^2) are marked with dashed lines.[16] Also, the open circuit potential of β-phase (not included in the figure) is -1.162 V$_{SCE}$.[17]

Finally, in the case of the 1D wire, propagation was only observed on galvanostatic holds at 0.8 mA/cm^2 and above. This implies that for a 1D degree of connectivity, a higher critical current density is necessary for IGC to propagate. At the lower applied current density of 0.08 mA/cm^2, the limited β-phase sites on the 1D wire surface is not sufficient to trigger continuous active dissolution for IGC initiation, as in the case of 2D or 3D degree of connectivity. Instead passive dissolution at this rate occurs on the α-matrix, which took longer time to develop substantial depth. The lowest damage depth of 76.3 µm observed correspond to an E$_{crit}$ of -0.85 V$_{SCE}$. The limited data with a narrow range of damage depth and

197

potential observed for the 1D (Figure 4.23) wire made data fitting difficult, and the relationship between growth rate and potential inconclusive for the 1D wire.

4.5.3 Influence of Degree of Connectivity on Intergranular Propagation Growth Kinetics

Long-term potentiostatic holds were conducted on AA5083-H131 sensitized to 39 mg/cm^2 with different surface geometries exposed to 0.6 M NaCl solution with pH 8.3 to investigate if IGC stifling or even IGC arrest occurs. Figure 4.24 to Figure 4.26 display current density behavior as a function of exposure time and applied potential for 1D wire, 2D foil, and 3D planar surface (degree of connectivity), respectively. For all three specimen geometries, at an applied potential of -0.80 V$_{SCE}$ the current density started out cathodic, and slowly crossed over to the anodic region, but remained very low in the order of 10^{-4} A/cm^2 even at long exposure periods of 960 h. For the two higher applied potentials, -0.73 V$_{SCE}$ and -0.75 V$_{SCE}$ (Figure 4.24), the current density behavior of 1D wire now shows a four-stage behavior instead of the typical three stage shown earlier for short term test (Figure 4.16). The first three stages remained the same as evident by the sharp rise in initial current density, followed by the current decay, and the steady-state dissolution at low current density. Although, it has to be noted that for these long-term exposure the steady-state dissolution is accompanied by a significant amount of noise, which could be attributed to activation-repassivation events on the roughened wire surface. This stage was followed by a final drop in the current

density to values in the order of 10^{-5} A/cm^2, with instances of cathodic current densities, which indicates propagation stifling and arrest. For -0.75 V_{SCE}, this stage occurred after approximately 300 h of exposure, earlier than the 500 h for -0.73 V_{SCE}, which implies that the drop in current density is an effect of ohmic potential drop with propagation.
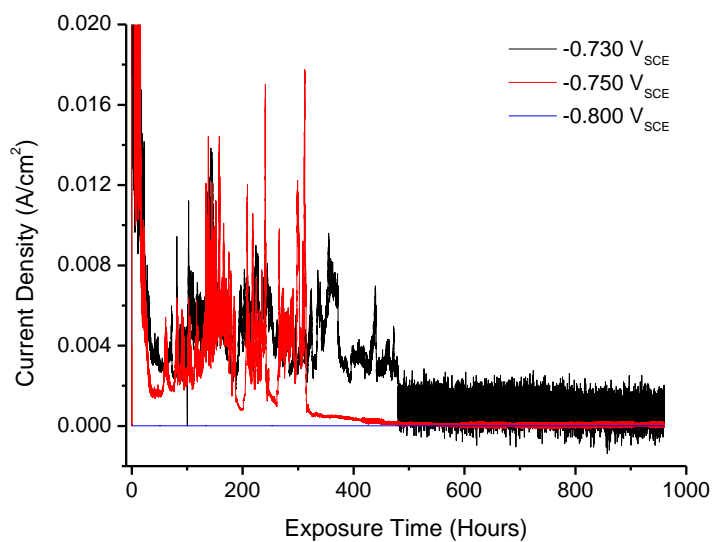
Figure 4.24. Potential as a function of exposure time and applied potential for 1D wire specimens of an AA5083-H131 sensitized to 39 mg/cm^2 and exposed to 0.6 M NaCl solution at pH 8.3 for 960 h.
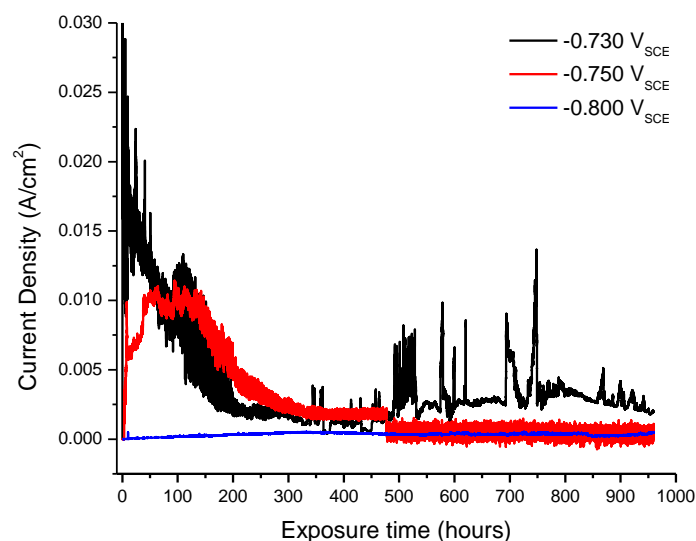
Figure 4.25. Potential as a function of exposure time and applied potential for 2D foil specimens of an AA5083-H131 sensitized to 39 mg/cm^2 and exposed to 0.6 M NaCl solution at pH 8.3 for 960 h.
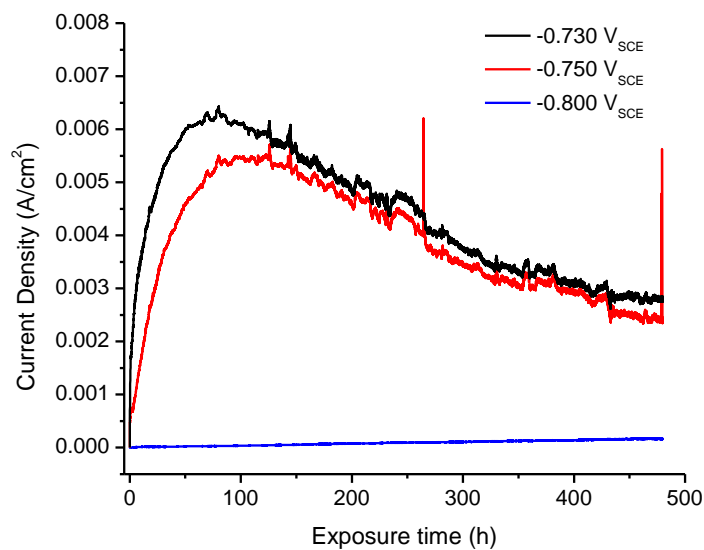
Figure 4.26. Potential as a function of exposure time and applied potential for 3D planar surface specimens of AA5083-H131 sensitized to 39 mg/cm^2 and exposed to 0.6 M NaCl solution at pH 8.3 for 960 h.
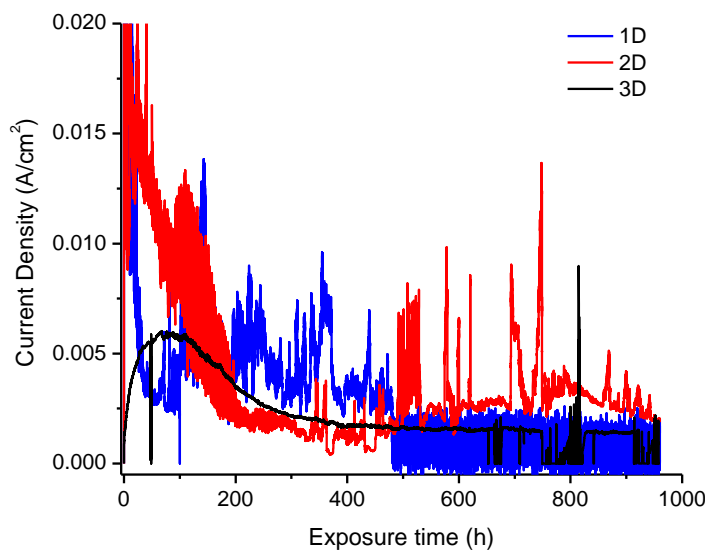
Figure 4.27. Potential as a function of exposure time and degree of connectivity for AA5083-H131 sensitized to 39 mg/cm^2 and exposed to 0.6 M NaCl solution, pH of 8.3, held at -0.730 V_{SCE} for 960 h.

The current density behavior of the 2D foil specimen only exhibited the first three stages and all four stages for applied potentials of -0.73 V_{SCE} and -0.75 V_{SCE}, respectively (Figure 4.25). While the 3D planar (Figure 4.26 and Figure 4.27) surface specimens had an initial incubation period to reach the steady state current density, followed by a steady-state dissolution, and a current density decay to a lower current density plateau. The current density decay with exposure time for both the 2D foil and the 3D planar surface signifies that IGC propagation rate slows down with time for a given applied potential. This is in agreement with the observed maximum IGC depth, plotted as a function of time and applied potential, for the different specimen geometries in Figure 4.28 to Figure 4.31.

201
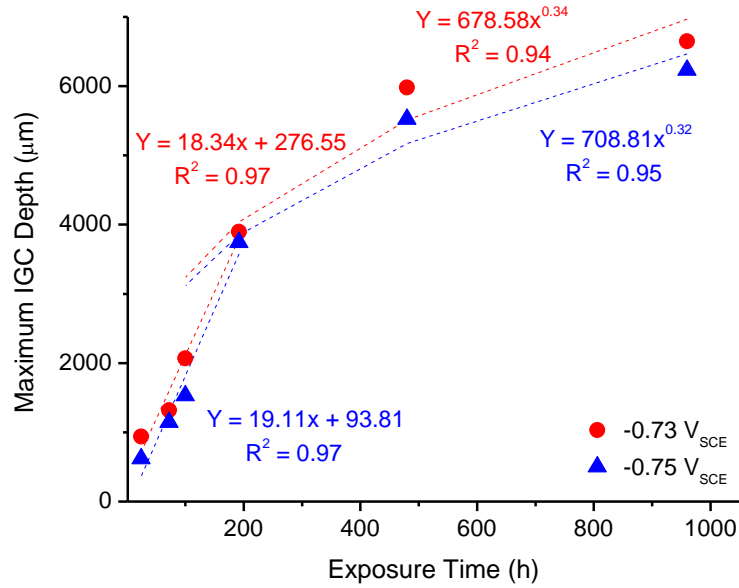
Figure 4.28. Maximum IGC damage depth from fissure measurements in L direction propagating from ST surface as a function of exposure time and applied potential for 3D planar surface specimens of AA5083-H131 sensitized to 39 mg/cm^2 in 0.6 M NaCl solution, pH 8.3.

In all three sample geometries (Figure 4.28 to Figure 4.30), the IGC propagation rate is faster at -0.73 V$_{SCE}$ over the entire range of exposure times, as would be expected from the relationship between IGC and potential. In the case of the 3D planar surface (Figure 4.28), the IGC damage depth propagates linearly with time until about 192 h, beyond which the kinetics transitions into a power law behavior. This transition means IGC stifling occurred at extended exposure times, as manifested by decrease in anodic current density (Figure 4.26). It was discussed in an earlier section that the 3D degree of connectivity in these specimens keeps the effective resistance constant resulting in negligible ohmic potential drop within the

fissure. Although propagation of multiple IGC network still ensued at these extended periods of time, the combination of the corrosion products accumulation and H_2 bubbles evolution within the fissures can result in an increase in resistance, subsequently decreasing the fissure tip potential and anodic dissolution rate. This is highly possible especially because the electrolyte was never replaced or replenished even for the potentiostatic holds up to 960 h (40 days). At a lower applied potential of -0.80 V_{SCE}, IGC propagation was not observed until after 100 h and carried on at a slow rate following power law kinetics. At this potential, only isolated IGC was observed such that influence of IGC network on effective resistance does not hold.
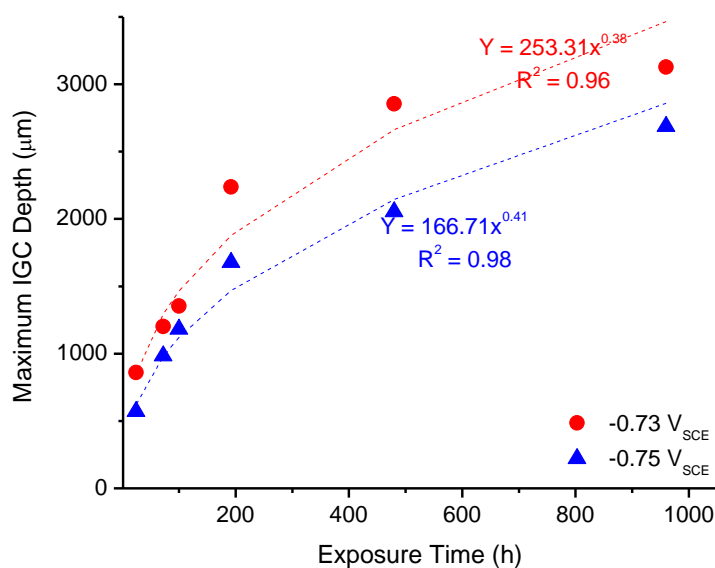
Figure 4.29. Maximum IGC damage depth from fissure measurements in L direction propagating from ST surface as a function of exposure time and applied potential for 2D foil specimens of AA5083-H131 sensitized to 39 mg/cm^2 in 0.6 M NaCl solution, pH 8.3.
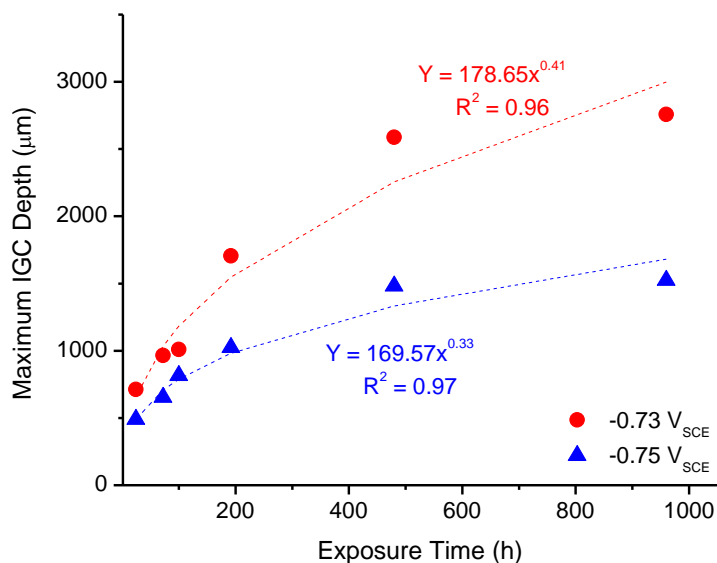
Figure 4.30. Maximum IGC damage depth from fissure measurements in L direction propagating from ST surface as a function of exposure time and applied potential for 1D wire specimens of AA5083-H131 sensitized to 39 mg/cm^2 in 0.6 M NaCl solution, pH 8.3.
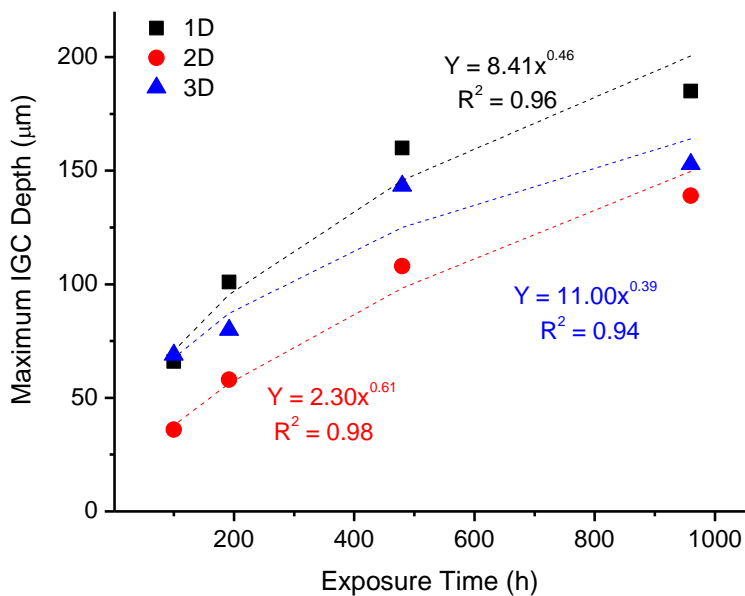
Figure 4.31. Maximum IGC damage depth from fissure measurements in L direction propagating from ST surface as a function of exposure time and degree of connectivity for AA5083-H131 sensitized to 39 mg/cm^2 in 0.6 M NaCl solution, pH 8.3 held at -0.80 V_{SCE}.

In the case of the 2D foil (Figure 4.29), linear kinetics were also observed at the short exposure times (<100 h), and quickly transitioned to power law kinetics. As in the case of the 3D planar surface, the linearity at the beginning is an effect of the IGC network. However, this regime is short-lived because the interconnectedness of the network is limited in 2D, such that the effective resistance could only be reduced by so much. In conjunction with this, the system was also more prone to grain fall-out such that the influence of the IGC network on the effective resistance waned so much faster as compared to 3D. Similar to the case of the 3D planar surface, only power law behavior was also observed at -0.8 V_{SCE} (Figure 4.31). In contrast, the IGC propagation kinetics in the 1D wire for all applied potential (Figure 4.30 and Figure 4.31) follows a power law behavior from the beginning, typical of localized corrosion propagation.[9,18–20]

4.5.4 Influence of Degree of Connectivity on the Relationship between Intergranular Corrosion Propagation Rate and Potential

Long-term galvanostatic holds were conducted on AA5083-H131 sensitized to 39 mg/cm^2 with different surface geometries exposed to 0.6 M NaCl solution with pH 8.3 to investigate if the critical electrochemical conditions for IGC propagation still apply. Figure 4.32 to Figure 4.35 display potential as a function of exposure time, applied current density, and degree of connectivity. As in the case of short-term exposures, each of the galvanostatic curves started at a high

potential followed by a rapid decrease in potential until a stable potential was reached after 12 to 13 h of exposure for the 2D foil and 3D planar surface (Figure 4.33 and Figure 4.354). The 1D wire (Figure 4.32) registered a lower stable potential that is accompanied by a lot of noise, which is attributed to the build-up of corrosion products. This noise was also observed on the 2D foil and 3D planar surface (Figure 4.33 and Figure 4.355), but only after longer exposure times. For the 3D planar surface, a second drop in potential occurred after 100 h of exposure and reached a plateau at approximately 200 h for the two lower applied current densities (Figure 4.34). It has to be noted that this only occurred for the 480 h exposure, but not for the 960 h (Figure 4.35). As such, it is difficult to speculate the reason behind this second plateau.
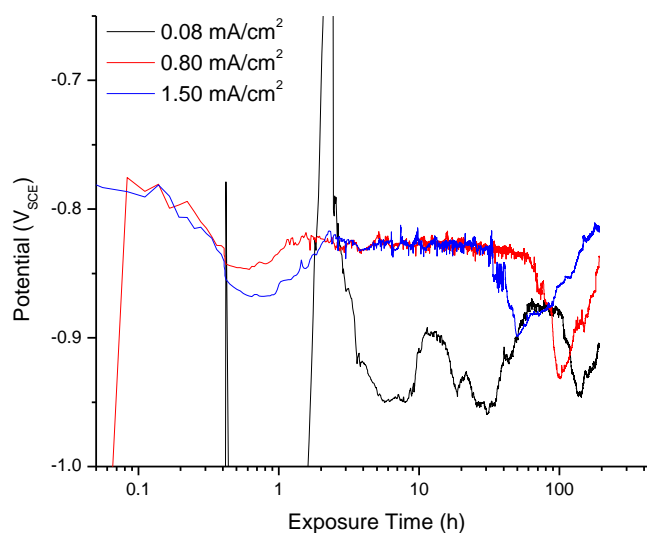
Figure 4.32. Potential as a function of exposure time and applied current density for 1D wire specimens of AA5083-H131 sensitized to 39 mg/cm^2 exposed to 0.6 M NaCl solution at pH 8.3 for 192 h.

Figure 4.36 shows the maximum IGC rate as a function of average potential and exposure times for the 3D planar surface. Only the potentials from 50 h onwards were considered in the average. The 100 h data were included for comparison purposes. It is apparent that only the data from 192 h exposure fit the linear potential dependence. In general, the exposures after 480 h and 960 h exhibited slower IGC propagation rates. This is because as IGC propagates, the total area of passive IGC flanks increases, reducing the true active current density. Additionally, surface recession was exhibited for 980 h exposures at 0.8 and 1.5 mA/cm^2, as well as 480 h at 1.5 mA/cm^2. A cross-section micrographs in Figure 4.37 showed that the original surface receded by almost 2500 μm, as a result of a combination of grain fall-out and passive dissolution of the α-matrix grains. Given the damage generated at these long periods of exposures, there was an accumulation of corrosion products within the fissures and on the specimen surface, which resulted in an increase in resistance within the fissures. This also implies that the observed potentials at this long-term exposures could be affected by ohmic drop, thus deviating from linear potential response. Additionally, a lower E_{crit} of -0.87 V_{SCE} was observed, but only for the 480 h exposures. Whereas the 960 h exposure exhibited an E_{crit} of -0.84 V_{SCE}, close to the -0.83 V_{SCE} observed at 100 h. Although the reason behind this difference is unclear, both measurements were on or above -0.87 V_{SCE}, the breakdown potential of the α-matrix phase in the suggested fissure chemistry between 80% to 100% stoichiometric dissolution of Al-4% Mg solid solution.[21–24].
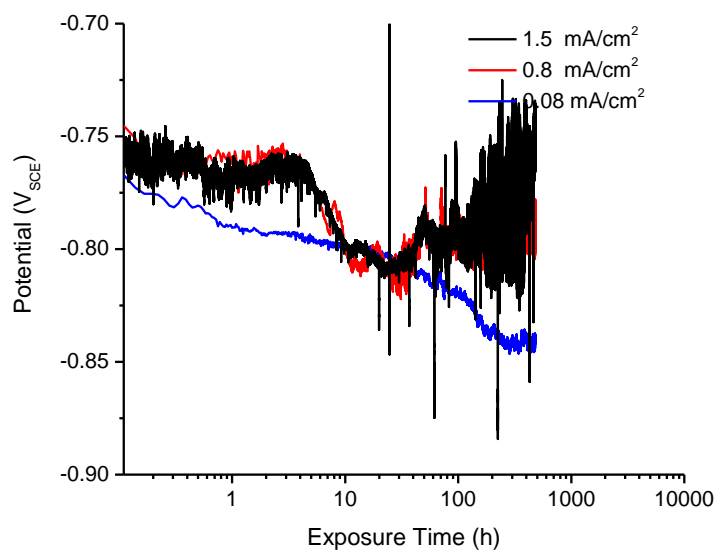
Figure 4.33. Potential as a function of exposure time and applied current density for 2D foil specimens of AA5083-H131 sensitized to 39 mg/cm^2 exposed to 0.6 M NaCl solution at pH 8.3 for 960 h.
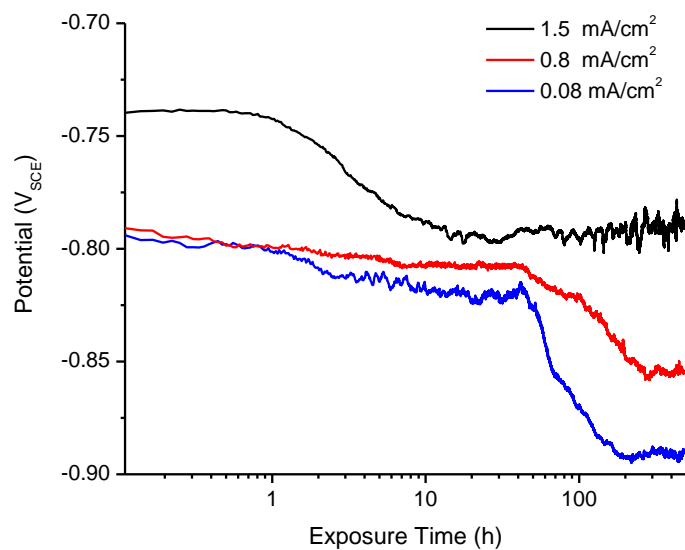
Figure 4.34. Potential as a function of exposure time and applied current density for 3D planar surface specimens of AA5083-H131 sensitized to 39 mg/cm^2 exposed to 0.6 M NaCl solution at pH 8.3 for 480 h.
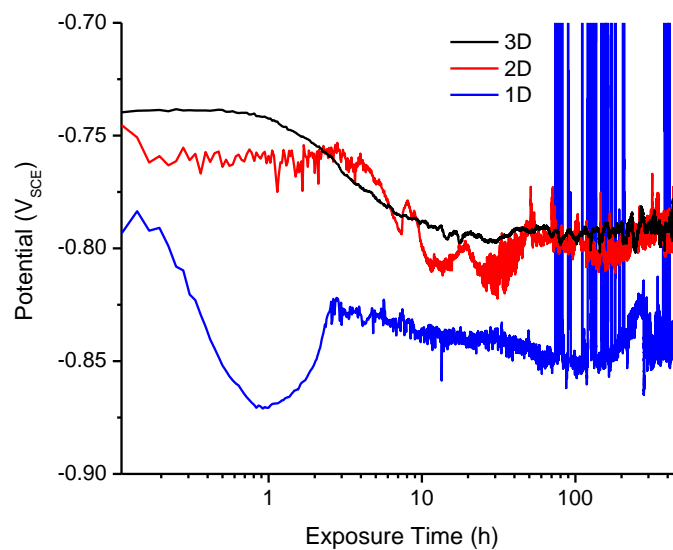
Figure 4.35. Potential as a function of exposure time and degree of connectivity for AA5083-H131 sensitized to 39 mg/cm^2 exposed to 0.6 M NaCl solution at pH 8.3 galvanostatically held at 1.5 mA/cm^2 for 480 h.
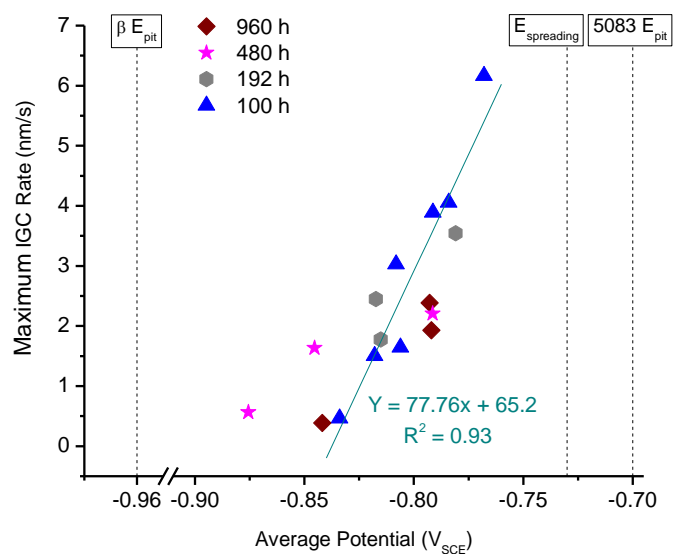
Figure 4.36. Maximum IGC rate in the L direction from fissure measurements as a function of average potential and exposure time for 3D planar surface specimens of AA5083-H131 sensitized to 39 mg/cm^2 and galvanostatically held in 0.6 M NaCl

solution at pH 8.3. Only the measured potentials from 50 h onwards were included in the average. Additional data points for 100 h exposure were taken from earlier measurements at various applied current densities (Chapter 3). As a comparison, the IGC spreading potential for sensitized AA5083 and the pitting potential for unsensitized AA5083 (2 mg/cm^2) are marked with dashed lines.[16] Also, the open circuit potential of β-phase (not included in the figure) is -1.162 V$_{SCE}$.[17]

Figure 4.37. Cross-section image showing damage surface recession in the L direction from ST surface of AA5083-H131 sensitized to 39 mg/cm^2 and exposed to 0.6 M NaCl solution, pH 8.3, for 960 h at -0.73 V$_{SCE}$.
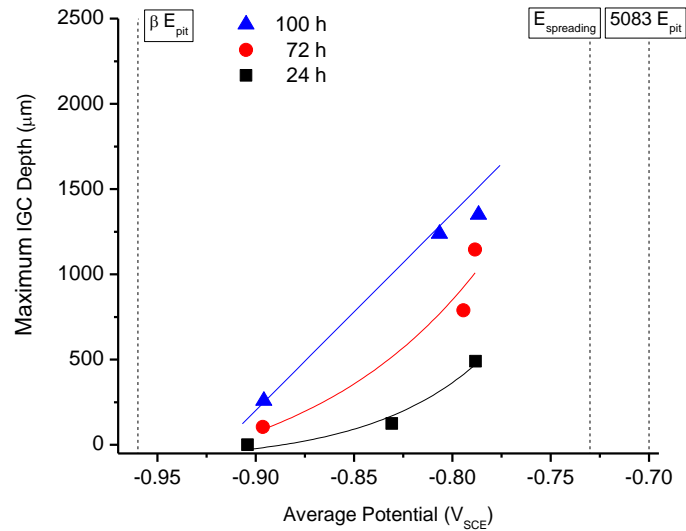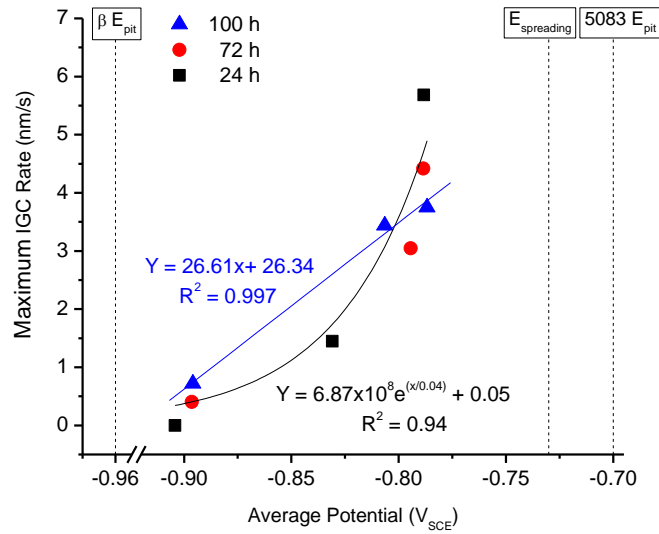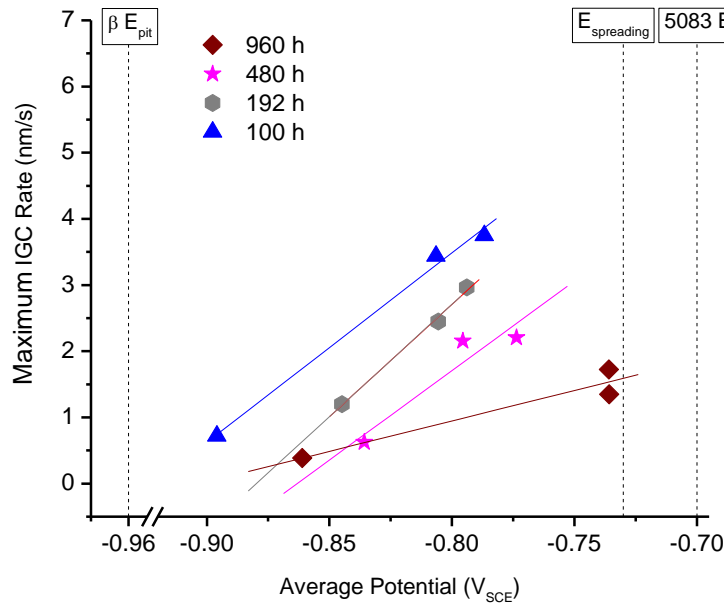
Figure 4.38. Maximum IGC rate in the L direction from fissure measurements as a function of average potential and exposure time for 2D foil specimens of AA5083-H131 sensitized to 39 mg/cm^2 and galvanostatically held in 0.6 M NaCl solution at pH 8.3. Only the measured potentials from 50 h onwards were included in the average. Additional data points for 100 h exposure were taken from earlier measurements at various applied current densities (Chapter 3). As a comparison, the IGC spreading potential for sensitized AA5083 and the pitting potential for unsensitized AA5083 (2 mg/cm^2) are marked with dashed lines.[16] Also, the open circuit potential of β-phase (not included in the figure) is -1.162 V$_{SCE}$.[17]

The maximum IGC rate as a function of average potential and exposure time for the 2D wire is displayed in Figure 4.38. Data fitting demonstrated that the propagation growth rate was linear with potential for all exposure times. Additionally, based on the slope, the linear dependence decreases with increasing exposure time, such that more positive potentials were observed at longer exposure times. Surface recession was exhibited in all long-term exposures except for the 192 h exposure at 0.08 mA/cm^2. As such, the decrease in slope at the longer exposure times is attributed to the potential drop due to ohmic resistance. Hence,

the true applied potential must be lower than the observed potentials. Ohmic control was also observed in the case of the 1D wire (Figure 4.39) for the two longer exposure times (480 h and 960 h). The maximum IGC rate shows linear dependence with potential, with the dependence decreasing with exposure time.
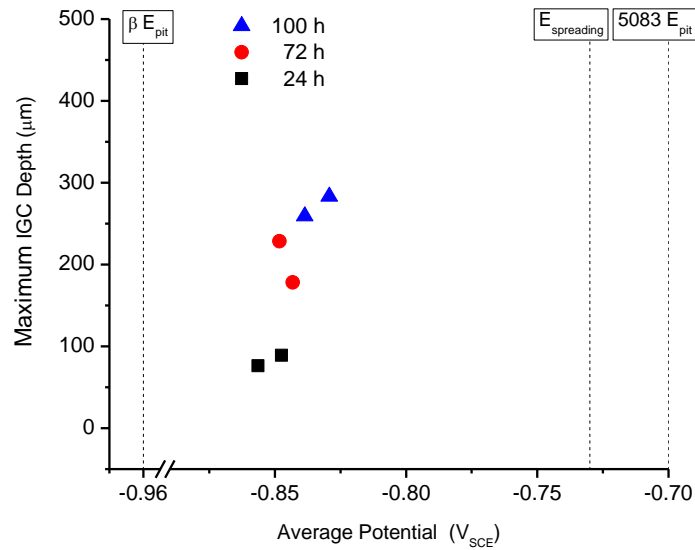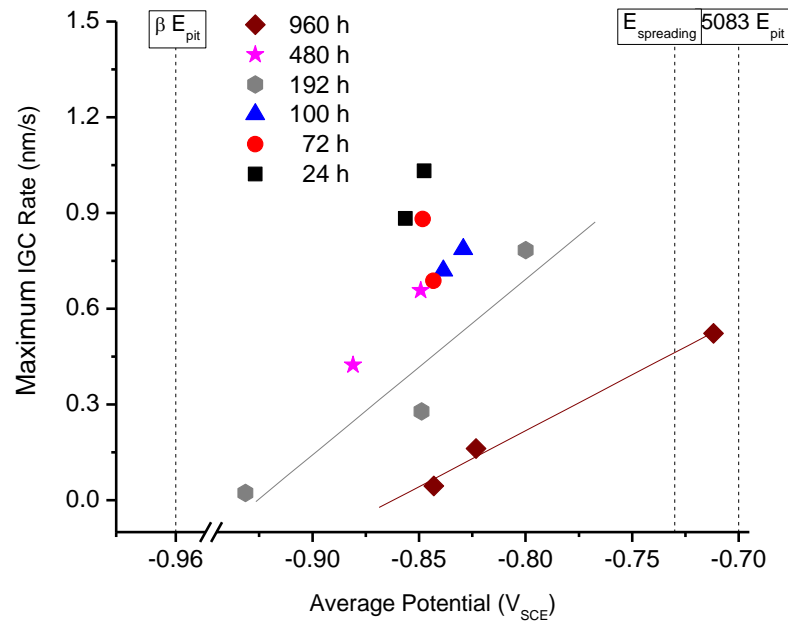

Figure 4.39. Maximum IGC rate in the L direction from fissure measurements as a function of average potential and exposure time for 1D wire specimens of AA5083-H131 sensitized to 39 mg/cm^2 and galvanostatically held in 0.6 M NaCl solution at pH 8.3. Only the measured potentials from 50 h onwards were included in the average. Additional data points for 100 h exposure were taken from earlier measurements at various applied current densities (Chapter 3). As a comparison, the IGC spreading potential for sensitized AA5083 and the pitting potential for unsensitized AA5083 (2 mg/cm^2) are marked with dashed lines.[16] Also, the open circuit potential of β-phase (not included in the figure) is -1.162 V$_{SCE}$.[17]

4.6   Discussion

4.6.1   Quantitative Relationship between Intergranular Corrosion Depth and Time

The IGC propagation in AA5083-H131 sensitized to 39 mg/cm^2 and exposed to 0.6 M NaCl solution with pH 8.3 at an applied potential near the spreading potential (-0.73 V$_{SCE}$) exhibited linear kinetics for short exposure times (<192 h) and transition to power law kinetics at longer times (Figure 4.28 to Figure 4.31). The transition from linear kinetics to power law kinetics as influenced by degree of connectivity, occurred at an earlier time (100 h) 2D degree of connectivity, whereas 1D degree connectivity only demonstrated power law behavior. Similarly, only power law behavior was exhibited at the lowest applied potential (-0.80 V$_{SCE}$) for all three degrees of connectivity.

The IGC power growth kinetics can be described as

$$d = Kt^n \hspace{4cm} \text{(Equation 4.1)}$$

where d is the IGC depth in µm, K is a constant associated with potential and electrolyte conditions, t is the exposure time in hour, and n is a system dependent constant. The quantitative relationship between maximum IGC depth and time, in terms of power law constants, as a function of applied potential and degree of connectivity is summarized in Table 4.2. It has to be recognized that the power law

213

kinetics only applies for 2D beyond 100 h, and 3D beyond 192 hrs. For the shorter

exposure times for linear kinetics applies, power law exponent is equivalent to 1.

For a 3D connectivity, the system dependent constant, n, for the two higher

applied potentials (-0.73 and -0.75 V_{SCE}) are nominally the same (0.34 and 0.32),

while a higher value of 0.39 was observed at -0.8 V_{SCE}. Similar trend of increasing

n values were observed for the 2D connectivity (0.38, 0.41, and 0.61) and for the

1D connectivity (0.33, 0.41, and 0.46).   This suggests that at higher applied

potentials, the IGC propagation kinetics slows down faster with time or decelerates

at a higher rate. At -0.73 V_{SCE}, the value of n increases with decreasing degree of

connectivity, implying IGC rates decelerates faster at higher degree of connectivity.

However, this is not the trend for the lower applied potentials, where the n value

increased from 3D to 2D connectivity and then decreased from 2D to 1D.

Table 4.2. Intergranular corrosion propagation power law growth kinetics constants

Applied Potential (V_{SCE})	Degree of Connectivity					
	1D (wire)		2D (foil)		3D (planar surface)	
	K	n	K	n	K	n
-0.73 V_{SCE}	178.65	0.41	253.31	0.38	678.58	0.34
-0.75 V_{SCE}	169.57	0.33	166.71	0.41	708.81	0.32
-0.80 V_{SCE}	8.41	0.46	2.30	0.61	11.00	0.39

Except for the case of 2D wire at -0.8 V_{SCE}, the fitted n values are within

the range of 0.32 to 0.46 across the different degrees of connectivity. These values

are lower than 0.5, the experimentally determined value for pure aluminum pitting

under both ohmic and mass transport controlled propagation.[18–20] However,

these values are within the range of 0.31 to 0.47, observed for IGC propagation rate in AA7075 in aerated 1 M NaCl solution obtained via foil penetration experiments at -0.725 V_{SCE}.[5]

The potential and electrolyte composition dependent constant, K, is two orders of magnitude lower at the applied potential of -0.8 V_{SCE}, whereas a small difference can be observed between -0.75 V_{SCE} and -0.73 V_{SCE} for the 3D connectivity. The same trend is exhibited in the 2D and 1D connectivity, albeit at lower values as an effect of the generally shallower damage depths observed. For the two higher potentials, the K values increases with increasing degree connectivity, suggesting that this constant is not only dependent on potential and electrolyte, but also on the mode of corrosion (e.g. spreading).

4.6.2 Validation of Constant Effective Resistance in Network of Multiple Intergranular Paths

It is hypothesized that the degree of connectivity influences the extent of ohmic potential drop within the fissure depth, thereby affecting the dissolution kinetics at the fissure and thus IGC propagation kinetics. The hypothetical schematic of this notion, with each grain boundary segment acting as a resistor, for three different degrees of connectivity is presented in Figure 4.3. The effective resistance at fissure tips was evaluated by employing computational analysis of resistor networks. The resistor networks were built considering each resistor to

215

represent a corroded grain boundary segment. The average grain widths of AA5083-H131 in the L and S directions are 80 and 20 μm, respectively. Taking this anisotropic nature into account, unit resistors in the L and S directions were assigned values of 4 and 1 ohm, as per grain aspect ratios.

For a single fissure propagating in a perfectly straight path (e.g. in the L-direction), the grain boundary segments are connected in series, such that the effective resistance increases linearly with fissure depth. More often than not, the IGC also branches (e.g. in S- and T-directions) along perpendicular grain paths, and separate fissures connect through this branching, forming interconnected IGC networks. This arrangement is analogous to resistor networks involving connections both in series and parallel. Because resistors connected in parallel always yield a lower effective resistance, an IGC fissure network is expected to have a lower effective resistance at the fissure tip than would a single fissure.

The voltage drop across a unit resistor network was analyzed by employing Kirchoff's current law and Ohm's law to calculate the effective resistance. For increasing rows and columns of resistors, a system of equations and unknowns were formulated by applying Kirchoff's current law and Ohm's law on each network node to establish a matrix problem. Numerical coding was utilized to evaluate the matrix and calculate the effective resistance. An example of the code can be found in the Appendix section.

Three IGC fissure network (Figure 4.40) scenarios were considered: (1) network of 2 parallel propagating fissures in L, fully connected in the S direction;

(2) network of multiple fissures propagating into a new grain boundary layer at equal rates in both L and S directions; and (3) inverted Christmas tree or network of multiple fissures branching on both sides in the S directions per layer grain boundary propagation in the L direction. Figure 4.41 shows the simulated effective resistances after certain propagation depths or number of grain boundary layers propagated in the L direction, N. In both scenarios involving interconnections, the effective resistance of the networks were substantially reduced. The extent of reduction increases with increasing depth. At depths of $N > 4$, the effective resistance at the tip of an IGC network is lower than that of a single fissure, implying that the potential drop in IGC network will be relatively small because the increase in resistance with depth is offset by the more greatly connected paths. For example, simulations of the resistance of the tip of a 900 µm fissure in L that was part of an interconnected network in the form of an inverted Christmas three would be $< 3\%$ of that of a single fissure, leading to IR drops of 3 mV or less, even for the maximum IGC rates observed, using the appropriate electrochemical kinetics for α-matrix and β-phase in simulated fissure chemistries (Chapter 3).
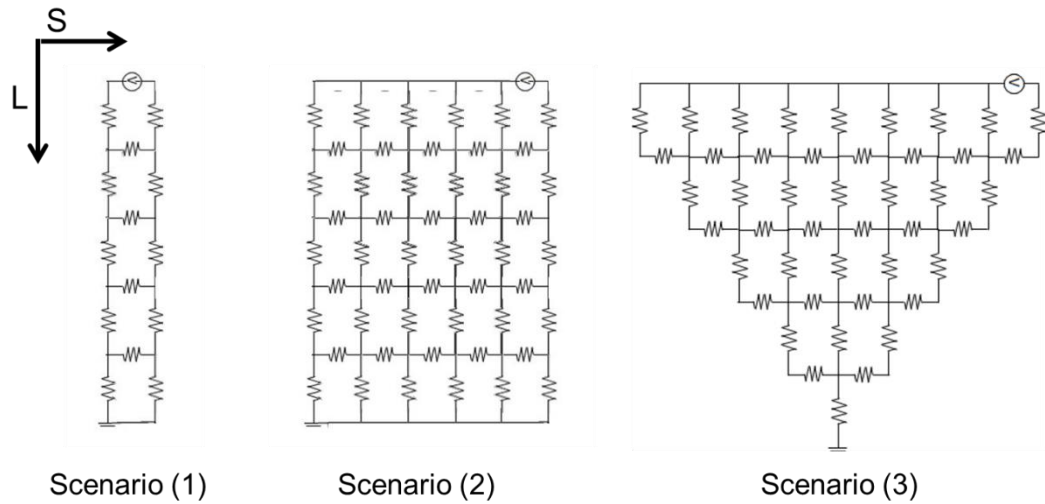
Figure 4.40. Schematics of the three IGC fissure networks considered for simulating effective resistance. Scenario (1) is a network of 2 parallel propagating fissures in L, fully connected in the S direction; (2) network of multiple fissures propagating into new grain boundary layer at equal rates in both L and S directions; and (3) inverted Christmas tree or network of multiple fissures branching on both sides in the S directions per layer grain boundary propagation in the L direction.

An additional simulation was also conducted looking at the interactive effects of multiple IGC networks as in scenario (1). These IGC networks are not fully connected in mesh, rather each IGC network is treated as a parallel resistor. A maximum nearest neighbor of 6 IGC networks was considered with each IGC network propagated to a depth of 10 grain boundary layer. Figure 4.42 shows that even without the connection, the effective resistance still dropped to low values. As such, with sufficient damage depths and fissure count, isolated IGC fissures generated from low DoS or low applied potentials or low current densities can also lead to significantly reduced effective resistance.

218
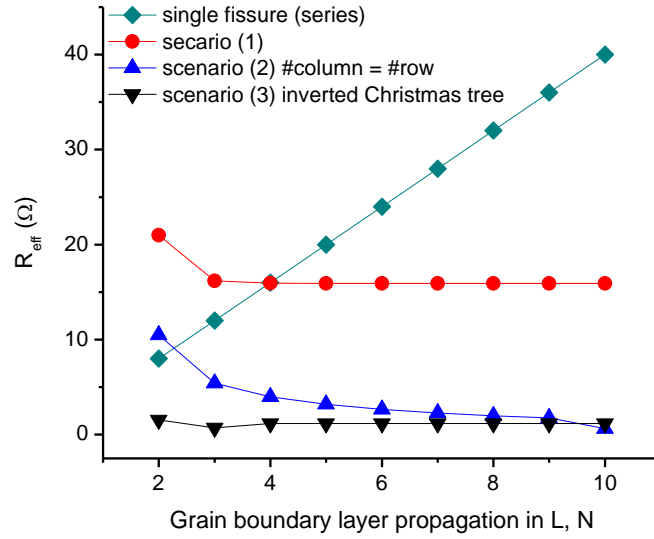
Figure 4.41. Simulated effective resistance as a function of grain boundary layer propagation, for a single fissure with resistors connected in series and three scenarios of interconnected fissures. The resistance values utilized in L and S are 4 Ω and 1 Ω, respectively, following microstructure anisotropy.
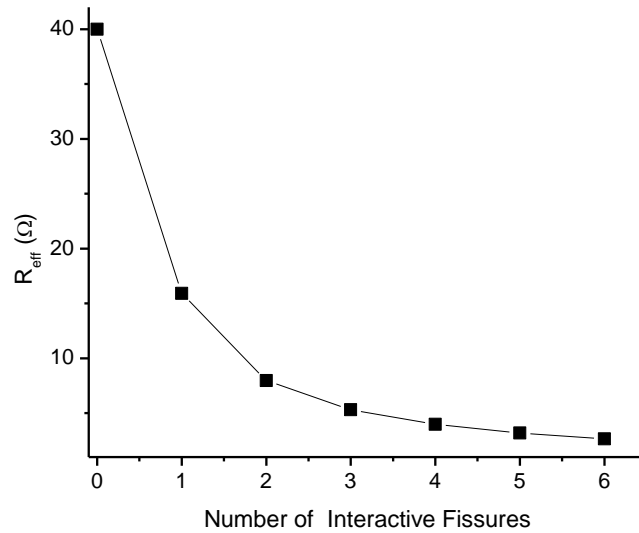
Figure 4.42. Simulated effective resistance as a function of interactive fissures. This involves interaction of network of 2 parallel propagating fissures (scenario 1 in Figure 4.41) treated as parallel resistor units.

219

4.6.3 Influence of Active Passive Surface Area Partition

The active and passive area partitioning during IGC propagation appears to be another significant factor that dictates IGC propagation rate and or applied potential response. The distribution of the applied current density between the active and passive areas can be expressed as:

$$(i_{pass})(1 - f_{act}) + (i_{act})(f_{act}) = (i_{app})A \qquad \text{(Equation 4.2)}$$

where i_{pass} is the passive current density, f_{act} is the fraction of active area, i_{act} is the active current density, i_{app} is the applied current density, and A is the specimen surface area. Assuming an i_{pass} of 1 x 10^{-5} A/cm^2, the f_{act} for the 3D planar surface can be estimated using the E-log i behavior for either the 1D wire or the 2D foil to represent 100% active. Figure 4.43 shows the average applied potential as a function of applied current density and specimen geometry. Only the potentials from the last 50 hours of galvanic hold were considered in the average to represent the stable potential. At a given applied current density, the i_{act} can be extrapolated from the E-log i data as the current density at the stable potential of the 3D planar surface. For example, at the stable potential of -0.774 V_{SCE} for an i_{app} of 1.5 x 10^{-3} A/cm^2, the i_{act} is approximately 3 x 10^{-2} A/cm^2 and 3.5 x 10^{-3} A/cm^2, assuming 1D wire and 2D foil as the 100% active, respectively. For a 3D planar surface area of 0.36 cm^2 in Equation 4.2, the f_{act} is estimated to be 0.018 and 0.15, respectively.

The total active current can also be estimated using the observed maximum damage depth and the number of fissures. Utilizing Faraday's law, the IGC depth

at a given exposure time can be converted to the active current density. The number of fissures, on the other hand, can be utilized to estimate the total active area. Assuming that each fissure has a fissure width of 0.1 µm and a fissure gap equal to a grain width in the S direction, 60 µm, the active area for each fissure is 6 x 10^{-8} cm^2. Take for example the case of 100 h exposure at 1.5 mA/cm^2, the observed damage depth of 1460 µm is equivalent to 11.7 mA/cm^2. A rough fissure count from two cross-section planes of 6 mm x 6 mm yields 400. Suppose the area of 0.36 cm^2 specimen have 40,000 fissures, the total active current is 0.028 mA. This is about 5.2% of the actual applied current of 0.54 mA. Coincidentally, this value is within the bounds estimated from the E-log i extrapolation. Even though these are merely rough estimates, this percentage demonstrates that virtually the majority of the current at these applied current densities is passive. More importantly, it shows another side effect of the degree of connectivity on IGC propagation kinetics, in addition to ohmic potential drop. As IGC propagates under constant applied current in specimens with high degree of connectivity, the fraction of passive current increases while the anodic dissolution current decreases, subsequently slowing the IGC propagation kinetics.
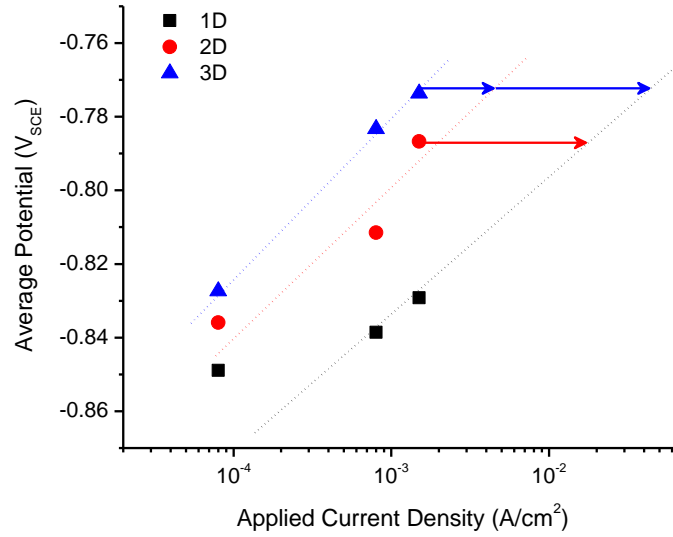
Figure 4.43. Average potential as a function of applied current density and degree of connectivity for AA5083-H131 sensitized to 39 mg/cm^2 galvanostatically held for 100 h in 0.6 M NaCl solution at pH 8.3. Only the potential for the last 50 h, where the potential is stable, was considered in the average potential.

4.7   Conclusions

1. The linear IGC propagation kinetics with potential and depth of AA5083-H131 in 0.6 M NaCl solution is elucidated via specimen geometries with varying degrees of connectivity:

   a. At or near the spreading potential (-0.73 V$_{SCE}$), the 3D specimen exhibited linear propagation kinetics up to 192 h, and transitioned to power law kinetics due to ohmic potential drop as a result of corrosion product accumulation and H$_2$ bubbles evolution. For the 2D specimen, the linear propagation kinetics is only observed up to 100 h due to the restricted

spreading, as well as vulnerability to grain fall-out. Only power law kinetics is observed for the 1D specimen.

b. At lower applied potentials (-0.80 V_{SCE}), only power law kinetics is observed for all three specimen geometries. This potential is not sufficiently high to trigger immediate active IGC damage. The current densities observed are in the passive regime, in the orders of 10^{-4} A/cm^2.

c. The relationship between the IGC rates and potential for the 3D degree of connectivity showed a single strong linear trend up to an exposure time of 192 h. For the 1D and 2D degree of connectivity, at exposure time of 100 h and longer, linear dependence of IGC rate on potential was also observed, with the dependence decreasing to a lesser extent with increasing exposure time due to larger ohmic resistance.

2. Computational resistor network analysis validated that the absence of ohmic potential drop on the IGC kinetics is driven by the multiple, interconnected fissures leading to effective resistance at the fissure tip.

3. The quantitative relationship of damage depth with time established via power law fitting suggested that the power law exponent n was primarily influenced by applied potential, with secondary effects from degree of connectivity.

4. Simple calculations suggest that the active and passive area partitioning during IGC propagation appears to be another significant factor that dictates IGC propagation rate and or applied potential response.

4.8   References

[1]   W. Zhang, G.S. Frankel, Anisotropy of Localized Corrosion in AA2024-T3, Electrochem. Solid-State Lett. 3 (2000) 268–270. doi:10.1149/1.1391121.

[2]   T.-S. Huang, G.S. Frankel, Kinetics of sharp intergranular corrosion fissures in AA7178, Corros. Sci. 49 (2007) 858–876. doi:10.1016/j.corsci.2006.04.015.

[3]   W. Zhang, G.S. Frankel, Localized Corrosion Growth Kinetics in AA2024 Alloys, J. Electrochem. Soc. 149 (2002) B510–B519. doi:10.1149/1.1513984.

[4]   T.-S. Huang, G.S. Frankel, Influence of grain structure on anisotropic localised corrosion kinetics of AA7xxx-T6 alloys, Corros. Eng. Sci. Technol. 41 (2006) 192–199. doi:10.1179/174327806X120739.

[5]   T.-S. Huang, G.S. Frankel, Effects of Temper and Potential on Localized Corrosion Kinetics of Aluminum Alloy 7075, Corrosion. 63 (2007) 731–743. doi:10.5006/1.3278422.

[6]   S. Zhao, D.A. Wolfe, T.-S. Huang, G.S. Frankel, Generalized model for IGC growth in aluminum alloys, J. Stat. Plan. Inference. 137 (2007) 2405–2412. doi:10.1016/j.jspi.2006.09.021.

[7]   X. He, J.J. Noël, D.W. Shoesmith, Crevice corrosion damage function for grade-2 titanium of iron content 0.078 wt% at 95 °C, Corros. Sci. 47 (2005) 1177–1195. doi:10.1016/j.corsci.2004.06.022.

[8]   Z. Szklarska-Smialowska, Pitting corrosion of aluminum, Corros. Sci. 41 (1999) 1743–1767. doi:10.1016/S0010-938X(99)00012-8.

[9]   G.S. Frankel, The growth of 2-D pits in thin film aluminum, Corros. Sci. 30 (1990) 1203–1218. doi:10.1016/0010-938X(90)90199-F.

[10]   D. Mizuno, R.G. Kelly, Galvanically Induced Intergranular Corrosion of AA5083-H131 Under Atmospheric Exposure Conditions: Part 1—Experimental Characterization, Corrosion. 69 (2013) 580–592. doi:10.5006/0812.

[11]   M.L.C. Lim, J.R. Scully, R.G. Kelly, Intergranular Corrosion Penetration in an Al-Mg Alloy as a Function of Electrochemical and Metallurgical Conditions, Corrosion. 69 (2013) 35–47. doi:10.5006/0722.

[12]   M.L. Lim, R. Kelly, J. Scully, Overview of Intergranular Corrosion Mechanisms, Phenomenological Observations, and Modeling of AA5083, Corrosion. (2015). doi:10.5006/1818.

[13]   R. Howard, N. Bogh, D.S. Mackenzie, Heat Treating Processes and Equipment, in: G.E. Totten, D.S. Mackenzie (Eds.), Handb. Alum., Marcel Dekker, Inc., New York, NY, 2003.

[14]   ASTM, ASTM: G67-04 Standard Test Method for Determining the Susceptibility to Intergranular Corroaion of 5XXX Series Aluminum Alloys by Mass Loss After Exposure to Nitric Acid (NAMLT Test), ASTM International, West Conshocken, PA, 2004.

[15]   A.B. Cook, D.L. Engelberg, N.P. Stevens, N.J. Laycock, S. White, M. Ghahari, et al., Pit Propagation in Pure Aluminum Investigated via the 1D Artificial Pit Technique: Growth Regimes, Surface Morphology and Implications for Stability Criteria, ECS Trans. 41 (2012) 121–132. doi:10.1149/1.3697583.

[16]   S. Jain, M.L.C. Lim, J.L. Hudson, J.R. Scully, Spreading of intergranular corrosion on the surface of sensitized Al-4.4Mg alloys: A general finding, Corros. Sci. 59 (2012) 136–147. doi:10.1016/j.corsci.2012.02.018.

[17]   N. Birbilis, R.G. Buchheit, Electrochemical Characteristics of Intermetallic Phases in Aluminum Alloys - An Experimental Survey and Discussion, J. Electrochem. Soc. 152 (2005) B140–B151. doi:10.1149/1.1869984.

[18]   D.W. Buzza, R.C. Alkire, Growth of Corrosion Pits on Pure Aluminum in 1M NaCl, J. Electrochem. Soc. 142 (1995) 1104–1111. doi:10.1149/1.2044137.

[19]   K.P. Wong, R.C. Alkire, Local Chemistry and Growth of Single Corrosion Pits in Aluminum, J. Electrochem. Soc. 137 (1990) 3010–3015. doi:10.1149/1.2086150.

[20]   F. Hunkeler, H. Bohni, Determination of Pit Growth Rates on Aluminum Using a Metal Foil Technique, Corrosion. 37 (1981) 645–650. doi:10.5006/1.3577553.

[21]   E. Bumiller, Intergranular corrosion in AA5XXX aluminum alloys with discontinuous precipitation at the grain boundaries, PhD Dissertation, University of Virginia, 2011.

[22]   E.M. Bumiller, R.G. Kelly, Intergranular corrosion in AA5XXX: a case for continuous attack with a discontinuous active path, in: Dep. Def. Corros. Conf., NACE, Palm SPrings, CA, 2011.

[23]   C. Crane, R. Kelly, R. Gangloff, Crack Chemistry Control of Intergranular SCC in Sensitized Al-Mg, Corrosion. (2015). doi:10.5006/1852.

[24]   C.B. Crane, Validation of the Coupled Dissolution-Hydrogen Embrittlement Mechanism of IGSCC in Low Temperature Sensitized AA5083-H131, PhD Dissertation, University of Virginia, 2013.

4.9   Appendix

```
%    Resistor Network
%    4R in L and R in S (single fissure)

% Set problem parameters
N=1;          % Number of repetitive units
R=1;          % Resistance [Ohm]
V0=1;         % Applied voltage [V]

% Start clock
tic;

% Set up matrix A
A=zeros((N+1)^2);
a=18/20/R;
b=33/20/R;
c=10/4/R;
d=-1/5/R;
e=-1/4/R;

% Set up first row
A(1,1)=a;

%Set up diagonal elements
i=1;
```

```
while (i<=((N+1)^2))
      if (i==N^2+1||i==(N+1)^2+1)
            A(i,i)=c;
      else A(i,i)=b;
      end;
      i=i+1;
end;

% Set up elements d
k=1; l=1;
while (k<=((N+1)^2))
      while (l<=N)
      if (k==N^2+1&&l==(N-1)^2+1)
            A(k,l)=d;
            A(l,k)=d;
      end;
      if (k==(N+1)^2&&l==(N)^2)
            A(k,l)=d;
            A(l,k)=d;
      end;
      l=l+1;
      end;
      l=1;
      k=k+1;
end;

%Set up elements e
m=N^2+2; q=N^2+2;
while (m>=N^2+2&&m<=(N+1)^2);
      p=m-1;
      A(m,p)=-1;
      A(p,m)=-1;
      m=m+1;
end;
while (q>=N^2+2&&q<=(N+1)^2-1);
      r=q-2*N;
      A(q,r)=-1;
      A(r,q)=-1;
      q=q+1;
end;

A=sparse(A);

% Set up constant vector b
b=zeros(((N+1)^2),1);
```

```
b(1)=V0/4/R;

% Solve equation system AV=b
V=A\b;

% Calculate total current through the network
I11=(V0-V(1))/R;

% Calculate effective resistance
Reff=V0/I11;

% Print results and elapsed time to screen
fprintf('I11(N=%i)  : %5.4f A\n',N,I11);
fprintf('Reff(N=%i) : %5.4f Ohm\n\n',N,Reff);

% End clock
toc
```

5 Understanding of Intergranular Corrosion Propagation Stabilization and Repassivation Tendencies

5.1 Abstract

The criteria for stable intergranular corrosion (IGC) propagation in AA5083-H131 were quantified in terms of repassivation potential (E_{rp}) and pit stability product (i*x). Further insight was developed on the origins of the critical potentials. The as-received AA5083-H131 exhibited a higher E_{rp} of -0.87 V_{SCE} as compared to the -0.90 V_{SCE} of the sensitized condition. The pit stability products for both as-received and sensitized AA5083-H131, were shown to be bounded by a potential below which only cathodic currents were exhibited. These bounding potentials were also compared to the E_{rp} values for both the as-received and sensitized conditions. A comparison of these potentials with the IGC propagation threshold potentials (E_{crit}) suggested that the fissure tip repassivation in the more aggressive fissure chemistry is the basis for the absence of IGC propagation at potentials below the E_{crit}. The lower E_{rp} for the sensitized condition was driven by the influence of the β-phase dissolution, in terms of the impact of Mg^{2+} concentration, on the fissure chemistry. The Mg^{2+} decreased the pH of the fissure chemistry, resulting in a more aggressive chemistry, which requires a lower repassivation potential, as well as a lower critical pit stability product, for the sensitized condition. These observations were utilized to establish a physical

229

phenomenon for stable IGC propagation in the context of applied potential, applied current density, and DoS.

5.2   Introduction

Intergranular corrosion along a grain boundary occurs in several stages: IGC initiation and spreading (dissolution at the alloy/solution interface), IGC penetration, IGC stifling, and finally, IGC arrest. As in pitting, the IGC phenomena in each of these stages involve complex interaction between the prevailing environment, metallurgy, and the electrode potentials at the alloy surface and fissure tip with its microstructural features exposed. However, these controlling processes for IGC in 5XXX alloys have not yet been determined. Nonetheless, some data on AA5083 regarding the existence of a threshold potential for IGC;[1,2] the potential dependence of IGC initiation and incubation time;[1,3,4] the local solution chemistry and fissure tip potential required for sustained propagation;[5] and the absence of an IGC stifling stage even after long exposures[4] are available in the literature. As such, potential, local chemistry, and microstructure likely play a key role in defining limitations for IGC stability.

The general consensus is that stable localized corrosion, assuming the Galvele acid pitting mechanism, requires a sufficiently aggressive condition at the localized corrosion site to depassivate the intergranular corrosion site. Two electrochemical criteria are known to determine whether these conditions are sustained assuming the acid pit mechanism, a critical potential, E_{crit}, and a stability

product, $(i*x)_{crit}$.[6–9] Conditions are sustained as long as the potential is more positive than E_{crit}, or when the product of dissolution current density, i, and propagation depth, x, exceeds $(i*x)_{crit}$, allowing localized corrosion to propagate stably.

While the concept of E_{crit} is well accepted, what constitutes a critical potential is still debated. For localized corrosion, E_{crit} is usually characterized by the repassivation potential, E_{rp}, the potential at which stably growing localized corrosion will cease to grow. Unfortunately, measurements are not currently available for AA5083-H131. Neither the IGC spreading potential (-0.73 V_{SCE}) nor the β breakdown potential (-0.96 V_{SCE}) in 0.6 M NaCl solution is the basis for the observed IGC threshold potential in Chapter 3. Bumiller[5] proposed that this threshold potential is related to the breakdown potential of the matrix, α-solid solution phase, in the fissure solution, 80% to 100% saturated with Al-4wt% Mg (the α-phase solid solution composition). Interestingly enough, Bumiller found the breakdown potential of α in the fissure solution to be -0.87 V_{SCE},[5] which is within the range of measured IGC threshold potentials (Chapter 3, Figure 3.25). Knowing that the grain boundaries are not fully covered with β to form a continuous network, it is highly possible that during IGC penetration the exposed phase at the fissure tip or pit surface is the matrix α and not the β phase. For corrosion to proceed, it is necessary that the applied potential be above the critical potential for α pitting in fissure solution to enable breakdown of the passive film and dissolution of the α-

phase. However, this can only be true if the local fissure chemistry is within the saturation levels stated above.

The second electrochemical criterion, the stability product (i*x), was first developed by Galvele[7,8,8] for a one-dimensional pit model based on a reaction-mass transport type model where a critical chemistry must be maintained. He demonstrated that the anodic reaction in the local environment must be able to sustain sufficient chloride concentration by inward electromigration and acidity, via cation hydrolysis to depassisivate a pit bottom, in the face of the outward diffusion of the aggressive environment. Sufficient acidity and depassivating anion concentration form a critical chemistry for pit stability, as characterized by the pit stability product. The relationship between the critical chemistry and the pit stability product can be described by the following expression:

$$(i * x)_{crit} = nFD(C_{crit} - C_{bulk})$$
(Equation 5.1)

where n is the valence of the metal dissolution reaction, F is the Faraday's constant, D is the diffusivity of metal cation, C_{crit} is the metal cation concentration below which the pit base repassivates, and C_{bulk} is the concentration of the metal cation in the bulk solution. For a given system with (i*x)$_{crit}$, the smaller the pit depth or diffusive path, the greater the critical current density required to cause stable pit growth. Noticeably, the pit stability product as originally constructed is independent of potential, which means that the pit can continue to propagate as long as the current density satisfies the pit stability product. However, in reality, there

are a number of important potentials. For instance, the potential at the pit base can only decrease down to the material's corrosion potential in the saturated pit solution, OCP_{sat}. Therefore, the minimum potential to maintain critical chemistry for pit propagation cannot be lower than OCP_{sat}. In fact, the minimum potential has to be more positive than OCP_{sat} because at the corrosion potential, the cathodic water reduction reaction rate is equal to the anodic dissolution reaction rate consuming protons, increasing the local pH, and loss of stability. As such, the pit stability criterion has to be bounded by a potential. This brings forth the question of how this bounding potential relates to the IGC threshold potential or the E_{crit} criterion.

Although the pit stability product has been utilized extensively in pit growth studies across a number of metal systems, there are currently no pit stability product measurements for Al-Mg alloys. For pure Al, the pit stability product was estimated to be 0.01 A/cm via artificial pit experiments.[10,11] The pit stability product for alloys may vary from that of pure Al for two reasons – shift in pH regime for passive oxide stability and occluded chemistry difference due to hydrolysis of additional cations. Mg does not have a stable oxide at low pH,[12] and therefore is not expected to enhance the oxide stability of Al. In contrast, Mg exhibits hydrolysis equilibrium that is less favorable towards H^+ production than Al,[13] yielding a higher pH solution saturated with metal cations, which should increase the critical pit stability product. Thus, there is a need to measure critical

pit stability products for both the unsensitized and the sensitized AA5083 to clarify how Mg, and subsequent sensitization, influences $(i*x)_{crit}$ of Al.

5.3   Objective

The primary objective of this chapter is to gain a fundamental understanding of what microstructural, chemical, and electrochemical factors control stable IGC propagation in sensitized AA5083-H131, taking into account the heterogeneous grain boundary metallurgy, the fissure chemistry, and the local electrochemistry. The stability criteria for IGC propagation based on the Galvele framework will be established via repassivation potential and pit stability product measurements. These criteria will be compared to the IGC threshold potential reported in Chapter 3 to examine their roles in propagation stabilization.   Finally, a physical phenomenon behind the critical pit stability criterion in the context of factors such as applied potential, applied current density, and DoS will be developed.

5.4   Experimental Procedures

5.4.1   Materials, Microstructure, and Degree of Sensitization

5.4.1.1 Bulk Materials

The commercial AA5083 (UNS A95083) plates utilized in this work were provided by the Aluminum Company of America (Alcoa), in H131 temper with plate thickness of 2.25" (5.715 cm). In the H131 temper state, the AA5083 is strain hardened without supplementary thermal treatment to have a mean ultimate tensile

strength (UTS) equivalent to three-eighths of the UTS of a full-hard condition (about 75% cold reduction after full annealing) for this alloy.[14]   The nominal chemical composi`tion of all AA5083 used in this study is presented in Table 5.1. The orientation convention and the microstructure of the three tempers showing anisotropic unrecrystallized grains after Barker's etching are given in Figure 5.1. The average grain widths at the relevant mid-thickness location in the longitudinal (L), long transverse (T), and short transverse (S) directions is 80 µm, 60 µm, and 20 µm, respectively.

Table 5.1. Nominal composition of AA5083 (UNS A95083)

Component	Al	Mg	Mn	Fe	Si	Cu	Cr	Zn	Ti	Others
Weight %	Bal	4.4	0.7	0.22	0.1	0.05	0.08	0.02	0.02	< 0.01
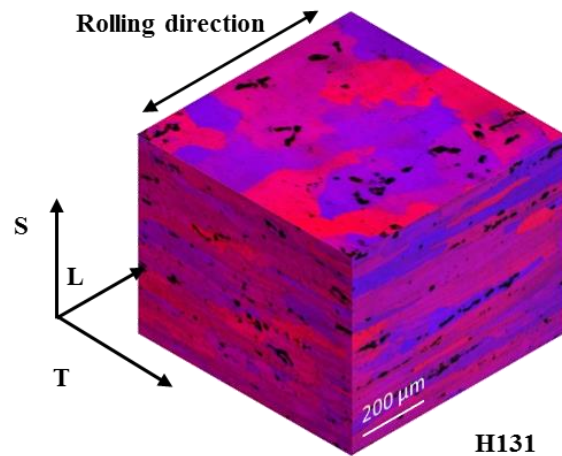
Figure 5.1 Microstructure of AA5083-H131 after electrolytic etching Barker's etching revealing elongated grain structure.

The specimens were cut from the center of the plate (S/2) into standard ASTM-G67[15] size of 5.1 cm x 2.5 cm x 0.6 cm (L x S x T) pieces, and were

utilized in as-received and sensitized conditions. The sensitized specimens were heat treated at 100°C for 30 days. Duplicate specimens was prepared in accordance with ASTM G-67 for measurement of DoS via the nitric acid mass loss test (NAMLT).[15] After immersing the specimens in 70% (v/v) HNO$_3$ for 24 h at 30°C, an average DoS of 3 and 50 mg/cm^2 were measured for the as-received and the sensitized conditions.

Bulk α-matrix specimens were synthesized via induction melting of high purity aluminum and magnesium (99.99% and 99.9999%, respectively).[1] The magnesium slug and aluminum shot were proportioned by weight to obtain the final composition ratio of the α-matrix. The materials were then combined in a boron-nitride-coated crucible and inductively melted under an Argon atmosphere. The specimens were cooled, solidified, and homogenized at 285°C for 10 h. Table 5.12 shows the nominal chemical composition of the α-matrix obtained via inductively coupled plasma – optical emission spectroscopy (ICP-OES) technique.[5]

Table 5.2. Nominal composition of cast α-matrix phase

Component	Al	Mg	Mn	Fe	Si	Cu	Cr	Zn	Others
Weight %	96.08	3.78	<0.01	0.06	0.05	0.02	<0.01	<0.01	< 0.01

5.4.1.2 Wire Materials

Three wire materials were utilized in this study: AA5083-H131, magnesium, and aluminum. The AA5083-H131 wires with 112 µm diameter were prepared from the same bulk AA5083-H131 as described above through the

---

[1] α-matrix phase specimens were synthesized by Gary Shiflet at the University of Virginia.

Materials Preparation Center at Ames Laboratory, which is supported by the US DOE Basic Energy Sciences. The AA5083-H131 wire was utilized both in the as-received (unsensitized) state as well as the sensitized state. Sensitization heat treatment was conducted at 100°C for 30 days, with a DoS of 50 mg/cm^2. The DoS value was adapted from that of the bulk AA5083-H131 subjected to the same sensitization heat treatment condition.

The 127 µm diameter 99.99 % Mg wire from Sigma-Aldrich and the 50 µm diameter 99.99 % Al wire from California Fine Wires were used in artificial pit experiments. Table 5.3 and Table 5.4 show the nominal chemical composition of the Al and Mg wires, respectively.

Table 5.3. Nominal composition of 99.99% Mg wire used in this study

Component	Mg	Al	Fe	Cu	Zn	Mn	Ni	Others
Weight %	Bal	0.02	0.008	0.003	0.03	0.005	0.01	< 0.01

Table 5.4. Nominal composition of 99.99% Al wire used in this study

Component	Al	Mg	Fe	Cu	Zn	Mn	Si	Others
Weight %	Bal	0.003	0.006	0.006	0.003	0.005	0.003	< 0.005

5.4.2   Sample Preparation for Electrochemical Testing

All bulk AA5083-H131 samples were cut from the center of the plate (S/2) into 6mm x 6mm x 6mm pieces. Samples were mounted in Buehler EpoThin epoxy resin and allowed to cure at room temperature (~25°C) for 9 h. All wire samples were also encapsulate in epoxy resin in a lead in pencil setup. The mounted samples were alternatingly ground with SiC paper and rinsed with water down to 1200 grit.

The samples were then polished with 1 μm diamond paste and finished with 0.06 μm colloidal silica. Samples were ultrasonically cleaned in ethanol to remove any silica debris and air dried prior to testing.

5.4.3 Experimental Setup for Electrochemical Testing

A three-electrode cell setup, composed of a working electrode, a reference electrode and a counter electrode, was utilized for electrochemical testing. In all cases, a platinum mesh was utilized as the counter electrode. For the setup involving 3D planar and thin foil working electrodes, a saturated calomel electrode (SCE) equipped with a Luggin capillary was used as the reference electrode in a conventional flat cell setup. Whereas a vertical cell setup limiting possibility of trapped gas bubbles, and allowing a SCE reference electrode to be situated close enough to the working electrodes, was used for the wire specimens. This setup was connected to a potentiostat (Gamry PCI4, or Biologic VMP 3) with a computer interface software to control and measure potential and current during DC electrochemical experiments. For experiments involving wire specimens, Gamry Femto-stat, Gamry Reference 600, and Biologic SP-200, which are capable of low current measurements, were utilized.

5.4.4 Anodic Potentiodynamic Scan on α-matrix Phase

Anoidc potentiodynamic scans were conducted on 1 cm^2 α-matrix phase specimens in freshly prepared quiescent solutions of 2 M $AlCl_3$ and $MgCl_2$. The

MgCl$_2$ concentrations ranged from 0.1 to 1.5 M. The potentiodynamic scans from -0.15 V vs. OCP up to a cut off current density of 25 mA/cm2 at a scan rate of 0.5 mV/s were conducted after a 5 minute open circuit potential (OCP) hold.

5.4.5 Potentiodynamic Scans for Repassivation Potential Measurements

Potentiostatic holds on bulk as-received and sensitized AA5083-H131 for various lengths of time were conducted to generate various levels of accumulated charge density in quiescent 0.6 M NaCl solution at a pH 8.3. An applied potential of -0.73 V$_{SCE}$ was selected to ensure the mode of corrosion is IGC. Exposure time ranged from 1 minute to 72 h. Potentiodynamic scans from -0.73 V$_{SCE}$ to -0.15 V vs OCP at a scan rate of 0.5 mV/s were conducted immediately after IGC generation. The repassivation potential was taken as the potential at which the current density is 30 μA/cm^2.

5.4.6 Pit Stability Product Measurements

Pit stability product was evaluated by potentiostatic holds on flush mounted wires of as-received and sensitized AA5083, and Mg in an artificial pit configuration using a flat cell setup. An artificial pit was initiated and grown by a potentiostatic hold in quiescent 0.6 M NaCl solution at pH of 8.3. The cross-sectional surfaces of the wires were exposed to open circuit potential for 30 minutes and then held at an anodic potential of 1 V$_{SCE}$ for 1200 s, followed by a fast scan down at 25 mV/s to a lower applied potential of interest. Specimens were held at

the lower potential for 100 s. This was conducted on a range of lower applied potentials from -1.05 to -0.55 V_{SCE}. The measured current was integrated to determine the net charge, which was utilized to calculate the theoretical artificial pit depths via Faraday's law. The theoretical pit depths were corrected for local cathodic distribution using the respective current efficiency factor for each material to obtain the actual pit depth. The pit stability product at a given potential is the product of the actual depth and the average current density over the 100 s hold.

5.4.7 Anodic Kinetics in Pit Chemistry

One dimensional growth of the pit was examined by potentiostatic hold on flush mounted wires of as-received and sensitized AA5083 an artificial pit configuration using a flat cell setup. An artificial pit was initiated and grown by a potentiostatic hold in quiescent 0.6 M NaCl solution at pH of 8.3. The cross-sectional surface of the wires were exposed to open circuit potential for 30 minutes and then held at an anodic potential of 1 V_{SCE} for various lengths of time depending on pit depth of interest. Three pit depths were generated: 1000, 1500, and 2000 µm. Following the potentiostatic hold, the pit was allowed to dilute from 100% saturation under open-circuit conditions for different periods of time, as determined from a diffusion model for a one dimensional semi-infinite system, in order to attain different surface concentrations. The diffusion model assumes a 3.11 M Al^{3+} as 100% saturation based on the 100% saturation for stoichiometric dissolution of α-phase (Al-4wtMg).[5] A rapid anodic polarization scan at 100 mV/s to a final

potential of 1 V_{SCE} was performed once each surface concentration was attained. Each successive dilution was carried out as soon as the previous polarization scan had been completed. In this manner, at every pit depth attained, a series of anodic kinetics scans was obtained for a range of surface concentrations. Each set of kinetic measurements were made once the pit had grown to the following depths: 1000 μm, 1500 μm, and 2000 μm.

This fast scan allows for the preservation of the pit solution, where the diffusion length of the ionic species ($\sqrt{\pi D t}$) is smaller than the pit depth during the potentiodynamic downward scan. Given the diffusivity of Al^{3+} and the scan range of 1 V_{SCE} to -1.25 V_{SCE}, the diffusion length at the end of the scan (t = 45 s) is 160 μm. This is a smaller length than the artificial pit depths generated and examined in this study.

5.4.8   Hydrolysis Calculations

Hydrolysis reaction occurs when metal cations reacts with water to form hydroxides in aqueous solution. The following sets of monomeric hydrolysis equilibrium reactions, and the respective formation constants, were used to construct the individual stability diagrams:[13]

Aluminum:

$$Al^{3+} + H_2O \leftrightarrow AlOH^{2+} + H^+ \qquad pK_{11} = 4.97 \qquad \text{(Equation 5.2)}$$

$$Al^{3+} + 2H_2O \leftrightarrow Al(OH)_2^+ + 2H^+ \qquad pK_{12} = 9.3 \qquad \text{(Equation 5.3)}$$

$$Al^{3+} + 3H_2O \leftrightarrow Al(OH)_3 + 3H^+ \qquad pK_{13} = 15.0 \qquad \text{(Equation 5.4)}$$

$$Al^{3+} + 4H_2O \leftrightarrow Al(OH)_4^- + 4H^+ \qquad pK_{14} = 23.0 \qquad \text{(Equation 5.5)}$$

Magnesium:

$$Mg^{2+} + H_2O \leftrightarrow MgOH^+ + H^+ \qquad pK_{11} = 11.44 \qquad \text{(Equation 5.6)}$$

$$Mg^{2+} + 2H_2O \leftrightarrow Mg(OH)_2 + 2H^+ \qquad pK_{12} = 11.15 \qquad \text{(Equation 5.7)}$$

Manganese:

$$Mn^{2+} + H_2O \leftrightarrow MnOH^+ + H^+ \qquad pK_{11} = 10.59 \qquad \text{(Equation 5.8)}$$

$$Mn^{2+} + 2H_2O \leftrightarrow Mn(OH)_2 + 2H^+ \qquad pK_{12} = 22.2 \qquad \text{(Equation 5.9)}$$

$$Mn^{2+} + 3H_2O \leftrightarrow Mn_2(OH)_3^- + 3H^+ \qquad pK_{13} = 34.8 \qquad \text{(Equation 5.10)}$$

$$Mn^{2+} + 4H_2O \leftrightarrow Mn(OH)_4^{2-} + 4H^+ \qquad pK_{14} = 48.3 \qquad \text{(Equation 5.11)}$$

Only monomeric hydrolysis products were considered since they form rapidly and reversibly and can easily establish an equilibrium in response to changes in concentrations of reactants or products.[13] In a a survey of cation hydrolysis, Baes and Mesmer estimated the interaction coefficients of Al^{3+}, Mg^{2+}, and Mn^{2+} were independent of ionic strength.[13]

The stability diagrams were constructed independently, such that it was assumed that there is no interaction amongst the hydrolysis species of the three different cations. Mass action equations were written for all of the hydrolysis

242

equilibrium reactions for a given cation. Take for instance the formation of $Al(OH)^{2+}$, the mass action expression would be:

$$[AlOH^{2+}] = Q_{11} \frac{[Al^{3+}]}{[H^+]}$$ (Equation 5.12)

Similar reaction sets are written for each of the other remaining hydrolysis species. These expressions are simply rearranged to give the concentration of hydrolysis species in terms of formation quotient, cation concentration, and pH. In the case of $Al(OH)^{2+}$, the fraction of hydrolysis species, F, is

$$F_{AlOH^{2+}} = \frac{[AlOH^{2+}]}{[Al^{3+}]+[AlOH^{2+}]+[Al(OH)_2^+]+[Al(OH)_3]+[Al(OH)_4^-]}$$ (Equation 5.13)

Each of the species in the above equation is written in terms of $[Al^{3+}]$, $[H^+]$, and K_{sp}. The $[Al^{3+}]$ terms cancel, which leaves the $[H^+]$ as the independent quantity in the expression. The quantity $[H^+]$ is then varied over the pH range 0 to 14 to generate distribution diagrams. Diagrams of magnesium and manganese were constructed in the same manner.

Each metal cation produced consumes some hydroxyl, the precise number is pH-dependent. The extent of hydrolysis is expressed quantitatively as the number of hydroxyl ions consumed per cation produced from dissolution. The consumption of hydroxyl ions is dependent on the availability of hydroxyl ions, which is determined by the rate of the local cathodic reactions. Assuming the

cathodic reactions are hydrogen evolution or water reduction, then one hydroxyl is generated per electron released by the cation, independent of pH. As such, pH can be utilized as a metric related to the cathodic reaction rate. Complete cation hydrolysis occurs when the number of hydroxyl ions consumed per cation is equal to the valence of the cation. Thus, the number of hydroxyl ions consumed per cation can also be estimated as a function of pH. The hydrolysis of AA5083 cation was considered to follow the congruent hydrolysis of the three major metal cations, Al^{3+}, Mg^{2+}, and Mn^{2+} in the same stoichiometric ratio present in the alloy. Similarly, Al^{3+} and Mg^{2+} were considered for the hydrolysis of cations generated from dissolution of α-phase and β-phase.

5.5   Results

5.5.1   Dissolution Kinetics of α-Matrix Phase

The IR-corrected anodic polarization curves for α-phase in solution of 2 M $AlCl_3$ with varying concentrations of $MgCl_2$ are shown in Figure 5.2. Individual replicate scans varied little in terms of potential and current density. The variation in potential were 5 mV, whereas the variations in current density were an order of magnitude lower than the measured. It has to be noted, however, that significant variations in both potential and current density were observed in a one day old electrolyte. The pH of these solutions was measured to be lower than the pH of freshly mixed solutions. The open circuit potentials and corrosion rates extracted from the polarization curves were plotted in Figure 5.3 as a function of $MgCl_2$

concentration. The corrosion rates measured were at the same order of magnitude across the range of concentration. This implies that at OCP, the α-phase reactivity does not change with MgCl$_2$ concentration. However, open circuit potentials of the α-phase increases with increasing MgCl$_2$ concentration, within the range of 100 mV. This suggests that the increase in MgCl$_2$ concentration can serve to polarize the α-phase to slightly anodic potentials.
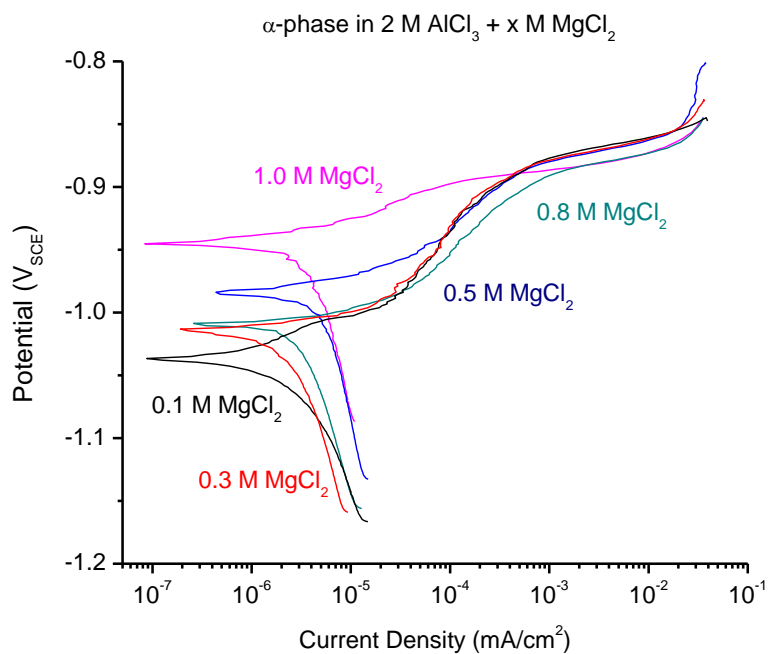
Figure 5.2. Polarization behavior of Al-4Mg (α-phase) in 2 M AlCl$_3$ with varying amounts of MgCl$_2$.
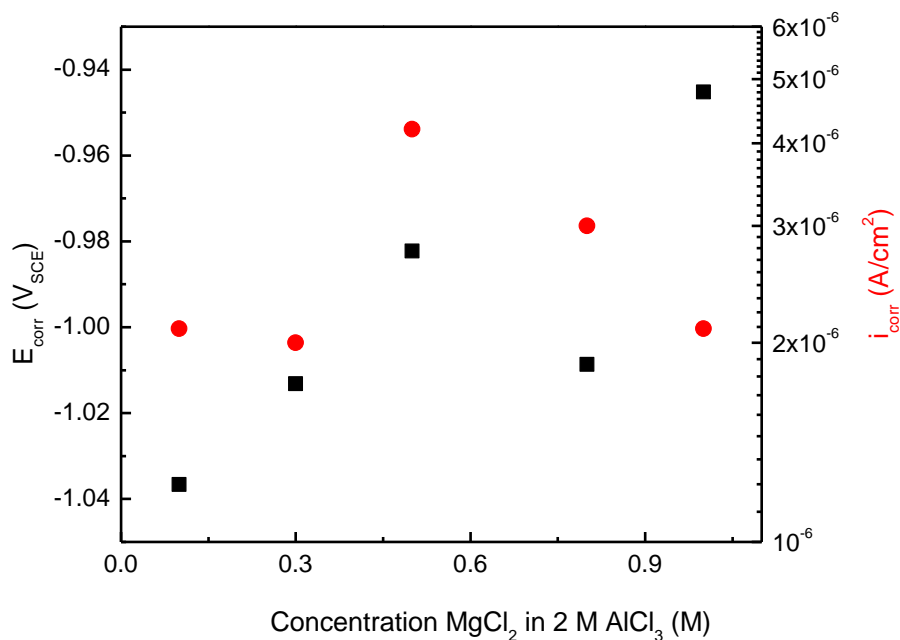
Figure 5.3 Open circuit potential and corrosion rate of α-phase in 2 M AlCl₃ as a function of MgCl₂ concentration.

5.5.2 Repassivation Potential for As-received and Sensitized AA5083

The repassivation potential of as-received and sensitized AA5083-H131 in 0.6 M NaCl solution, pH 8.3 was evaluated as a function of charge passed after pit generation at -0.3 V_{SCE} or IGC generation at -0.73 V_{SCE}, for pit and bulk specimens, respectively. A threshold current density of 30 $\mu A/cm^2$ was utilized to identify the E_{rp} from potentiodynamic scans conducted immediately after the potentiostatic holds. Figure 5.4 and Figure 5.5 show typical polarization curves for artificial pit specimens of as-received and sensitized AA5083-H131 at a charge density of ~100 C/cm^2 (depth of ~ 50 μm). In both conditions, noisy current density response were observed during the downward scan is due to the presence of salt film at the pit

surface. The waning noise as the downward scan ensued implies pit chemistry dilution and dissolution of the salt film, where the shoulder formed. At a higher charge density of ~2000 C/cm^2 (depth of ~920 µm), the polarization curves exhibited noise throughout the downward scan. For both instances of low and high charge densities, the identified E_{rp} was near if not at the OCP. The E_{rp} values of the as-received condition were higher than those of the sensitized AA5083-H131.
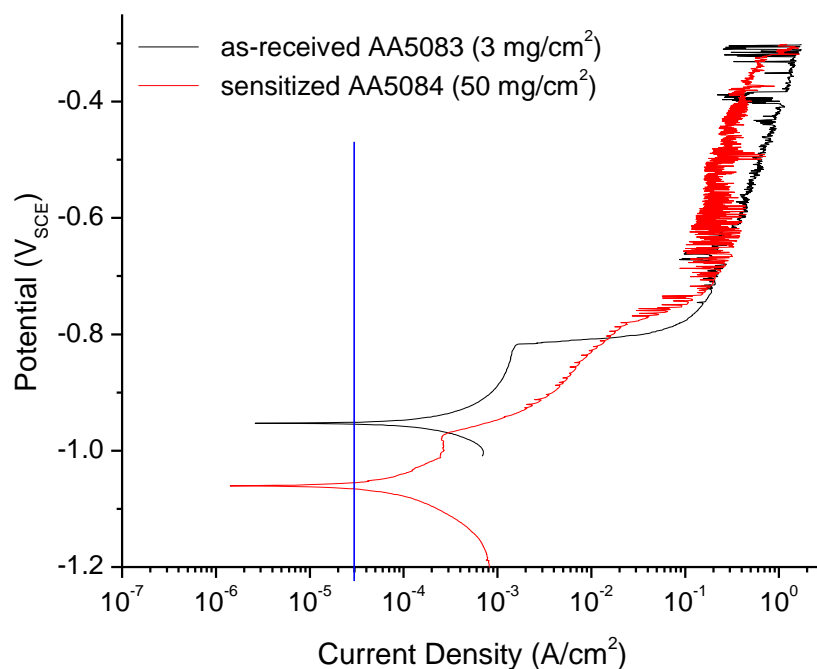
Figure 5.4.   Polarization curve of AA5083-H131 artificial pit in 0.6 M NaCl solution with 97 C/cm^2 and 112 C/cm^2 accumulated charge density for the as-received and sensitized condition, respectively.
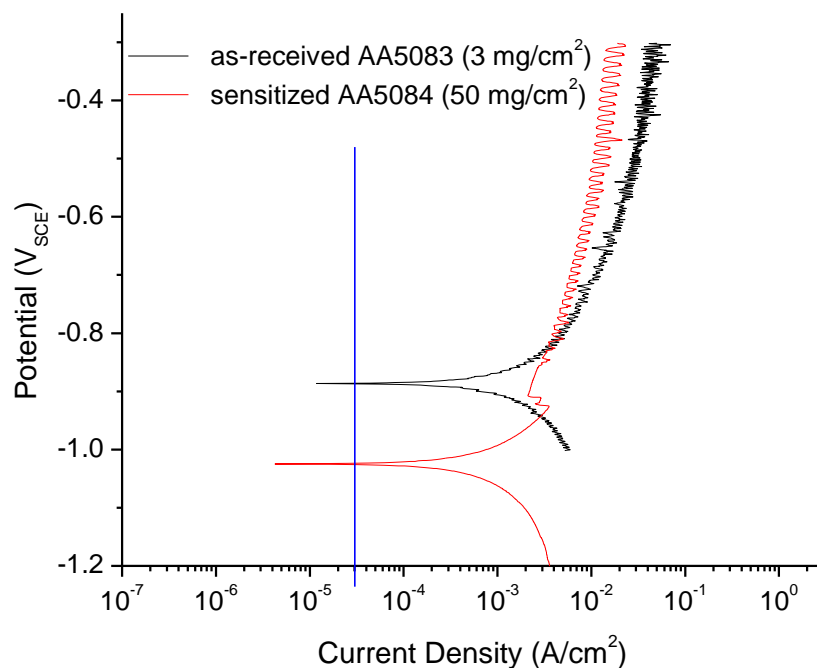
Figure 5.5. Polarization curve of AA5083-H131 artificial pit in 0.6 M NaCl solution with 2000 C/cm^2 and 1795 C/cm^2 accumulated charge density for the as-received and sensitized condition, respectively.

The polarization curves for bulk as-received and sensitized AA5083-H131 at a charge density of 5 C/cm^2 and 200 C/cm^2 are shown in Figure 5.6 and Figure 5.7, respectively. For both instances, the polarization curves are smooth, without evidence of salt film, which forms at high potential and dissolves at low potential. Similar to the artificial pit specimens, the E_{rp} values of the as-received condition were higher than those of the sensitized AA5083-H131. The measured E_{rp} as a function of charge density for bulk as-received and sensitized AA5083-H131 specimens is shown in Figure 5.8. For the as-received AA5083-H131 bulk specimens, E_{rp} decreased with increasing charge density, and started to plateau at a

charge density of 40 C/cm^2. Above this charge density, the E_{rp} measured is within a narrow range of -0.878 to -0.862 V_{SCE}. This decrease to a constant E_{rp} behavior as a function of charge density is consistent with the observations made on pitting and crevice corrosion of aluminum and stainless steel.[16,17] The bulk sensitized specimens also followed the same trend of decreased in E_{rp} with increasing charge density, although at steeper slope yielding lower E_{rp} values. Above a charge density of 3 C/cm^2, the E_{rp} plateau within the range of -0.981 to -0.968 V_{SCE}, lower than the range observed for the as-received material. However, this plateau was only maintained up to charge densities of 50 C/cm^2. At higher charge densities, the E_{rp} increased and exhibited a second plateau between -0.904 and -0.897 V_{SCE}. The repassivation observed at the more anodic initial plateau at -0.968 V_{SCE} is believed to be dominated by β-phase, whereas the second plateau at -0.90 V_{SCE} is associated with α-phase repassivation.
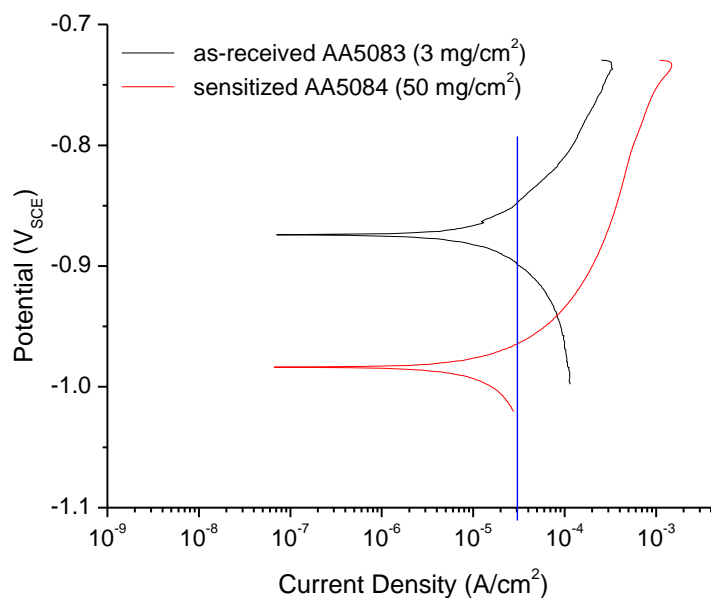
Figure 5.6. Polarization curve of AA5083-H131 bulk samples in 0.6 M NaCl solution with 200 C/cm^2 accumulated charge density for the as-received and sensitized condition, respectively.
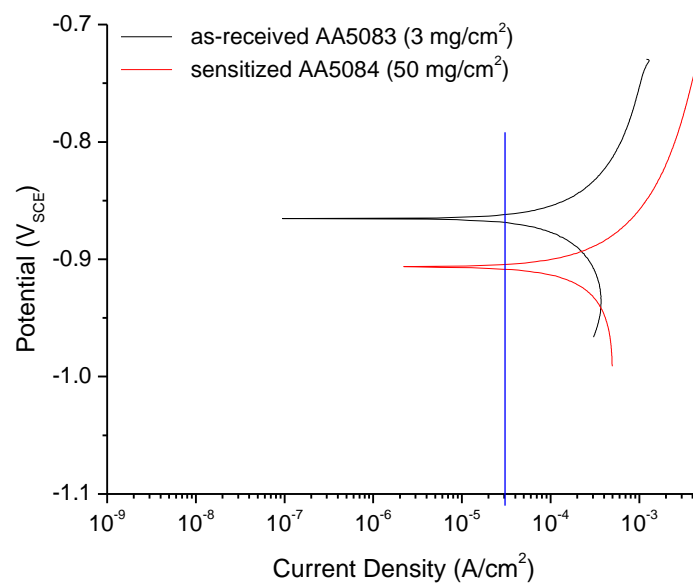
Figure 5.7. Polarization curve of AA5083-H131 bulk samples in 0.6 M NaCl solution with 5 C/cm^2 accumulated charge density for the as-received and sensitized condition, respectively.
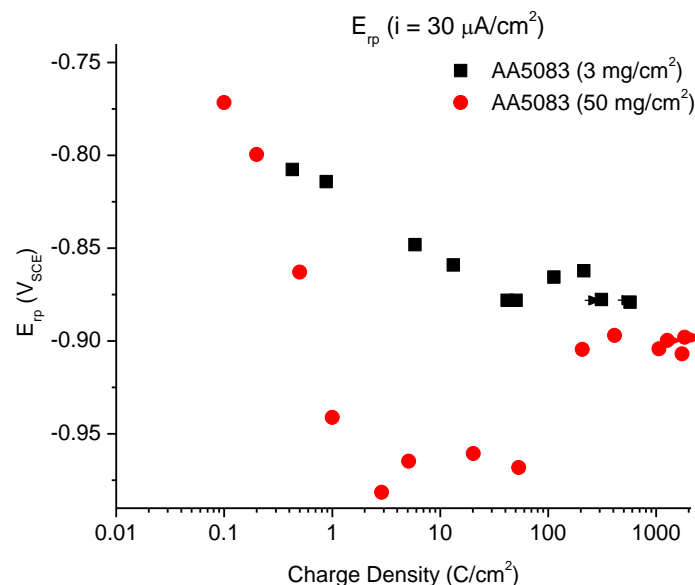
Figure 5.8. Repassivation potential as a function of charge density for as-received and sensitized AA5083-H131 bulk specimen in 0.6 M NaCl solution. The repassivation potential is taken as the potential at a current density of 30 µA/cm^2 during the downward polarization scan.

The E_{rp} measurements for the artificial pit specimens of as-received and sensitized AA5083-H131 are shown in Figure 5.9. The E_{rp} values for the sensitized specimens are lower than the as-received specimen, similar to the bulk specimens. However, the trend of decreasing E_{rp} with increasing charge density was not observed. On the contrary, an initial plateau was observed, which was followed by a trend of increasing E_{rp} with increasing charge density for both conditions. As shown earlier, the polarization curves at the high charge density manifested presence of salt film or at least high saturation levels of salt, making these values unreliable. If the plateau potentials are to be considered as the E_{rp}, the as received and sensitized AA5083-H131 is within the range of -0.963 to -0.949 V_{SCE} and -

1.063 to -1.029 V_{SCE}. These E_{rp} measurements are low as compared to those for

the bulk specimens. These difference could be an effect of the generally lower OCP

values of the wire relative to the bulk specimens.
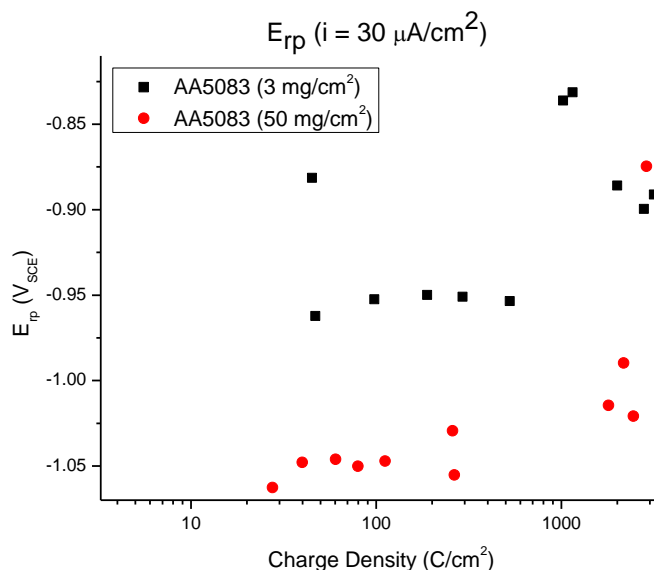
Figure 5.9. Repassivation potential as a function of charge density for as-received and sensitized AA5083-H131 artificial pit specimen in 0.6 M NaCl solution. The repassivation potential is taken as the potential at a current density of 30 µA/cm^2 during the downward polarization scan.

5.5.3   Pit Stability Product for Artificial Pit

Figure 5.10 shows typical data from an artificial pit experiment designed to

determine pit stability products of AA5083 and high purity polycrystalline Mg. In

this Figure, the initial applied potential of 1 V_{SCE} was held for 1200 s to generate

the pit in sensitized AA5083-H131. The potential was then stepped down to -0.7

V_{SCE} and held for 100 s. The apparent current density and the apparent pit stability

product are shown in addition to the applied potential. The charge data from the

same sequence of experiment shown in Figure 5.11 demonstrate negligible additional charge was generated during the latter potential hold. This can be translated to mean that the additional damage depth is insignificant.
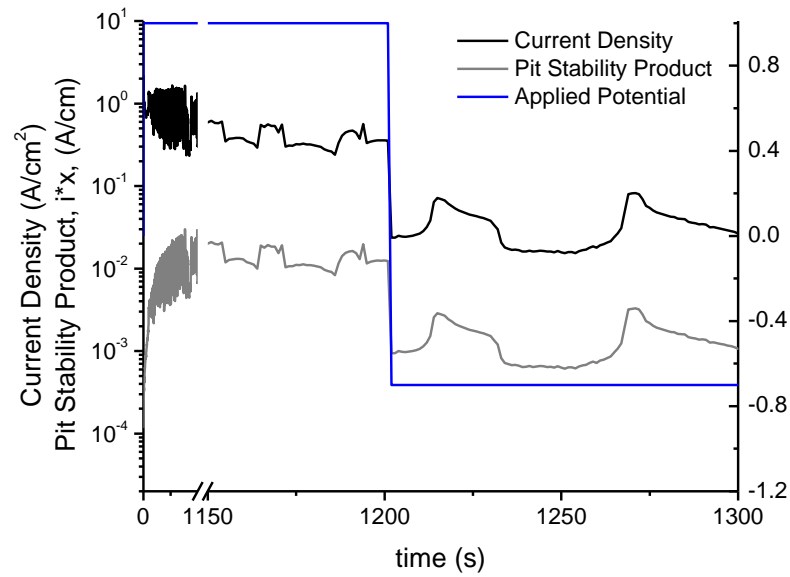
Figure 5.10. Apparent current density and apparent pit stability product as a function of time, involving a 1200 s of potentiostatic hold at 1 V_{SCE} followed by a 100 s hold at -0.7 V_{SCE} in 0.6 M NaCl solution for as-received AA5083-H131 artificial pit specimen.
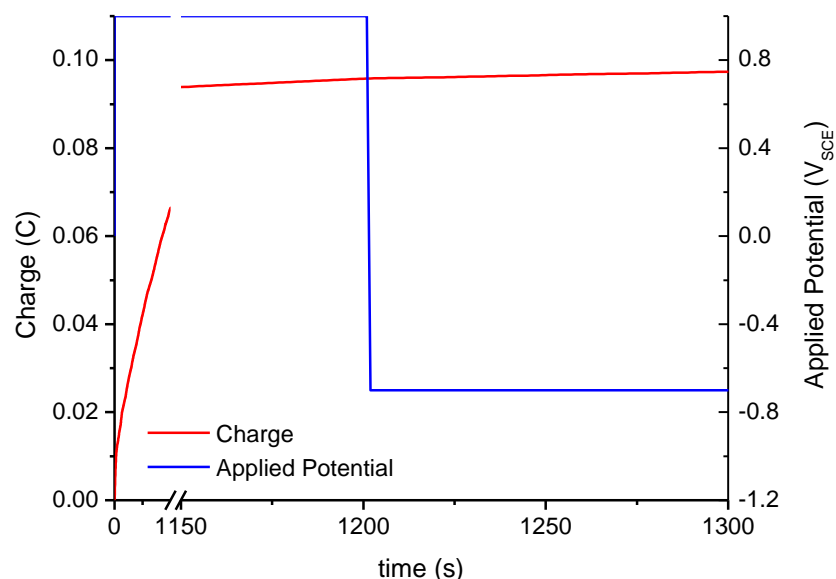
Figure 5.11. Charge as a function of time, involving a 1200 s of potentiostatic hold at 1 V_{SCE} followed by a 100 s hold at -0.7 V_{SCE} in 0.6 M NaCl solution for as-received AA5083-H131 artificial pit specimen.

The apparent current density and apparent pit stability product for the high purity Mg wire held at a latter potential of -0.7 V_{SCE} shown in Figure 5.12 did not exhibit a change in current density response following the potential step down. This implies that the artificial pit is growing under mass-transport control. The current densities are also higher relative to those measured on the as-received AA5083-H131. A comparison of the behavior of the as-received and sensitized AA5083-H131 at -0.7 V_{SCE} (Figure 5.14) shows that the apparent current density and the apparent pit stability product of the two conditions are within the same order of magnitude, 10^{-2} and 10^{-3}, respectively. As expected, for both the as-received and the sensitized AA5083-H131, the apparent current density and the apparent pit

stability product shown in (Figure 5.10, and Figure 5.13 to Figure 5.15) for -0.7 V_{SCE} and -0.8 V_{SCE} decreases with decreasing applied potential. At a lower applied potential of -0.9 V_{SCE}, a cathodic apparent current density was observed for the as-received, whereas anodic current density was still observed on the sensitized AA5083-H131. This implies that there is a bounding potential for pit stability, which is a function of sensitization.
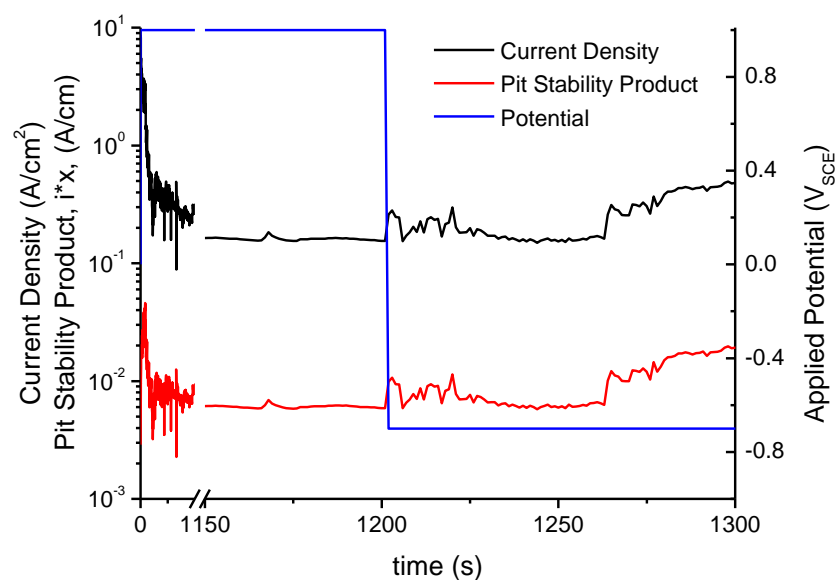
Figure 5.12. Apparent current density and apparent pit stability product as a function of time, involving a 1200 s of potentiostatic hold at 1 V_{SCE} followed by a 100 s hold at -0.7 V_{SCE} in 0.6 M NaCl solution for high purity Mg artificial pit specimen.
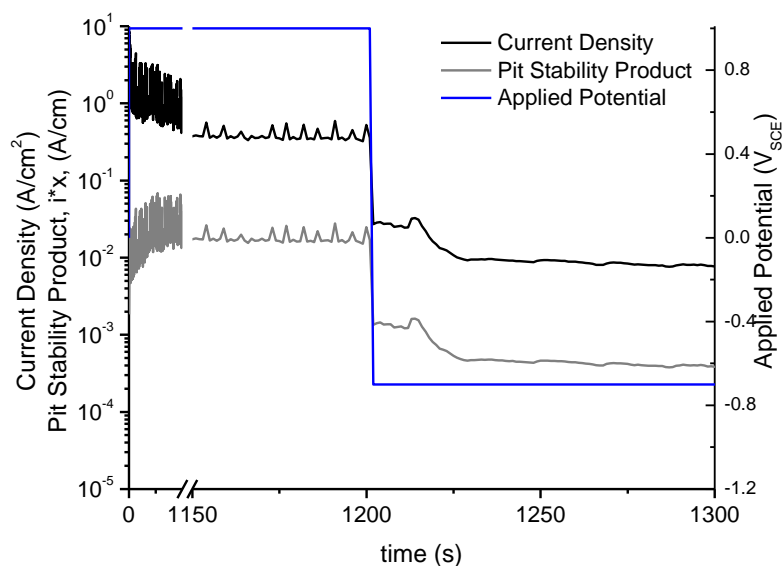
Figure 5.13. Apparent current density and apparent pit stability product as a function of time, involving a 1200 s of potentiostatic hold at 1 V_{SCE} followed by a 100 s hold at -0.7 V_{SCE} in 0.6 M NaCl solution for sensitized AA5083-H131 artificial pit specimen.
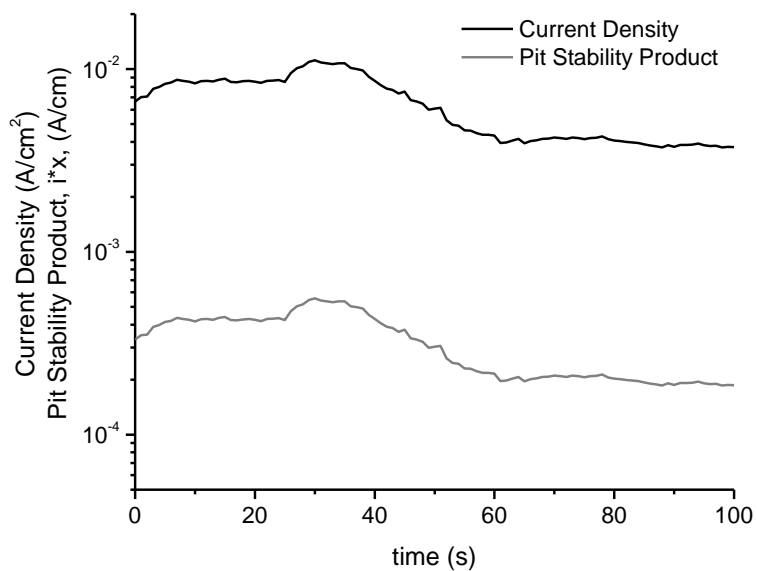
Figure 5.14. Apparent current density and apparent pit stability product as a function of time for sensitized AA5083-H131 artificial pit specimen held at -0.8 V_{SCE} in 0.6 M NaCl solution after a 1200 s potentiostatic hold 1 V_{SCE}.
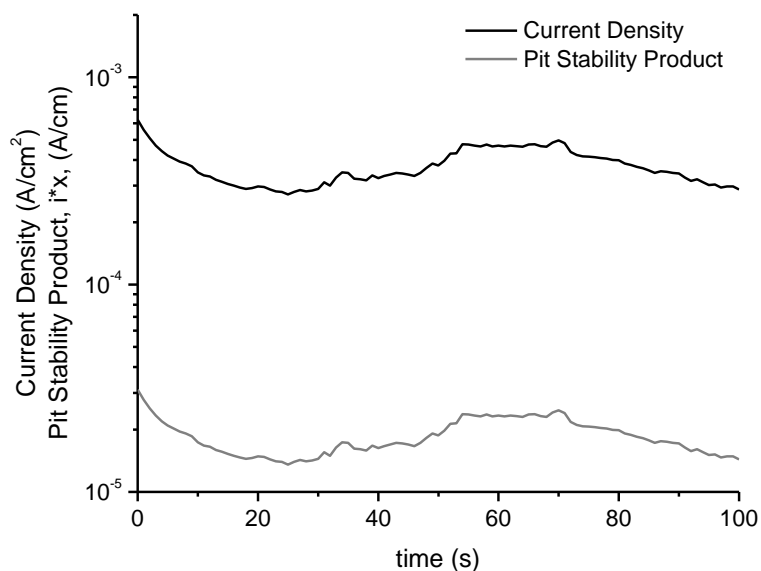
Figure 5.15. Apparent current density and apparent pit stability product as a function of time for sensitized AA5083-H131 artificial pit specimen held at -0.90 V_{SCE} in 0.6 M NaCl solution after a 1200 s potentiostatic hold 1 V_{SCE}.
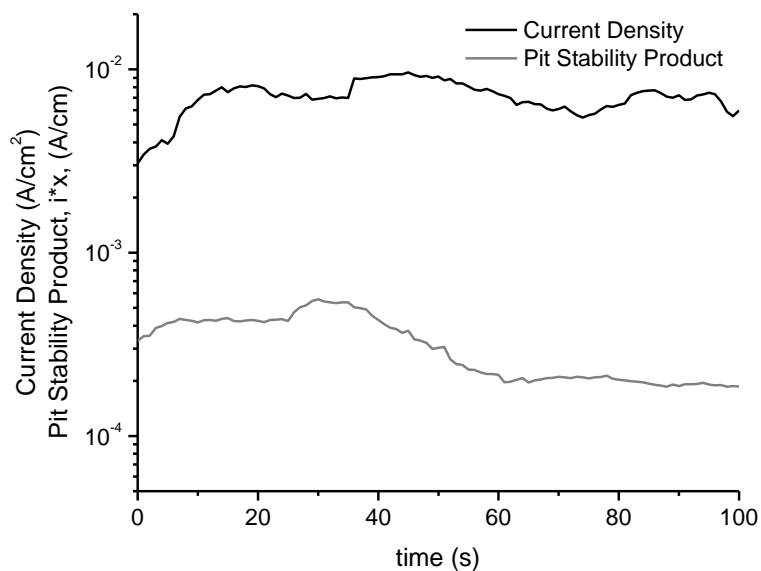
Figure 5.16. Apparent current density and apparent pit stability product as a function of time for as-received AA5083-H131 artificial pit specimen held at -0.80 V_{SCE} in 0.6 M NaCl solution after a 1200 s potentiostatic hold 1 V_{SCE}.
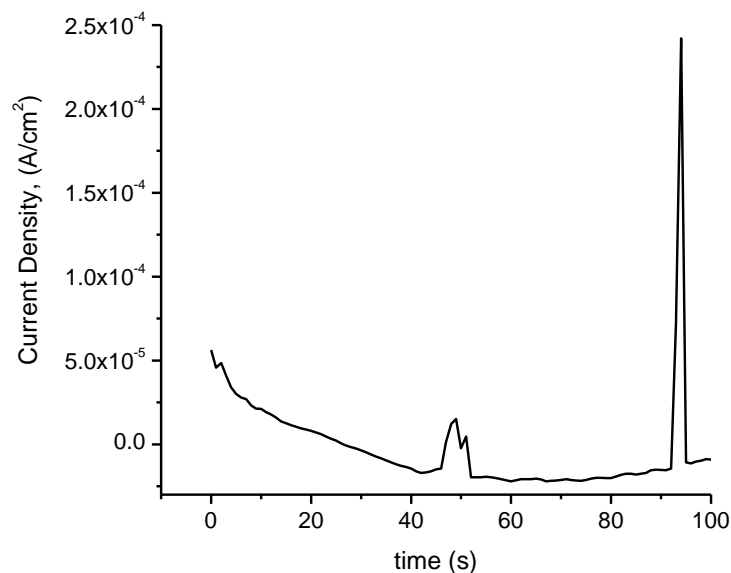
Figure 5.17.Apparent current density as a function of time for as-received AA5083-H131 artificial pit specimen held at -0.90 V_{SCE} in 0.6 M NaCl solution after a 1200 s potentiostatic hold 1 V_{SCE}.

The respective current efficiency factor for each material (Chapter 3) was used to correct the Faradaic damage depths to obtain the true damage depths. The true pit stability products as a function of applied potential for the different materials are displayed in Figure 5.18. For all the materials, a decrease in the average pit stability product was observed with decreasing potential. The plot indicates that the pit stability product is influenced by alloying and sensitization. At -0.55 V_{SCE}, the pit stability product of the as-received AA5083-H131 is 0.003 A/cm, which is lower than the 0.005 A/cm^2 observed for high purity Al,[18] but higher than the 0.002 A/cm of the sensitized AA5083-H131. At -0.75 V_{SCE}, the pure Al exhibited a dramatic drop in pit stability product, which was not observed

with the alloys, such that the pit stability products of the alloys are higher. Instead this drop was shown to occur on the as-received and sensitized AA5083-H131 at -0.825 V_{SCE} and -0.90 V_{SCE}, respectively. The decrease in i*x as a function of applied potential suggests that the pit chemistry is getting diluted faster than the dissolution rate at the pit bottom. The arrows represent the bounding potentials for pit stability product, below which cathodic currents were observed. The bounding potential for Al, as-received AA5083-H131, and sensitized AA5083-H131 is -0.80 V_{SCE}, -0.85 V_{SCE}, and -0.90 V_{SCE}, respectively. Neither the drop in pit stability product nor the bounding potential was observed with the high purity Mg, suggesting that the influence of sensitization is due to β-phase instead of Mg.

Figure 5.18. Average pit stability product (i*x) as a function of applied potential for different materials in 0.6 M NaCl solution.

5.5.4 Anodic Kinetics of Fissure Tip in Pit Chemistry

In order to probe the critical solution for stable pit growth, the anodic polarization scans were conducted on artificial pit specimens of various depth in different saturation levels of pit chemistry. Five levels of saturation were considered: 40%, 50%, 70%, 80%, and 90%. The IGC propagation threshold potential of -0.87 V_{SCE} or the breakdown potential of α-phase in saturated Al-4Mg solution was considered as a figure of merit because this is the E_{rp} value observed for the unsensitized AA5083. The current density at this potential, taken as the critical current density, was compared at different saturation levels, damage depths, and sensitization condition.

The anodic kinetics obtained at successively dilute surface concentrations at each of the three depths for the as-received and sensitized AA5083-H131 artificial pit are shown in Figure 5.19 to Figure 5.24. For all pit depths, in both the as-received and the sensitized conditions, a shift in the anodic polarization curves is apparent at 70% saturation. In general, the OCP decreases with decreasing saturation level. The critical current density was extracted from the curves and plotted as a function of level of saturation Figure 5.25 and Figure 5.26. At a depth of 1000 µm, the sensitized AA5083-H131 exhibited a current density of 0.009 A/cm^2 for 90% and 80% saturation, decreased to 0.002 A/cm^2 at 70% saturation, followed by a drop to 0.0002 A/cm^2 at 50% and 40%. This trend was observed for both the sensitized and the as-received AA5083-H131 across all the depths, which

indicates that below 70% saturation, the solution is not aggressive enough to support high dissolution rate inside the pit.
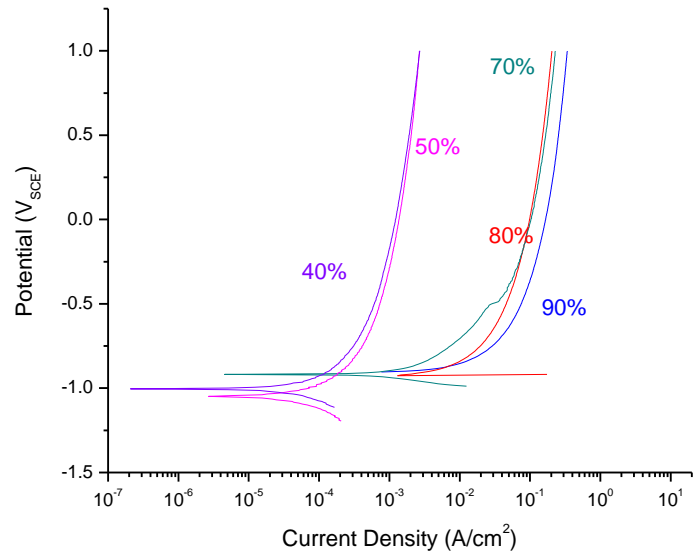
Figure 5.19. Anodic kinetics of a 1000 µm sensitized AA5083-H131 artificial pit in solutions of fissure tip chemistry of different saturation levels.
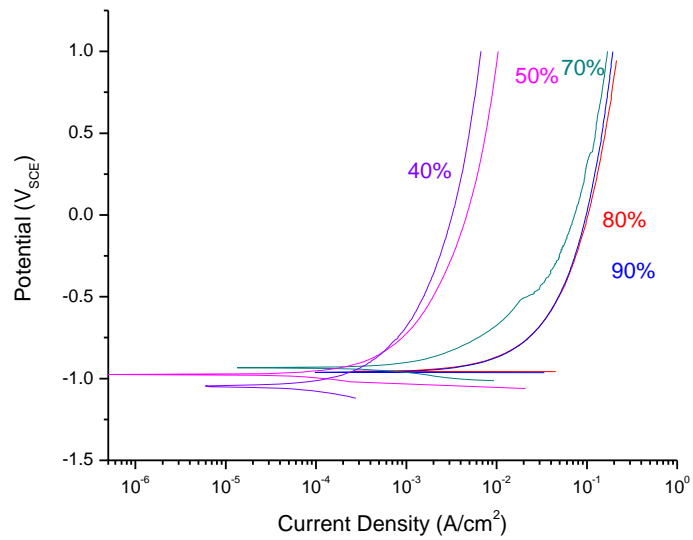
Figure 5.20. Anodic kinetics of a 1500 µm sensitized AA5083-H131 artificial pit in solutions of fissure tip chemistry of different saturation levels.
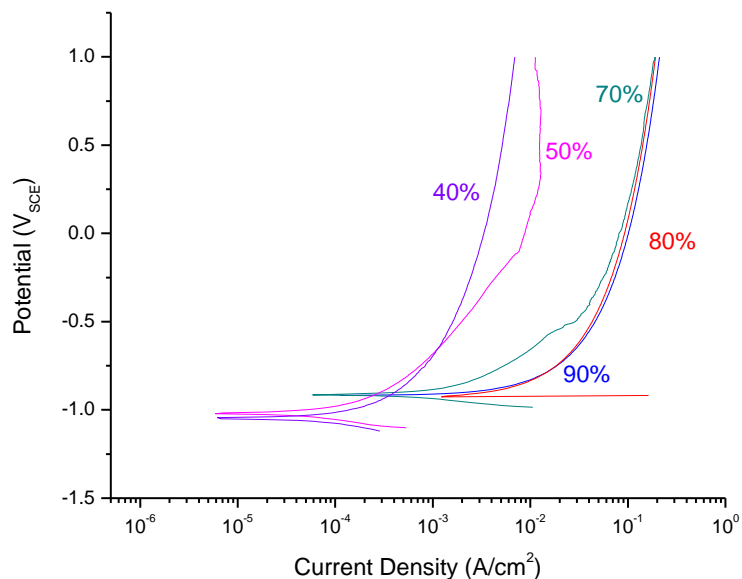
Figure 5.21. Anodic kinetics of a 2000 µm sensitized AA5083-H131 artificial pit in solutions of fissure tip chemistry of different saturation levels.
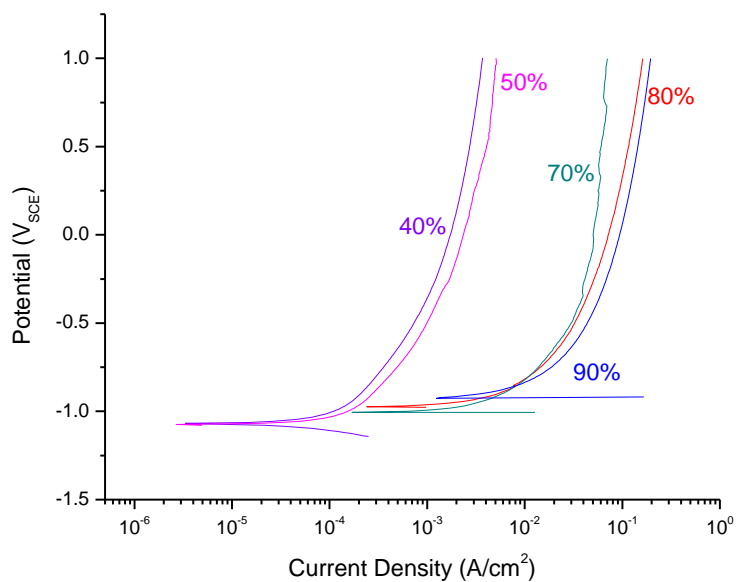
Figure 5.22. Anodic kinetics of a 1000 µm as-received AA5083-H131 artificial pit in solutions of fissure tip chemistry of different saturation levels.
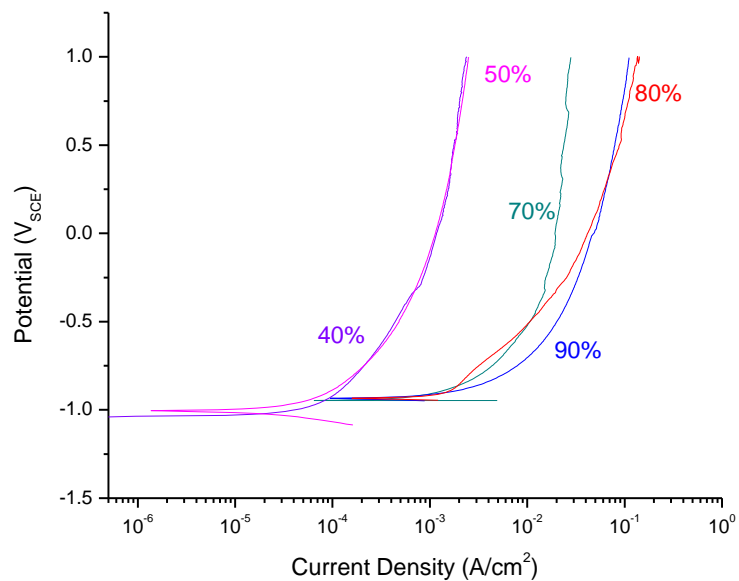
Figure 5.23. Anodic kinetics of a 1500 µm as-received AA5083-H131 artificial pit in solutions of fissure tip chemistry of different saturation levels.
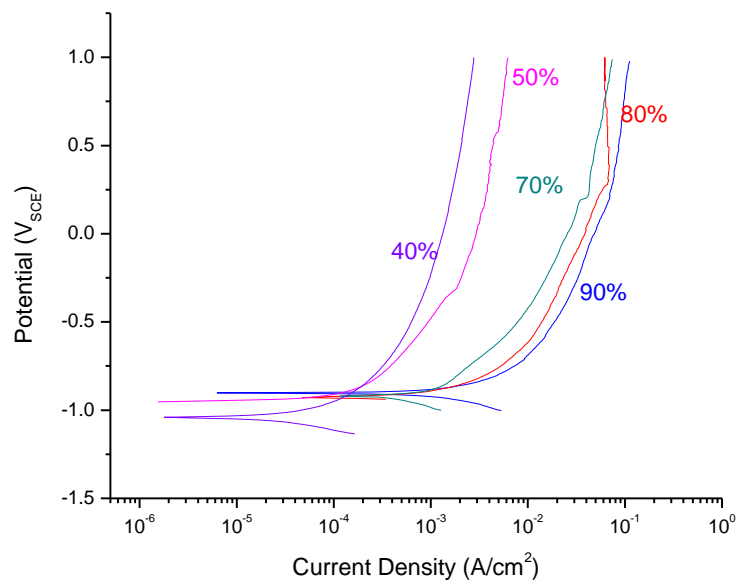
Figure 5.24. Anodic kinetics of a 2000 µm as-received AA5083-H131 artificial pit in solutions of fissure tip chemistry of different saturation levels.
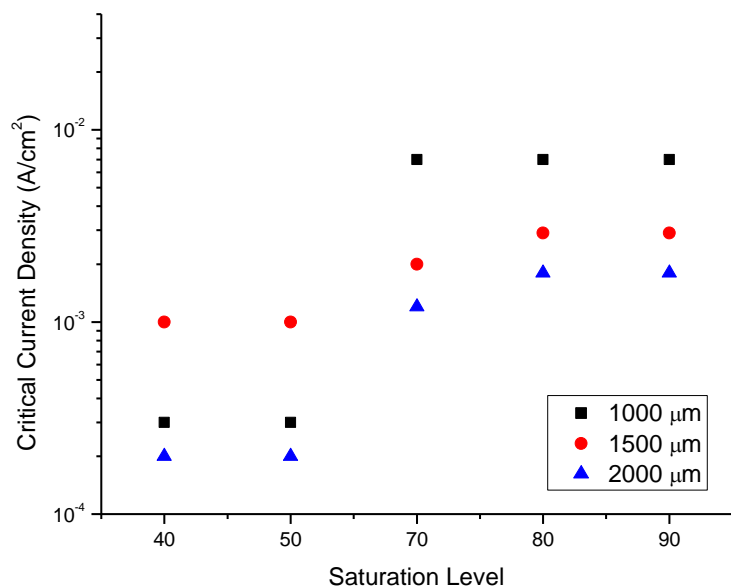
Figure 5.25.Critical current density taken at -0.87 V_{SCE} as a function of fissure chemistry saturation level in as-received AA5083-H131 artificial pit of various depths.
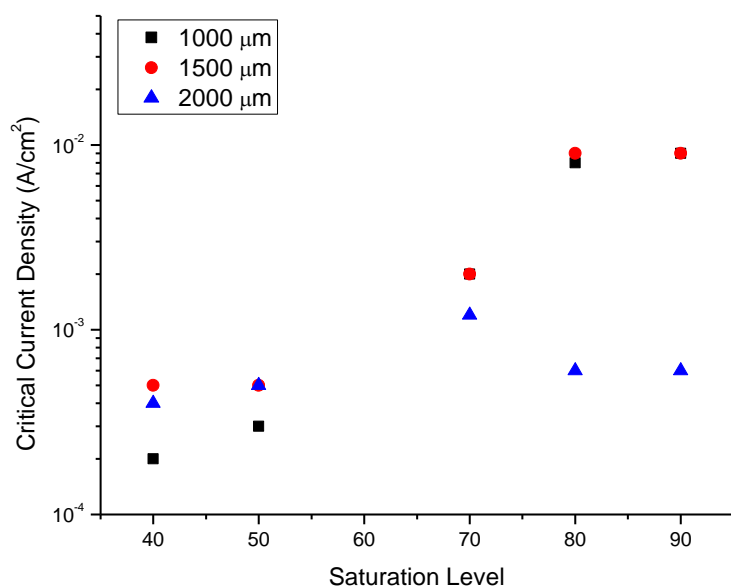
Figure 5.26. Critical current density taken at -0.87 V_{SCE} as a function of fissure chemistry saturation level in sensitized AA5083-H131 artificial pit of various depths.

For a given damage depth, the critical current density of the as-received is lower, albeit the same order of magnitude, relative to the sensitized AA5083-H131 for all saturation levels. The critical current density decreases with increasing damage depth, as expected from the pit stability product relationship. For the as-received AA5083-H131, the current density decreased from 0.007 A/cm^2 for a 1000 µm depth to 0.0029 A/cm^2 for a 1500 µm pit depth at a 90% saturation level.

5.5.5 Hydrolysis Calculations and Local pH

The distribution of Al hydrolysis products, shown in Figure 5.27, demonstrates that the alkalinization process dominates in most cases. In the acidic regime, few Al^{3+} ions form complexes, in that essentially all the cations are not attached on hydroxyl ions. Under these conditions, less than one OH$^-$ is consumed per Al^{3+} on the average. However, cathodic reactions required to generate the Al^{3+} ion from an Al atom produced three OH$^-$, such that the electrochemical dissolution of Al at low pH's tends to increase the solution pH. With increasing pH, the average number of OH$^-$ consumed per Al^{3+} also increases. The number of hydroxyls consumed per Al^{3+} was generated by summing the products of the fraction of each species multiplied by the number of hydroxyl ions consumed per ion of that species. At some point, the number of hydroxyl ions consumed by Al^{3+} hydrolysis is equivalent to the number of hydroxyl generated by the cathodic reaction, such that there is no net gain or loss of OH$^-$. For pure aluminum, this occurs at pH 6.7. At pH's below 6.7, the production of OH$^-$ exceeds its consumption, resulting in a more

alkaline solution. At high pH's values, the solution will acidify because the amount of hydroxyl consumed by Al^{3+} hydrolysis outweighs the number of hydroxyl produced.
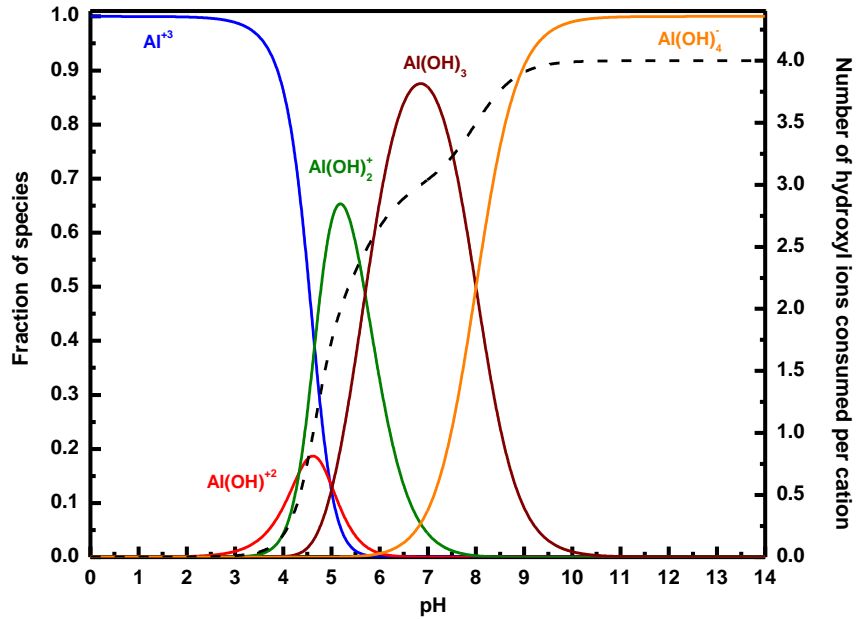
Figure 5.27. Stability diagram for aluminum hydrolysis species as a function of pH.

This type of analysis can be employed to consider hydrolysis of alloys. Figure 5.28 shows the number of hydroxyl ions consumed per average cation resulting from the oxidation of Al, AA5083, and β-phase. The mix of ions produced by the assumed stoichiometric dissolution of AA5083 produces an average valence of 2.95. The corresponding pH at which this number of hydroxyl consumed is 7, slightly higher than for pure Al. The change is small when considering bulk corrosion of the alloy because the composition is dominated by

Al. This type of analysis can also be used to estimate the amount of cathodic reaction that occurs locally based on the local pH. The fraction of anodic current that must be met locally by the cathodic reaction to maintain a given pH is plotted in Figure 5.29. If the hydroxide consumed by Al^{3+} hydrolysis is completely balanced locally by an OH^- producing reaction, the equilibrium pH is 6.7 for pure Al.
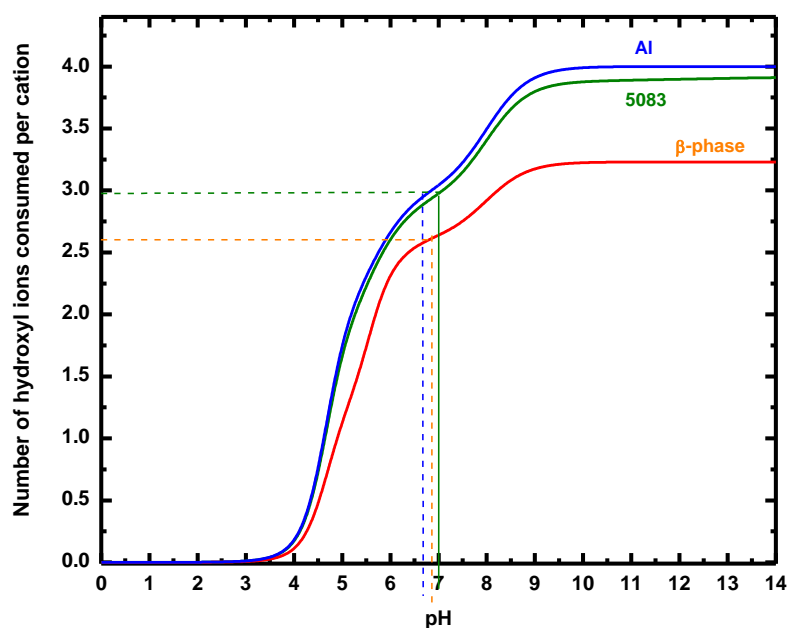
Figure 5.28. Plot of number of hydrolysis consumed per average cation of Al, AA5083, and β-phase as a function of pH.

The anodic kinetics of the fissure tip in the pit chemistry can be utilized in conjunction with this hydrolysis map to probe the critical local pH and the critical saturation level. For example in Figure 5.30, the anodic and cathodic current

densities of the sensitized AA5083-H131 in 70% saturated fissure tip chemistry can be extract via Tafel slope extrapolation. The cathodic and anodic current density at -0.87 V_{SCE} is 3.9 x 10^{-5} A/cm^2 and 2.1 x 10^{-3} A/cm^2, respectively. The ratio of the two current densities can be utilized to estimate the fraction of electrons consumed locally, which can be used to track the local pH. In this particular example, the ratio is 0.019, which corresponds to a pH 3.6 in Figure 5.29. The same procedure was employed on for the kinetics of an as-received specimen, and yield a ratio of 0.085, which corresponds to a pH of 4.2. These values are nominally close, although the lower critical pH for the fissure chemistry for the sensitized AA5083-H131 may be due to contributions from Mg^{2+}. Cathodic kinetics and additional analysis have to be performed in order to provide a solid conclusion.
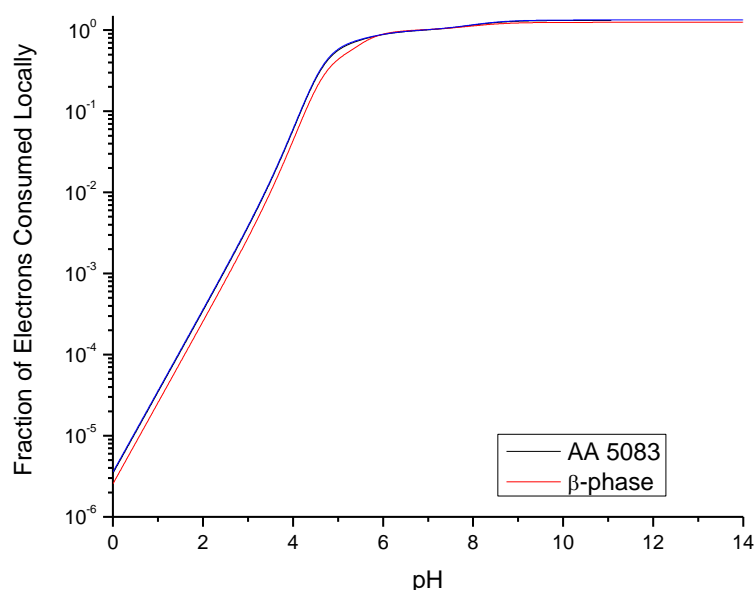
Figure 5.29. Fraction of anodic current that must be met locally by the cathodic reaction to maintain a given pH for AA5083 and β-phase.
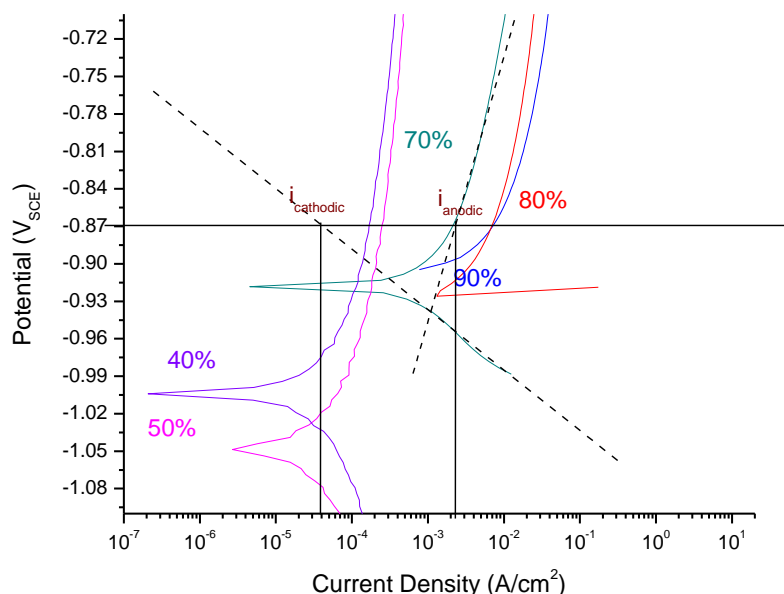
Figure 5.30. Anodic kinetics of a 1000 µm sensitized AA5083-H131 artificial pit in solutions of fissure tip chemistry of different saturation levels. The dash lines represent Tafel slopes for the 70% saturation, utilized to extract anodic and cathodic current densities at -0.87 V_{SCE}.

5.6 Discussion

5.6.1 Correlation between Intergranular Corrosion Propagation Stability Criteria and Threshold Propagation Potential

The measured E_{rp} for the as-received and sensitized AA5083-H131 in 0.6 M NaCl was added to the plot of pit stability products as a function of applied potential in Figure 5.31. It is evident that the E_{rp} and the bounding potentials for pit stability are one and the same, suggesting that the stability process associated with these two criteria are linked to each other. The pit stability product i*x decreases as it approached the bounding potentials, suggesting that the pit

chemistry is getting diluted faster than the dissolution rate at the bottom of the pit. Consequently, the aggressive chemistry at the pit bottom is not sustained to support depassivation and dissolution rate of the pit bottom and repassivation occurs. The range of pit stability product observed at the range of E_{crit} (-0.85 to -0.8 V_{SCE}) is 1.5 x 10^{-3} to 4 x 10^{-3} A/cm for the sensitized AA5083-H131 (Figure 5.18). Anodic kinetics of artificial pits suggests a critical saturation level of 70%, below which the current density drops from 10^{-3} to 10^{-4} A/cm^2 (Figure 5.25 and Figure 5.26). Below a certain dilution level, the pit bottom repassivates and propagation arrest commences.

A summary of the characteristic potentials associated with α-phase, β-phase, and AA5083-H131 were given in Table 5.5. The E_{rp} and the bounding potentials for pit stability product are highlighted. The observed range of IGC propagation threshold potentials, E_{crit}, for sensitized AA5083-H131 in 0.6 M NaCl is -0.85 to -0.80 V_{SCE}. The IGC spreading potential, -0.73 V_{SCE}, and the breakdown potential of β-phase, -0.96 V_{SCE}, in 0.6 M NaCl solution, were both ruled out as the basis of this E_{crit}. The E_{rp} at -0.87 V_{SCE} suggests that repassivation of the fissure tip in fissure tip chemistry is the basis for the absence of IGC propagation below the E_{crit}. Moreover, the breakdown potential of the α-phase in the saturated Al-4Mg acidic solution is also at -0.87 V_{SCE}. This also implies that open circuit potential of α-phase in Al-4Mg, -1.05 V_{SCE} is not controlling IGC propagation.
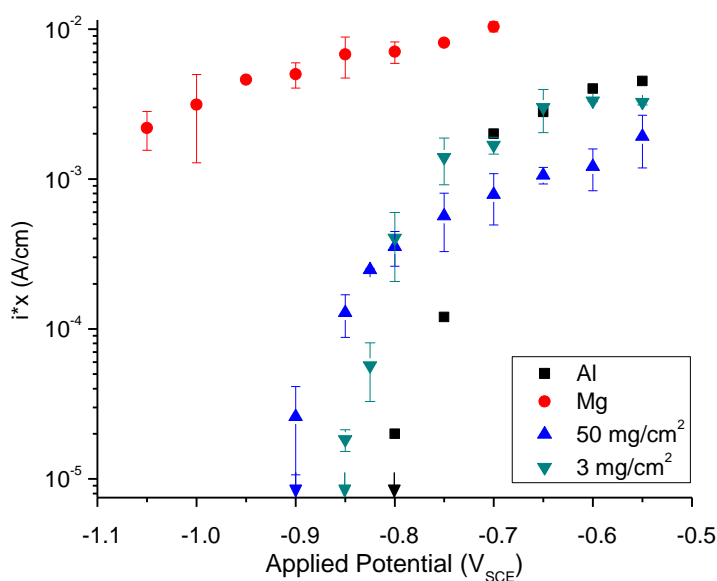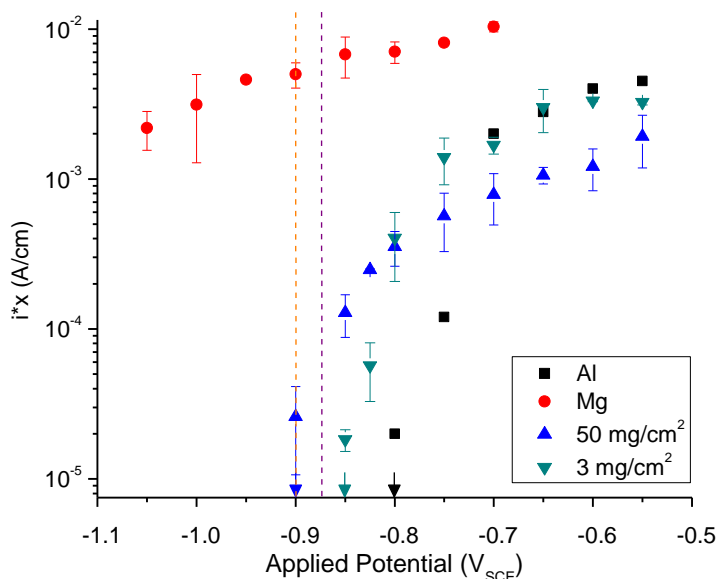
Figure 5.31. Average pit stability product (i*x) as a function of applied potential for different materials in 0.6 M NaCl solution. The repassivation potentials for as-received and sensitized AA5083-H131 were added as purple and orange lines, respectively.

The lower E_{rp} observed at -0.90 V_{SCE} for the sensitized AA5083-H131 is believed to be driven by the influence of β-phase in the fissure chemistry. The breakdown potential of α-phase in Al_3Mg_2 acidic solution is observed to be at -0.9 V_{SCE}. For the saturated solutions, stoichiometric dissolution of Al_3Mg_2 would result in a Mg^{2+} concentration of 1.3 M, whereas stoichiometric dissolution of Al-4%Mg would lead to a Mg^{2+} concentration of 0.14 M.[5] The fissure tip chemistry of sensitized AA5083-H131 is expected to be somewhere between these two. Measurements of pH were made for a bulk 2 M $AlCl_3$ solution, with increasing concentration of $MgCl_2$ (Chapter 3). There is a steady-sharp drop in the pH of

271

AlCl$_3$ solution for Mg concentrations above 0.1 M. These measurements suggest that the β-phase dissolution, which produces Mg^{2+} cations contributes to a substantial decrease in pH at the fissure tip, leading to a more aggressive chemistry. This more aggressive chemistry led to a lower repassivation potential, as well as a lower critical pit stability product, for the sensitized AA5083-H131.

Table 5.5. Summary of characteristic potentials for α-phase, β-phase, and AA5083-H131

Potential (V$_{SCE}$)	Description
-0.700	Breakdown potential of unsensitized AA5083[3]
-0.730	IGC spreading potential of sensitized AA5083[3]
-0.790	Breakdown potential of α-phase in 0.6 M NaCl solution, pH 6[19]
-0.850 to -0.800	Range of observed IGC propagation threshold potentials for sensitized AA5083-H131 in 0.6 M NaCl solution, pH 8.3[2]
-0.850	Bounding potential for pit stability product of AA5083-H131
-0.870	Breakdown potential of α-phase in saturated Al-4%Mg acidic solution, pH -0.12[5,20]
-0.875	Repassivation potential of as-received AA5083-H131
-0.900	Repassivation potential of sensitized AA5083-H131 Bounding potential for pit stability product of sensitized AA5083-H131
-0.900	Breakdown potential of β-phase in Al$_3$Mg$_2$ acidic solution
-0.960	Breakdown potential of β-phase in 0.6 M NaCl solution[21]
-1.015	Breakdown potential of β-phase in saturated Al-4%Mg acidic solution, pH -0.12[5,20]
-1.05	Open circuit potential of α-phase in in saturated Al-4%Mg acidic solution, pH -0.12[5,20]

The repassivation potential as the basis for E$_{crit}$ was validated via 10-day potentiostatic holds at -0.87 and -0.95 V$_{SCE}$ of sensitized AA5083-H131 bulk

specimens after 1 h of activation in -0.73 V_{SCE} in 0.6 M NaCl solution. The

observed current density as a function of exposure time for the two potentials is

displayed in Figure 5.32 and Figure 5.33, respectively. Both potentials started out

with cathodic current densities. The current density at -0.87 V_{SCE} crossed over to

anodic current density at 100 h, while the -0.95 V_{SCE} remained cathodic throughout

the 10 day exposure.
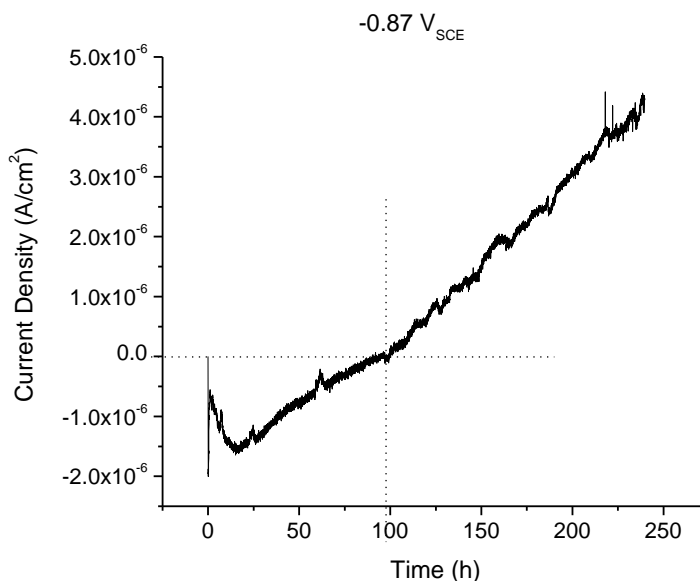
Figure 5.32. Current density as a function of time for an AA5083-H131 bulk specimen sensitized to 50 mg/cm^2 and potentiostatically held at -0.87 V_{SCE} in 0.6 M NaCl solution for 10 days.
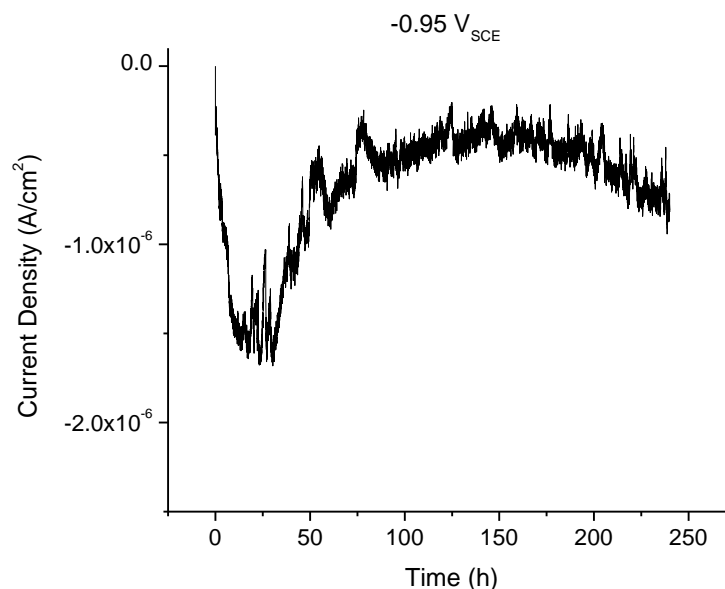
Figure 5.33. Current density as a function of time for an AA5083-H131 bulk specimen sensitized to 50 mg/cm^2 and potentiostatically held at -0.95 V$_{SCE}$ in 0.6 M NaCl solution for 10 days.

5.6.2 Physical Phenomenon for Intergranular Corrosion Propagation Stability

The IGC propagation in sensitized AA5083-H131 is complicated by the fact that the sensitized grain boundary is composed of ligaments of α-phase and β-phase. This means that there is a continuously changing chemistry at the fissure bottom or tip and along the fissure as the IGC progresses. The change in chemistry is dependent on the dissolution rate of the component phases. Although β-phase is the culprit for IGC, it was demonstrated that α-phase dissolution is the rate controlling step in IGC propagation.[5] Given that the suggested fissure chemistry is 80 to 100% saturation of Al4Mg solution,[5,19] the role of the α-phase as the rate

274

controlling step is not only significant in terms of dissolution rate, but is also essential in developing the acidic chemistry expected at the fissure tip to support IGC propagation above E_{crit}. This suggest that the initiation of IGC is dependent on the pitting of β-phase, while the propagation of IGC is dependent on the dissolution of α-phase.

Despite literature report on Mg's more alkaline hydrolysis equilibrium relative to Al,[13] the addition of Mg^{2+} to $AlCl_3$ solutions actually drops the pH. This suggest that the additional dissolution of β during IGC propagation delivers a local surge of Mg^{2+} concentration, acidifying the fissure tip environment, thereby generating a more aggressive condition, which depassivates and corrodes the α-phase in between β precipitates. This implies that the β-phase ahead initiates IGC and triggers α-phase dissolution to provide the fissure chemistry, while the β-phase behind would replenish the Mg^{2+} necessary to maintain the aggressive environment for continuous propagation.

A proposed physical phenomenon displayed in Figure 5.34 shows the dissolution of a grain boundary β precipitate along a propagating IGC fissure leaves a high $[Mg^{2+}]$ fissure tip environment. All the α-phase, including parts of the fissure flanks, exposed to this critical $[Mg^{2+}]$ aggressive solution will depassivate and corrode. Through time, the cations will diffuse out from the fissure into the bulk solution causing a concentration gradient across the fissure length. As such, for the fissure flanks, the corrosion rate dwindles as it gets farther away from the fissure

tip, limiting the fissure width growth as observed in Chapter 2 and Chapter 3. At the fissure tip, when a critical $[Mg^{2+}]$ can be maintained, α dissolution can be sustained, and IGC propagates stably. However, when considerable concentration of Mg^{2+} diffused out, the α-phase repassivates, and IGC propagation ceases. This suggests that the IGC propagation stability is dependent on the maintenance of the critical $[Mg^{2+}]$ at the fissure tip to corrode through the length of the α-phase before the IGC fissure reaches another β-phase, which will replenish the Mg^{2+} depletion.
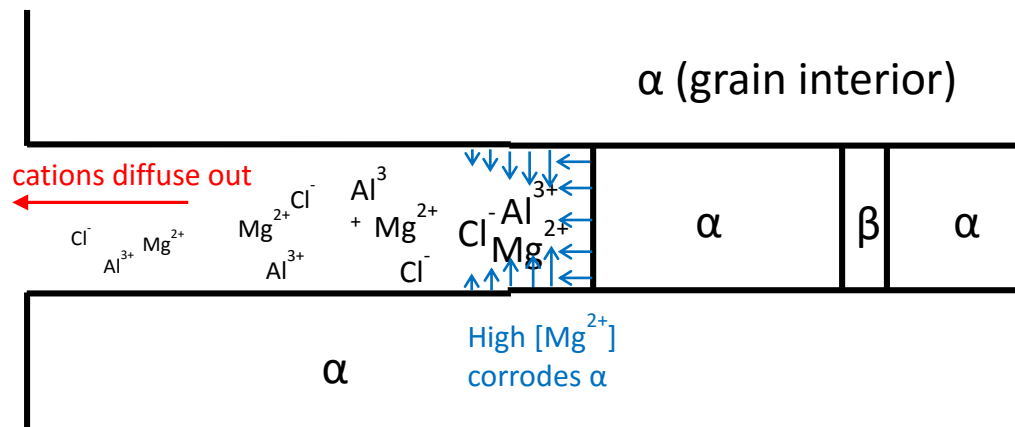
Figure 5.34. A hypothetical schematic of IGC propagation stability considering heterogeneous grain boundary metallurgy and local chemistry changes.

Because the $[Mg^{2+}]$ is driven by DoS, as characterized microstructurally by the size, spacing, and distribution of β-phase along the grain boundaries, this implies that DoS has a direct impact on the IGC propagation stability. At higher DoS where the β-phase distribution is high and β-phase spacing is shorter, Mg^{2+} is easily replenished, allowing for maintenance of critical $[Mg^{2+}]$ at the fissure tip. At lower DoS, where the size and spacing of β-phase is small, Mg^{2+} can deplete to

concentration below the critical $[Mg^{2+}]$, causing repassivation and unstable IGC propagation. This implies that there is also a critical β-phase spacing associated with stable IGC propagation.

5.7 Conclusions

1. The repassivation potentials of as-received and sensitized AA5083-H131 in 0.6 M NaCl solution are determined for both artificial pit and bulk specimens. The E_{rp} for bulk sensitized AA5083-H131 exhibited two repassivation potentials, -0.90 and -0.97 V_{SCE}, the former was believed to be α-phase driven, while the latter is associated with β-phase. Whereas the as-received AA5083-H131 only exhibited one repassivation potential, -0.87 V_{SCE}.

2. The pit stability products of as-received and sensitized AA5083-H131 in 0.6 M NaCl solution are determined as a function of potential. The pit stability product is shown to be bounded by a potential, below which only cathodic currents were observed. The range of pit stability product observed at the range of E_{crit} (-0.85 to -0.8 V_{SCE}) is 1.5 x 10^{-3} to 4 x 10^{-3} A/cm for the sensitized AA5083-H131.

3. Anodic kinetics suggests that a fissure chemistry with a 70% saturation level has to be maintained for stable pit propagation to progress.

4. The bounding potentials for pit stability correlated well with the repassivation potential for both the as-received and the sensitized AA5083-H131, confirming that the two criteria are associated with each other.

5. Comparison of the repassivation potential with the IGC threshold potential and characteristic potentials of α-phase in saturated Al-4Mg and Al_3Mg_2 solution suggests that the repassivation of the fissure tip in fissure chemistry is the basis for the observed lack of IGC propagation at potentials below the threshold potentials.

6. A physical mechanism for stable IGC propagation is established on the basis of pit stability in the context of applied potential, applied current density, and DoS.

5.8   References

[1]   D. Mizuno, R.G. Kelly, Galvanically Induced Intergranular Corrosion of AA5083-H131 Under Atmospheric Exposure Conditions: Part 1—Experimental Characterization, Corrosion. 69 (2013) 580–592. doi:10.5006/0812.

[2]   M.L.C. Lim, J.R. Scully, R.G. Kelly, Critical Electrochemical Conditions for Intergranular Corrosion in Sensitized AA5083-H131, in: Dep. Def. Corros. Conf., NACE International, 2013.

[3]   S. Jain, M.L.C. Lim, J.L. Hudson, J.R. Scully, Spreading of intergranular corrosion on the surface of sensitized Al-4.4Mg alloys: A general finding, Corros. Sci. 59 (2012) 136–147. doi:10.1016/j.corsci.2012.02.018.

[4]   M.L.C. Lim, J.R. Scully, R.G. Kelly, Intergranular Corrosion Penetration in an Al-Mg Alloy as a Function of Electrochemical and Metallurgical Conditions, Corrosion. 69 (2013) 35–47. doi:10.5006/0722.

[5]   E. Bumiller, Intergranular corrosion in AA5XXX aluminum alloys with discontinuous precipitation at the grain boundaries, PhD Dissertation, University of Virginia, 2011.

[6]   J.R. Galvele, Transport Processes and the Mechanism of Pitting of Metals, J. Electrochem. Soc. 123 (1976) 464–474. doi:10.1149/1.2132857.

[7]   J. Galvele, Transport processes in passivity breakdown—II. Full
        hydrolysis of the metal ions, Corros. Sci. 21 (1981) 551–579.
        doi:10.1016/0010-938X(81)90009-3.

[8]   S.M. Gravano, J.R. Galvele, Transport processes in passivity
        breakdown—III. Full hydrolysis plus ion migration plus buffers, Corros.
        Sci. 24 (1984) 517–534. doi:10.1016/0010-938X(84)90034-9.

[9]   Z. Szklarska-Smialowska, Pitting corrosion of aluminum, Corros. Sci. 41
        (1999) 1743–1767. doi:10.1016/S0010-938X(99)00012-8.

[10]   A.M. Lucente, J.R. Scully, Localized Corrosion of Al-Based Amorphous-
        Nanocrystalline Alloys with Solute-Lean Nanocrystals: Pit Stabilization, J.
        Electrochem. Soc. 155 (2008) C234–C243. doi:10.1149/1.2868764.

[11]   F. Hunkeler, H. Bohni, Determination of Pit Growth Rates on Aluminum
        Using a Metal Foil Technique, Corrosion. 37 (1981) 645–650.
        doi:10.5006/1.3577553.

[12]   M. Pourbaix, Atlas of Electrochemical Equilibria in Aqueous Solutions,
        NACE International, Houston, TX, 1974.

[13]   C.F. Baes, R.E. Mesmer, The hydrolysis of cations, Wiley, 1976.

[14]   R. Howard, N. Bogh, D.S. Mackenzie, Heat Treating Processes and
        Equipment, in: G.E. Totten, D.S. Mackenzie (Eds.), Handb. Alum., Marcel
        Dekker, Inc., New York, NY, 2003.

[15]   ASTM, ASTM: G67-04 Standard Test Method for Determining the
        Susceptibility to Intergranular Corroaion of 5XXX Series Aluminum
        Alloys by Mass Loss After Exposure to Nitric Acid (NAMLT Test),
        ASTM International, West Conshocken, PA, 2004.

[16]   N. Sridhar, D.S. Dunn, Effect of Applied Potential on Changes in Solution
        Chemistry Inside Crevices on Type 304L Stainless Steel and Alloy 825,
        Corrosion. 50 (1994) 857–872. doi:10.5006/1.3293476.

[17]   S.T. Pride, J.R. Scully, J.L. Hudson, Metastable Pitting of Aluminum and
        Criteria for the Transition to Stable Pit Growth, J. Electrochem. Soc. 141
        (1994) 3028–3040. doi:10.1149/1.2059275.

[18]   Y. Shi, Experimental Evaluation and Modeling For Galvanically-Induced
        Localized Corrosion of AA7075-T6, PhD Dissertation, University of
        Virginia, 2015.

[19]   C.B. Crane, Validation of the Coupled Dissolution-Hydrogen Embrittlement Mechanism of IGSCC in Low Temperature Sensitized AA5083-H131, PhD Dissertation, University of Virginia, 2013.

[20]   E.M. Bumiller, R.G. Kelly, Intergranular corrosion in AA5XXX: a case for continuous attack with a discontinuous active path, in: Dep. Def. Corros. Conf., NACE, Palm SPrings, CA, 2011.

[21]   N. Birbilis, R.G. Buchheit, Electrochemical Characteristics of Intermetallic Phases in Aluminum Alloys - An Experimental Survey and Discussion, J. Electrochem. Soc. 152 (2005) B140–B151. doi:10.1149/1.1869984.

6 Conclusion

6.1 Chapter 2 – Factors Governing Intergranular Corrosion Propagation

1. IGC penetration rate in AA5083 in 0.6 M NaCl solution is governed by orientation of propagation, degree of sensitization, temperature of sensitization and exposure time.

    a. The morphology and distribution of β-phase precipitates was dictated by the sensitization conditions. IGC penetration rate increased sharply with sensitization for DoS above 24 mg/cm^2; however, IGC occurred for DoS between 2 and 24 mg/cm^2.

    b. IGC also propagated on grain boundaries without a continuous path.

    c. The IGC penetration rate showed strong anisotropy, with L direction penetration faster by a factor of 1.7 relative to the slowest (S) direction. The S direction exhibited more grain fall-out for the same amount of depth penetration than the L or T directions owing to small grain widths in this direction.

    d. Incubation time for IGC penetration is a function of DoS for conditions studied.

2. IGC damage distributions can serve as inputs for IGC models that predict IGC depth of penetration as a function of material conditions and time.

    a. IGC propagation depths can be well described by a three-parameter log-logistics distribution.

b. The phenomenological model herein can determine IGC damage prognosis as influenced by DoS, time of exposure, and orientation of propagation in seawater environment (0.6 M NaCl solution, pH 8.3, V_{app} = -0.73 V_{SCE}).

3. Sensitization temperature significantly influences the IGC propagation rates even for material with the same ASTM G-67 DoS value.

6.2   Chapter 3 – Critical Role of Potential on Intergranular Corrosion Propagation

1. The partial IGC study involving the effect of cold work temper on sensitization revealed that:

   a. DoS does not vary significantly with tempers when exposed to the same sensitization heat treatment conditions.

   b. The IGC fissure morphologies of H116 and H131-SHT/Q tempers are short and wide, whereas those of H131 are long, sharp, and narrow.

   c. For the same DoS, the depth distribution after various periods of exposure times to 0.6 M NaCl solution at -0.73 V_{SCE} showed that H131 exhibited fastest IGC propagation kinetics, while H116 and H131-SHT/Q exhibited nominally the same kinetics.

2. The IGC propagation depth in AA5083-H131 exposed to 0.6 M NaCl solution depends linearly on potential. This potential dependence of IGC propagation increases with increasing DoS.

3. The true E-i behavior during IGC follows Tafel behavior and illuminates the constant IGC propagation rates with time (and depth).

4. A threshold potential (-0.85 to -0.8 V_{SCE}) exists where no IGC, but only pitting, was observed. This threshold potential was found to be more positive than the β breakdown potential, but more negative than the IGC spreading potential.

5. A saturated or nearly saturated solution of Al-4Mg in the majority of the fissure with a saturated solution of Al_3Mg_2 at the fissure tip provides the best fits for the IGC propagation rates of the sensitized AA5083-H131.

6. Analysis using the total rate equation suggested effective grain boundary β-phase coverage and connectivity to justify the characteristic IGC propagation rates observed. The effective β-phase coverage explains the additional Mg^{2+} concentration required to maintain stable IGC propagation following Galvele's critical pit stability product. The predicted θ_β illustrated the significance of the connectedness of susceptible grain boundaries for a favorable IGC path.

6.3 Chapter 4 – Linear Dependencies of Intergranular Corrosion Propagation Depth with Time and Potential

1. The linear IGC propagation kinetics with potential and depth of AA5083-H131 in 0.6 M NaCl solution is elucidated via specimen geometries with varying degrees of connectivity:

a. At or near the spreading potential (-0.73 V_{SCE}), the 3D specimen exhibited linear propagation kinetics up to 192 h, and transitioned to power law kinetics due to ohmic potential drop as a result of corrosion product accumulation and H_2 bubbles evolution. For the 2D specimen, the linear propagation kinetics is only observed up to 100 h due to the restricted spreading, as well as vulnerability to grain fall-out. Only power law kinetics is observed for the 1D specimen.

b. At lower applied potentials (-0.80 V_{SCE}), only power law kinetics is observed for all three specimen geometries. This potential is not sufficiently high to trigger immediate active IGC damage. The current densities observed are in the passive regime, in the orders of 10^{-4} A/cm^2.

c. The relationship between the IGC rates and potential for the 3D degree of connectivity showed a single strong linear trend up to an exposure time of 192 h. For the 1D and 2D degree of connectivity, at exposure time of 100 h and longer, linear dependence of IGC rate on potential was also observed, with the dependence decreasing to a lesser extent with increasing exposure time due to larger ohmic resistance.

2. Computational resistor network analysis validated that the lack of ohmic potential drop effect on the IGC kinetics is driven by the multiple, interconnected fissures leading to effective resistance at the fissure tip.

3. The quantitative relationship of damage depth with time established via power law fitting suggested that the power law exponent n was primarily

influenced by applied potential, with secondary effects from degree of connectivity.

4. Simple calculations suggest that the active and passive area partitioning during IGC propagation appears to be another significant factor that dictates IGC propagation rate and or applied potential response.

6.4   Chapter 5 – Intergranular Corrosion Propagation Stabilization and Repassivation

1. The repassivation potentials of as-received and sensitized AA5083-H131 in 0.6 M NaCl solution are determined for both artificial pit and bulk specimens. The E_{rp} for bulk sensitized AA5083-H131 exhibited two repassivation potentials, -0.90 and -0.97 V_{SCE}, the former was believed to be α-phase driven, while the latter is associated with β-phase. Whereas the as-received AA5083-H131 only exhibited one repassivation potential, -0.87 V_{SCE}.

2. The pit stability products of as-received and sensitized AA5083-H131 in 0.6 M NaCl solution are determined as a function of potential. The pit stability product is shown to be bounded by a potential, below which only cathodic currents were observed. The range of pit stability product observed at the range of E_{crit} (-0.85 to -0.8 V_{SCE}) is 1.5×10^{-3} to 4×10^{-3} A/cm for the sensitized AA5083-H131.

3. Anodic kinetics suggests that a fissure chemistry with a 70% saturation level has to be maintained for stable pit propagation to progress.

4. The bounding potentials for the pit stability correlated well with the repassivation potential for both the as-received and the sensitized AA5083-H131, confirming that the two criteria are associated with each other.

5. Comparison of the repassivation potential with the IGC threshold potential and characteristic potentials of α-phase in saturated Al-4Mg and Al_3Mg_2 solution suggests that the repassivation of the fissure tip in fissure chemistry is the basis for the observed lack of IGC propagation at potentials below the threshold potentials.

6. A physical phenomenon for stable IGC propagation is established on the basis of pit stability in the context of applied potential, current density, and DoS.

7 Appendix A: Model to Predict Intergranular Corrosion Propagation in Three Dimensions in AA5083-H131

7.1 Abstract

A three-dimensional (3-D) granular model that has the capability of predicting time-dependent intergranular corrosion (IGC) damage propagation depths in AA5083-H131 exposed to 0.6 M NaCl solution under potential control is presented. The geometry of grains and degree of sensitization (DoS) of grain boundaries were utilized as inputs, organized in a database, which informed the model to produce IGC damage depth distributions. The dependencies of IGC damage depth with exposure time, DoS, and orientation of propagation, both in terms of propagation kinetics and damage morphology, are outputs from the model. The model was calibrated by comparing outputted damage depths to IGC damage depth data from experiments. Model validation was achieved by comparing the predicted to experimental IGC damage depths based on image analyses of metallographic cross-section of AA5083-H131 exposed under the same conditions. The relevance and limitations of the current version of the model are discussed.

7.2 Introduction

The AA5XXX Al-Mg class of alloys are increasingly used as lightweight substitute for steel due to their high strength-to-weight ratio, weldability, and good uniform corrosion resistance.[1–3] This combination of material properties makes such alloys the material of choice in applications involving corrosive environments.

Although these alloys are designated as marine grade aluminum alloys, during service these alloys can become susceptible to intergranular corrosion (IGC) and intergranular stress corrosion cracking (IGSCC) in marine environments due to a sensitization involving β-phase (Al_3Mg_2) precipitation on grain boundaries.[3–14] When alloys containing more than 3 wt. % Mg are exposed to standard service temperatures as low as 50°C for long periods of time, β-phase precipitates form at the grain boundaries of these non-heat-treaTable 7. alloys as a response to the supersaturation of Mg in the α-solid solution matrix.[3–11,15–19] The β-phase precipitates, which are more anodic to the bulk α-matrix, satisfy an electrochemical framework for an IGC path and associated sTable 7. IGSCC evolution.[5,10,12,13,20–22]

Recent IGC studies of AA5083 (UNS A95083) in seawater environment showed that the IGC propagation rate is governed by applied potential, degree of sensitization (DoS), and orientation of propagation relative to the rolling direction.[23–25] The maximum IGC damage depth in the longitudinal (L) direction for sensitized AA5083-H131 after 100 hours was observed to increase linearly with applied potential above a threshold potential of -0.86 V_{SCE}.[24,25] This linear relationship was found for all DoS, with the dependence of rate on potential increasing with DoS.[24,25] At a given applied potential, the IGC propagation rate was observed to increase sharply with sensitization, specifically at a DoS level above 24 mg/cm^2. This DoS level is specified as IGC susceptible as per ASTM G67.[23,26] The IGC penetration rate also showed strong anisotropy,

with propagation depth in the L direction of rolled plate faster by a factor of 1.7 relative to the slowest in the short transverse (S) direction, albeit at the same linear IGC rate per unit length of grain boundary.[23]

The impact of IGC and IGSCC on structural integrity poses a major maintenance challenge. In the US Department of Defense alone, approximately 23.2% of the annual $22 billion expenditures on corrosion is spend on repairs associated with marine applications.[27] A predictive model for IGC propagation depths as a function of inputs such as DoS, exposure time, and grain orientation, can be utilized to illuminate what is important in material design, as well as to inform repair intervals, replacement planning, and component life of Al-Mg structures.

To date, there exist only two models for predicting IGC damage in sensitized AA5XXX alloys. Jain et al.[28,29] developed a continuum granular micrometer scale model that simulates the spreading of IGC on the surface of AA5083 as a function of DoS. The model utilized electrochemical, metallurgical, and physical variables as inputs to explain the interactive effects of local acidification, spatial proximity of β-phase, chloride concentration, and applied potential on IGC spreading. The fraction of area corroded and the total IGC length via spreading were predicted to be a function DoS and increased sharply beyond a threshold value, in accordance with experimental observations. Mizuno and Kelly[30] developed a computational model that predicts IGC damage depths caused by galvanic interactions between AA5083-H131 and AISI 4340 (UNS

G43400) steel under atmospheric conditions. This computational model utilizes experimentally-derived electrochemical boundary conditions to calculate local galvanic potential distributions, which were then employed to predict IGC depths after 100 h. The model demonstrated that although DoS has a significant effect on the IGC damage depth, the properties of the electrolyte film, as dictated by the salt loading density and the RH, also affect the IGC propagation kinetics. The former model only covered IGC spreading,[28,29] and did not include the transition to IGSCC or failure by IGC penetration. Although the latter involved propagation into depth, propagation was only considered in the longitudinal direction such that anisotropic IGC behavior was not addressed.

Statistical models [31–35] for AA2XXX and AA7XXX have been developed to rationalize the relationship between IGC growth rate and alloy microstructural anisotropy, and to estimate the minimum IGC path length. In these models, a three-dimensional brick-shaped granular model was utilized to build the array of grains, where grain dimensions were approximated by gamma distribution functions with parameters that were fitted based on the observed 3D grain sizes. The IGC damage path length through a material in a given direction was estimated by construction of the simplified six-sided grains in 2D, wherein propagating IGC on a single path was given various options for path continuity at grain intersections depending on assigned probabilities to move past an intersection, split, or turn upward. A good fit between the estimated deepest depth and the experimental deepest depth obtained by foil penetration was achieved using an appropriate

combination of probabilities. Although these statistical models were able to explain and estimate the anisotropy of IGC kinetics in all three orientations of propagation, the models were built on results based from simplistic foil penetration experiments, wherein the fastest IGC growth corresponds to the minimum IGC path length. However, this minimum path length is only pertinent if the local IGC growth rate is identical for each grain boundary in all directions, regardless of metallurgical heterogeneity. Very little consideration was placed on the influence of metallurgical factors, such as strengthening grain boundary phases or any precipitate free zone, on the IGC growth rate. Additionally, the statistical model was only 2D, such that the complication of the 3D tetradecahedron grains with three- and six-sided faces, enabling IGC to propagate in the third dimension was not taken into account.

Notably, probability concepts and statistical procedures have been extensively utilized in corrosion and corrosion-induced cracking studies of various material systems for a wide range of industrial applications.[36] In addition to the gamma distribution in the above IGC statistical model, some of the principally employed probability distributions include: normal distribution for pitting potential,[37] Gumbel distribution for maximum pit depth,[38] Poisson distribution for two-dimensional distribution of pits,[39] and exponential, log-normal, and Weibull distributions for stress corrosion cracking and hydrogen embrittlement failure time.[40–43] These statistical distributions and models were developed to understand the influence of metallurgy, chemistry, electrochemistry, and

mechanical parameters on the physical degradation processes and the subsequent implications of materials and environment on structure design, as well as to provide statistically distributed input parameters for damage evolution, structure lifetime prediction, and reliability engineering models.[43–51]

The objective of the present paper is to develop a granular model capable of predicting the 3-D IGC damage propagation in sensitized 5XXX alloys, using data from AA5083-H131 as a function of metallurgical factors, electrochemical factors, orientation of propagation, and exposure time. The model is based on an earlier publication[23] on experimental IGC propagation data for AA5083-H131 (UNS A95083) in full immersion via electrochemical experiments coupled with metallographic techniques, image analyses, and statistical evaluation. The effects of DoS, orientation of propagation, exposure time, and sensitization temperature on IGC damage depth were quantified after various exposure times and compared to experimental results.

7.3   Experimental Procedures

7.3.1   Materials and Electrochemical Test[23]

The AA5083-H131 alloys used had a nominal composition given in Table 7.1. The orientation and the microstructure of AA5083-H131 after Barker's etching of the longitudinal by long transverse (LT), short transverse by long transverse (ST), and longitudinal by short transverse (LS) surfaces are shown in Figure 7.1a. Potentiostatic holds were conducted on silica finished AA5083-H131 specimen

with surface area of 0.36 cm^2, in 0.6 M NaCl solution (pH 8.3) at -0.73 V$_{SCE}$ for 24, 72, or 100 h. The tests were performed on the LT, ST, and LS surfaces of specimens of various sensitization levels ranging from 2 to 49 mg/cm^2. Post-test, images of cross-sectioned specimens were taken with the optical microscope to determine average and distribution of IGC damage depth. A total cross-sectional area of 72 mm^2 was evaluated for each condition.
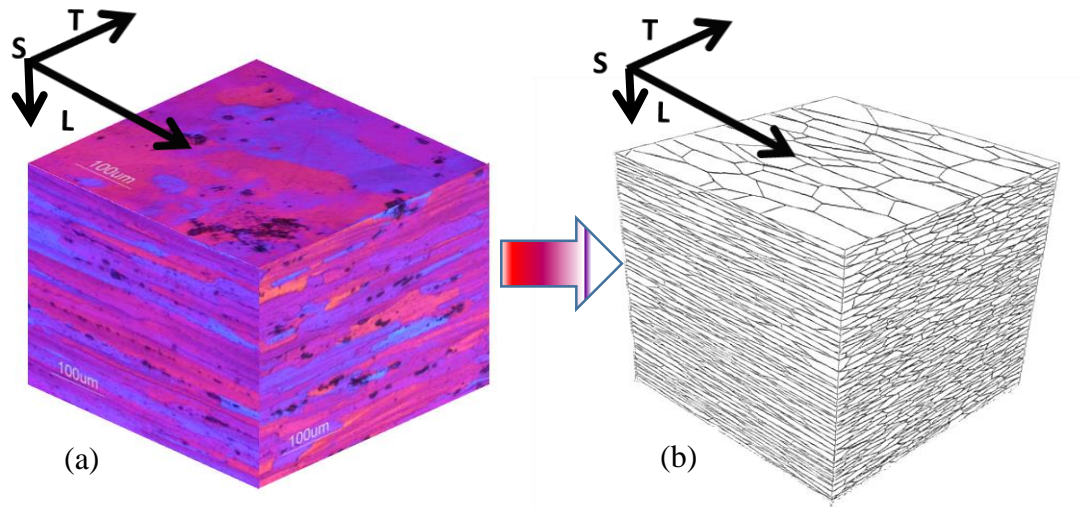
Figure 7.1. (a) Barker's etch image of the SL, ST, and LT grain structures in AA5083-H131. (b) Voronoi cell structure simulating AA5083-H131 grain morphology.

Table 7.1. Nominal composition of AA5083 (UNS A95083)

Component	Al	Mg	Mn	Fe	Si	Cr	Cu	Zn	Ti	Others
Weight %	Bal	4.4	0.7	0.22	0.1	0.08	0.05	0.02	0.02	< 0.01

7.3.2   Modeling Methodology

7.3.2.1   Model Inputs

The inputs for the model were determined experimentally.   The methodology by which these inputs were obtained is discussed elsewhere.[23]

7.3.2.1.1   Geometry of Grains

To properly predict the IGC damage propagation depths, it was essential to have a fair representation of the actual material microstructural geometries in terms of grain size and grain shape. The Barker's etch micrographs (Figure 7.1a) were utilized to create a 3D Voronoi cell structure (Figure 7.1b), a simulated body of multifaceted grains with appropriate grain aspect ratios representative of the unrecrystallized, rolled microstructure of AA5083-H131. The Voronoi algorithm offers the possibility of reconstructing a given microstructure based on a set of randomly generated points called Voronoi sites.[52] The random number states for the Voronoi sites can be varied suitably to obtain various grain size distributions in a Voronoi microstructure.   Details of the Voronoi algorithm can be found elsewhere.[52] The size of the Voronoi cell structure used for modeling was 1 mm x 1 mm x 1 mm, comprised of 5,000 grains with grain aspect ratio of 13:5:1 in the L, T, and S directions, respectively. A total of five statistically similar realizations of a volume element of a polycrystalline material with 5,000 grains Voronoi cell structure in each 1 mm^3 volume was utilized in the model. There is an average of 29, 18, and 9 grains in a 1 mm line on the S, T, and L directions, respectively. A 1 mm^2 surface area of ST, LS, and LT contains an average of 1052, 682, and 158

grains, respectively. It is recognized that grain boundary characteristics such as misorientation angles[6,53,54] and grain boundary plane orientation[55] influence beta precipitation and DoS, and subsequently IGC spreading and propagation. For this model, however, each simulated grain boundary facet was only characterized with a facet surface area and a facet shape factor, the number of grains sharing the facet.

7.3.2.1.2 IGC Damage Distribution

The IGC damage depth distributions of unsensitized and sensitized AA5083-H131 potentiostatically held at -0.73 V_{SCE} for various lengths of time in 0.6 M NaCl solution, pH 8.3, were obtained through a combination of metallographic techniques, image analyses, and statistical analyses. A sample cross-section image of a sensitized specimen with DoS of 49 mg/cm^2 after 100 hours of exposure is shown in Figure 7.2. The horizontal dark IGC regions propagate from the left exposed ST surface towards the right in the L direction. Point by point measurements of IGC damage depth measurements were taken to populate IGC damage distributions or the range of depths at one applied potential, DoS, exposure time, and orientation of propagation. A three-parameter log-logistics distribution function best fits these experimental damage depth histograms as verified with a Kolmogorov-Smirnov test.[56] The histograms and the fitted probability distribution functions (PDF), as well as the cumulative distribution function (CDF) curves in the L direction for a single sensitization level (DoS) at three exposure times for AA5083-H131 are shown in Figure 7.3 and 7.4,

respectively. Each unique combination of DoS, exposure time, and direction of propagation has its own set of fitted log-logistics PDF and CDF curves.
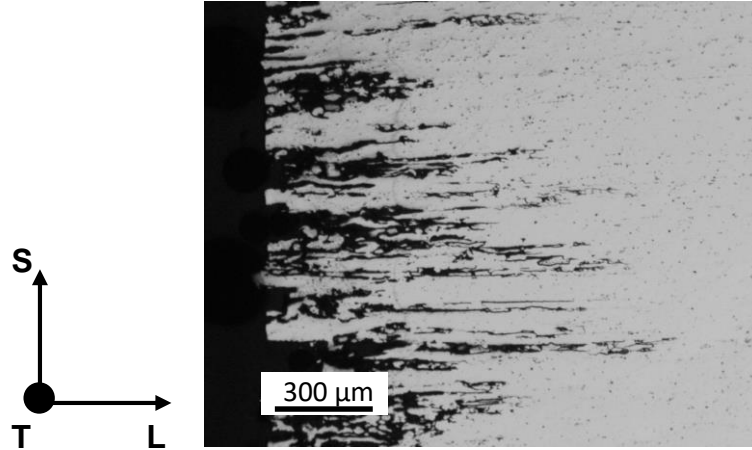
Figure 7.2. Optical micrograph showing damage depth in the L direction from ST surface of sensitized AA5083-H131 exposed to 0.6 M NaCl solution, pH 8.3, for 100 hours at -0.73 V_{SCE}.
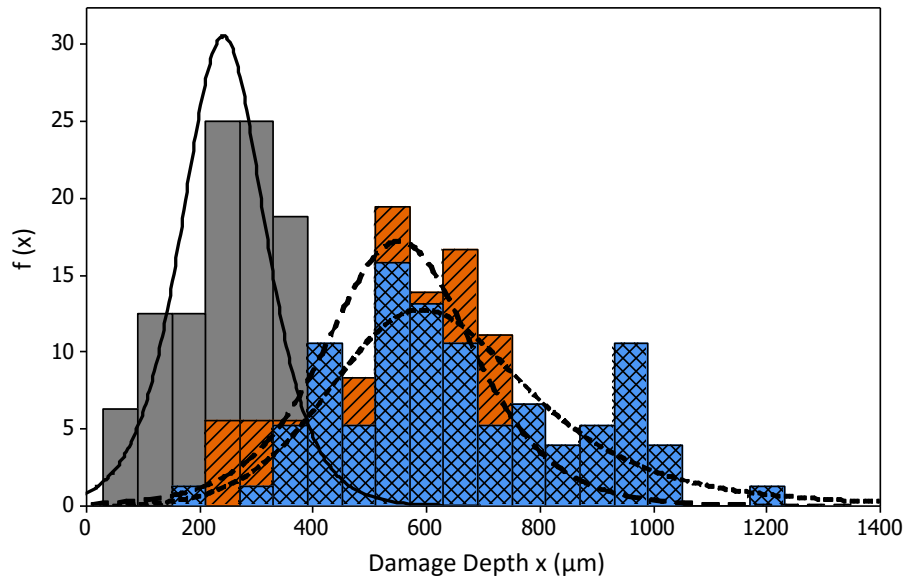
Figure 7.3. IGC damage depths histograms (bar) in the L direction for 39 mg/cm^2 after 24 (gray), 72 (orange), and 100 (blue) h of exposure in 0.6 M NaCl solution, pH 8.3 at -0.73 V_{SCE}, utilized to construct their respective probability distribution function (PDF), f(x) curves.
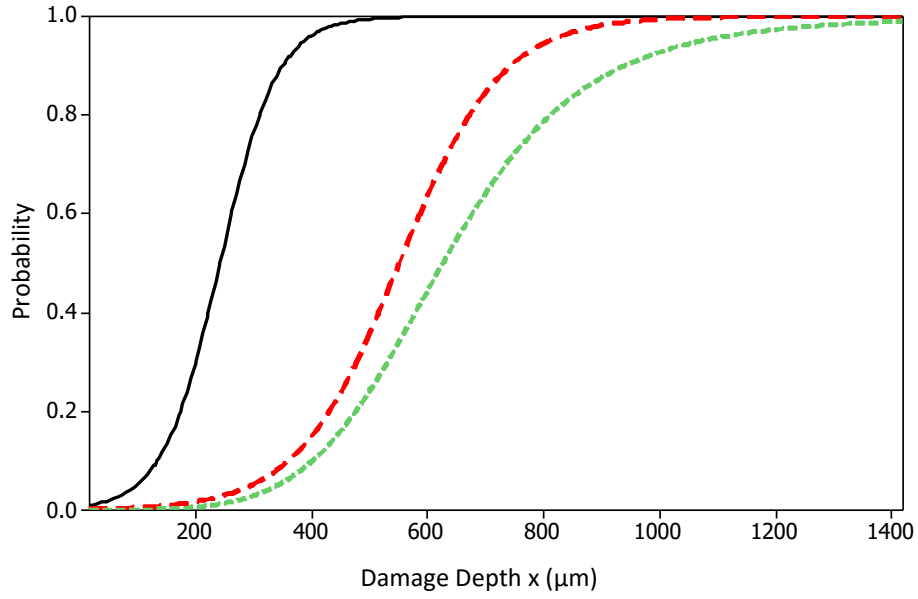
Figure 7.4. Cumulative distribution function (CDF) curves of experimental IGC damage depths in the L direction for 39 mg/cm^2 after 24 (black), 72 (red), and 100 (green) h of exposure in 0.6 M NaCl solution, pH 8.3 at -0.73 V$_{SCE}$, fitted with three parameter log-logistics distribution functions.

In the model generation of IGC depths, the three-parameter log-logistics CDF was described by the following expression:

$$F(x: \alpha, \delta, \gamma) = \left[1 + \left(\frac{\delta}{x-\gamma} \right)^{\alpha} \right]^{-1}$$
(Equation 7.1)

where x is the damage depth in micrometers, α is the shape factor, δ is the scale factor, and γ is the location factor. These parameters are utilized for the Monte Carlo sampling of the time to corrode (dtC) for each grain boundary facet in the Voronoi cell, which is discussed in the ensuing sections.

7.3.2.2 3-D Granular IGC Model

7.3.2.2.1 Model and Simulation Approach

The Voronoi cell structure was incorporated into the model representing a pristine starting structure for the simulation. As in the experiments,[23] only one face of the 1 mm^3 model cube was exposed to the corrosive environment, such that general IGC depth propagation was in the direction perpendicular to the exposed surface.[1] The IGC damage progression was simulated through the microstructure grain boundary facet by grain boundary facet following the exposure and corrosion rules. In the model, each grain boundary facet of the Voronoi cell structure was considered to have a dtC, which is the time it takes for a facet to fully corrode once exposed. Given a network of grain boundary facets (Figure 7.5), a facet is eligible for corrosion only once it was exposed to the environment. A facet was considered exposed as soon as a neighboring facet became fully corroded and a connected path with the bulk environment was established. A grain fell out when all of its facets in 3D were fully corroded separating the grain from the alloy. Thus, for this particular model, the IGC depth progression was highly dependent on the dtC of each facet.

---

[1] The path along the Voronoi structure of underlying grains can occur at any angle.
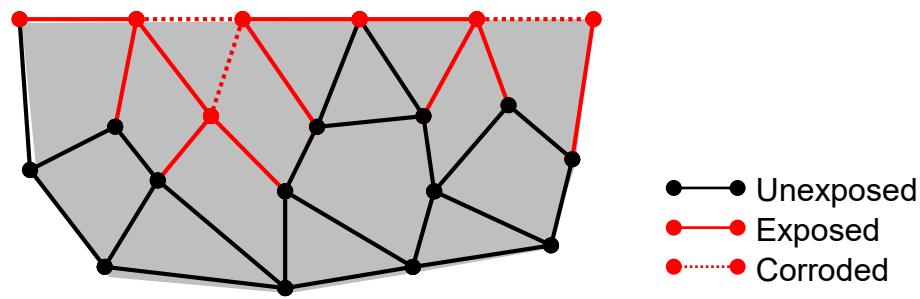
Figure 7.5. Schematic of IGC damage progression process and rules through the microstructure grain boundary facet by grain boundary facet after arbitrary time steps. Red dotted grain boundaries are corroded, red grain boundaries represent exposed grain boundaries or grain boundaries adjacent to corroded grain boundaries, and black grain boundaries are unexposed.
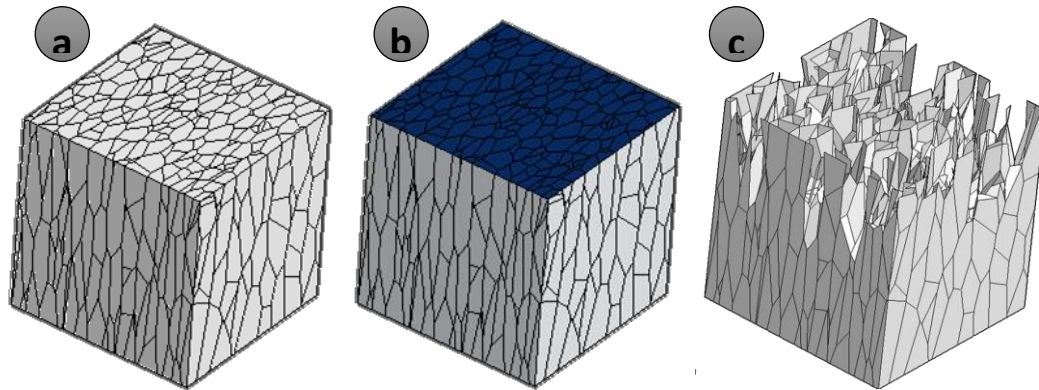
Figure 7.6. Schematics of the IGC propagation simulation approach, starting with (a) a pristine Voronoi cell structure; followed by (b) exposure of one of the faces to corrosive environment, and subsequent (c) IGC damage progression through the microstructure after a given number of time steps.

Using the Monte Carlo approach, dtC for each facet was assigned based on appropriate experimental statistical IGC rate distribution built into the model. The dtC distribution was independent of growth depth. This simulation approach is summarized in Figure 7.6. A program, written in Python^{TM}, was used to simulate and generate time-dependent IGC damage distributions in the three orientations of propagation in AA5083-H131 alloys exposed to 0.6 M NaCl solution.

7.3.2.2.2 Model Calibration

Calibration is one of the vital steps needed for an accurate simulation model in terms of forecasting experimental damage depths. During calibration, the model inputs were systematically fine-tuned on a small subset of the experimental data in an attempt to output data that accurately reflected experimental results. Previous experimental work showed that the IGC damage distribution was a strong function of DoS and direction of propagation.[23] As noted above, the IGC damage depth progression in the model was highly dependent on the dtC of each grain boundary facet. However, the IGC log-logistics damage distribution did not provide the direct value of dtC for a given DoS and propagation direction. It was thus essential to calibrate the model so that it depicted the influence of DoS and orientation on dtC, in order to accurately return the IGC propagation depth distributions as observed in the experiments.

Because dtC is the time to corrode an entire facet, the characteristic dimensions of each facet in terms of facet area and facet shape factor were also considered. Taking these characteristics into account, dtC was described in the IGC model by the following expression:

$$dtC = \xi * (A_{facet} * SF_{facet})^{0.5} * Q_{corr}^{0.5} \qquad \text{(Equation 7.2)}$$

where ξ represents the log-logistics distribution, A_{facet} is the facet area, SF_{facet} is the facet factor, and Q_{corr} is a corrosion direction orientation factor. With the elements A_{facet} and SF_{facet} inherent to the Voronoi microstructure and fixed for a given structure, the model calibration only involved the statistical distribution ξ and Q_{corr}.

Calibration was based on experimental data for this particular alloy and temper, and range of DoS.[2]
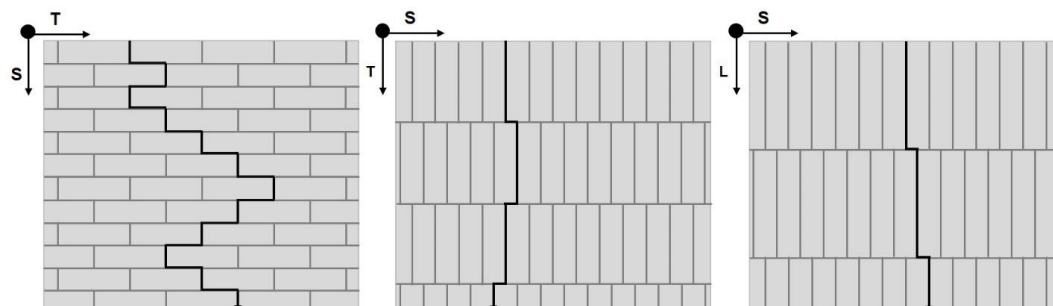
Figure 7.7. Two-dimensional grain structure model represented by pancake AA5083-H131 grain morphology showing the tortuous IGC damage path in the S direction (left), and the fairly direct path in the T (middle) and L (right) directions, with the top surface as the exposed surface. A single IGC path is depicted to highlight tortuosity. Note that grain sizes are not drawn to scale.

The strong orientation dependence of IGC propagation was attributed to the microstructural anisotropy of rolled product (Figure 7.1a). The IGC propagation in the L and T directions can follow a fairly direct corrosion pathway, whereas in the S direction the path are rather tortuous with many opportunities for branching and propagation occurring parallel to the surface along the T and L directions as shown in Figure 7.7.[3] It was then reasonable to apply the grain aspect ratios with respect to the L direction as the corrosion direction orientation factor. Thus, the model was calibrated such that Q_{corr} was assigned values of 0.077, 0.385, and 1 for IGC propagation in the S, T, and L directions, respectively.

---

[2] In this way, any Al-Mg alloy with more than 3 wt. % Mg that forms β-phase precipitates could be attempted.

[3] Even if the linear propagation rate on a given boundary was the same, the depth perpendicular to the surface would be less in the S direction for a given linear length of propagation in the L, T, or S direction.
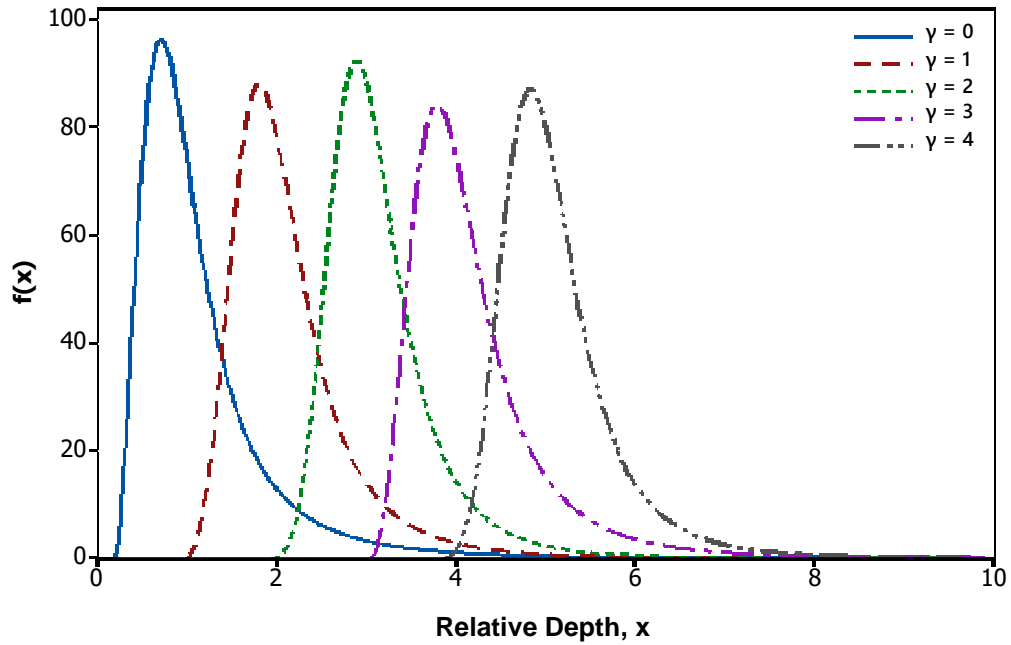
Figure 7.8. Influence of location factor, γ, on log-logistics probability distribution function, f(x), with a scale factor, δ, and a shape factor, α, of 1 and 3, respectively.

The IGC damage depth log-logistics distribution, ξ, as expressed in Equation 7.1, was unique for each combination of DoS, exposure time, and direction of propagation. For the model, the distribution ξ, as defined by its parameters, was standardized and calibrated to consider the influence of DoS for a time series independent of orientation of propagation. DoS was not assigned on a grain by grain basis based on individual grain properties in the Voronoi microstructure. Instead, the entire population of boundaries was assigned a probability of fast or slow IGC rate based on the overall alloy DoS value. The distribution of the IGC rates (i.e., dtC) followed the experimental log-logistics distribution ξ.
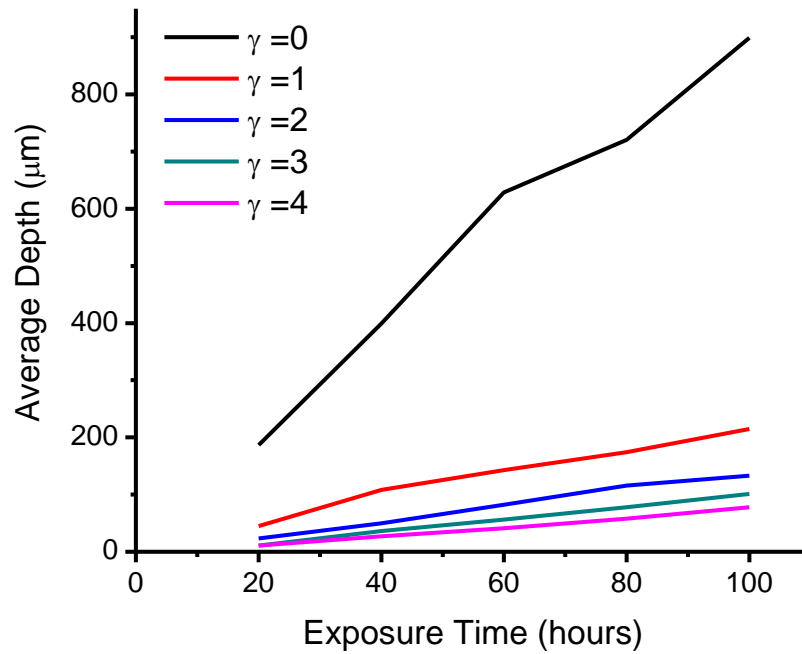
Figure 7.9. Effect of location factor, γ, on the average predicted IGC damage depth for a dtC log-logistics distribution with a fixed scale factor, δ, and a shape factor, α, of 0.3 and 3, respectively.

Previous analysis of IGC damage depth distribution and construction of CDF curves suggested that amongst the three parameters, DoS influenced the scale factor, δ, and the location factor, γ most significantly.[23] By definition, the location factor, γ, positions the distribution along the abscissa (i.e., the dtC rate, or the inverse of the IGC rate). Changing the value of γ has the effect of sliding the distribution and its associated function either to the left or to the right as shown in Figure 7.8. This parameter provides an estimate of the earliest time to corrode or dtC, or graphically, the dtC or damage depth at zero probability. A positive γ denotes that the time period from 0 to γ is a corrosion-free operating period. As such for fixed values of δ and α, an increase in γ reduced the damage depth (Figure

7.9). This implies that γ must be less than or equal to the shortest dtC. For this model, it was assumed that γ or the shortest dtC was zero, such that corrosion can commence immediately upon exposure.
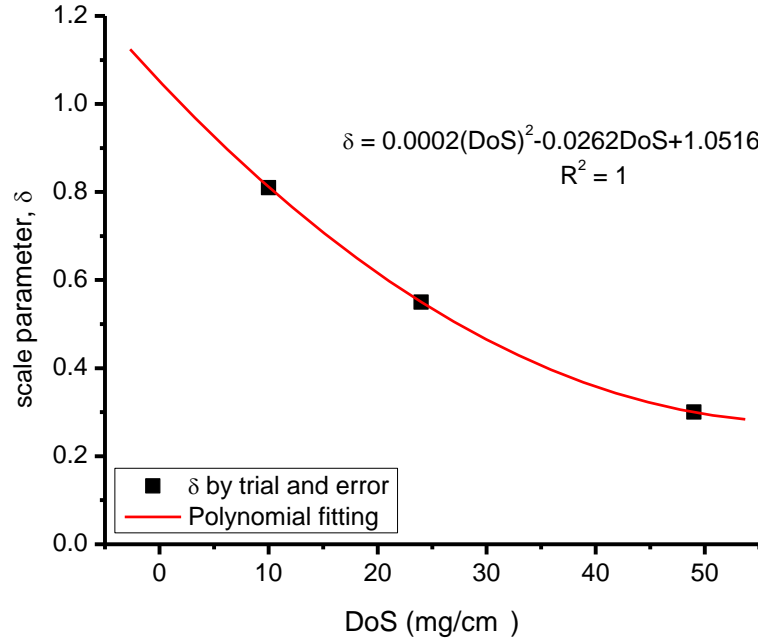
Figure 7.10. Model calibration showing relationship between log-logistics scale parameter, δ, and DoS for AA5083-H131 sensitized at 100°C.

With the value of γ fixed, the effect of DoS was incorporated via the scale factor, δ, or the distribution width. Given that the log-logistics distribution is a continuous probability distribution for a non-negative random number,[57] δ must have values greater than zero. Additionally, the median of a log-logistics distribution is equivalent to the sum of γ and δ. Because γ was set to zero, the median for the log-logistics distribution of dtC was simply δ. This indicates that increasing the value of δ would increase the median dtC, subsequently decreasing the IGC damage depth for a given propagation direction and exposure time. Thus,

the appropriate relationship must be that of a decreasing δ with increasing DoS.

Three experimental data points were used to calibrate the model and to provide an

expression for the relationship between δ and DoS. The experimental data points

used were limited to the average IGC damage depths, in the T direction after 100

hours in 0.6 M NaCl solution, pH 8.3 at -0.73 V_{SCE}, of specimens with DoS of 10,

24, and 49 mg/cm^2.[4] The suitable δ values found by trial and error for the given

DoS levels after sensitization at 100°C were fitted to a second order polynomial

expression as shown in Figure 7.10.

---

[4] In this type of database model of IGC, the variation of parameters in the log-logistics distribution can be readily updated to reflect material, metallurgical, or environmental conditions as available experimentally.
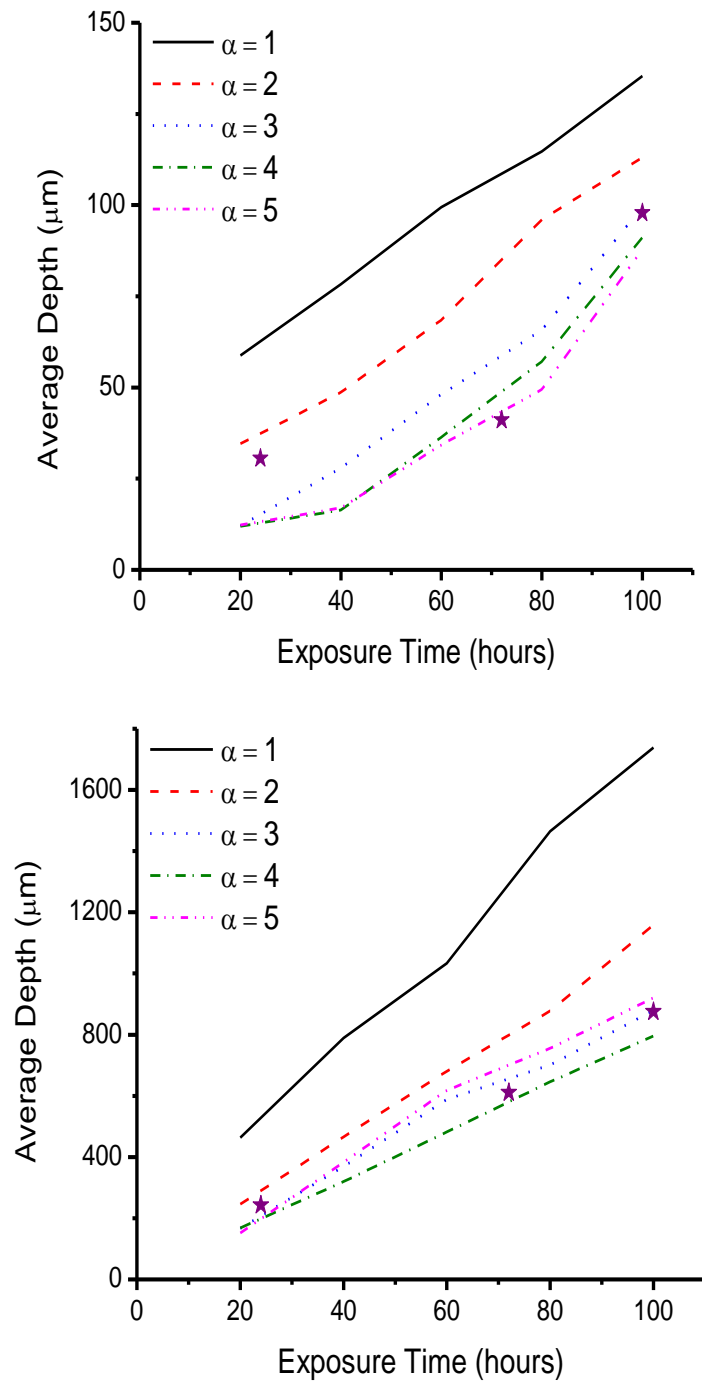
Figure 7.11. Influence of shape factor, α, on the simulated average IGC depth in the T direction predicted as a function of time for AA5083-H131 with a DoS of 10 mg/cm^2 (top) and a DoS of 49 mg/cm^2 (bottom). Experimental data for each DoS level, plotted as ★, were included for comparison purposes.
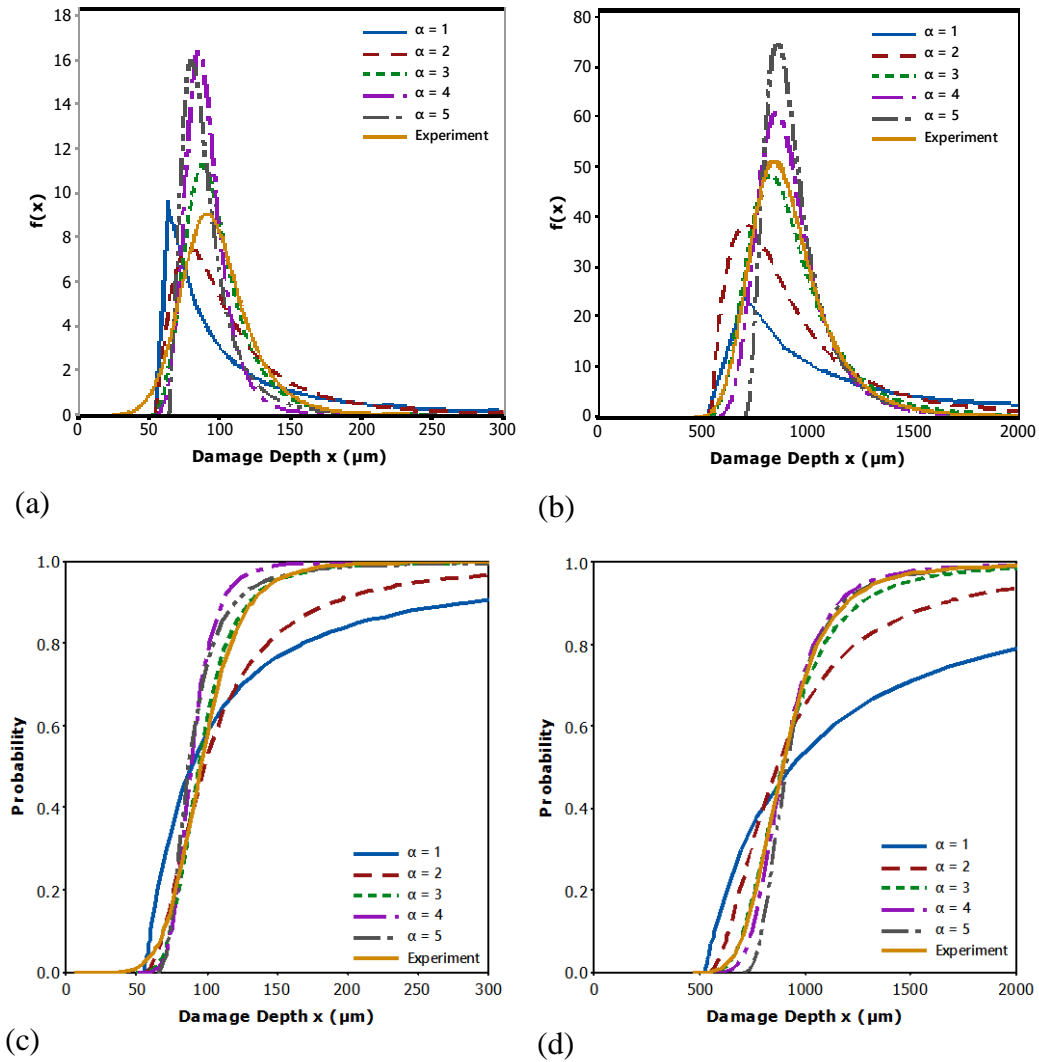
Figure 7.12. Influence of shape factor, α, on the IGC damage depth log-logistics PDF and CDF curves for 100 h and propagation in the T direction for AA5083-H131 with a DoS of 10 mg/cm^2 (a and c) and a DoS 49 mg/cm^2 (b and d). Experimental data for each DoS level were included for comparison purposes as solid orange curves.

Although DoS only has secondary effects on the shape factor, α, it is still imperative to define a set value for this parameter. By definition, α is the tilt or skewness of the distribution curve with respect to a cumulative probability of 0.5.

Simulations were carried out to test the sensitivity of this parameter on the IGC damage depth distribution, as well as the average IGC damage depth. The influence of α was examined on two sets of simulations: one at a low DoS of 10 mg/cm^2 ($\gamma=0$ and $\delta=0.81$) and another at a high DoS of 49 mg/cm^2 ($\gamma=0$ and $\delta=0.3$). The plots of average IGC damage depth as a function of exposure time (Figure 7.11) show that a shape factor of 2 and below overestimates average depths for both DoS levels. The effect of shape factor is also less significant for values ranging from 3 to 5. Further analysis was conducted based on the IGC damage depth distribution PDF and CDF curves (Figure 7.12), where an α value of 3 proved to have the closest fit in terms of skewness of the CDF curves, as well as the height of the PDF curves.

7.3.2.2.3 Model Validation

This model simulated the IGC propagation in AA5083-H131 with a single plate surface exposed to 0.6 M NaCl solution, pH 8.3 at -0.73 V_{SCE}, given the DoS and orientation of propagation. The IGC damage depth at a given exposure time was calculated as the distance between the exposed surface and the centroid of the farthest corroded facet. The IGC damage distribution, as well as the average damage depth, after 20, 40, 60, 80, and 100 h was reported for each simulation. Cross-section images illustrated IGC propagation morphology into the depth were generated for each exposure time step. The average IGC damage depth and the propagation morphology were validated by comparing the simulated results with the experimental results. Five different DoS conditions, ranging from 2 to 49 mg/cm^2, were used with the ST, LS, or LT surface exposed allowing IGC to

propagate in the in L, T, or S direction, respectively. A total of five Voronoi realizations, each with fifteen simulations, were completed for each combination of DoS and propagation direction.

7.4 Comparison of Simulated Results with Experimental Data

7.4.1 IGC Propagation Morphology

A series of time-dependent cross-sectional images generated from the model showing IGC propagation in the T directions for a DoS of 49 mg/cm^2 are displayed in Figure 7.13. The horizontal yellow grain boundaries associated with IGC grew from the left exposed surface towards the right in a relatively straight path, as expected for the T direction. The effect of exposure time was captured by the simulation as seen from the increase in damage depth (i.e., the distance from the exposed edge covered with yellow grain boundaries). After 20 hours, the cross-section image is dominated by red, intact corroded grain boundaries with a few corroded yellow grain boundaries. As exposure time progressed, the IGC had grown in depth and branched out extensively in the S direction, forming IGC networks.

The simulated cross-sectional images showing the IGC propagation in the L direction for five DoS levels after 100 hours of exposure is shown in Figure 7.14. The few short IGC damage depths illustrated in the low DoS of 2 and 10 mg/cm^2 resembled typical experimental IGC damage observations for sensitization conditions categorically considered as IGC resistant (< 15 mg/cm^2). For the IGC

susceptible DoS conditions, the effect of DoS was demonstrated by the increase in both the number of IGC fissures as well as depth of corrosion after a given time considering a DoS of 24 mg/cm^2 to DoS of 49 mg/cm^2.

Figure 7.13. Time-dependent simulated IGC damage propagation in the T direction from the exposed LS surface of AA5083-H131 alloy with DoS of 49 mg/cm^2 after (a) 20 hours, (b) 80 hours, and (c) 100 hours of exposure in 0.6 M NaCl solution, pH 8.3 at -0.73 V$_{SCE}$. IGC damage initiated at the exposed left vertical surface. The yellow lines are the corroded grain boundaries and the red lines are the non-corroded grain boundaries after the indicated exposure times. Note difference in magnification.

The simulated IGC results in the T and S directions for a DoS of 49 mg/cm^2 over a range of exposure times are shown in Figure 7.s 13 and 15. Propagation in the S direction followed a tortuous path, where IGC originated from the left surface, then branched and progressed in the perpendicular direction along the L direction, as initially anticipated in the brick wall models in Figure 7.7. On the contrary, propagation in T and L (Figure 7.s 13 and 14) directions followed a fairly direct path, in complete agreement with the IGC found in Figure 7.7 as well as in the cross-section image shown in Figure 7.2.

(a) DoS = 2 mg/cm^2 (b) DoS = 10 mg/cm^2

(c) DoS = 24 mg/cm^2 (d) DoS = 39 mg/cm^2 (e) DoS = 49 mg/cm^2
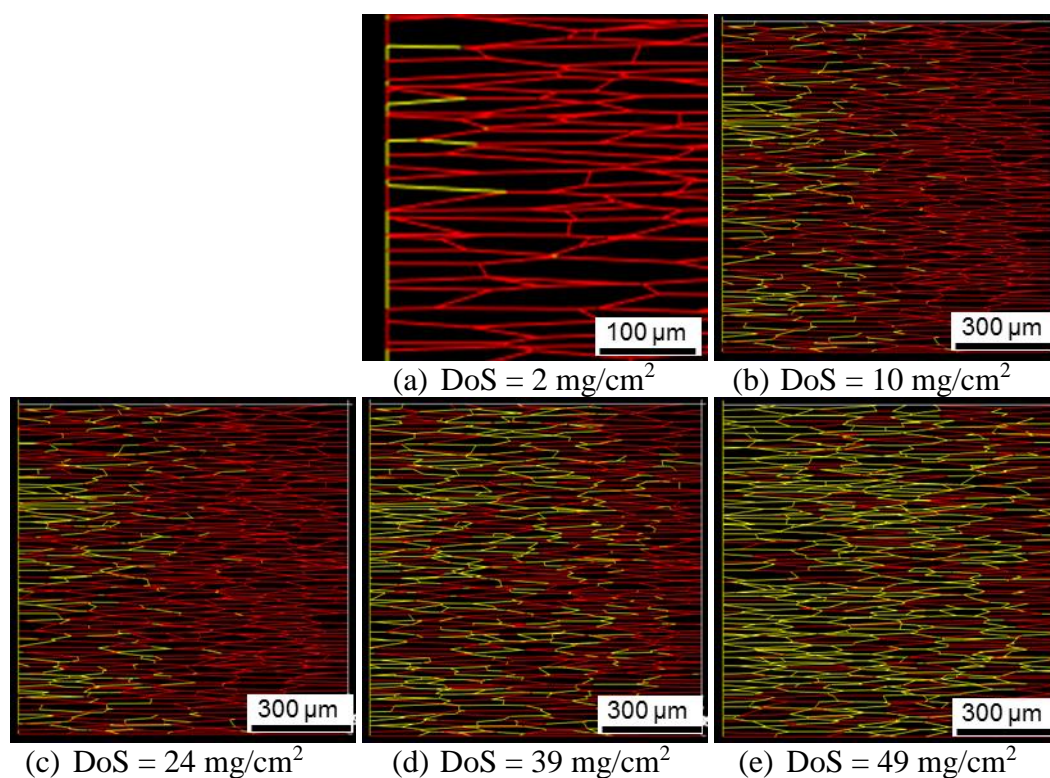
Figure 7.14. Simulated IGC damage propagation in the L direction from the exposed ST surface of AA5083-H131 with different degrees of sensitization (DoS) after 100 h of exposure in 0.6 M NaCl solution, pH 8.3 at -0.73 V$_{SCE}$. IGC damage was initiated at the exposed left vertical surface. The yellow lines are the corroded grain boundaries and the red lines are the non-corroded grain boundaries after the indicated exposure times. Note the difference in magnification.

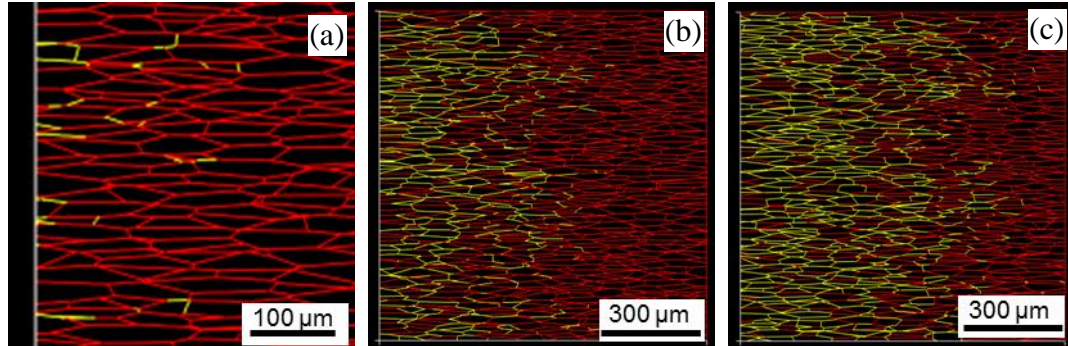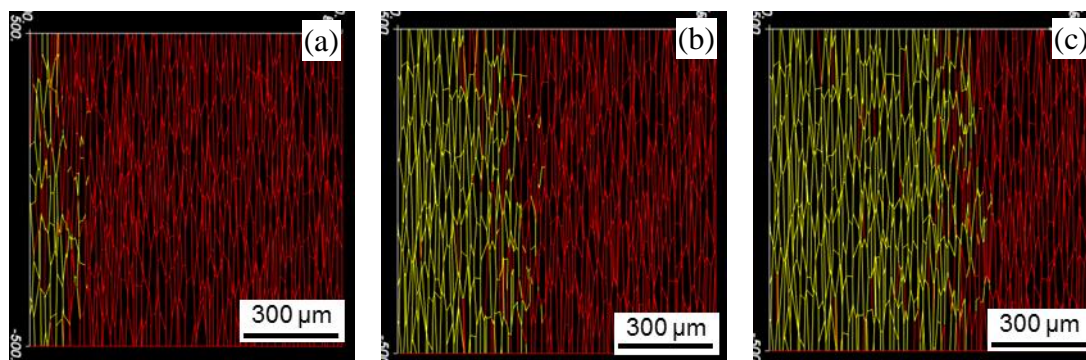Figure 7.15. Simulated IGC damage propagation in the S direction from the exposed LT surface of AA5083-H131 with DoS of 49 mg/cm^2 at different exposure times: (a) 20 h, (b) 80 h, and (c) 100 h. IGC damage initiated at the exposed left vertical surface. The yellow lines are the corroded grain boundaries and the red lines are the non-corroded grain boundaries after the indicated exposure times.

311

7.4.2   IGC Damage Depths

The average IGC damage depths taken from a total of 75 simulations for each combination of DoS and orientation of propagation are displayed as a function of exposure time for the five DoS conditions in the three propagation directions in Figure 7.s 16, 17, and 18. In each Figure 7., the lines represent the simulated data, whereas the experimental data are represented by the symbols. The circled data in Figure 7.16 are the experimental data used for calibrating the model. Although the model was calibrated with three experimental data points from the T direction, the simulated results were comparable with the experimental results, especially in the L direction. The model captured the observed dependencies of IGC damage depth on the exposure time, DoS, and orientation of propagation. Increasing the DoS increased the IGC damage depth for a given exposure time and orientation of propagation. Additionally, the influence of DoS was markedly displayed by the increase in the slopes of the IGC damage vs. time lines with DoS. The sharp increase in slope between DoS of 10 mg/cm^2 and 24 mg/cm^2 indicated a shift from IGC resistance to susceptibility, which was in complete agreement with the experimental results,[23] as well as with the sensitization categories suggested in the ASTM G-67 Standard.[26]   In terms of propagation direction, the model correctly simulated the anisotropy of IGC propagation rate, where the damage depths were shortest in the S direction, followed by that in the T direction, while depths were deepest in the L direction.
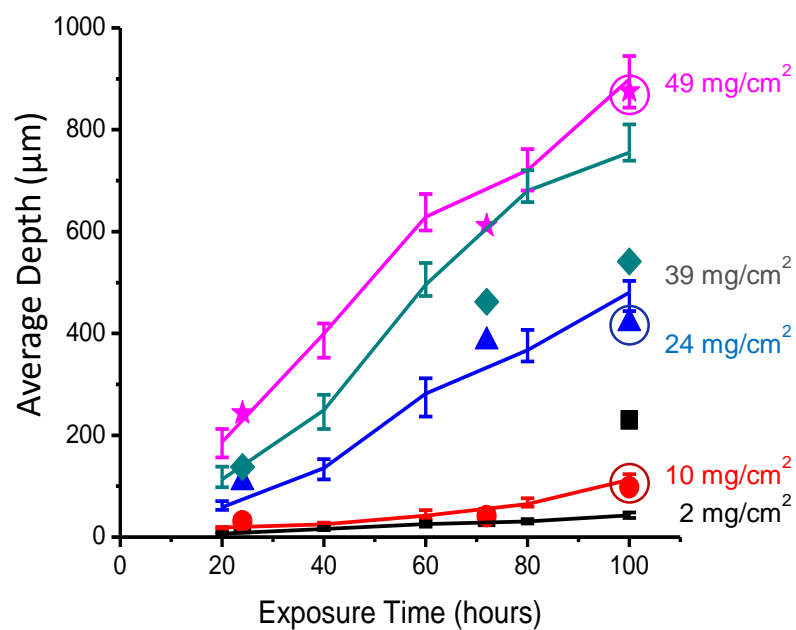
Figure 7.16. Average IGC damage depth in T direction from LS surface as a function of DoS and exposure time for AA5083-H131 in 0.6 M NaCl solution, pH 8.3 at -0.73 V_{SCE}. The simulated data after 5 realizations with 15 simulations each are shown as solid lines, with error bars representing one standard deviation in model outputs. The experimental average IGC damage depth data are presented in symbols, with model calibration points encircled.
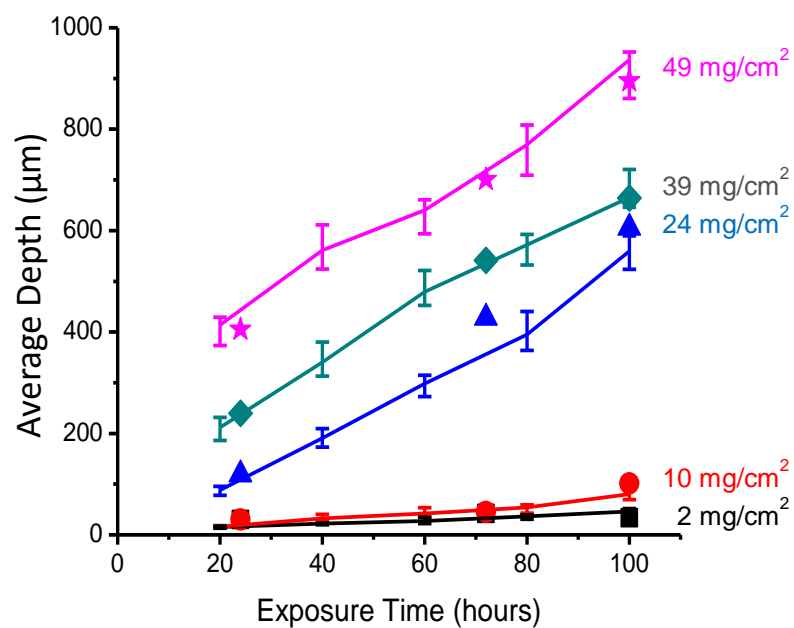
Figure 7.17. Average IGC damage depth in L direction from ST surface as a function of DoS and exposure time for AA5083-H131 in 0.6 M NaCl solution, pH 8.3 at -0.73 V_{SCE}. The simulated data after 5 realizations with 15 simulations each are shown as solid lines, with error bars representing one standard deviation in model outputs, whereas experimental average IGC damage depth data are presented in symbols.
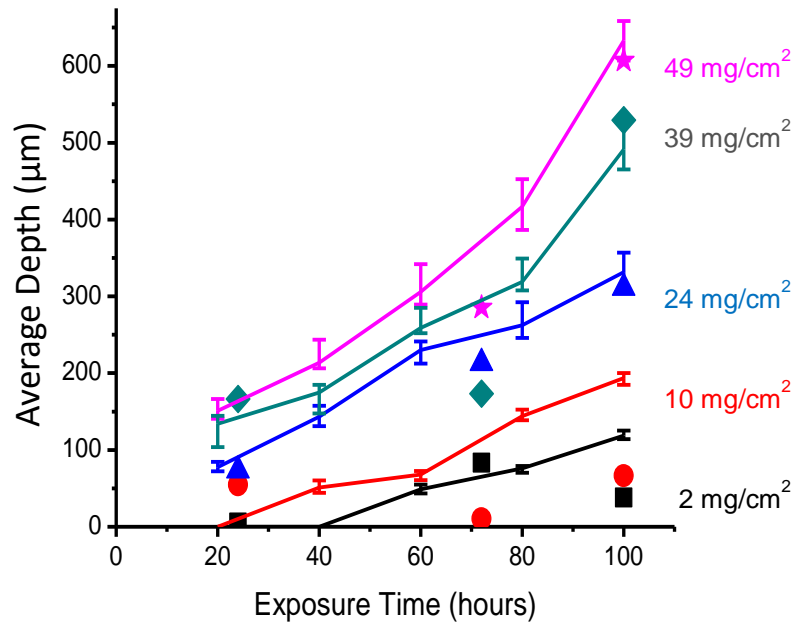
Figure 7.18. Average IGC damage depth in S direction from LT surface as a function of DoS and exposure time for AA5083-H131 in 0.6 M NaCl solution, pH 8.3 at -0.73 V_{SCE}. The simulated data after 5 realizations with 15 simulations each are shown as solid lines, with error bars representing one standard deviation in model outputs, whereas experimental average IGC damage depth data are presented in symbols.

7.5   Discussion

7.5.1   Relevance of the Model

The objective of this paper is to establish a 3-D granular model with the capability to output the statistically distributed depths of IGC damage propagation in a 5XXX alloy. Data for AA5083-H131, specifically, in 0.6 M NaCl solution as a function of exposure time, given the microstructure and the sensitization conditions were simulated. As discussed above, the simulated results were in agreement with the experimental observations of IGC damage depths (Figure 7.s 16 to 18). The model not only captures the dependencies of IGC propagation on

DoS and orientation of propagation, but also enables prediction of the IGC damage depth kinetics distribution. A second iteration of the model incorporating the influence of sensitization temperature, which includes another set of suiTable 7. δ values found by trial and error for the given DoS levels after sensitization at 80°C, was validated in two propagation directions, S and T.

The accurate time-dependent prediction of IGC damage depth distribution can be utilized in component life models as well as quantitative risk assessment. Literature provides numerous tools and models for predicting the evolution of cracks and component failure based on finite element analysis of the local stresses and linear elastic fracture mechanics.[58–62] However, the methodology for dealing with the evolution of the initial damage stages, which may occupy the most significant portion of component life, is less well developed. In the case of crack evolution from IGC controlled by metallurgical and electrochemical factors, the distributed nature of IGC damage depths and associated growth rates can provide a more realistic approach to address the steps leading up to crack evolution. Particularly, the damage distribution has to be understood and factored into models because cracks do not emanate only from the IGC sites with maximum damage depths. In SCC, crack initiation is primarily due to the stress amplification brought on by the initial localized corrosion damage sites.[63] Highly angular corrosion morphologies like that of IGC have crack-like shape that may influence stress intensity differently than a hemispherical pit. Additionally, the path tortuosity and branching of IGC as dictated by orientation of propagation (i.e., the exposed

316

surface) have an added effect on stress intensity. Multiple neighboring IGC sites that are sufficiently close to each other can brought on interactive effects on the stress intensity along the inner portions of IGC, thereby causing accelerated cracking.[64,65] The capability of a cracking model to capture a starting damage due to IGC could significantly enhance the prediction of subcritical crack growth-to-failure, better guide determination of inspection and maintenance schedules, and improve component life assessment in general. Thus, this 3-D granular IGC model can be used as a process model to provide the necessary initial damage distribution for cracking models developed for AA5083-H131 in seawater environment.

7.5.2   Accuracy of the Model

The model predicted the trend of increasing IGC damage depths with exposure time, with the simulated and experimental data for propagation in the L direction (Figure 7.17) corresponding very well for all exposure times. However for the damage depths in the S and T directions, suiTable 7. values were estimated for exposure times of 24 and 100 h, while those for 72 h were overpredicted. The IGC anisotropy in the model is dictated by the grain aspect ratios in the Voronoi cell structure and Q_{corr}. Between these two governing factors, it is speculated that the discrepancy in the results is associated with Q_{corr}. In Equation 7.2, dtC is exponentially proportional to Q_{corr} with 0.5 as the exponential parameter. For propagation in the L direction, Q_{corr} takes the value of 1, remaining constant regardless of the exponential parameter, and does not have an effect on dtC.

317

However Q_{corr} values for the T and S directions are not equal to 1, subsequently influencing dtC. As such, there exists a directionality dependence of dtC on Q_{corr}, as controlled by the assigned Q_{corr} values, the exponential parameter, or both. Calibration of these parameters will have to be considered for future iterations of this IGC model.

7.5.3   Limitations of the Model

The fundamental steps in the overall process of IGC development involve IGC initiation and spreading, IGC propagation, IGC stifling, and IGC arrest.[21] Because the model was built on empirical experimental observations, one of the major limitations of the model is that it can only be used to predict damage depths within the parameter space for which they are created. The model was based on a maximum exposure time of 100 h, over which the IGC propagation rate is constant with respect to time.[23] At longer exposure times, IGC can stifle and cease to propagate and this stage was not modeled. Recent electrochemical tests on sensitized AA5083-H131 involving longer exposure times, 480 h and 960 h, have shown some indications of IGC stifling.[66] IGC stifling likely occurs due to the ohmic potential drop associated with the current flowing through the fissure solution of finite resistance, which decreases the potential at the fissure tip as the IGC propagates. This limitation highlights the significance of both the applied potential at the fissure mouth and the residual potential at the fissure tip. Related studies[24,25] have shown that up to 100 h, IGC propagation rate depends linearly

318

on applied potential, with the existence of a threshold potential below which no IGC was observed. The potential dependence of IGC propagation was reported to increase with increasing DoS. On the contrary, the dependency of IGC propagation on the residual potential at the fissure tip is complicated by the need to quantify the fissure tip potential itself. The residual potential at the fissure tip will depend on both the fissure geometry including path tortuosity and the local chemistry changes as a result of the anodic dissolution, the hydrolysis of the metal cations, the hydrogen bubbles generated, the corrosion products formed, the ingress of the Cl^- anions from the bulk environment, the effective length of the fissure, and cathode area relative to the anode fissure tip. As such, a more rigorous model for local chemistry and fissure tip potential prediction, in conjunction with the knowledge of linear dependence on potential, is require for utilization as a feedback process in order to define the appropriate IGC propagation rate using a detailed electrochemical model.

The utility of a Voronoi cell structure is that it accurately depicts the grain structure of AA5083-H131. However, there are other microstructural features, such as β-phase precipitates and constituent particles, which also contribute to IGC evolution. The current model assumed that DoS parameter is a reasonable first approach to encapsulate sensitization on the microstructural level. Studies[23,24] involving the individual effects of sensitization temperature and cold work temper on sensitization and IGC propagation revealed that IGC propagation rates are different as a function of thermo-mechanical processing with the same DoS. It was

speculated that the different IGC propagation rates could indicate the influence of temperature and cold work on the β-phase precipitation kinetics, subsequently influencing the β-phase morphology and β-phase distribution at the grain boundaries versus that in the matrix.

Moreover, the amount of the β-phase, as well as the proximity of these β-phase precipitates along a boundary path, aids the progression of IGC.[20,23,28] IGC spreading studies also observed a decrease in β-phase precipitate spacing for the LS and ST surfaces in comparison to the LS surface.[29] The IGC propagation through these discontinuous anodic path is dependent on the length of α-matrix or the β-phase precipitate spacing that has to be corroded through.[21] As such, the β-phase number density and spacing describe length scales vital to IGC propagation.   Additionally, precipitation of β-phase also occur near constituent particles.[18,19,67] Jain, et al.[28] found that microgalvanic coupling between cathodic constituent particles and the alloy increases the initial dissolution probability of the β-phase precipitates present around the constituent particles. Therefore, β-phase precipitates and constituent particles distribution studies are necessary to facilitate better microstructure representation of the sensitized alloys. Another limitation is the assumption of immediate IGC propagation upon exposure. In the present model, the existence of incubation period,[23] the slight delay caused by any altered surface layer,[68] and IGC spreading[20] phenomenon were not considered.   Phenomenological models developed for IGC propagation have established the existence of an incubation time under potentiostatic conditions that

decreases with increased DoS and potential.[23] It is suggested that the incubation period is the time necessary for β-phase breakdown or for a chain of β-phase pits to develop into a network of IGC. The probability of spreading is dependent on the spacing of β-phase precipitates.[20] The larger spacing in low DoS conditions limits chances of spreading and resulted in more random pitting events on the surface, delaying IGC depth penetration. On the contrary, the shorter spacing in high DoS conditions aided spreading and yielded IGC networks on the surface, creating multiple IGC penetration sites. While IGC propagation into the depth commenced and progresses, IGC spreading on the surface can still continue. This combined IGC phenomenon gives rise to IGC fissures of varying damage depth. The combination of IGC spreading and IGC propagation will not only yield more accurate damage depth distributions, but would also provide a three-dimensional initial damage distribution that is more applicable for cracking and component life models.

7.5.4 Design of Materials

In addition to forecasting damage evolution, the utility of a validated model is in its ability to inform attributes or conditions critical to material design. One parameter that is critical to both risk assessment and IGSCC modeling is the allowable or critical corrosion penetration depth. In this case, the model can be used to inform conditions at which IGC is within the allowable damage depth. For instance, Figure 7.16 indicates the large difference between the IGC depths after

100 hours for a DoS of 24 mg/cm^2 versus that for a DoS of 10 mg/cm^2. Despite the difference, the latter still achieved a depth of 94 µm, which could potentially be higher than a designated corrosion allowance. Should that be the case, a material with a DoS level of 10 mg/cm^2, although designated as IGC resistant as per ASTM G-67, will be deemed unsatisfactory.

The effect of orientation of propagation on IGC in terms of morphology and depth profiles, as depicted by the model (Figure 7.s 13 to 18), denotes the significance of grain shape for material design. For a rolled microstructure, exposing the plate surface orthogonal to the rolling direction or ST surface to corrosive media leads to worst IGC depth damages, whereas plate surface parallel to the rolling direction or LT surface leads to more grain-fall out, and potential exfoliation damages. Moreover, this implies that materials with small equiaxed grains, given the same DoS, will have isotropic IGC behavior, with shallower depth profiles and extensive grain fall-out. The predicted depths in the L or T directions can be utilized in conjunction with DoS for making go/no go decisions as described above. On the other hand, the predicted depth in the S direction or grain fall-out can be exploited for corrosion allowance on material thickness in structure design.

7.6   Conclusions

A 3-D granular model that simulates IGC damage propagation in AA5083-H131 was developed. The model developed utilizes experimentally acquired microstructure geometry and IGC damage depth distributions as inputs. IGC

damage progression was simulated through the model grain boundary facet by grain boundary facet. Although parameters used in the model were calibrated with limited IGC damage data from the T direction, both the predicted IGC propagation kinetics and the predicted IGC damage morphology in all three directions were in good agreement with the experimental results. The model successfully captured the dependencies of IGC damage depth with exposure time, DoS, and orientation of propagation, assuming an infinite cathode in this version of the model. Such model can be utilized as a process model input in cracking models to guide maintenance schedule and predict component life of structures made with this alloy class.

7.7 Acknowledgement

7.8 References

[1]   G.C. Blaze, Alcoa Green Letter: The 5000 Series Alloys SuiTable 7. for Welded Structural Applications, Aluminum Corporation of America, New Kensington, PA, 1972.

[2]   R.L. Holtz, P.S. Pao, R.A. Bayles, T.M. Longazel, R. Goswami, Corrosion-Fatigue Behavior of Aluminum Alloy 5083-H131 Sensitized at 448 K (175 °C), Metall. Mater. Trans. A. 43 (2011) 2839–2849. doi:10.1007/s11661-011-0866-x.

[3]   I.N.A. Oguocha, O.J. Adigun, S. Yannacopoulos, Effect of sensitization heat treatment on properties of Al–Mg alloy AA5083-H116, J. Mater. Sci. 43 (2008) 4208–4214. doi:10.1007/s10853-008-2606-1.

[4]   J.L. Searles, P.I. Gouma, R.G. Buchheit, Stress Corrosion Cracking of Sensitized AA5083 (Al-4.5Mg-1.0Mn), Mater. Sci. Forum. 396 (2002) 1437–1442. doi:10.4028/www.scientific.net/MSF.396-402.1437.

[5]   J.L. Searles, P.I. Gouma, R.G. Buchheit, Stress corrosion cracking of sensitized AA5083 (Al-4.5Mg-1.0Mn), Metall. Mater. Trans. A. 32 (2001) 2859–2867. doi:10.1007/s11661-001-1036-3.

[6]   A.J. Davenport, Y. Yuan, R. Ambat, B.J. Connolly, M. Strangwood, A. Afseth, et al., Intergranular Corrosion and Stress Corrosion Cracking of Sensitised AA5182, Mater. Sci. Forum. 519-521 (2006) 641–646. doi:10.4028/www.scientific.net/MSF.519-521.641.

[7]   D.R. Baer, C.F. Windisch, M.H. Engelhard, M.J. Danielson, R.H. Jones, J.S. Vetrano, Influence of Mg on the corrosion of Al, J. Vac. Sci. Technol. A. 18 (2000) 131–136. doi:10.1116/1.582129.

[8]   G.M. Scamans, Low Temperature Sensitization of AA5XXX Alloys, Innoval, Oxon, UK, 2008.

[9]   G.M. Scamans, N.J.H. Holroyd, C.D.S. Tuck, The role of magnesium segregation in the intergranular stress corrosion cracking of aluminium alloys, Corros. Sci. 27 (1987) 329–347.

[10]   R.H. Jones, D.R. Baer, M.J. Danielson, J.S. Vetrano, Role of Mg in the stress corrosion cracking of an Al-Mg alloy, Metall. Mater. Trans. A. 32 (2001) 1699–1711.

[11]   J.S. Vetrano, R.E. Williford, S.M. Bruemmer, R.H. Jones, Influence of microstructure and thermal history on the corrosion susceptibility of AA 5083, in: Alum. Alloys, Orlando, FL, 1997.

[12]   R.H. Jones, J.S. Vetrano, C.F. Windisch, Stress Corrosion Cracking of Al-Mg and Mg-Al Alloys, Corrosion. 60 (2004) 1144–1154. doi:10.5006/1.3299228.

[13]   C. Crane, R. Gangloff, Stress Corrosion Cracking of Al-Mg Alloy 5083 Sensitized at Low Temperature, Corrosion. (2015). doi:10.5006/1766.

[14] N. Birbilis, R. Zhang, S. Knight, R. Holtz, R. Goswami, C. Davies, A Survey of Sensitisation in 5xxx series Aluminium Alloys, Corrosion. (2015). doi:10.5006/1787.

[15] H. Yukawa, Y. Murata, M. Morinaga, Y. Takahashi, H. Yoshida, Heterogeneous distributions of Magnesium atoms near the precipitate in Al-Mg based alloys, Acta Metall. Mater. 43 (1995) 681–688. doi:10.1016/0956-7151(94)00266-K.

[16] S. Nebti, D. Hamana, G. Cizeron, Calorimetric study of pre-precipitation and precipitation in Al-Mg alloy, Acta Metall. Mater. 43 (1995) 3583–3588. doi:10.1016/0956-7151(95)00023-O.

[17] F.J. Esposto, C.-S. Zhang, P.R. Norton, R.S. Timsit, Segregation of Mg to the surface of an Al-Mg single crystal alloy and its influence on the initial oxidation at room temperature, Surf. Sci. 302 (1994) 109–120. doi:10.1016/0039-6028(94)91101-0.

[18] R. Goswami, G. Spanos, P.S. Pao, R.L. Holtz, Precipitation behavior of the ß phase in Al-5083, Mater. Sci. Eng. A. 527 (2010) 1089–1095. doi:10.1016/j.msea.2009.10.007.

[19] R. Goswami, G. Spanos, P.S. Pao, R.L. Holtz, Microstructural Evolution and Stress Corrosion Cracking Behavior of Al-5083, Metall. Mater. Trans. A. 42 (2010) 348–355. doi:10.1007/s11661-010-0262-y.

[20] S. Jain, M.L.C. Lim, J.L. Hudson, J.R. Scully, Spreading of intergranular corrosion on the surface of sensitized Al-4.4Mg alloys: A general finding, Corros. Sci. 59 (2012) 136–147. doi:10.1016/j.corsci.2012.02.018.

[21] E. Bumiller, Intergranular corrosion in AA5XXX aluminum alloys with discontinuous precipitation at the grain boundaries, PhD Dissertation, University of Virginia, 2011.

[22] N. Birbilis, R.G. Buchheit, Electrochemical Characteristics of Intermetallic Phases in Aluminum Alloys - An Experimental Survey and Discussion, J. Electrochem. Soc. 152 (2005) B140–B151. doi:10.1149/1.1869984.

[23] M.L.C. Lim, J.R. Scully, R.G. Kelly, Intergranular Corrosion Penetration in an Al-Mg Alloy as a Function of Electrochemical and Metallurgical Conditions, Corrosion. 69 (2013) 35–47. doi:10.5006/0722.

[24] M.L.C. Lim, J.R. Scully, R.G. Kelly, Critical Electrochemical Conditions for Intergranular Corrosion in Sensitized AA5083-H131, in: Dep. Def. Corros. Conf., NACE International, 2013.

[25] D. Mizuno, R.G. Kelly, Galvanically Induced Intergranular Corrosion of AA5083-H131 Under Atmospheric Exposure Conditions: Part 1—Experimental Characterization, Corrosion. 69 (2013) 580–592. doi:10.5006/0812.

[26] ASTM, ASTM: G67-04 Standard Test Method for Determining the Susceptibility to Intergranular Corroaion of 5XXX Series Aluminum Alloys by Mass Loss After Exposure to Nitric Acid (NAMLT Test), ASTM International, West Conshocken, PA, 2004.

[27] E. Herzberg, The annual cost of corrosion for DoD, in: Dep. Def. Corros. Conf., McLean, VA, 2009.

[28] S. Jain, J.L. Hudson, J.R. Scully, Effects of constituent particles and sensitization on surface spreading of intergranular corrosion on a sensitized AA5083 alloy, Electrochimica Acta. 108 (2013) 253–264. doi:10.1016/j.electacta.2013.06.036.

[29] S. Jain, Surface Spreading of Intergranular Corrosion on Stainless Steels and Al-Mg (AA5XXX) Alloys, PhD Dissertation, University of Virginia, 2011.

[30] D. Mizuno, R.G. Kelly, Galvanically Induced Intergranular Corrosion of AA5083-H131 Under Atmospheric Exposure Conditions: Part 2—Modeling of the Damage Distribution, Corrosion. 69 (2013) 681–692. doi:10.5006/0813.

[31] S. Zhao, D.A. Wolfe, T.-S. Huang, G.S. Frankel, Generalized model for IGC growth in aluminum alloys, J. Stat. Plan. Inference. 137 (2007) 2405–2412. doi:10.1016/j.jspi.2006.09.021.

[32] W. Zhang, S. Ruan, D.A. Wolfe, G.S. Frankel, Statistical model for intergranular corrosion growth kinetics, Corros. Sci. 45 (2003) 353–370. doi:10.1016/S0010-938X(02)00090-2.

[33] T.-S. Huang, S. Zhao, G.S. Frankel, D.A. Wolfe, A Statistical Model for Localized Corrosion in 7xxx Aluminum Alloys, Corrosion. 63 (2007) 819–827. doi:10.5006/1.3278431.

[34]   S. Ruan, D.A. Wolfe, G.S. Frankel, Statistical modeling and computer simulation of intergranular corrosion growth in AA2024-T3 aluminum alloy, J. Stat. Plan. Inference. 126 (2004) 553–568. doi:10.1016/j.jspi.2003.08.008.

[35]   S. Ruan, D.A. Wolfe, W. Zhang, G.S. Frankel, Statistical Modeling of Minimum Intergranular Corrosion Path Length in High-Strength Aluminum Alloy, Technometrics. 46 (2004) 69–75. doi:10.1198/004017004000000121.

[36]   T. Shibata, Corrosion probability and statistical evaluation of corrosion data, in: R.W. Revie (Ed.), Uhligs Corros. Handb., 2nd ed., New York, NY, 2000: pp. 367–392.

[37]   T. Shibata, T. Takeyama, Stochastic Theory of Pitting Corrosion, Corrosion. 33 (1977) 243–251. doi:10.5006/0010-9312-33.7.243.

[38]   P.M. Aziz, Application of the Statistical Theory of Extreme Values To the Analysis of Maximum Pit Depth Data for Aluminum, Corrosion. 12 (1956) 35–46. doi:10.5006/0010-9312-12.10.35.

[39]   R.B. Mears, R.H. Brown, Corrosion Probability, Ind. Eng. Chem. 29 (1937) 1087–1091. doi:10.1021/ie50334a002.

[40]   M. Akashi, Localized Corrosion (Current Japanese Materials Research), in: F. Hine, K. Komai, K. Yamakawa (Eds.), Elsevier Applied Science, London and New York, 1988: pp. 176–196.

[41]   F.F. Booth, G.E.G. Tucker, Statistical Distribution of Endurance In Electrochemical Stress-Corrosion Tests, Corrosion. 21 (1965) 173–178. doi:10.5006/0010-9312-21.5.173.

[42]   W.L. Clarke, G.M. Gordon, Investigation of Stress Corrosion Cracking Susceptibility of Fe-Ni-Cr Alloys in Nuclear Reactor Water Environments, Corrosion. 29 (1973) 1–12. doi:10.5006/0010-9312-29.1.1.

[43]   R.W. Staehle, J.A. Gorman, K.D. Stravropoulos, C.S. Welty Jr., Application of statistical distributions to characterizing and predicting corrosion of tubing in steam generators of Pressurized Water Reactors, in: R.N. Parkins (Ed.), Life Predict. Corrodible Struct., NACE International, Houston, TX, 1994: pp. 1374–1399.

[44]   J. Stewart, D.B. Wells, P.M. Scott, D.E. Williams, Electrochemical noise measurements of stress corrosion cracking of sensitised austenitic stainless

steel in high-purity oxygenated water at 288°C, Corros. Sci. 33 (1992) 73–88. doi:10.1016/0010-938X(92)90018-X.

[45] J.E. Strutt, J.R. Nicholls, B. Barbier, The prediction of corrosion by statistical analysis of corrosion profiles, Corros. Sci. 25 (1985) 305–315. doi:10.1016/0010-938X(85)90109-X.

[46] Y. Kondo, Prediction of Fatigue Crack Initiation Life Based on Pit Growth, Corrosion. 45 (1989) 7–11. doi:10.5006/1.3577891.

[47] R.W. Staehle, Bases for predicting the earliest failures due to stress corrosion cracking, in: R.H. Jones (Ed.), Chem. Electrochem. Corros. Stress Corros. Crack. Symp. Honor. Contrib. RW Staehle, TMS, Warrendale, PA, 2001: pp. K1–K92.

[48] M.J. Robinson, N.C. Jackson, The influence of grain structure and intergranularcorrosion rate on exfoliation and stress corrosion crackingof high strength Al–Cu–Mg alloys, Corros. Sci. 41 (1999) 1013–1028. doi:10.1016/S0010-938X(98)00171-1.

[49] R.E. Melchers, Modeling of Marine Immersion Corrosion for Mild and Low-Alloy Steels—Part 1: Phenomenological Model, Corrosion. 59 (2003) 319–334. doi:10.5006/1.3277564.

[50] A. Turnbull, L.N. McCartney, S. Zhou, A model to predict the evolution of pitting corrosion and the pit-to-crack transition incorporating statistically distributed input parameters, Corros. Sci. 48 (2006) 2084–2105. doi:10.1016/j.corsci.2005.08.010.

[51] P. Novak, R. Yuan, B.P. Somerday, P. Sofronis, R.O. Ritchie, A statistical, physical-based, micro-mechanical model of hydrogen-induced intergranular fracture in steel, J. Mech. Phys. Solids. 58 (2010) 206–226. doi:10.1016/j.jmps.2009.10.005.

[52] C.B. Barber, D.P. Dobkin, H. Huhdanpaa, The Quickhull Algorithm for Convex Hulls, ACM Trans Math Softw. 22 (1996) 469–483. doi:10.1145/235815.235821.

[53] D. Scotto D'Antuono, J. Gaies, W. Golumbfskie, M.L. Taheri, Grain boundary misorientation dependence of β phase precipitation in an Al–Mg alloy, Scr. Mater. 76 (2014) 81–84. doi:10.1016/j.scriptamat.2014.01.003.

[54] N. Birbilis, The influence of grain size and grain orientation on sensitisation in AA5083, Corrosion. (2015). doi:10.5006/1703.

[55]   Y. Zhao, M.N. Polyakov, M. Mecklenburg, M.E. Kassner, A.M. Hodge, The role of grain boundary plane orientation in the β phase precipitation of an Al–Mg alloy, Scr. Mater. 89 (2014) 49–52. doi:10.1016/j.scriptamat.2014.07.003.

[56]   A.J. Hayter, Probability and Statistics for Engineers and Scientists, 3rd ed., Thomson Brooks/Cole, Belmont, CA, 2007.

[57]   N.L. Johnson, S. Kotz, N. Balakrishnan, Continuous Univariate Distributions, 2nd ed., John Wiley & Sons, New York, NY, 1995.

[58]   A.S. Kobayashi, S.T. Chiu, R. Beeuwkes, A numerical and experimental investigation on the use of J-integral, Eng. Fract. Mech. 5 (1973) 293–305. doi:10.1016/0013-7944(73)90024-6.

[59]   H. Andersson, The steadily growing, elastic-plastic crack tip in a finite element treatment, Int. J. Fract. 9 (1973) 231–233. doi:10.1007/BF00041867.

[60]   N. Moes, J. Dolbow, T. Belytschko, A finite element method for crack growth without remeshing, International Journal for Numerical Methods in Engineering. 46 (1999) 131–150.

[61]   AFGROW Reference Manual (4.0), Wright-Patterson Air Force Base, AFRL/VASM, 2003.

[62]   NASGRO Reference Manual (version 4.02), NASA Johnson Space Center and Southwest Research Institute, 2002.

[63]   E. McCafferty, Introduction to Corrosion Science, Springer, New York, NY, 2010.

[64]   A.P. Jivkov, N.P.C. Stevens, T.J. Marrow, A three-dimensional computational model for intergranular cracking, Comput. Mater. Sci. 38 (2006) 442–453. doi:10.1016/j.commatsci.2006.03.012.

[65]   K. Kishimoto, W.O. Soboyejo, J.F. Knott, R.A. Smith, A numerical investigation of the interaction and coalescence of twin coplanar semi-elliptical fatigue cracks, Int. J. Fatigue. 11 (1989) 91–96. doi:10.1016/0142-1123(89)90003-0.

[66]   S. Hallman, Unpublished Work, (2013).

[67]   L. Tan, T.R. Allen, Effect of thermomechanical treatment on the corrosion
        of AA5083, Corros. Sci. 52 (2010) 548–554.
        doi:10.1016/j.corsci.2009.10.013.

[68]   J. Seong, F. Yang, F. Scheltens, G.S. Frankel, N. Sridhar, Influence of the
        Altered Surface Layer on the Corrosion of AA5083, J. Electrochem. Soc.
        162 (2015) C209–C218. doi:10.1149/2.0321506jes.